Neo - Tectonic and Rock Magnetic Study of the Circum Troodos Sedimentary Succession, Cyprus

by

France Lagroix

Neo-Tectonic and Rock Magnetic Study of the Circum Troodos Sedimentary Succession, Cyprus

by
France Lagroix

Submitted in partial fulfilment of
the requirements for the degree of

Master of Science

Supervisor: Dr. Graham J. Borradaile

Department of Geology
Lakehead University
Thunder Bay, Ontario
Canada
November, 1999

Lakehead University
OFFICE OF GRADUATE STUDIES AND RESEARCH

Name of Student: France Lagroix

Title of Thesis: Neo-Tectonic and Rock Magnetic Study of the Circum Troodos Sedimentary Succession, Cyprus

Degree Awarded: Master of Science

This thesis has been prepared under my supervision and the candidate has complied with the Master's regulations.

GJBorradaile

Signature of Supervisor

June 11, 1999

Date

Abstract

The Circum Troodos Sedimentary Succession (Late Cretaceous to Recent) overlies the Troodos ophiolite of Cyprus, located in the Eastern Mediterranean. The pattern of neo-tectonic deformation was investigated through magnetic analysis of the tectonic petrofabrics. Anisotropy of magnetic susceptibility (AMS), anisotropy of anhysteretic remanence magnetization (AARM) and hysteresis loop parameters were determined in order to define the magnetic fabric and the magnetic mineralogy.

The study area extends over approximately 1000 km^2 mainly to the south of the exposed Troodos ophiolite. The sample suite includes 432 oriented hand samples, predominantly of the Lefkara and Pakhna Formations.

Field measurements indicate bedding predominantly dips less than 10° to the south, while stylolitic cleavage dips steeper than bedding in various directions. The bedding-cleavage relationship yields variable vergence directions suggesting gravity sliding of the sediments towards local sedimentary basins. Southwest of the Limassol Forest Block axial planar cleavage consistently defines a SW vergence with respect to bedding due to a locally different, Early to Middle Miocene compression along NNE to NE - SSW to SW azimuth.

Hysteresis loop analysis show that pseudo-single domain magnetite is the ferromagnetic contributor. Furthermore, in 71% of the samples, the ferromagnetic contribution provided more than 50% of the total susceptibility. Thus, the petrofabrics of traces of magnetite largely control the magnetic fabrics.

The AMS fabric, in part tectonic, is controlled by the preferred crystallographic orientation of diamagnetic calcite and paramagnetic clay minerals, as well as magnetite. Orientation directions of the principal axes relative to bedding and cleavage indicate incomplete overprinting of the primary sedimentary fabric in many cases. AMS foliation preferentially dips shallowly to the east and west. AMS lineation varies regionally, from west to east across the study area, from a NNE to NNW trends, respectively. The tectonic AMS fabric registers either a late Miocene supra-subduction extension regime due to southward migration of the reactivation Cyprean Arc or due to Pleistocene gravity sliding due to uplift of the Troodos Ophiolite Complex.

The AARM fabric is controlled exclusively by the preferred dimensional orientation of pseudo single domain magnetite. Excluding the area in proximity to the Limassol Forest Block, the AARM fabric orientations are regionally consistent. AARM foliation planes dip ~45° to the NW and AARM lineation is directed NE and SW, almost orthogonal to AMS lineation. In some cases, in proximity to the Limassol Forest, the AARM lineation results from the combined magnetic fabrics, parallel to cleavage and bedding and is parallel to the bedding-cleavage intersection lineation. The actual extension direction is to the WNW, represented by the $AARM_{int}$ principal axes. Southwest of the Limassol Forest Block the AARM fabric registers the Early to Middle Miocene SW- NE compression, and its tectonic expression is conventional, with $AARM_{max}$ oriented NW and SE, perpendicular to the maximum compression direction.

Acknowledgements

This project was funded by a Natural Sciences and Engineering Research Council of Canada (NSERC) research grant to Dr. Graham J. Borradaile. The rock magnetics laboratory at Lakehead University was funded throughout the years also by NSERC.

Numerous people made this project possible and should be acknowledge. First and foremost, my supervisor, Dr. G. J. Borradaile for giving me the opportunity to do this project, for enriching my knowledge of rock magnetics, and providing guidance and constructive criticism throughout all stages of this project.

I would like to thank Dr. Xenophontos and his colleagues at the Geological Survey of Cyprus for providing informational field excursions while in Cyprus. Thanks to Graham Borradaile for collecting a preliminary oriented sample suite during the 1997 field season and for his assistance during the 1998 field season in collecting over 400 samples and taking numerous field measurements. I would also like to acknowledge an undergraduate assistant, Mariah Mailman, who also helped with sampling.

Completing the seemingly endless task of reorienting, trimming and drilling the samples, in preparation for analysis, would not have been possible without the help of Anne Hammond. Sam Spivak provided valuable drafting advice and material which increase efficiency. Photographs of samples in Chapter 6 were taken by Peter Puna.

Finally, I would like to thank my family and friends for their love, support and encouragements.

Table of Content

List of Figures

List of Tables

Chapter 1 - Tectonic Evolution of Cyprus

Located in the eastern Mediterranean Sea, the island of Cyprus contains three tectonic terrains: the Kyrenia Terrain, the Mamonia Terrain and the Troodos Terrain (Figure 1-1). The purpose of this chapter is to outline chronologically the events which amalgamated these three Terrains to form the present geological configuration of Cyprus. Tectonic events which would contribute to the evolution of Cyprus began during the Permian.

1.1 Permian

The palaeogeography during the Permian places Gondwanaland to the South and Laurasia to the north separated by the Paleo-Tethys Sea (Figure 1-2). Shallow water limestones that accumulated on the northward dipping continental shelf of Gondwanaland are presently exposed in the eastern parts of the Kyrenia Terrains. These limestones form part of the Kantara Formation and represent the oldest rocks in Cyprus (Roberston and Woodcock, 1986). The transition from the Permian to the Triassic was marked by the breaking up of the northern margin of Gondwanaland driven by continental rifting and the opening of Neo-Tethys (Robertson, 1990).

1.2 Triassic

Continental rifting of Gondwanaland's northern margin produced a multitude

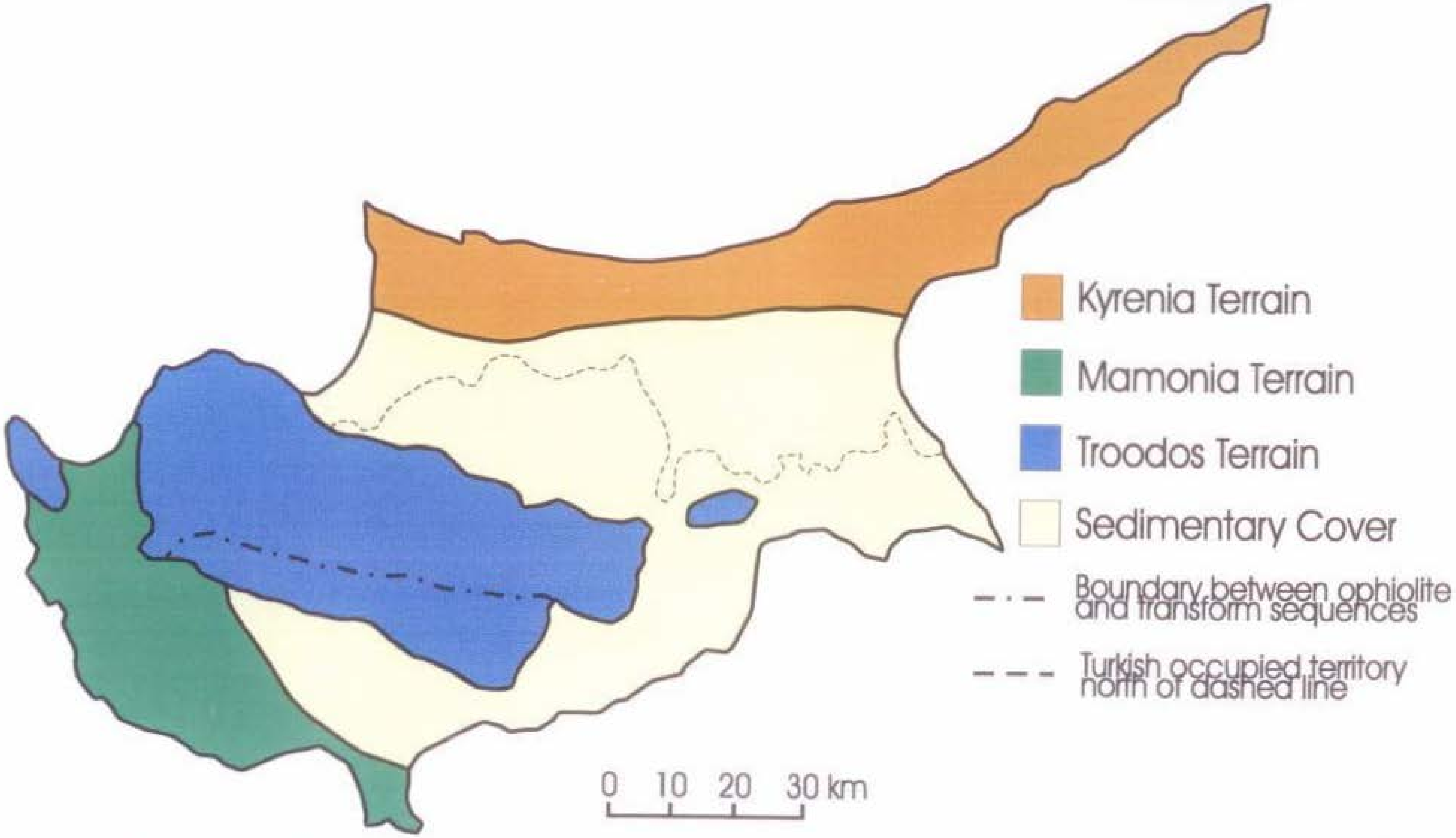

Figure 1-1 Spatial distribution of the tectonic terrains of Cyprus. (Government of Cyprus, Ministry of Agriculture, Natural Resources and Environment, 1995)

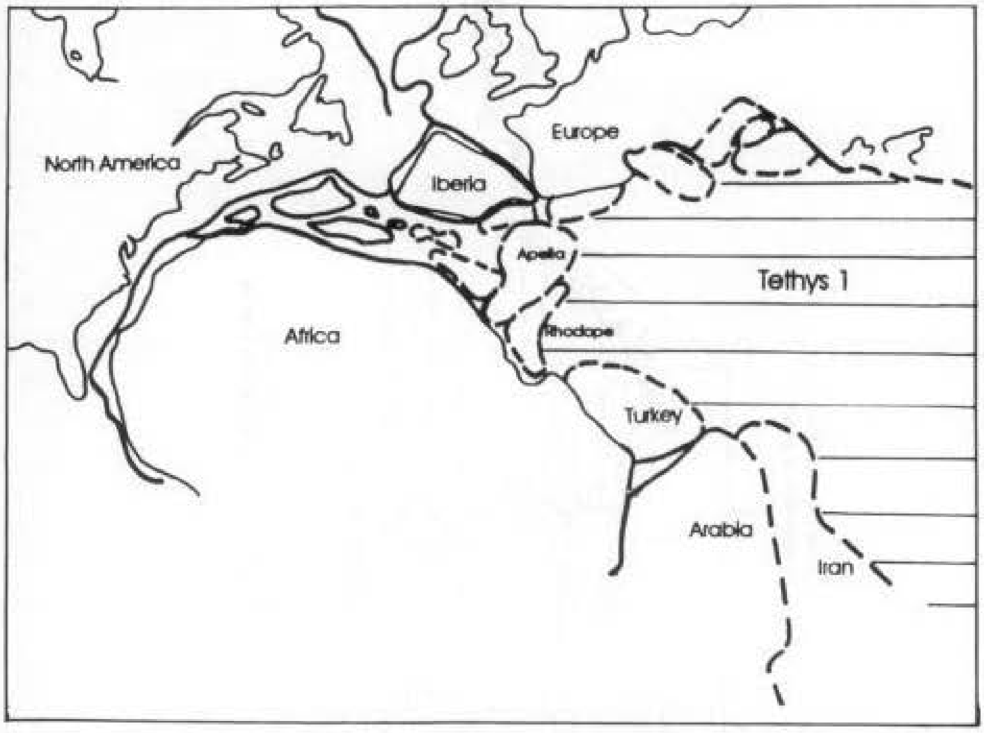

Figure 1-2 Proposed paleogeographic reconstruction of the North American, Europian and African continents for the Permian - Triassic transition period. Numerous microcontinents were present due to rifting, only a few are labelled here. Tethys 1 in the diagram is equivalent to Paleo-Tethys mentioned in the text (from Dewey *et al.*, 1973).

of microcontinents separating the Paleo- and Neo- Tethys Seas. It is suggested that the Mamonia Terrain originated as a microcontinental margin. Whether the Kyrenia Terrain formed as a microcontinent or formed an independent platform is still unknown (Robertson, 1990). Today, these microcontinents are predominantly scattered along the northern coast of the Mediterranean Sea. Evidence of Triassic continental rifting is seen within the lithology of the Mamonia Terrain.

The Mamonia Terrain comprises two rock groups. The sedimentary, Ayios Photios Group, documents the early stages of deposition within the continental rift, occurring in fault-bounded grabens. The volcanic, Dhiarizos Group, records the

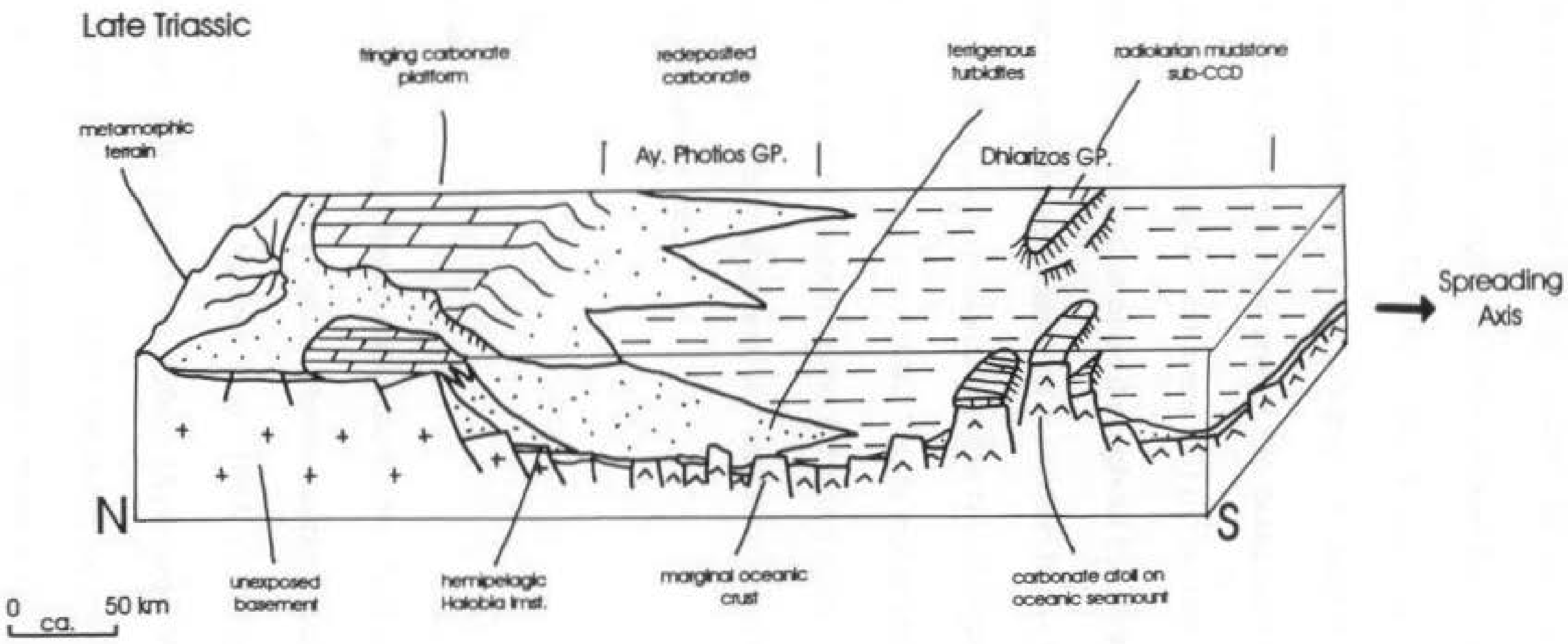

Figure 1-3 Block diagram of the Mamonia Terrain developing as a continental rift - small ocean basin during the Late Triassic. Metamorphic terrain in the diagram may represent a microcontinent which rifted from the northern margin of Gondwanaland (from Robertson, 1990).

volcanism related to the continental rifting initiated during the Late Triassic (Robertson and Woodcock, 1979). Figure 1-3 reconstructs the relationship of the two rock groups of the Mamonia Terrain within a continental rift system. Allochthonous material within the Ayios Photios sediments implies that sedimentation occurred on a margin near one of the detached microcontinents (represented by the metamorphic terrain in Figure 1-3) (Robertson, 1990).

The Neo-Tethys Sea continued to open throughout the Jurassic and Early Cretaceous. The African plate moved eastward in relation to the Eurasian plate and promoted spreading and strike-slip motion within the Neo-Tethyan Sea (Figure 1-4a). During the Middle Cretaceous (after 119Ma) plate motion changed and the African plate veered northward in relation to the Eurasian plate (Livermore and Smith, 1984) (Figure 1-4b). The change in plate tectonics initiated subduction, perhaps along existing strike-slip faults.

1.3 Late Cretaceous

1.3.1 *Troodos Terrain*

The converging plate setting initiated subduction within the Neo-tethyan Sea. The favoured model for genesis of the Troodos ophiolite supports supra-subduction zone spreading (Pierce *et al.*, 1984; Moores *et al.*, 1984; Clube and Robertson, 1986; Gass, 1990; Murton, 1990; Robertson, 1990). Miyashiro (1973) prefers an island setting for the Troodos ophiolite genesis model based on geochemical data. However, the well developed sheeted dike complex, that overlies the harzburgite

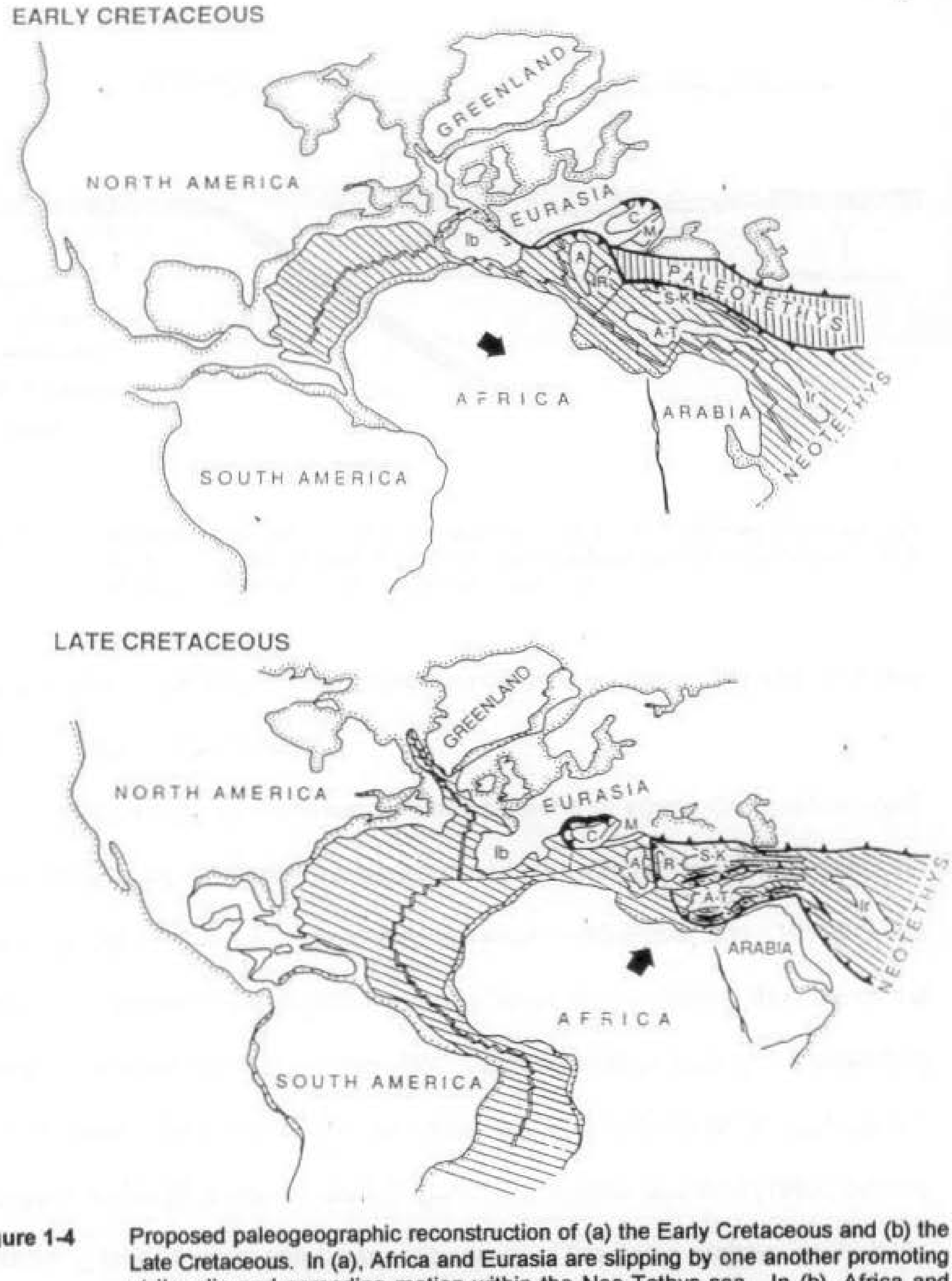

Figure 1-4 Proposed paleogeographic reconstruction of (a) the Early Cretaceous and (b) the Late Cretaceous. In (a), Africa and Eurasia are slipping by one another promoting strike-slip and spreading motion within the Neo-Tethys sea. In (b), Africa and Eurasia are converging promoting subduction within the Neo-Tethys sea. Arrows indicate the motion of Africa in relation to Eurasia. Key to abbreviations: A = Apelia, A-T = Anatolide-Tauride platform, C = Carnics, Ib = Iberia, Ir = Iran, M = Moesia, R = Rhodope, S-K = Sakarya-Kirsehir blocks (from Dilek *et al.*, 1990).

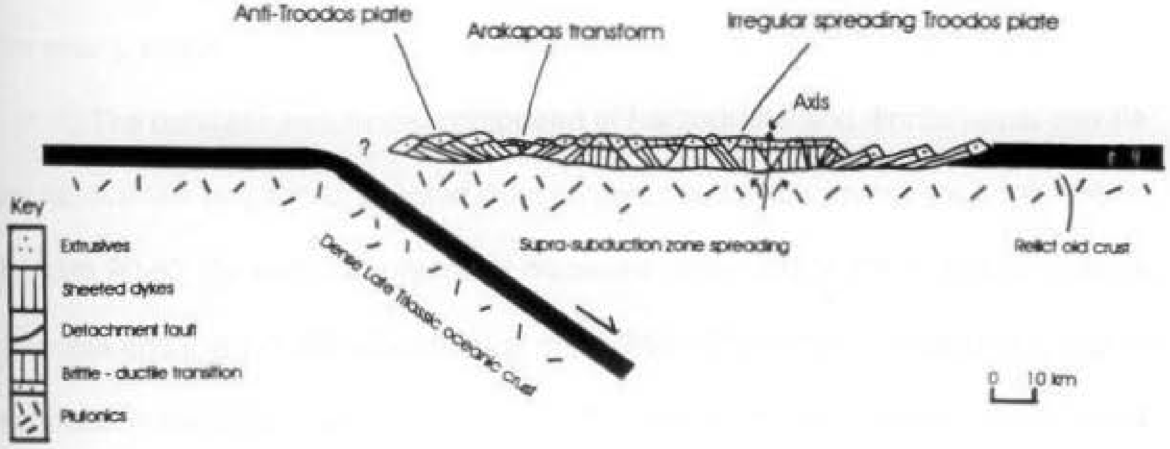

Figure 1-5 Suggested tectonic setting for the genesis of the Troodos ophiolite above an intra-oceanic subduction zone during the Late Cretaceous (from Robertson, 1990; spreading fabric based on Allerton and Vine, 1987).

core of Troodos, presents compelling evidence for a spreading component to the model (Robinson *et al.*, 1983).

Initially, subduction consumed small portions of young Cretaceous crust. Denser Triassic crust entering the trench caused the hinge of the subduction zone to migrate backward (i.e., oceanward or southward)(Robertson, 1990). The backward migration of the subduction zone hinge line increased the size of the mantle wedge above the subducting plate. Decompressing, melting and upwelling of the asthenosphere produced the spreading fabric observed throughout the Troodos ophiolite (Robertson, 1990) (Figure 1-5). Allerton and Vine (1987) defined a spreading fabric from a paleomagnetic survey of the Solea graben, in which the restoration of both dike samples to vertical and primary remanent magnetization to a derived structurally corrected remanent magnetization direction. Results indicated that dike rotations were consistent with the structure developing through an axial process.

The ophiolite sequence, composed of harzburgite and diorite upper mantle rocks, overlain by gabbro, sheeted dyke complex and pillow lavas sequence, began to form 90-92 Ma ago and presently occupies about 2/3 of the island of Cyprus (Bloome and Irwin, 1985; Staudigel *et al.*, 1986). The tectonic setting of a supra-subduction zone is the most widely accepted view for the formation of the Troodos ophiolite. The Troodos Terrain preserved relicts of the spreading axis as well as the transform fault. The Arakapas fault zone, which runs E-W, represents the remnant of a transform fault. The Solea Graben, oriented N-S and located north of Mt. Troodos, is thought to have been the spreading axis which contributed primarily to the formation of the Troodos ophiolite (Allerton and Vine, 1991). Younger crust formed along the Larnaca Graben, east of the Solea Graben, following an eastward jump of the ridge axis. The ridge migrated east after spreading ceased along the Solea Graben and the Arakapas transform fault became inactive. However, to accommodate spreading of the Lanarca Graben, a new transform fault, with a slightly more northerly orientation, extended at the eastern end of the Arakapas fault zone (Figure 1-6) (Allerton and Vine, 1991).

1.3.2 *Microplate Rotation*

The most significant tectonic activity during the Late Cretaceous, is the initiation of microplate rotation. Figure 1-7 illustrates the tectonic setting of the Troodos microplate and the surrounding Arabian, African and Turkish plates in

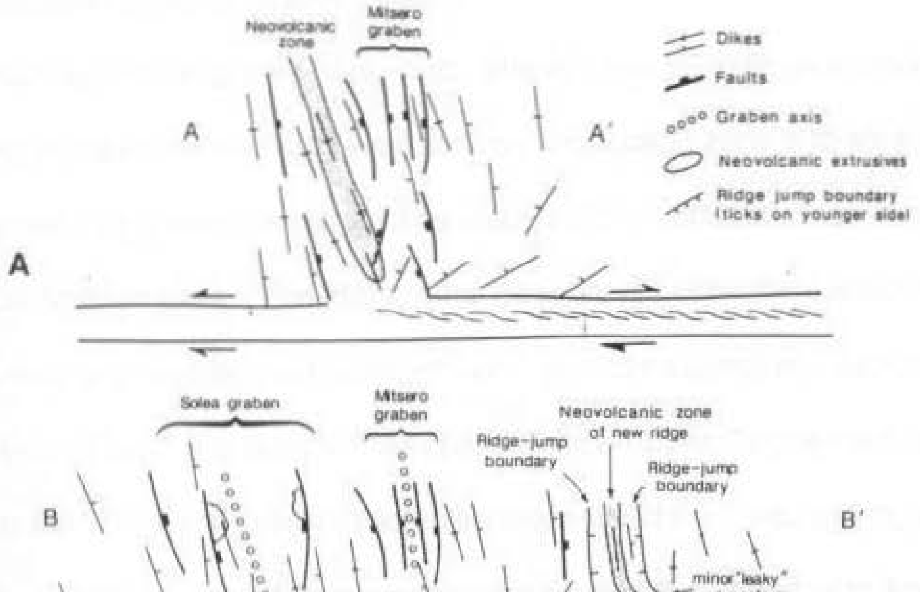

Figure 1-6 Spreading ridge axis and transform fault setting during the formation of the Troodos ophiolite. **A**: Illustrates the intersection between the dextrally moving Arakapas transform fault and the spreading axis labelled neo-volcanic zone. **B**: Spreading ceased and the Solea Graben is formed in the final stages of amagmatic spreading. A new dextrally moving transform fault accommodates spreading along a new spreading axis where young crustal material forms. **C**: Final stage of amagmatic spreading forms the Lamaca Graben (from Allerton and Vine, 1991). The geographical position of A and B can be seen in C. In C, the outline shows the whole of the Troodos Ophiolite terrain.

order to understand how the rotation began.

The African plate migrated northward. The Arabian plate or promontory, to the east, then collided with the east-west striking subduction zone and spreading centre that produced new ocean floor. The initial collision obducted some ocean floor onto the Arabian plate. The Hatay and Baer-Bassit ophiolites, exposed in southern Turkey and northern Syria respectively, provide evidence of obduction. Furthermore, the Hatay and Baer-Bassit ophiolite (pre-Upper Campanian) are of similar age to the Troodos ophiolite (Santonian to Maastrichtian; Robertson, 1990; Blome and Irwin, 1985). Continuous northward motion of the African and Arabian plates initiated an anticlockwise rotation of the microplate around a pivot point. Stable magnetization vectors with a uniform westerly azimuth retained for the Troodos ophiolite, the Arakapas transform fault, and the anti-Troodos plate (Limassol forest) indicate these areas were all within the boundaries of the rotating microplate. Similar preliminary analysis of rock samples from the Mamonia Terrain indicates that it was not within the boundaries of the rotating microplate and consequently suffered a different tectonic history (Clube and Robertson, 1986). It is also suggested that the collision and onset of rotation halted the spreading above the subduction zone (Robertson, 1990).

Palaeomagnetic studies provide the best evidence for microplate rotation. The stable characteristic part of the natural remanent magnetism (NRM) vector was isolated through thermal demagnetization and subsequent principal component analysis (PCA) of samples from various stratigraphic layers of the Troodos terrain.

These clearly illustrate the rotation. The present magnetic earth field (PEF) for Cyprus has a declination and inclination of 3° and 51° (calculated with the computer program Definitive International Geomagnetic Reference Field v. 1.4).

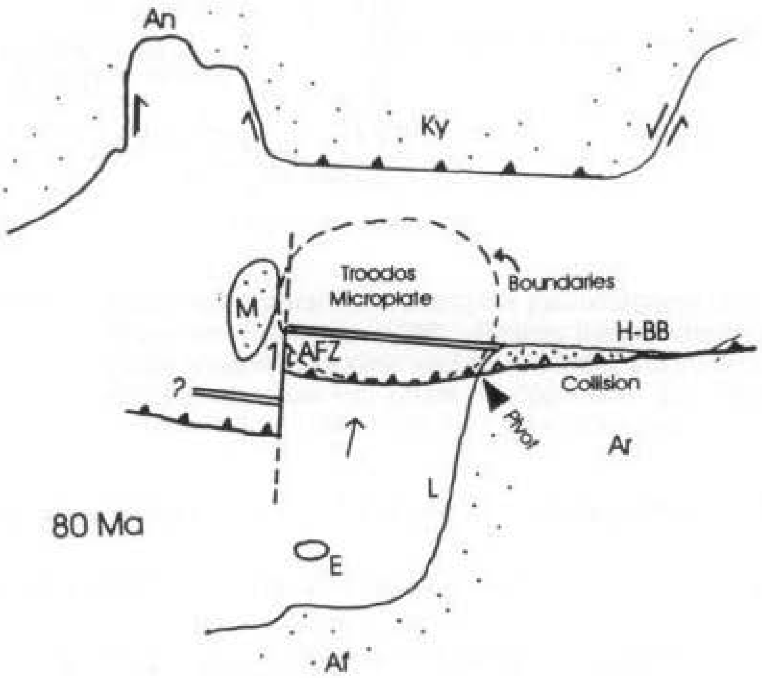

Figure 1-7 Tectonic setting for the initiation of microplate rotation during the Late Cretaceous. Key to abbreviations: Af = Africa, An = Antalya, Ar = Arabia, AFZ = Arakapas Fault Zone, E = Erastothenes Seamount, H-BB = Hatay and Baer-Bassit ophiolite, Ky = Kyrenia, L = Levant, M = Mamonia (from Robertson, 1990).

The oldest stratigraphic layer within the Troodos Terrain is the Troodos pillow lava sequence. Thermal demagnetization of the lavas isolated stable NRM vectors with declinations of 274°. The Umber Formation, interbedded with the Troodos lavas has a stable NRM vector declination of 279°. Radiolarites of the Perapedhi Formation (83-73 Ma) overlying Troodos lavas and umbers have a stable

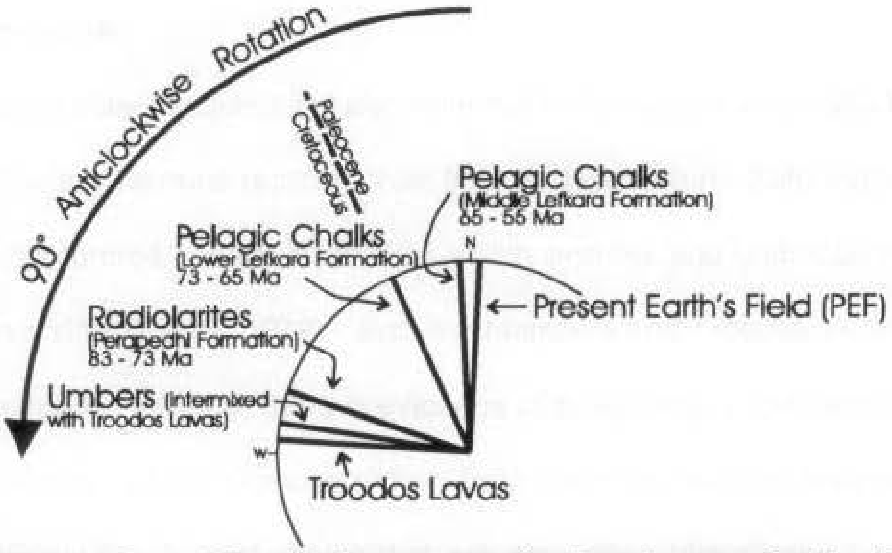

Figure 1-8 Schematic diagram presenting the paleomagnetic data of Clube and Robertson (1986). Plotting the declinations of stable remanent magnetic vectors illustrates the 90 degree anticlockwise rotation, where 60 degrees of the rotation occurred prior to the end of the Late Cretaceous.

NRM vector with a declination of 289°. The Late Cretaceous pelagic chalks of the Lefkara Formation (73-65 Ma) have stable NRM vector declination of 336° (paleomagnetic data: Clube and Robertson, 1986). Therefore, by the end the Cretaceous, The Troodos microplate had already undergone a 60 degrees anticlockwise rotation (Figure 1-8).

An additional 20 degrees of anticlockwise rotation occurred during the early Tertiary. Pelagic chalks of the Middle Lefkara Formation of Paleocene age (65-55 Ma) have stable NRM vectors with declinations of 357° (Clube and Robertson, 1986). Overall, between the Late Cretaceous and the Early Eocene, only some 25 Ma, the Troodos microplate underwent a 90 degree anticlockwise rotation to its present day geographical position (Figure 1-8).

1.4 Paleocene

Besides plate rotation, the Paleocene marks the period where the Mamonia and the Troodos Terrains reached their final amalgamation. Suturing is evident from the undeformed Lefkara Formation which overlies and unites both terrains (Robertson and Woodcock, 1979). Both the Mamonia and Troodos Terrains were then submerged. However, there is evidence of shallowing of the seas along the northern margins of the Troodos terrain from the presence of ferruginous and stratigraphically condensed chalks that are also often bioturbated (Robertson, 1977).

1.5 Eocene

The beginning of the Eocene period marks the end of the microplate rotation. Tectonic activity to the north (along the Eurasian plate southern margin) sends a compressional front southward. The Anatolian microcontinent, which also detached itself from the northern margin of Gondwanaland during the Triassic and migrated north, finally reaches the Eurasian plate. The collision closes up the ocean basin and raises the Kyrenia range in northern Cyprus. A compressional front migrates backward and thrusting the uplifted Kyrenia range southward, closer to the Troodos and Mamonia Terrains (Robertson and Woodcock, 1986).

1.6 Oligocene - Miocene

Closure of the oceanic basin, during the Eocene, and continued northward motion of the African plate caused northward underthrusting, which possibly reactivated zones of weakness. Possibilities include the relict Cretaceous subduction zone or the microplate boundary faults or both (Robertson, 1990). Whether or not an existing zone of weakness was reactivated, underthrusting occurred in approximately the same geographical area as the present Cyprean Arc. Underthrusting was never extensive, ($\leq$500 km) because of the slow movement of the African plate. In turn, major arc volcanism did not occur. Furthermore, underthrusting uplifted the Troodos and the Mamonia Terrains to form shallow seas and lagoonal environments. To the north of Troodos underthrusting caused the Kyrenia range to subside (Robertson, 1990). The Arakapas fracture zone, located south of Troodos, opened and thrusted southward producing the Yeresa fold and thrust belt (Robertson, 1977).

The Mid to Late Miocene period is marked by extensional growth faulting particularly to the north and northwest of Troodos (Follows and Robertson, 1990). The Polis graben, in the northwestern area of Cyprus resulted from extensional faulting. Before the end of the Miocene period sudden uplift raised most of Cyprus above sea level (Robertson, 1977).

1.7 Pliocene

During the Pliocene, a more localized uplift of Troodos subsided the surrounding areas (McCallum and Robertson, 1990). The overall tectonic regime from the Pliocene period to the present is extensional in nature. The extension direction ranges from NNW-SSE to NNE-SSW (Lapierre *et al.*, 1988). North of Troodos normal faulting produced half-grabens, such as the Ovgos fault, resulted from the extensional tectonic regime. Following the faulting, the Ovgos graben filled with 700 m of ophiolite derived clastics. The Kyrenia range north of the Ovgos fault remains a low landmass during the Pliocene (Robertson, 1990).

1.8 Pleistocene

The Pleistocene hosted the last drastic uplift. For the first time, all three tectonic terrains were uplifted as one unit. Even though the uplift was regional, extending some 250 km offshore eastward, the Mount Olympus area was uplifted more dramatically than anywhere else. This localized uplift is evident by the radial pattern of alluvial fans around Mount Troodos (Robertson, 1990).

The mechanism which could produce such a drastic localized uplift is still debated. A popular model suggests underthrusting of a microcontinent or seamount accompanied by serpentinite diapirism and upward movement of other fluids emanating from the downgoing slab. Underthrusting would also have reactivated the Troodos-Kyrenia boundary resulting in compression and uplift of the Kyrenia range to its present elevation (Robertson, 1990).

1.9 Recent

Presently the plate tectonic configuration around Cyprus has the Cyprean Arc running in an approximately east-west direction south of Cyprus. The Cyprean

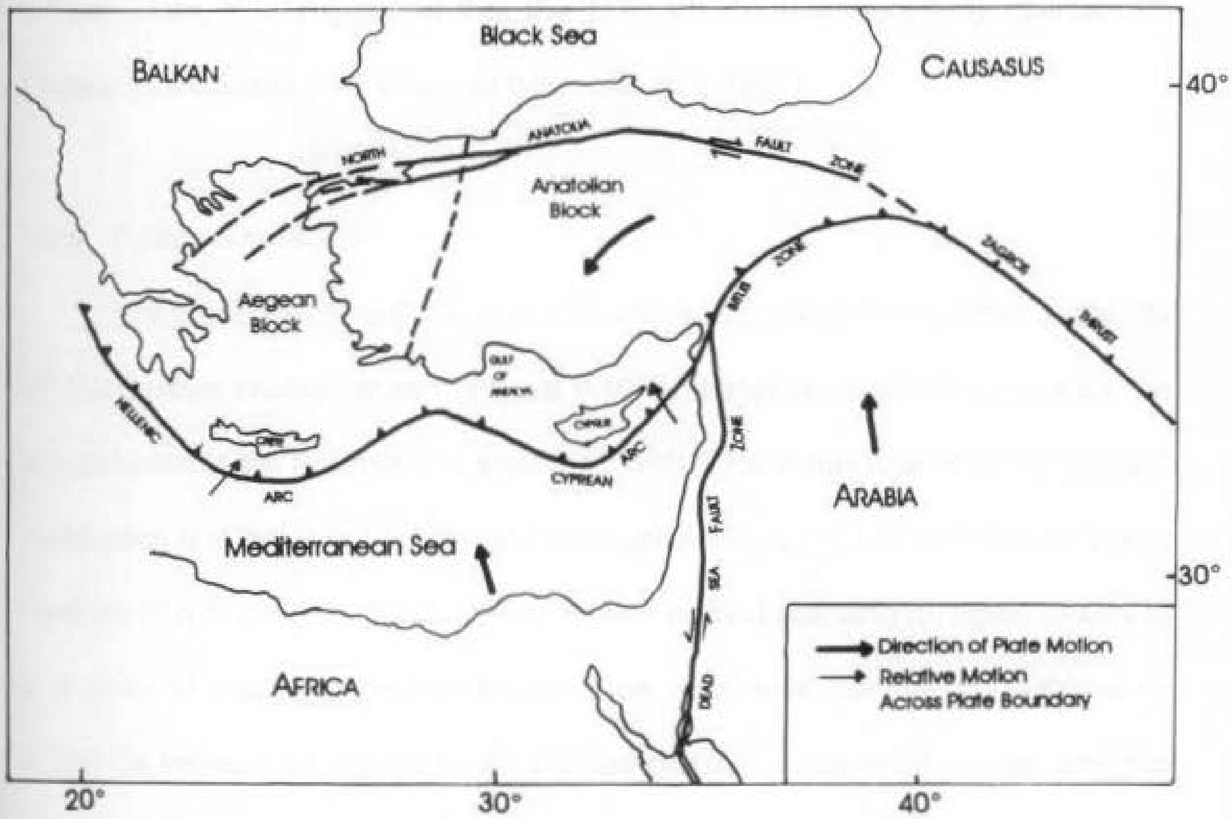

Figure 1-9 Present plate tectonic configuration of the eastern Mediterranean and the surrounding areas. Bold arrows show the direction of plate motion and more specifically the anticlockwise rotation of the Anatolian Block (Rotsein, 1984).

Arc extends into the Hellenic Arc to the west the and to the east it intersects the Dead Sea Fault, which extends into the Bitlis zone (Rotsein, 1984) (Figure 1-9). South and southwest of the island there is a segment of the Cyprean Arc called the Giermann fault. This segment also represents the actual plate boundary between the African and Turkish plates and is tectonically and seismically active. Along the Giermann fault, subduction is the mode of convergence and its polarity is northward. Just south of Cyprus, the Giermann fault is interrupted by the Eratosthene seamount. The tectonic setting of the Cyprean arc east of the Eratosthene seamount is unclear. Because of continued northward migration of the

African plate, it is suggested that the Eratosthene seamount may collide with Cyprus in the future (Kempler and Ben-Avraham, 1987).

1.10 Future Tectonics

The presence of the Eratosthene seamount signifies future tectonic instability for the Eastern Mediterranean. Figure 1-10 illustrates two possible scenarios. In (a), collision of the Eratosthene seamount with Cyprus terminates the northward subduction and initiates a southward subduction where the Levant platform would override (thrust over) the area north of it. The second scenario (b) again results in a reversal of polarity of the subduction zone. However, subduction in this case would be initiated along the North African passive continental margin and the oceanic Levant platform would be subducted beneath Africa (Kempler and Ben-Avraham, 1987).

On a larger scale, north of Cyprus there is located a tectonic block called the Anatolian Block. Similarly to the microplate rotation of the Late Cretaceous, the Anatolian block is presently undergoing anticlockwise rotation and will continue into the future (Figure 1-9). The northward motion of the Arabian plate (to the southeast of the block) and the dextral movement of the Anatolian fault (to the north of the block) are the driving tectonic mechanism of the block rotation (Rotsein, 1984). Therefore as long as these settings exist, anticlockwise rotation of the Anatolian Block, and consequently of Cyprus, should continue.

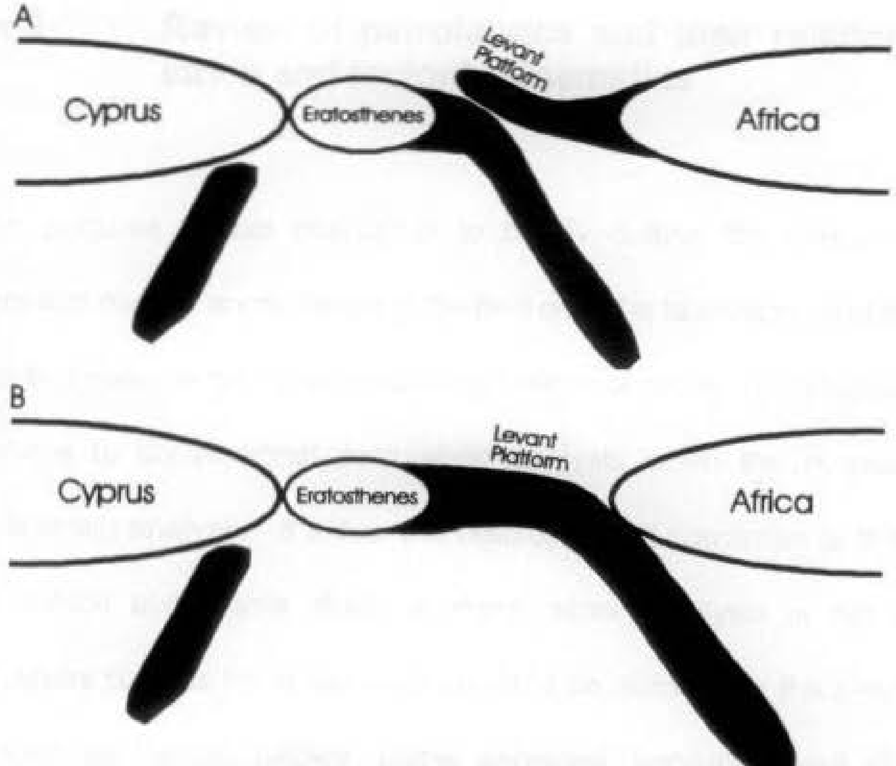

Figure 1-10 Illustration of possible scenarios for the future tectonics affecting Cyprus. In (a) the collision of the Eratosthene seamount with Cyprus causes the Levant Platform to override the area north of it. In (b) the collision of the Eratosthene seamount with Cyprus reactivates the North African passive continental margin with subduction of the Levant Platform under Africa (from Ben-Avraham and Nur, 1986).

Chapter 2- Review of petrofabrics and their relationship to strain and tectonic kinematics

The purpose of this chapter is to briefly outline the various types of petrofabrics that may be encountered in the field or in the laboratory, and how these fabrics can be related to the three principal directions of strain. Unfortunately, there are limitations to conventional petrofabric analysis when the purpose of the research is strain analysis. If either the outcrop, hand specimen or thin section does not exhibit observable strain markers, strain analysis is not possible. Therefore, areas suitable for strain studies would be dictated by the availability of markers such as fossils, pillows, pillow selvages, pebbles, sand dikes etc.. Moreover, very weakly strained rocks cannot be analysed. The second part of this chapter will review magnetic fabrics. Because magnetic susceptibility is a universal property of rocks, magnetic anisotropy can reveal strain directions in regions where conventional petrofabric analysis cannot. Furthermore, conventional strain markers are not needed, although many comparisons of strain markers and magnetic fabrics have been made in the field (Rathore, 1980; Borradaile, 1981; Kligfield *et al.*, 1981, 1982; Borradaile and Mothersill, 1984; Hirt *et al.*, 1988; Cogné and Perroud, 1988) and in the laboratory (Borradaile and Alford, 1987; Borradaile and Henry, 1997).

2.1 Petrofabrics

The term petrofabric was first introduced by Knopf and Ingerson (1938) to define the megascopic and microscopic study of rock fabric as a whole in its relation to the genesis of the rock. Consequently, petrofabric analysis is carried out both in the field (megascopic) and the laboratory (microscopic). A fabric includes structures, textures and preferred orientations and, more generally, preferred orientation distributions of mineral lattices or grain shapes. These can control the pattern of the external shape of the rock, for example its ability to split along the schistosity or pencil-cleavage lineations, as well as the pattern of the internal elements. At the grain level it describes the precise crystal space lattice orientation distribution. Where a fabric is repeated at a given scale, a pattern is produced. If the feature is only observed once, it does not contribute to the fabric (i.e. non-penetrative) (Hobbs *et al.*, 1976). If the feature is observed repeatedly it is called penetrative and constitutes a fabric. The scale at which one makes the observation will also dictate whether or not a fabric is observed. Obviously, features contributing to a fabric at the scale of an outcrop can be broadly distributed resulting in a pattern which would not be observed at the scale of a hand specimen. Similarly the penetrative and homogeneous appearance of a slaty cleavage in a hand specimen disappears at the scale of the Scanning Electron Microscope (SEM) observation.

In order to correctly interpret petrofabrics, we should distinguish between primary and secondary fabrics. Interpretations of primary fabrics will generally give some insight on rock genesis, whereas secondary fabrics can in some cases be related to applied strains to a rock during deformation. Primary fabrics may be exhibited in sedimentary rocks as bedding, in igneous rocks as gravitational banding and in metamorphic rocks as lithological layering. The focus of this chapter will be on the development of secondary or tectonic fabrics produced by a long strain history or short pulse of stress. Later in the chapter, conventional petrofabrics and their relation to strain and tectonic kinematics will be discussed.

2.1.1 Crystal Defects

At the smallest scale, fabric development is controlled in part by crystal defects. Within a crystal, the defects can be dimensionless, linear or planar. Dimensionless or point defects include missing atoms or vacancies, interstitial atoms, and clusters of atoms (Hobbs *et al.*, 1976). Point defects contribute to the development of a fabric by significantly decreasing the mechanical strength of the mineral (Griggs, 1967) and greatly increasing the ease by which the mineral may dynamically recrystallize, especially in silicates (Hobbs, 1968).

Linear defects or dislocations are of greater interest because these defects have a great influence on how a crystal will behave mechanically. Dislocations represent linear regions that have been elastically distorted. An elastic distortion involves an associated strain energy. As more dislocations occur within a crystal, the total free energy of the crystal increases. This, in turn, increases the amount of energy required for a dislocation to continue propagating itself. The difficulty of movement is responsible for the concept of strain hardening. At high temperatures or slow strain rates (typical upper crustal geological deformation at greenschist facies), the rate of solid-state diffusion can keep pace with the dislocation.

Therefore the dislocation line does not have to be constrained itself to one slip plane. A dislocation line can climb to the next dislocation plane causing the removal of an extra half plane of atoms. The result of a dislocation climb on the crystal is an extension or a shortening normal (perpendicular) to the extra half plane of the dislocation (Nicolas and Poirier, 1976). The working out of dislocations to the edge of crystals, is an important mechanism of their change in shape. New dislocations under plastic deformation are bred by Frank-Read Sources (Nicolas and Poirier, 1976).

Types of two-dimensional defects include stacking faults, dislocation walls, grain boundaries and interfaces (Nicolas and Poirier, 1976). All these involve a relative displacement of crystal lattice across a given plane.

2.1.2 Preferred Crystallographic Orientation

Preferred crystallographic orientation (p.c.o.) may develop a fabric by means of two mechanisms. These mechanisms depend principally on the temperature or strain rate of deformation. At low temperatures or high strain rate, dynamic recrystallization is difficult, therefore p.c.o. may develop due to rotation of inequant grains or slippage within grains causing grain rotation, or particulate flow due to intergranular motion (Borradaile, 1981). Under high temperature or low strain rate conditions, where recrystallization is easier, the recrystallization process will be associated with the development of p.c.o. (Hobbs *et al.*, 1976).

2.1.2A *P.C.O. BY SLIP AND ROTATION*

The development of a preferred orientation where crystallographic slip is the

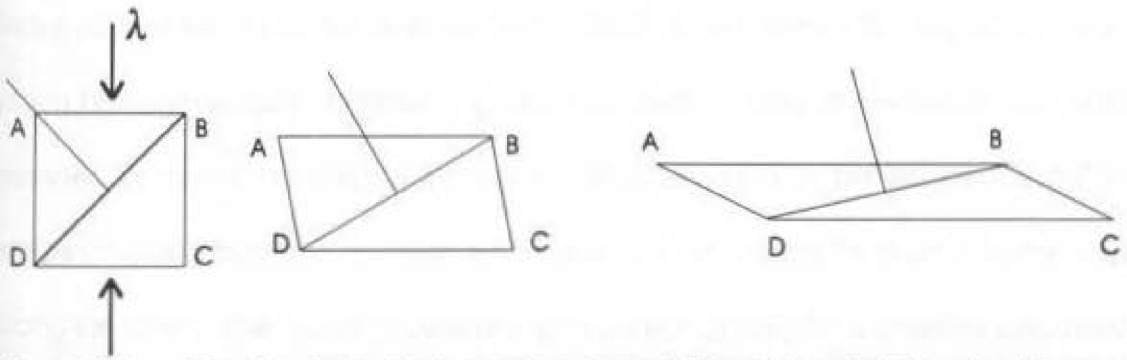

Figure 2-1 The development of a preferred crystallographic orientation by slip on a crystallographic plane BD and consequent rotation of a lattice. See text for explanation. (Modified from Hobbs *et al.*, 1976)

only active mechanism is illustrated in Figure 2-1. The hypothetical isolated grain is being shortened homogeneously parallel to the λ direction and contains only one slippage plane parallel to the diagonal BD. Given that slip is the only mechanism of deformation, the distance between BD or any grain dimension parallel to the slip direction will remain constant during deformation. Furthermore, a projection normal to the slip plane will remain normal throughout deformation. Increasing degrees of deformation will rotate the projection normal to the slip plane towards the shortening direction. We can transpose the concept of Figure 2-1 onto a quartz crystal, where the plane BD represents the basal slip plane of a quartz crystal and the normal, the crystal c-axis. This explains the common observation that quartz c-axes are sub-perpendicular to grain shape shistosity.

Realistically, grains within a rock are not isolated. Therefore, in order for ductile behaviour to occur, the grain boundaries must remain in constant contact or the rock will fail in a brittle manner (Hobbs *et al.*, 1976), or suffer interparticle slip by particulate flow (Borradaile, 1981). The von Mises condition states that if five independent slip systems operate within each grain, the rock may continuously strain homogeneously, maintaining grain contact instead of behaving in a brittle manner, or disaggregating. Two slip systems are said to be independent if the shape change produced by shear along one system cannot be produced by shear along the other. The reader is referred to Patterson (1969) for a detailed discussion of the von Mises condition. Unfortunately, few major rock forming silicates do not satisfy the Von Mises criterion (Nicolas and Poirier, 1976).

At higher temperatures cross slip of screw dislocations, thermally activated climb of edge dislocations (discussed earlier in section 2.1.1) and diffusion may contribute to the development of preferred orientations. Under these conditions the requirement of five independent slip system is modified by a decrease in the number of independent systems needed (Groves and Kelly, 1969). More generally, the "grain boundary sliding" can be controlled or uncontrolled by rate-determining crystal-deformation processes (Borradaile, 1979)(Figure 2-2).

Through fabric simulation studies, it has become evident that useful information can be obtained from plotting the orientation of the crystallographic axes on a stereographic projection. Different distribution patterns on a stereographic projection can distinguish between types of strain history (progressive shortening, extension, plane strain), identify whether strain was coaxial or noncoaxial, evaluate the amount of strain and assess the physical conditions of deformation. The interpretation of p.c.o. within the framework of strain will be further discussed later in this chapter.

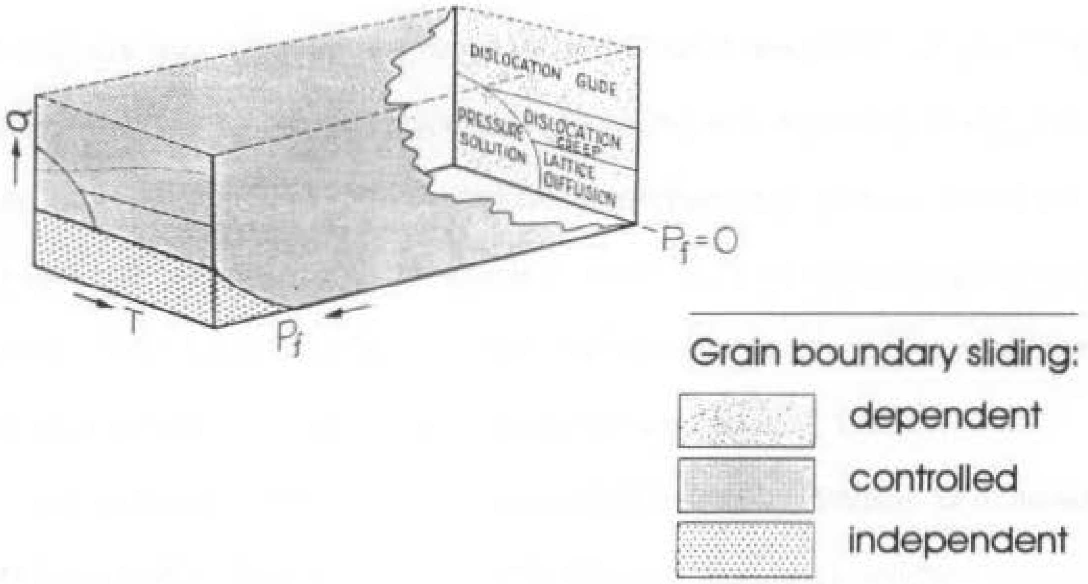

Figure 2-2 Tentative three dimensional deformation mechanism map for a monomineralic rock. The type of deformation mechanism a given mineral will undergo can be related to the differential stress (σ) and temperature (T) (rear wall of the diagram). The additional axis of pore fluid pressure (P_f) accounts for the behavior of an aggregate of grains (i.e. whether grain boundary sliding is dependent, controlled or independent) (from Borradaile, 1979).

2.1.2B *P.C.O. BY RECRYSTALLIZATION*

Preferred crystallographic orientation produced by dynamic recrystallization is a common process during deformation, as well as during other situations such as stress controlled nucleation during metamorphism and diagenesis. Hobbs *et al.* (1976) suggested that recrystallization involved nucleation of relatively strain free grains and the subsequent growth of some or all of the nuclei to form an aggregate of crystals with a preferred orientation. However, theoretical studies show that the mechanism of nucleation is extremely unlikely to occur (Cahn, 1970; Gottstein and Mecking, 1985) unless a chemical driving force is involved (Etheridge and Hobbs, 1974; Hay and Evans, 1987). Other than nucleation, there are a wide range of mechanisms associated with recrystallization. These mechanism can be related to two processes: grain boundary migration and formation of new grain boundary. The two processes define three major types of mechanisms, which can be subsequently subdivided into three types of recrystallization mechanisms: rotation, migration, and a general recrystallization mechanism which combines both rotation and migration. The subdivision of the types of mechanism characterizes whether the transformation is continuous or discontinuous (Drury and Urai, 1990).

The process of grain boundary migration involves the transfer of material across the boundary and only occurs when diffusion rates are significant. Coble creep and Nabarro-Herring creep are mechanisms of diffusion occurring along grain boundaries at high temperatures ($T_{melting}$ = ~0.6; Burton (1977) as reported by McClay, 1977) and along lattices a slightly higher temperature ($T_{melting}$ = ~0.9; McClay, 1977) , respectively. At lower temperatures, the transport of matter along grain boundaries in a liquid film describes the process of pressure solution, which can be treated similarly to Coble creep (Poirier, 1985). Pressure solution will be discussed in greater details in a later section.

The driving force of grain boundary migration can be to reduce stored energy (energy associated with dislocations, point defects...), or chemical free energy (Urai *et al.*, 1986). The formation of new grain boundaries can occur either by progressive misorientation of a stationary subgrain boundary or by migration of a subgrain boundary through an area of cumulative lattice rotation (Drury and Urai, 1990). The mechanism types are further subdivided when the degree of continuum of the process involved is assessed with respect to time during static recrystallization and strain during dynamic recrystallization.

The mechanism of rotation recrystallization primarily involves the processes of formation of new high angle grain boundary by either rotation of subgrains or by sub-boundary migration (Drury and Urai, 1990). Rotational recrystallization requires heterogeneous deformation. As previously discussed, heterogeneous strain at a grain-scale level can be related to the failure to satisfy the von Mises criterion (i.e. not enough slip systems).

The principal process in migration recrystallization mechanisms is grain boundary migration. Under low normalized stress or high temperature, the migration recrystallization is continuous and no new grain or new grain boundary develop (Drury and Urai, 1990). Discontinuous grain boundary migration has been observed. However, in all cases it is associated with the process of formation of new grain boundaries. Consequently the combination of both processes represents the third type of recrystallization mechanism. General recrystallization mechanisms combine both grain boundary migration and new grain boundary formation processes for the transformation of microstructures. Numerous different combinations of these two processes, combined with the two first mechanisms, are possible. The variability increases when adding continual and discontinual possibilities of the processes.

Drury and Urai (1990) recommend a systematic three step procedure in order to specifically describe the recrystallization mechanism contributing to the development of the preferred crystallographic orientation. The three steps are as follows:

1- How do the processes of grain boundary migration and new grain boundary formation combine to transform microstructures?

2- If the transformation involves new grain development, is it continuous or discontinuous?

3- If the transformation involves grain boundary migration, is it continuous or discontinuous, and what is the physical state of the boundary (i.e. presence of fluid-film assisting migration)?

2.1.2c PRESSURE SOLUTION

Pressure solution is a process derived from the rock deformation mechanism of diffusive mass transfer, which involves shape changes of individual grains by grain boundary diffusion assisted by the presence of a fluid film at the grain boundaries (Rutter, 1976). Rutter (1976) further described pressure solution as the summation of three basic processes:

1- transfer of material from the solid phase into a solution presumably forming the intergranular fluid film;

2- diffusive mass transfer through the stressed grain boundary region in response to a chemical potential gradient;

3- Precipitation in intergranular void space, or removal from the system altogether.

The area of dissolution along the grain boundary will be normal to the maximum compressive stress or the minimum tensile stress; whereas the precipitation or zone of crystal growth, if the transported material stays with the system, will be located along the grain boundary normal to the minimum compressive stress or the maximum tensile stress.

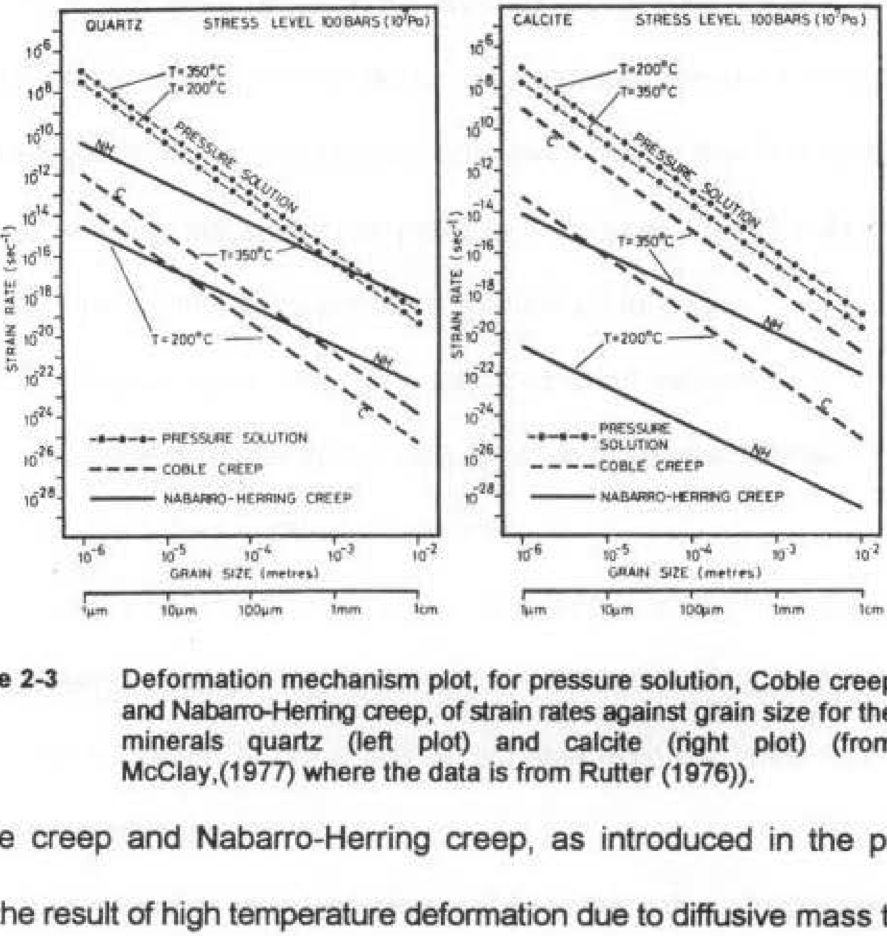

Figure 2-3 Deformation mechanism plot, for pressure solution, Coble creep and Nabarro-Herring creep, of strain rates against grain size for the minerals quartz (left plot) and calcite (right plot) (from McClay,(1977) where the data is from Rutter (1976)).

Coble creep and Nabarro-Herring creep, as introduced in the previous section are the result of high temperature deformation due to diffusive mass transfer processes. Figure 2-3 relates the three deformation processes of pressure solution, Coble creep and Nabarro-Herring creep to strain rates and grain size for the minerals quartz and calcite at temperatures of 200°C and 350°C and a pressure of 100 bars. Geologically significant strain rates able to produce natural ductile structures ranges between 10^{-9} and 10^{-14} sec^{-1} (Price, 1975). It is clearly demonstrated that pressure solution under low temperature deformation condition is the dominating deformational process, more so in quartz than calcite, where Coble creep at temperatures of 350°C (lower limit of greenschist facies metamorphism) may occur at similar strain rates and in rocks of similar grain size.

The low strain rates required for producing pressure solution somewhat inhibit the efficiency of studying experimentally textures resulting from pressure solution. However, there is much observable evidence in the field for pressure solution as a working deformational process. Ramsay (1967) lists the most important phenomena illustrating pressure solution as follows:

1- the mutual penetration of calcareous fossil fragments in limestones;
2- the development of pits in the pebbles of conglomerates where one pebble enters another by solution;
3- the elongation of clastic grains of quartz in slate as a result of silica overgrowths;
4- the migration of silica and carbonates from the limbs to the hinge zone of folds;
5- the migration of soluble material from the sides of stressed objects (e.g., pebbles) facing the principal load directions to the pressure shadows areas;
6- The development of a regular striping in slates which cross cuts the lithological layering.

Within the limestones, chalks and marls of the study area, the reoccurring evidence of pressure solution is stylolites. Bedding stylolites and tectonic stylolites result from pressure solution during diagenesis and during deformation, respectively. Photographs of samples exhibiting tectonic and bedding stylolites can be seen in Chapter 7, Figures 7-3, -5, -6, and -7. The photograph of sample FL98284 in Figure 7-3 clearly illustrates a tectonic stylolite cross-cutting a bedding stylolite. Stylolites become zones of accumulation, where commonly quartz phyllosilicates and clays are concentrated residues, giving the stylolite a darker color.

2.1.3 Foliations and Cleavages

Borradaile *et al.* (1982) recognize two definitions for foliations. The first describes a foliation as a planar location fabric usually defined by a compositional variation. Secondly foliation may also be defined as a penetrative preferred crystal (PCO) or dimensional (PDO) orientation in a thin section, hand sample or outcrop.

The cleavage of a rock may, in the majority of cases, be separated into two domainal structures: the cleavage domain (zone that tends to split or cleave) and the microlithons (zone where the rock is less cleaved) (Powell, 1979). Figure 2-4 presents the classification scheme of cleavages. Initial differentiation distinguishes cleavage as continuous or spaced. Determining whether the cleavage is one or the other is dependent on the scale of observation. At a given scale, if the observer can clearly recognize the microlithons from the cleavage domains, the cleavage is said to be spaced. If the alignment of mineral grains is evenly distributed throughout a rock or if cleavage domain are so closely spaced at a given scale that microlithons are unresolvable, the cleavage is said to be continuous.

2.1.3A *FOLIATIONS OR CLEAVAGES IN METAMORPHIC ROCKS*

In metamorphic rocks, foliation is the result of strain. Examples of metamorphic foliation (satisfying the second meaning of foliation by Borradaile *et al.*, 1982) could include gneissic structures, schistosity, phyllitic cleavage and slaty cleavage, which are all continuous cleavages. Stylolitic and crenulation cleavage, are spaced cleavages found in metamorphic rocks. Metamorphic rocks have by far the greatest number of cleavage and foliation textures. Furthermore, their development is dependent on the differential stress and strain rates, pressure, temperature and the availability of fluids (pore fluid pressure, P_f). Table 2-1 relates

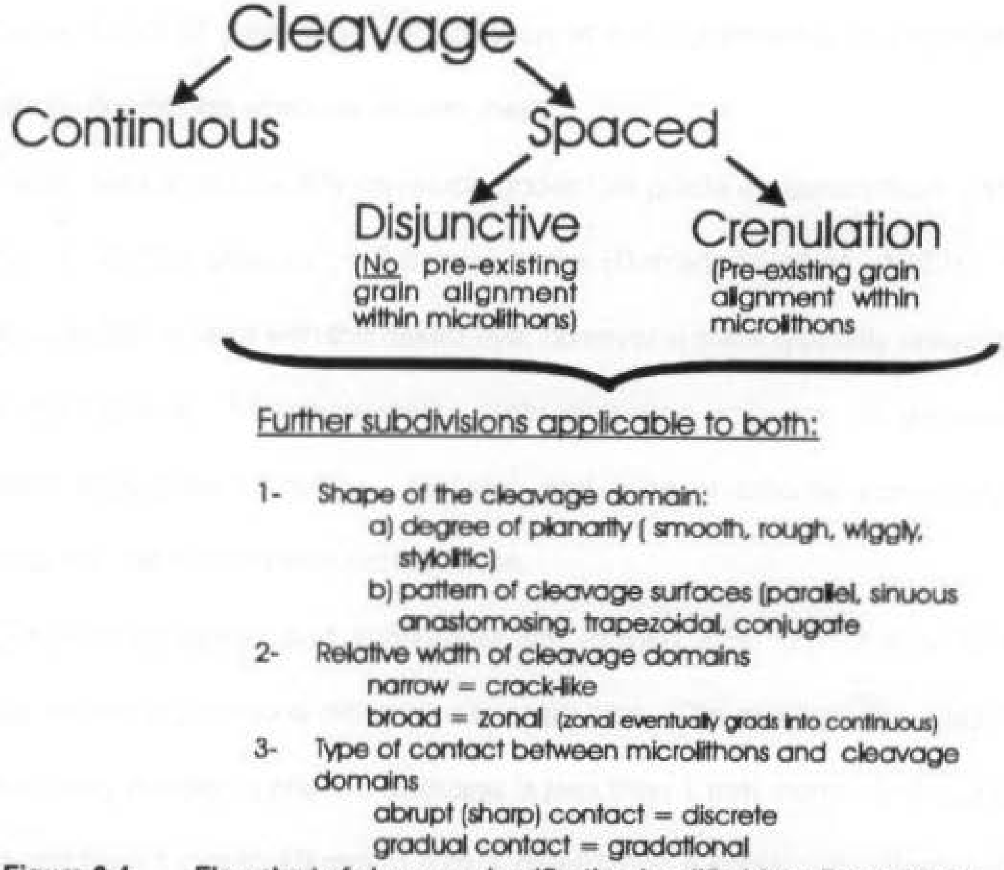

Figure 2-4 Flow chart of cleavage classification (modified from Borradaile *et al.*, 1982).

Table 2-1 List of some cleavage types and the associated deformation mechanism and physical conditions conducive to their development.

Type of cleavage	Deformation mechanism	Conditions
slaty cleavage	• grain rotation (p.d.o.) • recrystallization	T ≈ 250°C P ≈ 2 - 2.5 kbar (1)
schistose cleavage	• grain rotation (p.d.o. and/or p.c.o.) • recrystallization	T ≥ 400°C (2)
gneissic cleavage	• diffusion	$T_H \geq 0.5$ (2)
crenulation cleavage	• microfolding • pressure solution • mineral redistribution	P ≈ 3 - 4 kbar T ≈ 350°C (1)
stylolitic cleavage	• pressure solution	$T_H \leq 0.5$ (T≈250°C) P_f required P ≈ 2 - 2.5 kbar (1)
fracture cleavage	• hydraulic fracturing	P_f > confining pressure low T°C brittle conditions (depth < 4 km) (2)

(1) Borradaile *et al.* (1982); (2) Nicolas and Poirier (1976)

the various types of cleavages and foliation to the deformation mechanism and appropriate conditions which produces them.

Slaty cleavage typically develops under low grade metamorphism (refer to Table 2-1), in fine grained (< 0.5 mm) rocks (Borradaile *et al.*, 1982). Slaty cleavage cannot be seen with the naked eye; however a slate typically cleaves into tabular thin plates. Microscopically, slaty cleavage appears as discoidal to lenticular aggregates of quartz , feldspar and mica or chlorite surrounded by anastomosing mica or chlorite rich laminae.

Phyllitic cleavage and schistosity are formed in a similar way to slaty cleavage, where the obvious difference is grain size. The average grain size of a rock which may develop a phyllitic cleavage is less than 1 mm, compared to a grain size ranging from 1 mm to 10 mm in a rock developing a schistosity (Borradaile *et* *al.*, 1982).

The development of crenulation cleavage is evidence of a second phase or later phase of deformation. Crenulation cleavage develops when an already foliated rock (i.e. a rock that has either a slaty cleavage, phyllitic cleavage, schistosity or an earlier crenulation cleavage) is folded (crenulated) on a microscale. The axial surface of the microfolds or crenulation are subparallel to the crenulation cleavage. Typically, the cleavage domain is very rich in mica while the intervening microlithons, preserving the microfold hinge, preserves the pre-existing foliation and commonly host quartz and feldspar.

Crenulation cleavage may be discrete or zonal. Discrete crenulation cleavage appears as narrow mica-rich layers abruptly truncating the original foliation preserved in the quartz and feldspar rich zones. Discrete crenulation cleavage has a fault-like appearance as the quartz-feldspar foliated domains seem to be offset on either side of the cleavage domains. The offset appearance arises from the dissolved material removed due to pressure solution. Comparatively, zonal crenulation cleavage appears as wide mica rich domains connecting the fold limbs of the crenulated preexisting foliation in the quartz-feldspar domain. The finer grained foliated rocks (i.e. slates) tend to develop discrete crenulation cleavage, whereas coarser grained rocks (i.e. schists) tend to develop zonal crenulation cleavage. Both types of crenulation cleavage have spacings between cleavage plane that generally ranges from 0.1 mm to 1 cm generally proportional to grain size (Borradaile *et al.*, 1982).

During middle to high grade metamorphism, foliation is habitually expressed through gneissic structures (banding and layering). The banding or layering can appear as differentiation in mineralogy, colour and/or texture. Commonly, the differentiation results from one of recrystallization, mechanical shearing and dissolution mechanism. The most encountered type of banding takes the form of alternating mafic and felsic layers.

2.1.3B *FOLIATION IN SEDIMENTARY ROCKS*

Sedimentary rocks may develop textures related to the time of rock formation, such as bedding stylolites, or to a later deformational event, such as tectonic stylolites. Very often these are superimposed. These can be distinguished in the field by careful observation, however during magnetic fabric analysis special considerations must be taken to effectively separate the primary (bedding) and secondary (tectonic) fabric components.

Bedding fabrics are usually observed in sedimentary rocks. Bedding is an inherent fabric primarily because of the crystallographic shape of micas and because even less anisotropic minerals inevitably have longer dimensions that preferentially lies flat. Consequently, inherent fabrics are not indicative of tectonics and tectonic strain cannot be deduced from them.

Stylolitic cleavage produces a planar fabric due to the preferential arrangement of stylolites. Before stylolitic cleavage is used to suggest the principal orientations of strain, we must distinguish between diagenetic stylolites and tectonic stylolites. Diagenetic stylolites are formed due to gravitational loading and compaction. Furthermore, they are generally orientated parallel to sub-parallel with bedding and cannot be used for strain analysis. On the other hand, tectonic stylolites form under tectonic stress and generally align perpendicular to the maximum compression or shortening direction (Ramsay and Huber, 1983). Alvarez *et al.* (1978) proposed a classification scheme (see Table 2-2) in order to describe the type of intensity of the stylolitic cleavage and relate it to the amount of shortening represented by such an intensity. The intensity increases as the density of stylolites cleavage increases (i.e. as the distance between cleavage planes decreases).

Table 2-2 Classification of stylolitic cleavage in pelagic limestones after Alvarez *et al.* (1978)

Intensity Type	Characteristics of stylolites	Average distance between cleavage planes	Shortening accommodated by cleavage
Weak	toothed	> 5 cm	0 - 4 % shortening
Moderate	parallel	1 - 5 cm	4 - 25 % shortening
Strong	wispy and anastomosing	0.5 - 1 cm	25 - 35 % shortening
Very Strong	sigmoidal	< 0.5 cm	> 35 % shortening

This classification scheme must be referred to with precaution. The distance between stylolites (cleavage planes) cannot indicate the amount of shortening the rock has undergone. Determining the amount of rock dissolved would be a qualitative indicator of shortening. The simple observation of a stylolitic cleavage is a reassurance that the rock in question has most likely experienced shortening.

2.1.3c *FOLIATIONS RELATED TO FAULT ZONES*

Two types of foliations are routinely observed within fault or shear zones.

These were given the term of C-surfaces and S-surfaces by Berthé *et al.* (1979) and together they form an S-C fabric. The C-surfaces are shear planes of relative movement oriented parallel to the shear zone walls. S-surfaces are planes of flattening oriented initially at a 45° angle to the C-surfaces if there is **perfect** simple shear (Ramsay, 1967). The angle would be less if the shear was not a perfect simple shear. A non-simple shear zone results from a non-coaxial strain (as in perfect simple shear) combined with a coaxial strain component. This phenomenon is also called a transpressive shear zone indicating that the area has been sheared and compressed syntectonically. The compressive component produces an initial angle of separation less than 45° between S- and C- surfaces in a non-simple shear zone.

Progressive shearing of the C-surfaces, rotates the S-surfaces as to reduce their angle with the C-surfaces. S-surfaces extend between two C-surfaces which sandwich the S-surfaces. S-C fabric can develop and be observed in a handspecimen, an outcrop or even at a regional scale where the C- and S-surfaces can be traced for many kilometres. S-C fabrics are extremely useful in regional kinematic analysis as the relationship between the two surfaces indicates whether the shear zone has a dextral or sinistral sense of motion.

2.1.4 Lineations

Lineations, like foliations, are the result of strain and may be observed in all rock types (i.e. metamorphic, sedimentary and igneous). A lineation may be formed in numerous different ways. The most common types of lineations are intersection lineations, mineral lineations, grain shape lineations and crenulation lineations. Other less common types include slickensides striations.

2.1.4A NON PENETRATIVE LINEATION

Intersection lineations are the result of the intersection of two planes. These two planes can be two foliation planes, cleavage plane and bedding plane, the combinations are endless. These are non-penetrative fabric features and are not related directly to strain or stress. The important aspect for interpretations however is knowing what two types of plane are producing the intersection lineation.

Lineations indicating a relative movement are restricted to the surface of a plane and do not penetrate the entire rock. Such lineation are slickenside striations and grooves. These can be observed on fault surfaces representing the direction of relative movement. Slickensides may also occur on bedding surfaces of folds formed by flexural slip where individual layers glide on top of one another.

A crenulation lineation is most commonly developed in schists and phyllites that experienced two (or more) episodes of tectonic strain, causing S_1 to be crenulated. When looking in the plane of the crenulation cleavage, the lineation is defined by the straight or slightly curved line joining the series of crests and troughs of the tight microfolds, between the C-planes.

2.1.4B PENETRATIVE LINEATION

Mineral lineations and grain elongations are representative of the parallel alignment of elongate minerals or grain shapes. These fabric elements are normally penetrative and may be related to principal strain or perhaps principal stress directions. This type of lineation is very common in metamorphic rocks. The alignment of minerals form a preferred crystallographic orientation (p.c.o.) and the alignment of the grains form a preferred dimensional orientation (p.d.o.). As previously discussed, the preferred orientation is achieved by either recrystallization or mineral rotation. Commonly mineral lineation, in metamorphic rock, is found within the foliation plane and together help define the strain ellipsoid which will be discussed later in this chapter.

2.2 Strain and Kinematic Analysis

Kinematic analysis refers to how rocks moved during their formation and subsequent deformation, on a regional scale. Deformation of a rock is manifested through physical changes (strain) due to applied forces acting across or along an area (stress). Strain analysis of smaller structures disperse across a region leads into the possible interpretations of kinematic tectonics.

2.2.1 Theory of Strain Analysis

"Deformation" encompasses translation, rigid body rotation, dilation and strain. At the outcrop level, we are generally concerned with strain. It is defined as a change in shape of a body resulting from an applied stress field. We can schematically represent strain with a strain ellipsoid composed of three mutually perpendicular principal axes: X (maximum axis), Y (intermediate axis) and Z (minimum axis). These changes can also be accompanied by successive increments of strain, applied in different directions, in which case the strain is said to be non-coaxial. If the strain increments are added in the same directions, the strain is coaxial. A non-coaxial stain signifies that the principal strain axes change orientation with respect to the material throughout the strain history. An example of non-coaxial strain of very special restricted conditions, is simple shear (Figure 2-5). A coaxial strain retains a constant orientation of its principal strain axes with respect to the material. Such conditions define pure shear (Figure 2-5). Most "sheared" rocks actually result from transpression, a combination of shear strain and pure shear.

If strain effects a body uniformly, the body is homogeneously strained and consequently within the body straight lines will remain straight and parallel lines remain parallel. If strain varies throughout a body, the body is said to be

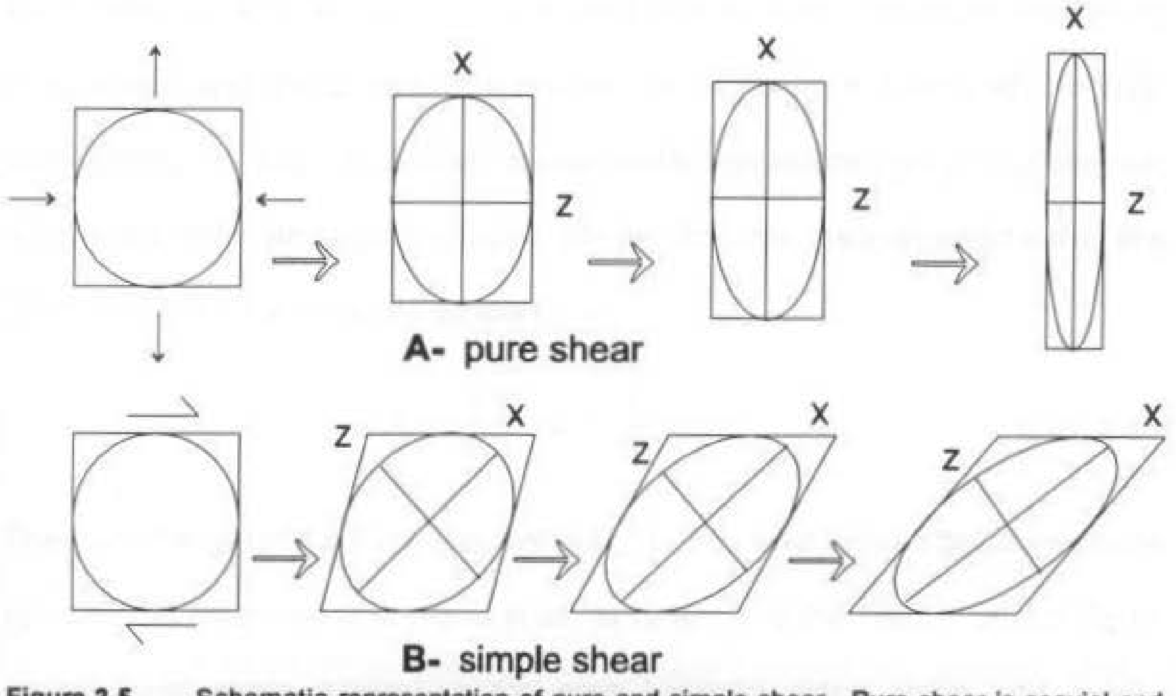

Figure 2-5 Schematic representation of pure and simple shear. Pure shear is coaxial and irrotational. Simple shear is non-coaxial and rotational.

heterogeneously strained and consequently straight lines become curved and parallel lines become non-parallel. For purposes of strain analysis homogeneously strained bodies are preferred. Usually a body will be heterogeneously strained on a large scale but may be broken down into smaller homogeneously strained domains for the application of strain analysis techniques.

There are two end-member types of homogeneous strain. Axially symmetric extension is characterized by a uniform extension along the X axis and equal shortening in all directions perpendicular to the X axis ($X > Y = Z$). The resulting strain ellipsoid has a prolate shape (rod-like) producing L-tectonites. Axially symmetrical shortening will have uniform shortening along the Z axis and equal extension in all directions perpendicular to the Z axis ($X = Y > Z$) producing S-tectonites. In this case, the strain ellipsoid has an oblate shape (disc-like). The intermediate case is plane strain, where the Y axis remains unchanged, the X-axis is extended and the Z axis is shortened ($X > Y = 1 > Z$ and $X/Y = Y/Z$). Traditionally, homogeneous strain is graphically represented on a Flinn diagram (Figure 2-6) for a structural geologist. On the diagram, the y-axis and x-axis are defined by Flinn's **a** and **b** parameters:

$$a = \frac{X}{Y} \; ; \; b = \frac{Y}{Z} \qquad \textbf{Eqn. 2-1}$$

The point of origin of the Flinn diagram is (1,1). The area located between axially symmetrical extension and plane strain is referred to the field of stretching or constrictional strain, where as the area between plane strain and axially symmetrical flattening is called the field of flattening strain. The Flinn diagram also relates to the shape of the ellipsoid, which is defined by the parameter **k** :

$$k = \frac{(a - 1)}{(b - 1)} \qquad \textbf{Eqn. 2-2}$$

The greater the distance between a plotted point and the origin of the Flinn diagram, the greater the degree of eccentricity of the corresponding ellipsoid. However the Jelinek plot is superior for both structural geology and magnetic fabric studies. It expands the scale for weak strains, because of its logarithmic scale. Moreover, the shape parameter (T_j) is represented by <u>an axis</u> and it is also symmetrical (+1 to -1), whereas Flinn's shape parameter (a-1)/(b-1) ranges from 0 to ∞.

Finally, we should note that strain develops in increments. What a geologist observes and measures in the field is a finite strain that resulted from the object being progressively strained through time, summing strain increments. Progressive deformation is the process leading from an initial to a final state of finite strain. Observation of a finite strain is **not** necessarily a key to the incremental steps suffered by the object during progressive deformation. Occasionally, evidence of progressive deformation may be observed in the field. If a fracture mineralizes, the vein minerals may grow as fibres parallel to the maximum extension direction (Ramsay and Huber, 1983; p. 236-262). Changes in orientation of the long axes, and growth stages on the fibres, would suggest a change in the orientation of the

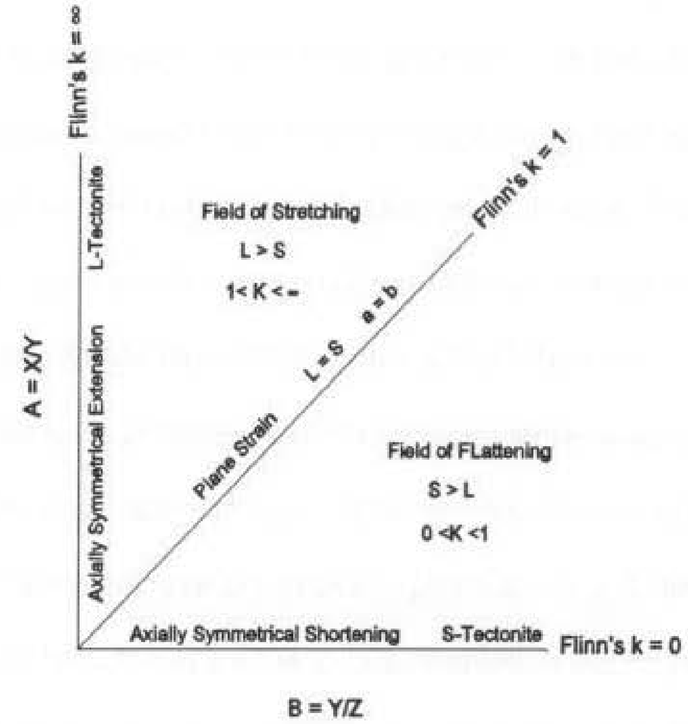

Figure 2-5 The Flinn Diagram as a graphical method for presenting the shape and degree of anisotropy of an ellipsoid. For comparison, a Jelinek plot is illustrated in Figure 3-2.

direction of maximum extension; hence proof of progressive non-coaxial strain. This phenomenon may also be observed microscopically in pressure shadows.

A concluding remark on the theory of strain brings attention to the relationship between strain and stress. Strain results from an applied stress field therefore it is reasonable to want to quantify this relationship. For a coaxial strain history, we can correlate the three principal strain axes with the three principal stress axes where Z is parallel to σ_1 (maximum stress axis), Y is parallel to σ_2 (intermediate stress axis), and X is parallel to σ_3 (minimum stress axis). For a non-coaxial strain history the simple correlation between principal axes does not apply because of the continuous change in orientation of the strain principal axes. However, if the non-coaxial strain history mechanism were the very special cases of simple shear, we can correlate the Y principal strain axis, which does not change orientation with respect to its initial position, with the intermediate stress axis (σ_2).

2.3.2 Analysing Strain from Conventional Petrofabrics

Determining the orientation of the principal strain axes is reasonably scene if the area under observation exhibits a foliation, that is a planar flattening fabric (S-tectonites). S-tectonites, that are principal plane structures, lie in the XY plane of the strain ellipsoid and therefore the Z-axis orientation will be perpendicular to the foliation or XY plane. If a lineation is present in the plane of foliation, then the X-axis orientation is defined by the elongated or stretched direction of the lineation.

Rocks which exhibit pervasive foliations (S-surfaces) and lineations are called L-S tectonites. Depending on which aspect of the fabric dominates, the tectonite may be classified as an L-tectonite, S-tectonite or an L-S-tectonite. Intermediate ranges between the two end-members of purely lineated or purely foliated tectonite are referred toas L>S tectonite where the lineation is more pronounced, or S>L tectonite, when the planar component dominates. These classification may be represented on a Flinn diagram introduced earlier, where an L-tectonite is the result of axially symmetrical extension, an S-tectonite is the result of axially symmetrical shortening and L-S tectonite is the result of plane strain (Figure 2-6).

However, in order to quantify the amount of strain, the extension (or shortening) along each strain axis must be measured. This requires the use of strain markers. Strain markers are objects that have been deformed but their original shape is known. Such objects include initially spherical objects (ooids, reduction spots, vesicules) conglomerates, pebbles, bilaterally symmetrical fossils, boudinaged layers and fold sets (Ramsay and Huber, 1983;p. 197).

Measuring the amount of strain can be achieved by considering the change in length of a line, change in angle between two lines and the change in volume. The variation in length of a line can be measured and defined by the following three parameters:

Eqn. 2-3

$$\textit{Extension} \; ; \quad e = \frac{(l - l_o)}{l_o}$$

$$\textit{Stretch} \; ; \quad S = \frac{l}{l_o}$$

$$\textit{Quadratic elongation} \; ; \quad \lambda = (\frac{l}{l_o})^2 = (1 + e)^2$$

The stretch parameter (Means, 1976) is useful when dealing with large scale crustal deformation. The extension corresponds to an elongation of the axis when the obtained value is positive, whereas a negative value indicates a shortening of the axis. In terms of extension, the principal strain axes X, Y, and Z correspond to $(1 + e_x)$, $(1 + e_y)$, and $(1 + e_z)$ respectively. Situations where shear is apparent, shear strain, γ (gamma), may be measured and is defined by the following equation:

$$\gamma = \tan \psi \qquad \textbf{Eqn. 2-6}$$

where ψ (psi) is the angular deflection of an original right angle.

Very commonly straining is accompanied by a certain amount of volume change. More often than not, the volume change is a volume loss (e.g. pressure solution). If volume change is not accounted for when determining the amount of strain the estimates will be misleading. The volume change, Δ (delta), is defined as:

$$\Delta = \frac{(V - V_o)}{V_o} \qquad \textbf{Eqn. 2-7}$$

where V_o is the initial volume and V the observed volume. However the change of volume may be directly related to the principal strain axes and to the extension suffered by each of the principal strain axes.

$$1 + \Delta = (1 + e_x)(1 + e_y)(1 + e_z) \qquad \textbf{Eqn. 2-8}$$

The measurement of these parameters require strain markers. Without any strain markers it becomes very difficult to assess the strain state in the field. We will now examine how strain may be determined from a variety of types of strain markers.

Elliptical objects that may have been initially spherical can be analysed by following two different methods. Such objects include ooids in sedimentary rocks, iron reduction spots in metamorphic rocks and vesicules in volcanic rocks. The first method measures the strain axes directly. The hand specimens must be cut parallel to three perpendicular sections, preferably corresponding to the principal planes XY, XZ and YZ. On these surfaces, the lengths of the long and short axes of the spheroidal objects are measured. Subsequently, the measurements are plotted on a cartesian graph where the (x,y) coordinates are (length of long axis, length of short axis). The slope of the line of best fit through the data represents the strain ratio Y/X for that plane of section.

An alternative to the direct measurement of the strain axes is the centre-to-centre method. This method reasons that the distance between centres of randomly oriented spheres alters systematically when being strained (Park, 1989). On a surface containing numerous strain markers the distance between two centres is recorded as well as the angle separating this line and an arbitrary reference line. Then, the (x,y) coordinate pairs corresponding to (angle of separation, distance) are plotted. The data will define a curved line which reaches a maximum and a minimum on the y(distance)-axis. The ratio between the minimum and maximum distance is equal to the strain ratio Y/X. The angles corresponding to the maximum and minimum distances represent the orientation of the X and Y principal strain axes orientation with respect to the reference line. This method presents the advantage of being applicable to even non-elliptical strain markers, however determining the actual centre position does present some problems, making the application of the method difficult. Moreover the results are generally poor.

The use of elliptical markers such as conglomerate pebbles, as passive loop markers, for strain analysis requires the use of a different graphical method. This alternate graphical method takes into account the final elliptical shape observed in the field as being a combination of the pebbles original elliptical shape and the tectonic strain. The graph plots the observed strain ratio (R), that is, the ratio between the short axis and long axis of the pebble, against the angle the long axis makes with an arbitrary reference line. The plotted data will either yield a peaked distribution indicating that R(strain) < R(initial) or a pear-like distribution, in which case R(strain) > R(initial). The R_{max} and R_{min} ratios can be quickly determined from a pear-like distribution. The maximum and minimum ratios define:

$$R_{max}^2 = R_T R_O \qquad \textbf{Eqn. 2-9}$$

$$R_{min}^2 = \frac{R_O}{R_T} \qquad \textbf{Eqn. 2-10}$$

where R_O is the original Y/X ratio and R_T is the tectonic strain Y/X ratio. By dividing equation 2-9 by equation 2-10 we obtain:

$$R_T = \frac{R_{max}}{R_{min}} \qquad \textbf{Eqn. 2-11}$$

This graphical method also yields the orientation of the maximum principal strain axes. The angle between the arbitrary reference line and the X principal strain axes is given by the vertically oriented symmetry axis of the distribution. The elementary application above is two-dimensional, but it has been extended to three-dimensional and also for cases of initial non-uniform particle shape and non-uniform particle orientation.

A more versatile method of analysing strain is the selvage rim method for certain closed loop markers with rims. This method can be used on numerous type of strain markers: vesicles, lapilli, reduction spots, weathered pebbles, and even pillow lavas, which are a non-spherical object. The method assumes that the rims which forms on the outside of these objects are uniform. The ratio of the thickest rim width and the thinnest rim width is equivalent to the strain ratio (Borradaile, 1987). Furthermore, the maximum extension direction would be parallel to the direction of the thickness rim width. Some caution is needed when using this method with pillow lavas. While pod-shaped pillow lavas will give strain ratios with 20% accuracy, the selvage rim method practised on tubular (tube-like) pillow lavas exposed on a two-dimensional outcrop surface is unlikely to be a suitable candidate for strain analysis (Borradaile, 1985).

This outlines a few simple methods which can quantify the amount of strain a certain rock suffered by analysing field observable strain markers. However strain markers are not very common and consequently only the orientation of strain through L-S fabrics can be inferred. If an outcrop is bare of strain markers and does not display any foliation or lineation, it was assumed the area was undeformed. However, with the use of magnetic fabrics it is possible to obtain the orientation of the principal strain axes even if the observed outcrop is barren of strain markers and appears undeformed.

Chapter 3 - Review of Magnetic Fabrics and their Relationship to Strain and Tectonic Kinematics

3.1 Magnetic Fabrics

The analysis of magnetic fabrics introduces an extra dimension to the analysis of conventional petrofabrics discussed in Chapter 2. However, in order to properly interpret magnetic fabrics, the geologist must have an understanding of the magnetic mineralogy of the rock as well as the magnetic properties of all types of minerals. There are two types of magnetic fabric that can be investigated. The susceptibility anisotropy defines a fabric where the mineralogy of the whole rock contributes; and the remanence anisotropy defines a fabric to which only ferromagnetic minerals contribute. In both cases the fabric may be characterised by an ellipsoid describing the shape and the orientation of the anisotropy tensor. In the last section of this chapter, we will investigate how conventional petrofabrics and magnetic fabrics can be related to strain and tectonic kinematics.

Before discussing how the anisotropy of various magnetic fabrics can be analysed, we will review the fundamentals of magnetism in the realms of mineralogy.

3.1.1 Magnetic Properties of Minerals

All material have a certain magnetization because of the electrons rotating around their spin axis and around a nucleus. In the presence of an applied magnetic field, the electrons' spin axes align themselves parallel to the applied field. Minerals can be classified as being diamagnetic, paramagnetic, ferromagnetic, antiferromagnetic or ferrimagnetic depending on how they respond when a magnetic field is applied and then subsequently removed (Figure 3-1).

A diamagnetic material in the presence of a magnetic field, will acquire a small induced magnetization in the opposite direction to the applied field. Once the magnetic field is removed, the diamagnetic material loses the induced magnetization. All materials react diamagnetically, but a material classified as diamagnetic, has no other type of magnetic response because its electron shells are complete and therefore the atoms do not possess a magnetic moment (Butler, 1992). Pure quartz, calcite and feldspar are examples of diamagnetic minerals and are characterized by having negative magnetic susceptibilities, in the order of -10^{-6} SI vol. (Hrouda, 1986; Voight and Kinoshita, 1907; and Borradaile *et al.*, 1987 as reported by Borradaile, 1988), which are independent of temperature. However, these minerals are rarely pure as they commonly contain non-diamagnetic inclusions.

Paramagnetic materials will acquire an induced magnetization parallel to the applied magnetic field. Their atoms do possess a magnetic moment, but do not interact with adjacent atomic moments. However, like diamagnetic responses, Paramagnetic material have magnetization equal to zero when the applied field is removed. The atomic moments are randomly distributed causing the resultant moment to equal zero. Most iron-bearing carbonates and silicates are paramagnetic. The magnetic susceptibility is positive and generally ranges between 10^{-2} to 10^{-4} SI vol., for common paramagnetic rock forming minerals (Dunlop and

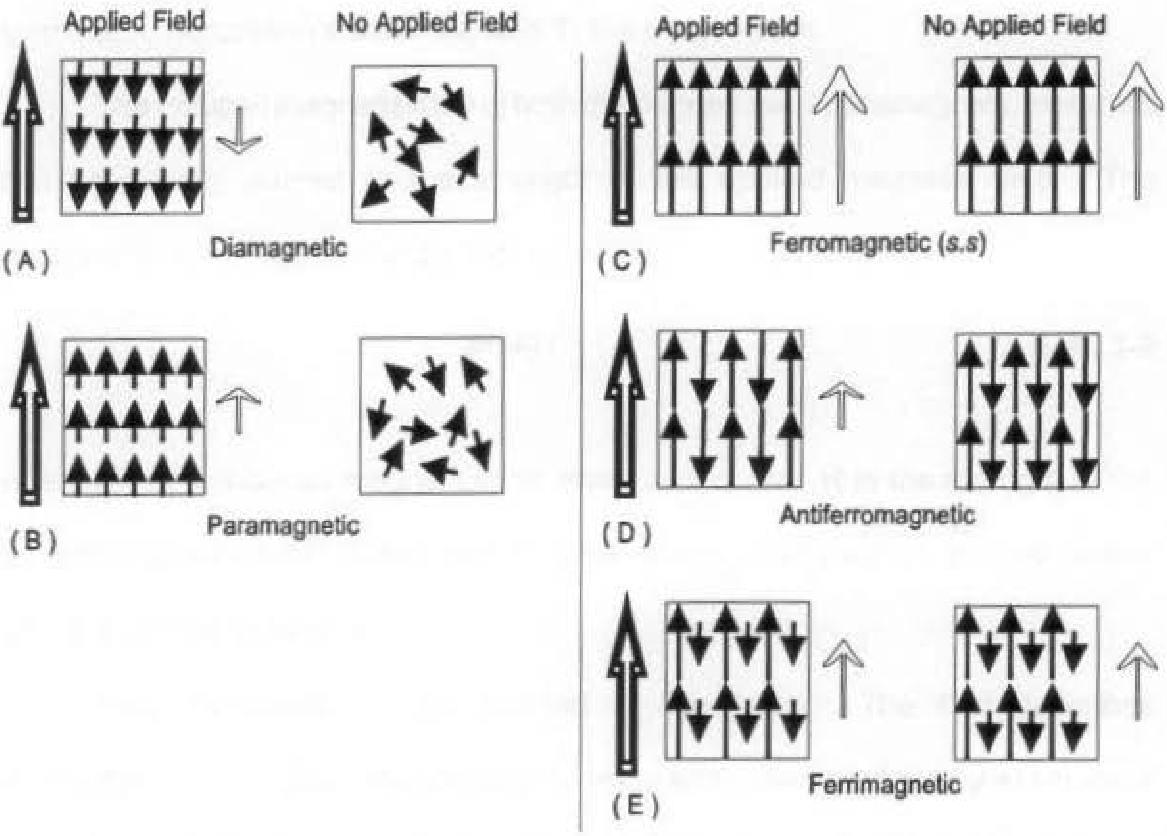

Figure 3-1 Different types of magnetization. The bold arrows to the left of the lefthand column indicate the direction of the applied field. The arrows to the right of the boxes indicate the sense and relative magnitude of magnetization when a magnetic field is applied (induced magnetization) and then removed (remanent magnetization). Refer to the text for further explanation. (Modified from Tarling and Hrouda, 1993)

Özdemir, 1997). Furthermore, paramagnetic minerals have susceptibilities which depend on temperature; as temperature increases, paramagnetic susceptibility decreases according to the Curie law of paramagnetic susceptibility (Butler, 1992).

$$\chi = \frac{J}{H} = \frac{NM^2}{3kT} \qquad \textbf{Eqn. 3-1}$$

where χ is the paramagnetic susceptibility, J, magnetization, H, the applied field, N, the atomic moments per unit volume of the paramagnetic solid, M, magnetic moment, k, Boltzmann's constant, and T, the temperature.

The induced magnetization of both diamagnetic and paramagnetic materials can be directly related to the strength of the applied magnetic field. The relationship is linear and can be expressed as:

$$M=KH \qquad \textbf{Eqn. 3-2}$$

where M is the induced magnetization measured in A/m, H is the strength of the applied magnetic field in A/m and K is the susceptibility which is used as the constant of proportionality.

Ferromagnetism can be defined in two ways. The first describes ferromagnetism in the general sense (i.e. *sensu lato*), characterized by a remanent magnetization (the ability of retaining a mangetization long after the removal of the external field). The umbrella term can be further divided into ferromagnetism, the specific term (i.e. *sensu stricto*), antiferromagnetism and ferrimagnetism. Ferromagnetism (*s.l.*) characterizes all materials that have strongly interacting neighboring atomic magnetic moments. Furthermore, ferromagnetic (*s.l.*) material can retain a magnetization long after the applied magnetic field is removed with the exception of perfect antiferromagnetic material. However, the spin moments in an antiferromagnetic material are commonly canted resulting in retention of some magnetization after the applied field is removed. These materials can acquire a magnetization up to a maximum, called saturation magnetization. The saturation magnetization decreases with increasing temperature until the saturation magnetization reaches zero. The corresponding temperature is termed the Curie temperature, a unique property for each ferromagnetic (*s.l.*) material. Above their Curie temperatures, ferromagnetic (*s.l.*) minerals behave paramagnetically. If temperatures were to fall back below the Curie temperature, the mineral would at that point regain its ferromagnetic (*s.l.*) properties.

The interaction between adjacent atomic magnetic moments can take the form of one of two types of quantum-mechanical coupling forces: exchange or superexchange coupling forces (Tarling and Hrouda, 1993). Exchange force is common in the metallic transition elements (iron, nickel, cobalt and some of their compounds) and consist direct coupling with adjacent electron spins of atoms. This results in having all magnetic vectors lying in the same direction, characteristic of ferromagnetism (*s.s.*). Magnetic moments of atoms within a single domain are all parallel.

More appropriately for compounds of Fe, Ni, T, etc is superexchange coupling, in which the coupling is done via an intermediate atom. This is common in more complex compounds such as oxides, where the oxygen atoms (anion) will act as a coupling bridge between two cations. Superexchange coupling forces result in having domains of atomic magnetic moments with opposing magnetic direction. That is atomic magnetic moments within a layer are still parallel but between layers there is an antiparallelism. If the magnetization is of equal strength in antiparallel layers the net magnetism is zero and the material is said to be antiferromagnetic. If the magnetization is **not** equal in antiparallel layers, a net magnetic direction will result and the material is called ferrimagnetic.

There are numerous ferromagnetic (*s.l.*) minerals and the Fe-Ti oxides account for the majority of them by far. Other mineral groups or minerals exhibiting ferromagnetic (*s.l.*) properties include goethite (an iron hydroxide), pyrrhotite and greigite (iron sulphides), and hydrated iron sulphate (resulting most commonly from the hydration of pyrite and marcasite which are very unstable when exposed to air). All these minerals have characteristically high magnetic susceptibilities (greater than paramagnetic minerals) ranging anywhere from 10^{-3} SI vol. to 10^{0} SI vol. (Carmichael, 1982 as reported by Borradaile, 1988). More importantly for paleomagnetism, they possess magnetic remanence.

3.1.2 Magnetic Anisotropy

The magnetic anisotropy of individual particles depends on two factors: the anisotropy of the particles themselves and the degree of the particles alignment (Tarling and Hrouda, 1993). The particle anisotropy is composed of a crystalline and a shape anisotropy component.

A crystalline anisotropy arises from lattice forces acting on the electron spin configuration of the particle. Particles (crystals) have certain crystallographic axes or planes in which electron spin axes will preferentially (more readily) align themselves, and magnetization will be greatest in these directions. These are termed easy axes or easy planes.

A shape anisotropy forms from the alignment of electron spin axis creating a north and south magnetic pole at opposite points on the surface of the grain. The magnetic poles are created by a net magnetization ,M, which may be an induced or a remanent magnetization. Internally, a demagnetizing field, H_d, is antiparallel to M. The magnetostatic energy, E_m, results from the dipole moment (μ) and the total internal magnetic field of the grain. This may be expressed as follows:

$$E_m = -\mu \cdot (H_o - H_d) \quad \text{Eqn. 3-3}$$

where H_o is the external field, $H_d = -N \cdot M$, and N is the demagnetization factor (Dunlop and Özdemir, 1997). Grains that are symmetrical will have poles that cluster, enhancing the magnetostatic force of the grain. In non-symmetrical grains, the poles are scattered, weakening the magnetostatic force of the grain (Tarling and Hrouda, 1993). Different minerals will have particle anisotropy controlled dominantly by their crystalline anisotropy (e.g. hematite) and others by their shape anisotropy (e.g. magnetite). The shape anisotropy of ferromagnetic (*s.l.*) grains depends entirely on grain size, as multi-domain and single domain grains behave differently. The susceptibility anisotropy is maximized if the orientation of the crystalline easy axes and the shape long axes of the grain coincides.

3.1.2A SUSCEPTIBILITY ANISOTROPY

The bulk susceptibility anisotropy measured in a weak magnetic field (≤1 mT) represents the sum of the susceptibility of all minerals present in the rock sample (diamagnetic, paramagnetic and ferromagnetic (*s.l.*)). However the presence of a certain volume percentage of some minerals can dominate the bulk susceptibility. For example, if magnetite (susceptibility of ~10^6 μSI vol.) is present in amounts exceeding 0.1 vol% of the total rock, it will , more often than not, dominate the bulk susceptibility of the sample. Where ferromagnetic (*s.l.*) minerals are absent, paramagnetic minerals (susceptibilities ~10^2 - 10^3 μSI vol.) will usually dominate the susceptibility anisotropy over the diamagnetic minerals (susceptibilities of -10^1 μSI vol.), unless the paramagnetic content of the rock is less than 1 vol%. In this latter case, the diamagnetic minerals will dominate the susceptibility anisotropy and the rock will have a negative bulk susceptibility.

Measuring the anisotropy of magnetic susceptibility (AMS) in an applied magnetic field of weak intensity ($\leq$ 1 mT) yields the susceptibility (K) in three principal orthogonal orientations: k_1 = maximum susceptibility direction, k_2 = intermediate susceptibility direction and k_3 = minimum susceptibility direction. Together the three principal susceptibility directions define the anisotropy of magnetic susceptibility ellipsoid. Numerous parameters defining various properties exist for the analysis of the AMS ellipsoid. These are listed in Table 3-1. However this extensive list of parameters in reality describes only two properties: the shape and the degree of anisotropy of the AMS ellipsoid (Jelinek, 1981). Traditionally, it was suggested that the AMS ellipsoid had four properties (shape, foliation, lineation and degree of anisotropy). However, foliation and lineation are basically the result of shape, and shape is synonymous with anisotropy degree. The analysis of the AMS ellipsoid can produce insight for strain and kinematic evolution. Careful considerations are necessary for meaningful interpretation and these will be discussed later.

3.1.2B REMANENCE ANISOTROPY

A magnetization which remains after the removal of a magnetic field is called a remanent magnetism. This is a property displayed only by ferromagnetic (*s.l.*) substances. Therefore the source of remanence anisotropy is much less variable than that of susceptibility anisotropy. Furthermore, the key ferromagnetic (*s.l.*) minerals mentioned in section 3.1.1 tend to form under different conditions which translate very often to a mono-mineralic contribution to the magnetic remanence of a rock sample. The identification of the contributing mineral is very important when

Table 3-1 List of some published parameters of anisotropy (modified after Tarling and Hrouda, 1993)

Property/Parameter	Equation	Reference
Magnitude of anisotropy		
CORRECTED ANISOTROPY DEGREE	$Pj = \exp \sqrt{\{2[(\eta_1-\eta_m)^2 + (\eta_2-\eta_m)^2 + (\eta_3-\eta_m)^2]\}}$	1
	where $\eta_i = \ln K_i$ and $i = 1,2,$ or 3 ; $\eta_m = (\eta_1 + \eta_2 + \eta_3)/3$	
ANISOTROPY DEGREE (P_2)	K_1/K_3	2
ABSOLUTE ANISOTROPY	$(K_1 - K_3) / K_2$	3
TOTAL ANISOTROPY	$(K_1 - K_3) / K_{mean}$	4
Lineation		
LINEATION (P_1)(Flinn's a - "L")	K_1/K_2	5, 6
MAGNETIC LINEATION (L)	$(K_1 - K_2) / K_{mean}$	7
LINEATION	$(K_1 + K_3) / 2K_2$	8
LINEATION DEGREE	$2K_1/(K_2 + K_3)$	9
Foliation		
FOLIATION (P_3)(Flinn's b - "S")	K_2 / K_3	6, 10
MAGNETIC FOLIATION (F)	$(K_2 - K_3) / K_{mean}$	7
FOLIATION	$(K_1 + K_2) / 2K_3$	5
FOLIATION DEGREE	$2K_2/(K_1 + K_3)$	8
Prolateness		
PROLATENESS	$(K_1 - K_2) / (K_2 - K_3)$	7
PROLATENESS	$(2K_1 - K_2 - K_3) / (K_2 - K_3)$	8
Oblateness		
OBLATENESS	$(K_2 - K_3) / (K_1 - K_2)$	7
OBLATENESS	$(K_1 + K_2 - 2K_3) / (K_1 - K_2)$	8
Shape		
SHAPE PARAMETER (T_j)	$(2\eta_2 - \eta_1 - \eta_3) / (\eta_1 - \eta_3)$	1
E-FACTOR	K_2^2 / K_1K_3	9
SHAPE INDICATOR	$(K_1K_3 - K_2K_3) / (K_1K_2 - K_1K_3)$	10
ELLIPSOID SHAPE	$(K_1 - K_2)(2K_1 - K_2 - K_3)/(K_2 - K_3)(K_1 + K_2 - 2K_3)$	8
SHAPE INDICATOR	$(K_1K_3 - K_2^2) / (K_1K_2 - K_1K_3)$	8

Reference numbers correspond to the following: (1)Jelinek, 1981; (2)Nagata, 1961; (3)Rees, 1966; (4) Owens, 1974; (5)Basley and Buddington, 1960; (6)Flinn, 1965; (7)Khan, 1962; (8)Urrita-Fucugauchi, 1980; (9) Hrouda *et al.*, 1971; (10)Stacey *et al.*, 1960 interpreting the remanence anisotropy. Not only mineral composition but also grain size and time are important control factors for a rock sample acquiring a remanent magnetization naturally or in the laboratory.

The concept of a remanent magnetization having a time dependency was developed by Néel (1955), and is expressed as

$$\tau = \frac{1}{C} \exp \left(\frac{vB_cJ_s}{2\kappa T_{abs}}\right) \qquad \textbf{Eqn. 3-4}$$

where τ is the relaxation time or the time required for the direction of magnetization of a magnetized grain to relax into the direction of an applied magnetic field. Other variables are: v, the volume of the grain, B_c, the coercivity, J_s, the spontaneous magnetization, κ, Boltzmann's constant, T_{abs}, the absolute temperature, and C, the frequency factor estimated at 10^8 s^{-1} (Butler, 1992) or 10^9 s^{-1} (Dunlop and Özdemir, 1997). In a laboratory setting, which is at room temperature, the relaxation time is greater then the duration of the experiment, therefore the temperature represents the blocking temperature, under cooling conditions, and the unblocking temperature, under heating conditions, comparable to the duration of the experiment. The maximum blocking temperature of all remanence is the Curie temperature discussed earlier. It is an important tool in identifying the mineral contributing to the remanence, whether the remanence is naturally (NRM) occurring or produce in the laboratory.

Naturally occurring remanent magnetization include principally thermal, chemical and depositional remanent magnetization. Isothermal remanent magnetization may occur naturally only via a lightning strike. However, remanence anisotropy studies generally restrict themselves to the study of remanences acquired in the laboratory.

The anisotropy of anhysteretic remanent magnetization (AARM) and anisotropy of isothermal remnant magnetization (AIRM) are both used extensively for the study of the remanence anisotropy ellipsoid. Understanding natural remnant magnetism (NRM) is key when conducting a paleomagnetic study.

Both anhysteretic remanence magnetism (ARM) and isothermal remanence magnetism (IRM) are remanences that are fabricated in the laboratory. The acquisition of ARM in order to study the anisotropy requires subjecting samples to a small direct field (0.1 mT) superimposed over a defined window of the alternating field (usually less than or equal to 100 mT). On the other hand, the acquisition of IRM subjects the samples to a strong direct field (usually greater than 500 mT depending on rock type and magnetic mineralogy). When determining the AARM or AIRM, the sample must be completely demagnetized prior to imposing the magnetic fabric. For this reasons samples where hematite is the ferromagnetic (*s.l.*) component, AARM and AIRM may not be determined because there is currently no instrument capable of completely demagnetizing a hematite bearing sample.

For studies on sediments, ARM better magnetizes the fine particles that carry the stable remanence, than IRM, and therefore, ARM gives a better approximation of the remanence anisotropy (Jackson, 1991).

Similarly to AMS, the measurement of the AARM (or AIRM) in several directions, yields three principal directions which correspond to an ellipsoid's maximum, intermediate and minimum axes. Again, the anisotropy ellipsoid is characterized by its shape (Tj) and degree of anisotropy (Pj) which can then perhaps be related to strain and tectonic kinematics.

3.2 Analysing Strain from Magnetic Fabrics

The use of magnetic fabrics as a strain indicator was first suggested by Graham (1954), however proper methods for the analysis were not developed until the 1970's. Relating the orientation of the magnetic anisotropy ellipsoid to that of the strain ellipsoids is quite straightforward. Generally, the X, Y and Z direction of principal strain correspond to the k_1, k_2 and k_3 direction of the AMS ellipsoid or that of the AARM or AIRM ellipsoids. This direct representation is commonly acceptable. However, there are some cases where this relationship cannot be assumed.

The first exception is where the AMS fabric does not completely erase the primary fabric (Borradaile and Henry, 1997). This is a common problem in weakly strained sedimentary rocks where the fabric acquired during deposition is difficult to overprint.

Secondly, rocks which produce inverse anisotropy will not have principal orientation corresponding to the equivalent principal strain orientations (Borradaile and Henry, 1997). The best known mineral which occasionally exhibits this property is single domain (SD) magnetite, but tourmaline and Fe-rich calcite may also yield inverse fabrics where the minimum susceptibility axis is parallel to the longest crystallographic axis (Rochette *et al.*, 1992). Since the anisotropy of magnetite is mostly controlled by the shape of the grain, SD magnetite will have AMS where k_{min} is parallel to the long axis of the grain, and k_{max} is perpendicular to the long axis. The determination of the AARM ellipsoid, will in this case yield a true representation of the shape fabric of the SD magnetite grains and confirm the presence of SD magnetite by exhibiting a fabric which is orthogonal to the AMS fabric. Other minerals such as tourmaline, carbonates and goethite, can produce an inverse fabric (Rochette *et al.*, 1992).

Third, where the fabric accumulation was non-coaxial, direct relationship between the orientation of the magnetic anisotropy ellipsoid and that of the strain ellipsoid may not be assumed (Borradaile and Henry, 1997). This third exception is self-explanatory. During a non-coaxial strain history the orientation of the principal strain axes varies, therefore the orientation of the AMS, AARM or AIRM ellipsoid will not be representative of the orientation of the strain axes through the entire strain history.

Fourth and lastly, when recrystallization fabrics dominate the principal directions of the AMS fabric will reveal the stress directions at the time of recrystallization. These directions will differ from the finite principal strain axes, unless the strain history, throughout the recrystallization event, remained coaxial. Commonly, in metamorphic rocks, the products of recrystallization are high susceptibility minerals, such as magnetite, pyrrhotite and ilmenite. These later growing phases will commonly use silicate minerals as templates complementing the principal AMS directions but possibly altering, unpredictably, the shape and degree of anisotropy of the susceptibility ellipsoid. Under these conditions, estimating strain magnitudes would be impossible (Borradaile and Henry, 1997).

Even though non-coaxial strain does not permit the determination of the orientation of strain, regional kinematics may still be interpreted. Non-coaxial strain means there has been a rotation or shearing of the rock. In metamorphic rocks where minerals have grown at different times; generally quartz and feldspar form first, followed by metamorphic phyllosilicates and lastly the late metamorphic magnetite, pyrrhotite and other remanence carrying minerals. The quartz and feldspar will give rise to schistosity, the phyllosilicate will dominate the AMS fabric and the remanence carrying minerals will produce the AARM fabric. The relationship between the orientation of the foliations of these three fabrics can define the sense of rotation or shear associated with non-coaxial strain. This type of analysis as a regional kinematic indicator has been used by Borradaile and Spark (1991), Borradaile and Dehls (1993), Borradaile *et al.* (1993a) and Werner and Borradaile (1996).

In section 3.1.2, it was said that the magnetic anisotropy ellipsoid can be described by two properties: the shape Tj and the degree of anisotropy (Pj)of the ellipsoid. In that section, we were referring to the AMS ellipsoid; however, these two properties also apply to the AARM and the AIRM ellipsoids. Traditionally, the shape of the magnetic ellipsoid was graphically represented on a Flinn diagram, the same way the strain ellipsoid was plotted. The Flinn diagram plots a against b (for the strain ellipse) or L against F (for the magnetic anisotropy ellipse)(see Figure 2-6). Therefore, the Flinn diagram tries to correlate two parameters which describe the shape. Hrouda (1982) introduced a graphical method using the Pj and Tj parameters of Jelinek (1981), which describes the degree of anisotropy and shape of the anisotropy ellipsoid respectively. These two parameters are defined by Hrouda (1982) by the following equations:

$$P' = \exp\sqrt{2(a_1^2 + a_2^2 + a_3^2)} \qquad \textbf{Eqn. 3-5}$$

$$T = \frac{2(\ln k_2 - \ln k_3)}{\ln k_1 - \ln k_3} - 1 \qquad \textbf{Eqn. 3-6}$$

where $a_i = \ln(k_i / kb)$ for i = 1 to 3 and $kb = (k_1 + k_2 + k_3)/3$. The result obtained form either of the *kb* definitions are acceptable as these do not vary significantly for the usual range of *k* (Borradaile, 1991). The Pj parameter plots on the x-axis and originates at 1 where Pj = 1 describes a unit sphere. The degree of anisotropy increases as Pj increases. The y-axis represents the shape, Tj, of the anisotropy ellipsoid. The axis ranges from -1 to 1 where Tj values above zero describe an oblate ellipsoid and Tj values below zero describe a prolate ellipsoid (Figure 3-2).

Unlike the fairly straightforward relationship between the orientation of the strain ellipsoid and the magnetic anisotropy ellipsoid, correlating the magnitude of the anisotropy ellipsoid with the magnitude of strain is more ambiguous. Borradaile (1991) showed that using the Pj parameter to describe both the magnetic

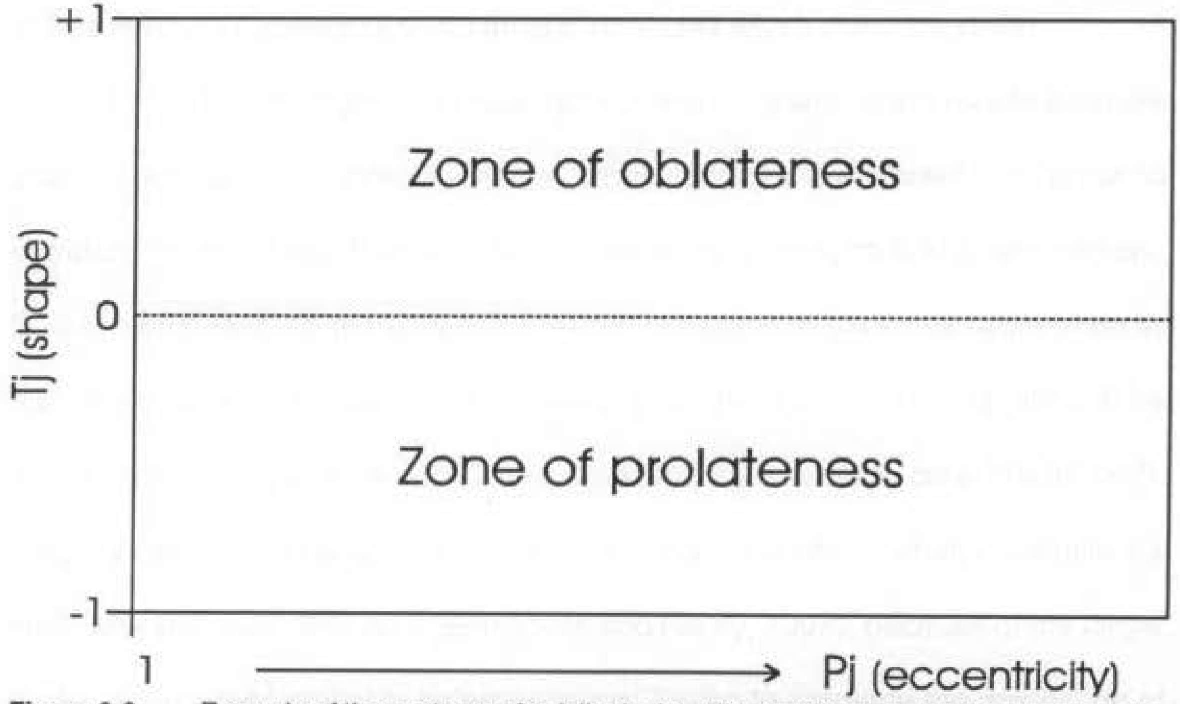

Figure 3-2 Example of the anatomy of a Jelinek plot. This graphical method is superior to the Flinn diagram for plotting the shape (T) and degree of anisotropy (Pj) of the magnetic fabric ellipsoids.

susceptibility anisotropy and strain ellipsoids produced the strongest correlation between their magnitudes. And, in experimental studies Borradaile and Alford (1987, 1988) found strong power law agreements. Correlation studies between magnitudes of strain and of magnetic fabric have only investigated the relationship of strain with AMS (Wood *et al.*, 1976; Rathore, 1980; Borradaile and Motherhill, 1984; Cogné and Perroud, 1988; and many others).

Correlation between Pj and strain have only been successful where the maximum shortening was in excess of 30% and less then 70% (Borradaile and Henry, 1997) *(note: strain is calculated by using equation 3-5 and substituting k_1, k_2, and k_3 by X, Y and Z)*. Beyond 30% shortening it is assumed that the primary fabric is completely overprinted and beyond 70% the mineral alignment is saturated and

Pj has reached a plateau and no longer increases with increasing strain.

We must not forget that the uniqueness of magnetic fabric was to estimate strain orientation and intensity where strain markers are absent. In order to correlate the AMS magnitude with strain each sample must contain strain markers. Furthermore the strain markers should strain homogeneously at the same scale as the AMS fabric. Pratically this means that the strain markers should be approximately of the same size as a standard AMS sample core (10.55 cm^3). Larger strain markers record strain on a scale which cannot be easily related to the scale of a standard AMS core (Borradaile and Henry, 1997); because of the larger scale, strain would probably heterogeneous. Trying to correlate the magnitude of AMS with strain seems to limit the potential of magnetic fabric analysis because of the limited amount of outcrops which satisfy all these conditions, and the additional problems of incomplete overprinting of primary fabric, saturation alignment near high strain and some fabrics caused by recrystallization and <u>not</u> strain, which must be considered.

3.3 Concluding Remarks

Analysing and comparing the magnetic foliation, magnetic lineation and the degree of anisotropy of AMS, ARM and IRM on a regional scale can suggest kinematic scenarios where strain markers or conventional petrofabric analysis could not. The main reason is the universal property of magnetism. Every mineral possesses a magnetic property whether it is diamagnetic, paramagnetic or ferromagnetic (*s.l.*).

Chapter 4 - Magnetic Mineralogy

4.1 Introduction

The magnetic mineralogy of sedimentary rocks, in this study predominantly pelagic chalks and marls and limestone, may be determined by several methods, however, most present greater limitations than advantages. Any identification method requiring a concentrated separation of the ferromagnetic minerals (ie: Curie temperatures, X-Ray diffraction) is difficult because it is rarely possible to separate enough of the ferromagnetic mineral to perform the test. Separation by HCl and acetic acid is commonly used but also commonly digests most, if not all of the iron oxides as well as the carbonates (Dunlop and Özdemir, 1997). The determination of blocking temperatures presents the complication of possibly producing hematite during demagnetization at temperatures above 310°C. Further discussion on limitations of other possible mineral identification methods can be found in Borradaile *et al.* (1993b) and a complete review in Lowrie and Heller (1982).

For this study, the magnetic mineralogy was determined by examining the hysteresis loop parameters and the coercivity of remanence. This data set permits estimation of the ferromagnetic mineralogy and its domain structure, the determination of the susceptibility of the matrix and the ferromagnetic content, as well as the degree of contribution of each phase to the total susceptibility.

Insight on the contribution of diamagnetic, paramagnetic and ferromagnetic phases to the total susceptibility can also be obtained from the measured mean susceptibility of the anisotropy of magnetic susceptibility (AMS).

4.2 Hysteresis Loop Parameters and Coercivity of Remanence

An alternating gradient force magnetometer (MicroMag) was used to determine the parameters of the hysteresis loop. The instrument was developed commercially by Princeton Measurements Corporation (Princeton, NJ, USA). The sample size required is very small. Dimensions are no more than 2mm x 2mm x 1mm and its weight can not exceed much more than 50 mg - 100 mg.

One limitation of this method becomes apparent when considering the size of the sample tested. The mean weight of the cores for this study is 23 grams, therefore, at the most the tested sample is representative of 0.04% of the core from which it is taken. If there is any heterogeneity within the core, which is most often the case, the tested sample may not represent the actual mean hysteresis loop parameter values of the core. Fortunately, the rocks studied are both fine-grained and homogeneous so that the small samples are representative.

From the hysteresis loop curve, the following parameters were determined:

- matrix susceptibility (χ_m)
- ferromagnetic susceptibility (χ_f)
- total susceptibility (χ)
- saturation magnetization (M_s)
- remanent magnetization (M_r) normalized as M_r / M_s
- coercivity (H_c)
- coercivity of remanence (H_{cr}) also normalized as H_{cr} / H_c

A complete list of the data for each measured sample can be found in APPENDIX D.

4.2.1 Identification of the Ferromagnetic Mineral

The review by Lowrie and Heller (1982) on the magnetic properties of marine limestones shows that the main contributor to the natural remanent magnetization of non-red marine sediments is magnetite. Goethite, pyrrhotite and maghemite may also have a minor contribution where goethite is the commonest of the three, being the only iron oxide in chemical equilibrium (regarding eH/pH) in seawater. Table 4-1 list some of the published data of the properties for both of single domain (SD) and multi domain (MD) magnetite.

Table 4-1 List of published parameters for single domain and multi domain magnetite. Source: Dunlop (1986)

Parameter	Single Domain	Multi Domain
H_c	10 - 40 mT	2.5 - 4 mT
M_r / M_s	0.5 - 0.9	0.01 - 0.03
H_{cr} / H_c	<2	>4

If we compare these published values with the averages obtained from this study listed in Table 4-2, we observe that the studies values for the magnetization ratio and the coercivity ratio fall between the ranges of SD and MD magnetite. The average coercivity (H_c) value is located in the lower limit of the SD range, however taking into account the standard deviation, the coercivity also straddles the SD and MD cases (Figure 4-1).

These mid range values between SD and MD magnetite clearly corresponds to pseudo-single domain (PSD) magnetite. By plotting the magnetization ratio (M_r/M_s) versus the coercivity ratio (H_{cr} / H_c) for magnetite in the manner described by

Day *et al.* (1977), it is evident the data points fall within the field of PSD magnetite (Figure 4-2).

Table 4-2 List of averages and standard deviation of measured parameters of this study's samples.

Parameter	Average	Standard Deviation	Standard Error
H_c	14.50 mT	13.23 mT	1.02 mT
M_r / M_s	0.18	0.056	0.004
H_{cr} / H_c	2.162	0.496	0.04

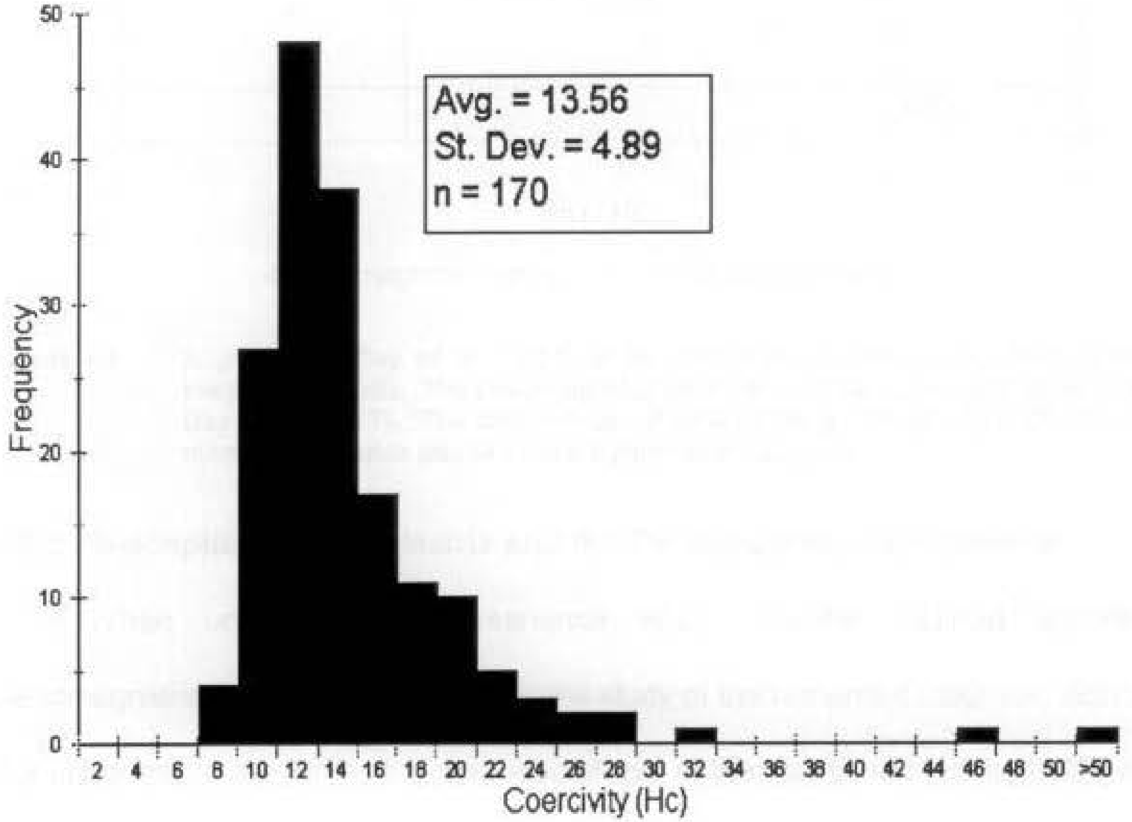

Figure 4-1 Frequency histogram of the coercivity values (in mT) of the measured samples. Results are characteristic for magnetite.

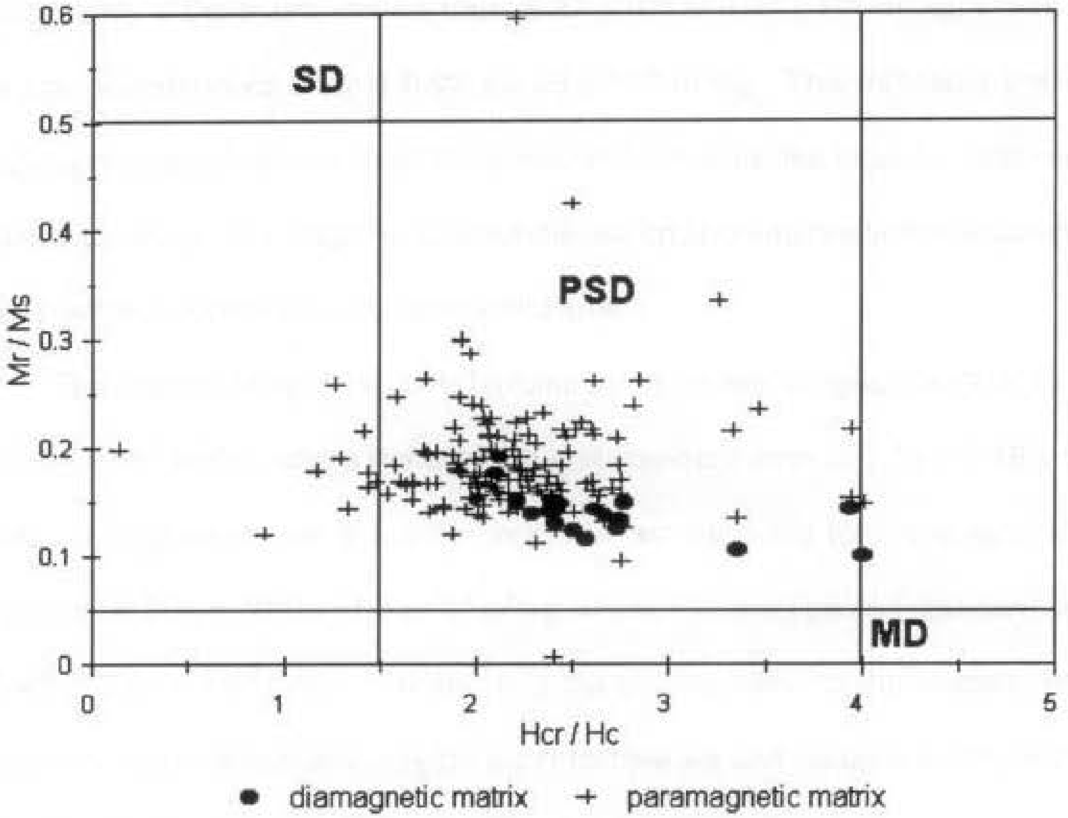

Figure 4-2 A plot (after Day *et al.*, 1977) of the hysteresis coercivity ratio versus the magnetization ratio. The phase boundaries are defined by values also taken from Day *et al.* (1977). The total number of data points is 170, of which 21 have a diamagnetic matrix and 149 have a paramagnetic matrix.

4.2.2 Susceptibility of the Matrix and the Ferromagnetic Components

When undertaking a remanence study, whether inclined towards paleomagnetism or in this case, towards the study of the remanent magnetic fabric, it is important to determine the magnetic phase of the matrix, the susceptibility of the matrix and the percent contribution of the matrix and the ferromagnetic component to the total susceptibility.

The pelagic to shallow marine limestones samples (n = 170) included in this part of the project have predominantly low positive susceptibilities. The susceptibility of the matrix ranges from -6.87 x 10^{-8} to 4.00 x 10^{-8} m^3/kg, where the average and standard error is 0.92 ± 0.09 x 10^{-8} m^3/kg. This indicates that the matrix is composed of a mixture of diamagnetic minerals like calcium carbonates and quartz, which have negative susceptibilities, and paramagnetic minerals which have positive but generally low susceptibilities.

The susceptibility of the of the ferromagnetic content ranges from 0.001 x 10^{-8} to 15.9 x 10^{-8} m^3/kg, where the average and standard error is 2.54 ± 0.18 x 10^{-8} m^3/kg. By combining these two components, we obtained total susceptibilities ranging from 0.34 x 10^{-8} to 17.9 x 10^{-8} m^3/kg, where the average and standard error is 3.46 ± 0.20 x 10^{-8} m^3/kg. By dividing the susceptibility of the ferromagnetic content by the total susceptibility for each sample we can determine the percent contribution of each component to the total susceptibility.

The interpretation of the plot in Figure 4-3 summarizes the observation that can be made about the magnetic nature of the matrix and the contribution each component brings to the total susceptibility. Figure 4-3 expresses the following relationship:

$$\frac{K_{ferro}}{K_{total}} = \frac{K_{ferro}}{K_{ferro} + K_{matrx}} \qquad \textbf{Eqn. 4-1}$$

A K_{ferro}/K_{total} ratio greater than 1 (11.8 % of the samples) indicates that the matrix is diamagnetic. Samples included within the field of 0 to 0.5 (17%) have paramagnetic matrix and the paramagnetic component contributes more than 50 %

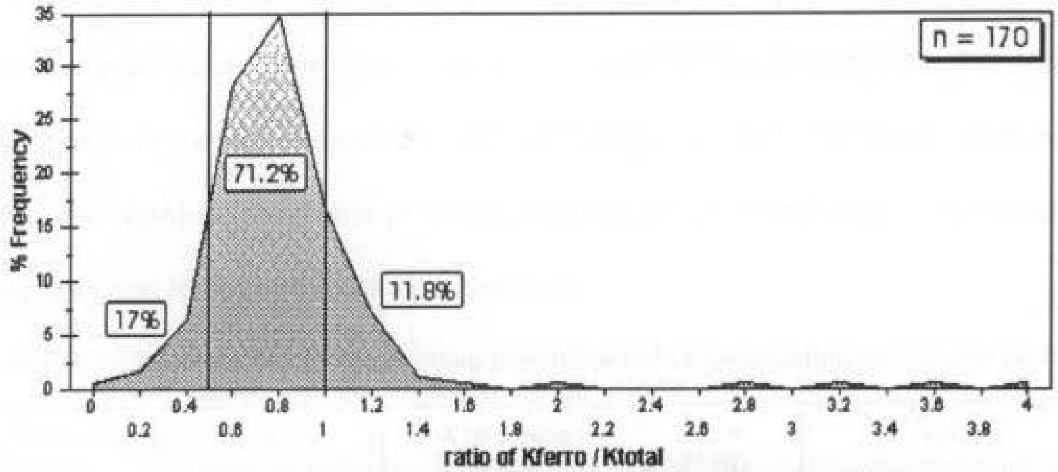

Figure 4-3 Frequency histogram of the percent susceptibility of the ferromagnetic content divided by the total susceptibility. See text for explanation of each subdivided field.

of the total susceptibility. Similarly, samples included within the field of 0.5 to 1 (71.2% of the samples) also have paramagnetic matrix but the paramagnetic minerals contribute less than 50% to the total susceptibility.

These are positive results for undertaking remanence studies because the ferromagnetic content seems to have a dominant presence within the tested samples. However we must keep in mind the limitation of this identification method discussed in section 4.2. The sample sizes are so small that they may not always represent the entire specimen. For this reason the bulk susceptibility measurements should give a better representation since the entire core is processed.

4.3 Mean or Bulk Magnetic Susceptibility

The anisotropy of magnetic susceptibility (AMS) measures the susceptibility of the diamagnetic, paramagnetic and ferromagnetic components of a core specimen. The bulk susceptibility of a specimen depends not only on the mineralogical content of the specimen, but more importantly on the volume percentage of the mineral content. Table 4-3 outlines two boundary cases of how volume percent of magnetite (a ferromagnetic mineral) and clays (paramagnetic minerals) can dictate the bulk susceptibility.

Table 4-3 Outline of boundary setting possibilities when considering the volume percent of magnetite and clays in a diamagnetic matrix.

K of magnetic content +	K of matrix = (average k = -10×10^{-6} SI)	Total K
0.1% magnetite x 500000 x 10^{-6} SI (average K for magnetite) = 500 x 10^{-6} SI	99.9% matrix x -10 x 10^{-6} SI = 9.99 x 10^{-6} SI	490.01 x 10^{-6} SI
1% clays (paramagnetic) x 1000 x 10^{-6} SI (average k for clays) = 10 x 10^{-6} SI	99% matrix x -10 x 10^{-6} SI = 9.9 x 10^{-6} SI	0.1 x 10^{-6} SI

The mean susceptibility, obtained during the AMS study, for the 1170 cores measured ranged from -33 to 4145 SI x 10^{-6} (Figure 4-4) of which 83% of the samples are within the range of -15 to 40 SI x 10^{-6}. Negative bulk susceptibilities were obtained in 37% of the cores. Therefore, it can be deduced that those samples are composed of much less than 0.1 vol% magnetite and of less than 1 vol% paramagnetic minerals. The majority of the cores yielding positive susceptibilities have mean values less than 100 SI x 10^{-6} (61.5%), indicating that paramagnetic clays dominant the AMS signal by virtue of their stronger anisotropy.

The cores producing mean values greater than 100 SI x 10^{-6} (1.5%) suggest a greater importance of magnetite. However, the abundance of magnetite within each core is still less than 0.1 vol% since the maximum mean susceptibility

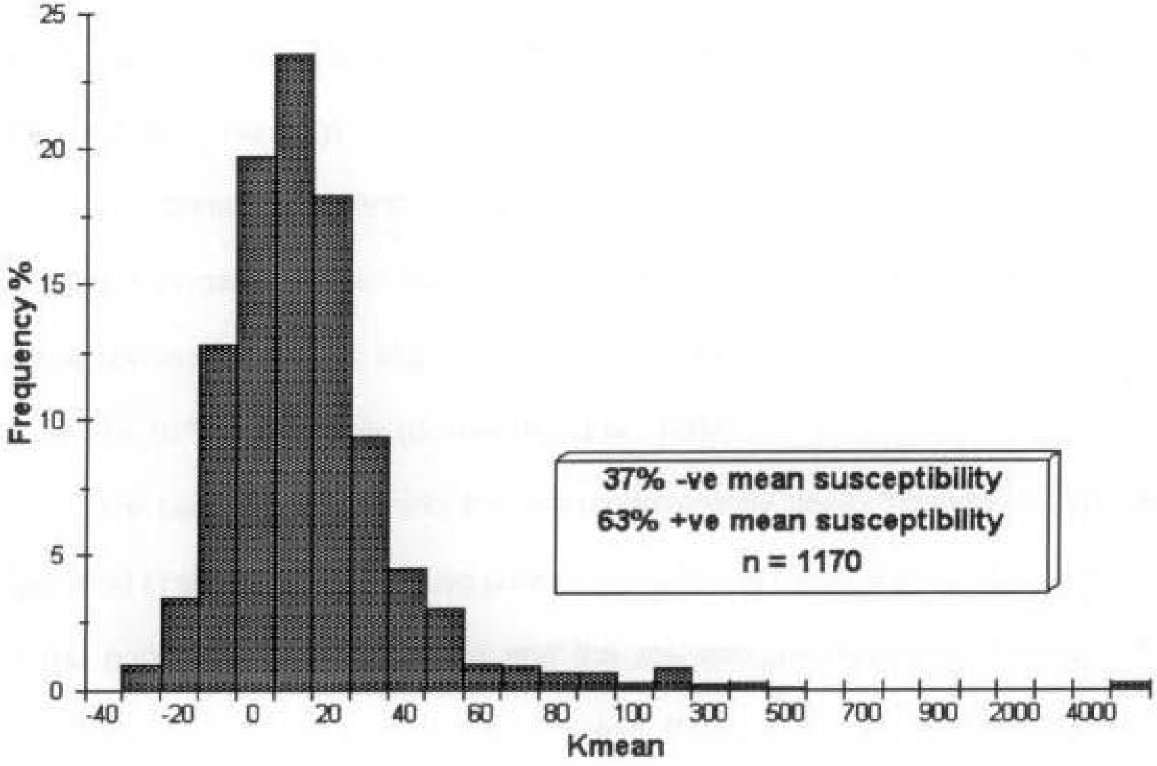

Figure 4-4 Percentile frequency distribution of the mean susceptibility values of 1170 cores.

recorded is 400 SI x 10^{-6}. Sample FL98344 is the only exception with its three cores recording mean susceptibility values of slightly more than 4000 SI x 10^{-6}. Sample FL98344 is a sandstone containing homogeneously distributed mafic clastic grains, therefore it is safe to assume that the high susceptibility values obtained from these cores in comparison to the rest of the sample suite is due to its different lithology.

4.4 Summary

The hysteresis and coercivity study included 170 cores, where the tested Micromag sample represented, at the most, 0.04 % of the core's mass. The AMS study included 1170 cores, where the entire core is measured. Consequently, the mean susceptibilities obtained through the AMS analysis are a better indicator of the magnetic mineralogy present, contributing to the magnetic fabric.

The diamagnetic contributors are predominantly calcite and quartz. Where measured negative mean susceptibility values correlate to published mean susceptibilities for natural, slightly impure calcite and quartz of -13.8 SI x 10^{-6} and -9.29 SI x 10^{-6}, respectively (Borradaile *et al.*, 1987).

The paramagnetic contributors are predominantly clays. Younger sediments deposited in shallower waters also contain terrigenous clastic input due to erosion of the ophiolitic Troodos Terrain and the metamorphic Mamonia Terrain. In samples with positive mean susceptibilities (66% of those measured), these paramagnetic minerals control the anisotropy of magnetic susceptibility. Therefore, the AMS fabric will portray the preferred crystallographic orientation of the paramagnetic content, dominantly clays.

The ferromagnetic contributor is identified as magnetite by the hysteresis loop and coercivity parameters. The AMS mean susceptibility values suggest its presence is less than 0.1 % of the cores' volumes. The concentration of magnetite grains is insufficient to control the anisotropy of the AMS fabric. However, the preferred dimensional orientation of the magnetite grains solely defines the anisotropy of anhysteretic remanent magnetization (AARM) fabric, since magnetite is the dominant and most likely the only mineral present in these rocks, that is able to acquire a magnetic remanence.

Chapter 5 - Anisotropy of Magnetic Susceptibility (AMS)

5.1 Introduction

The anisotropy of magnetic susceptibility (AMS), in this study, was measured in a weak magnetic field (0.05 mT) using a Sapphire Instrument SI-2. The weak magnetic field is important because it is comparable to the Earth's magnetic field. A solenoidal coil produces the low-field intensity with an external field frequency of 19 200 Hz. The older SI-2 used 750 Hz. Measuring at 19 200 Hz enhances the sensitivity but still retains a substantially in-phase component, reflecting susceptibility rather than electrical conductivity.

AMS measurements determine the bulk magnetic susceptibility (K) which represents how easily a rock magnetizes in the presence of an external field. An anisotropic sample subjected to a weak field will acquire an induced magnetization (M) in a direction generally not parallel to the applied field (H). The acquired induced magnetization is defined by three orthogonal components

$$\begin{aligned} M_x &= k_{xx}H_x + k_{xy}H_y + k_{xz}H_z \\ M_y &= k_{yx}H_x + k_{yy}H_y + k_{yz}H_z \\ M_z &= k_{zx}H_x + k_{zy}H_y + k_{zz}H_z \end{aligned} \qquad \textbf{Eqn. 5-1}$$

equivalent to

$$M_i = k_{ij}H_j \qquad \textbf{Eqn. 5-2}$$

where k_{ij} is a second-order tensor defined by the following matrix:

$$k_{ij} = \begin{matrix} k_{xx} & k_{xy} & k_{xz} \\ k_{xy} & k_{yy} & k_{yz} \\ k_{xz} & k_{yz} & k_{zz} \end{matrix} \qquad \textbf{Eqn. 5-3}$$

These nine parameters define six independent components which define the anisotropy of magnetic susceptibility ellipsoid. The measuring scheme, used for this study, follows Nye's 7 orientation procedure outlined in Figure 5-1 (Borradaile and Stupasky, 1995). The computer program SI298.exe designed by Dr. G. J. Borradaile computes the data of the seven orientation and yields the magnitude and orientation of the three orthogonal axes defining the AMS ellipsoid.

Since the k_{ij} are >0, the tensor can be represented by an AMS ellipsoid, characterized by the length and orientation of its three principal axes K_1 (maximum axis) $\geq K_2$ (intermediate axis) $\geq K_3$ (minimum axis). These in turn may may be used to give characteristic anisotropy parameters which are listed in Table 3-1. From this list, the following parameters were considered in this study: mean susceptibility

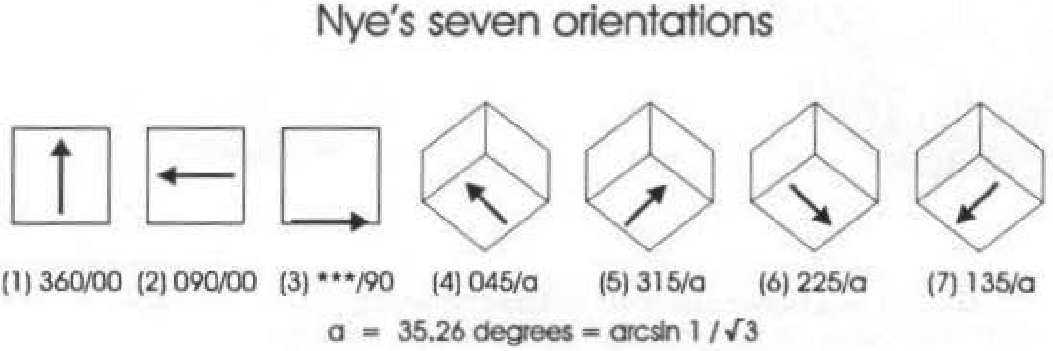

Figure 5-1 Cubical sample holders are shown in plan view, with insertion direction into induction coil being towards the top of the page.

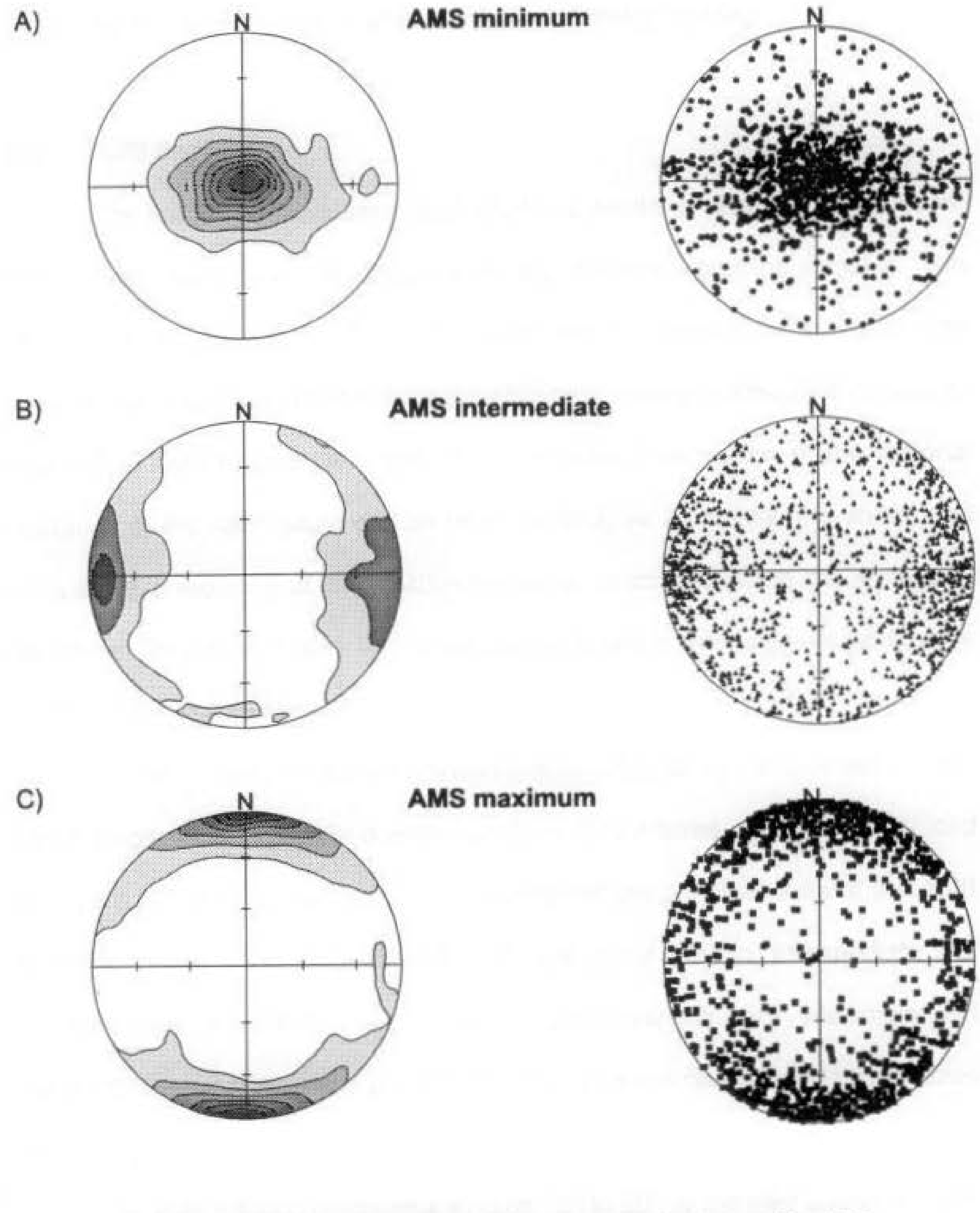

Figure 5-2 Stereographic projection of the three principal axes of the AMS ellipsoids. The number of data points for each projection is 1170. The contour interval increase from the expected value of 11.7 per 1% unit area by 2 standard deviation (S = 2.394) up to 28S for the minima and maxima, and 12S for the intermediate axes.

(K_m), shape of anisotropy (T_j), and the degree of anisotropy (P_j).

5.2 AMS Results

The AMS results are separated into three sections. The first analyses the mean susceptibility in order to define the magnetic mineralogy of the samples. This discussion can be found in the previous chapter in sections 4.3 and 4.4. The second considers the orientation of the ellipsoids' principal directions in order to define the AMS foliation and lineation. A detailed discussion of the regional variation of the AMS fabric can be found in Chapter 6. Lastly, the shape and degree of anisotropy of the AMS ellipsoid is described using the P_j and T_j parameters of Jelinek (1981). These are closely linked to the magnetic mineralogy and will be presented below.

The AMS study included 1170 cores, measuring 25 mm in diameter and 22 mm in length, drilled from 434 oriented samples (2 to 4 cores per sample). Plotted in Figure 5-2 are the stereographic projection of the principal axes of the AMS ellipsoid. Peak contouring trend and plunge of the minima, intermediate and maxima axes are 045/85, 270/09 and 180/00 respectively. Maximum and intermediate cluster within the plane of the AMS foliation represented by the poles to the minima axes.

The AMS foliation predominantly dips 10° to 20° to the east and west. The circular-normal distribution of the minima axes declinations (poles to foliation) in Figure 5-3a illustrates the preferred dip direction of the AMS foliation planes. The

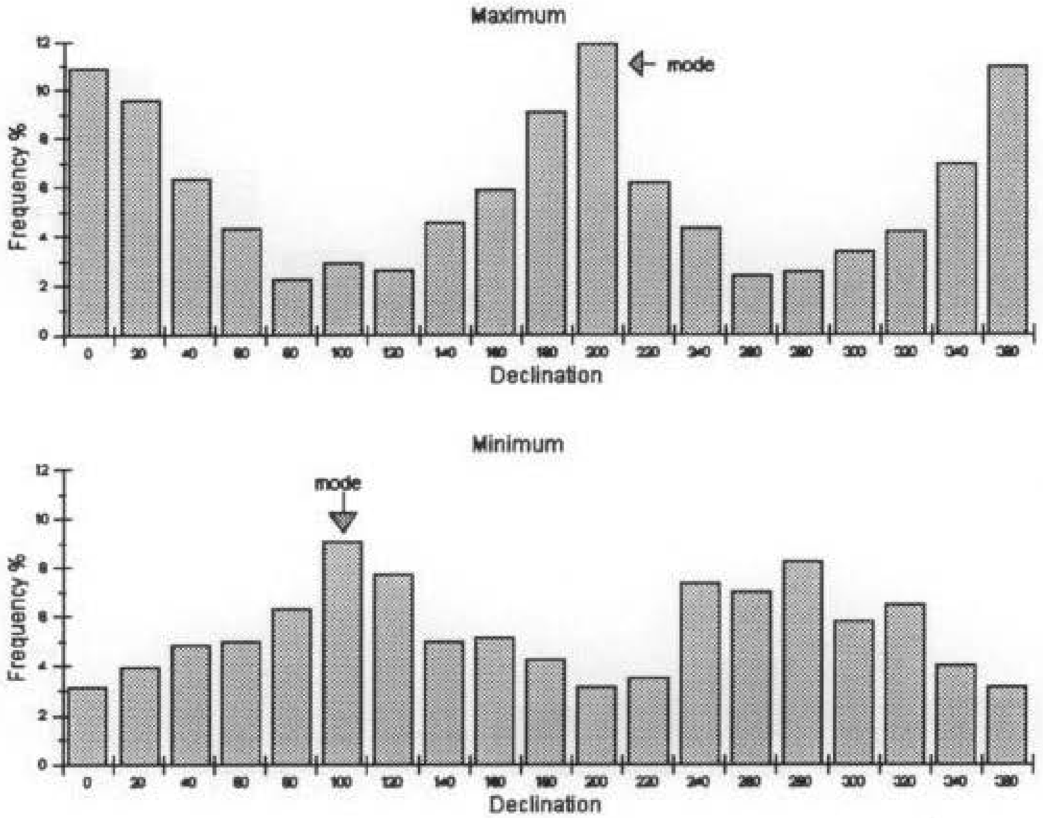

Figure 5-3a Circular -normal distribution of the percent frequency distribution of the AMS maxima and minima axes declinations (n = 1170).

circular-normal distribution of the inclinations for both minima and maxima are plotted in Figure 5-3b. The inclination of the minima axes concentrate at the 70 to 80 degree interval, however the variation of the distribution's amplitude is small. In other words, each inclination interval is represented by a substantial population, unlike the circular-normal distribution of the maximum axes inclination. The expression of the these contrasting circular-normal distribution of minimum and maximum axes inclinations can be seen in the stereographic projections of Figure 5-2a. The strong unimodal distribution of K_{max} axes expresses a cluster distribution, whereas the tendency towards a uniform distribution seen in the K_{min} axes

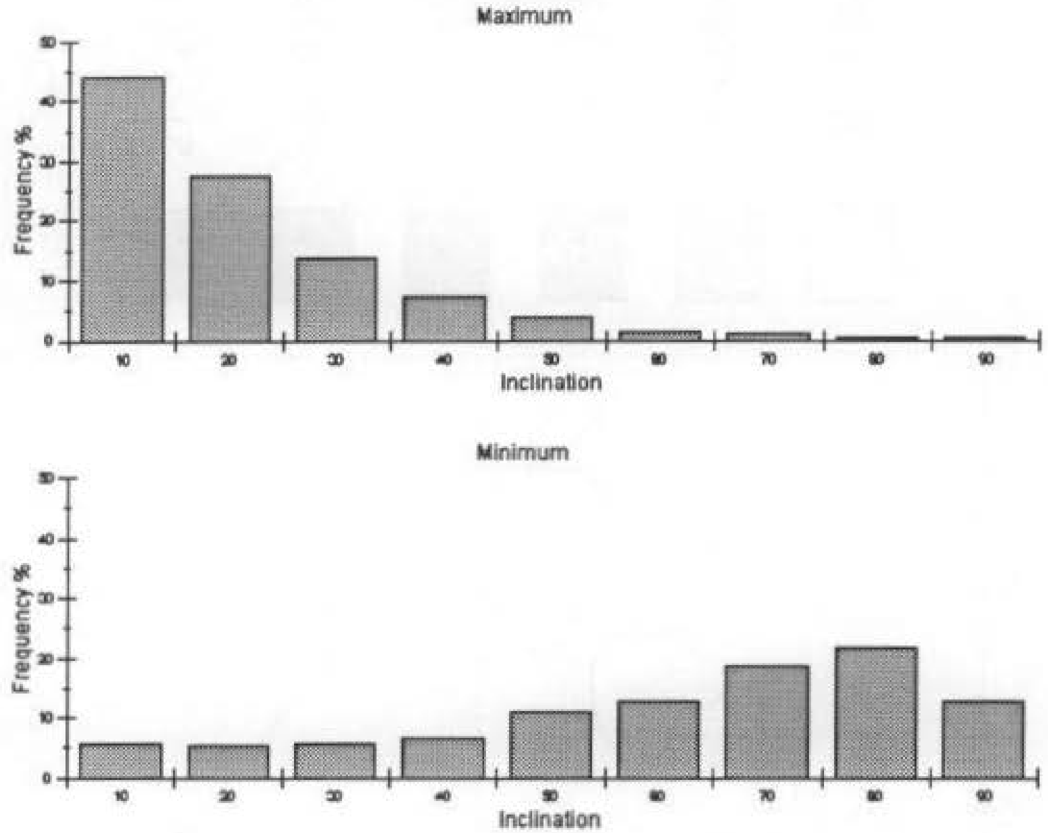

Figure 5-3b Histogram of the percent frequency distribution of the AMS maxima and minima axes inclinations (n = 1170).

distribution express a partial girdle on the stereographic projection.

The AMS lineation, represented by the direction of the maxima axes, cluster more and give a higher modal frequency than the minima axes. Histograms of the declination and inclination (Figure 5-3a and b) of the maxima show that the lineation predominantly plunges less than 20° and trends N-NNE and S-SSW.

In chapter 7, the origin of the partly tectonic AMS fabric will be discussed and interpreted on a regional scale.

5.2.1 Shape and Eccentricity of the AMS Ellipsoid

The anisotropy of the magnetic susceptibility ellipsoids can be defined by two

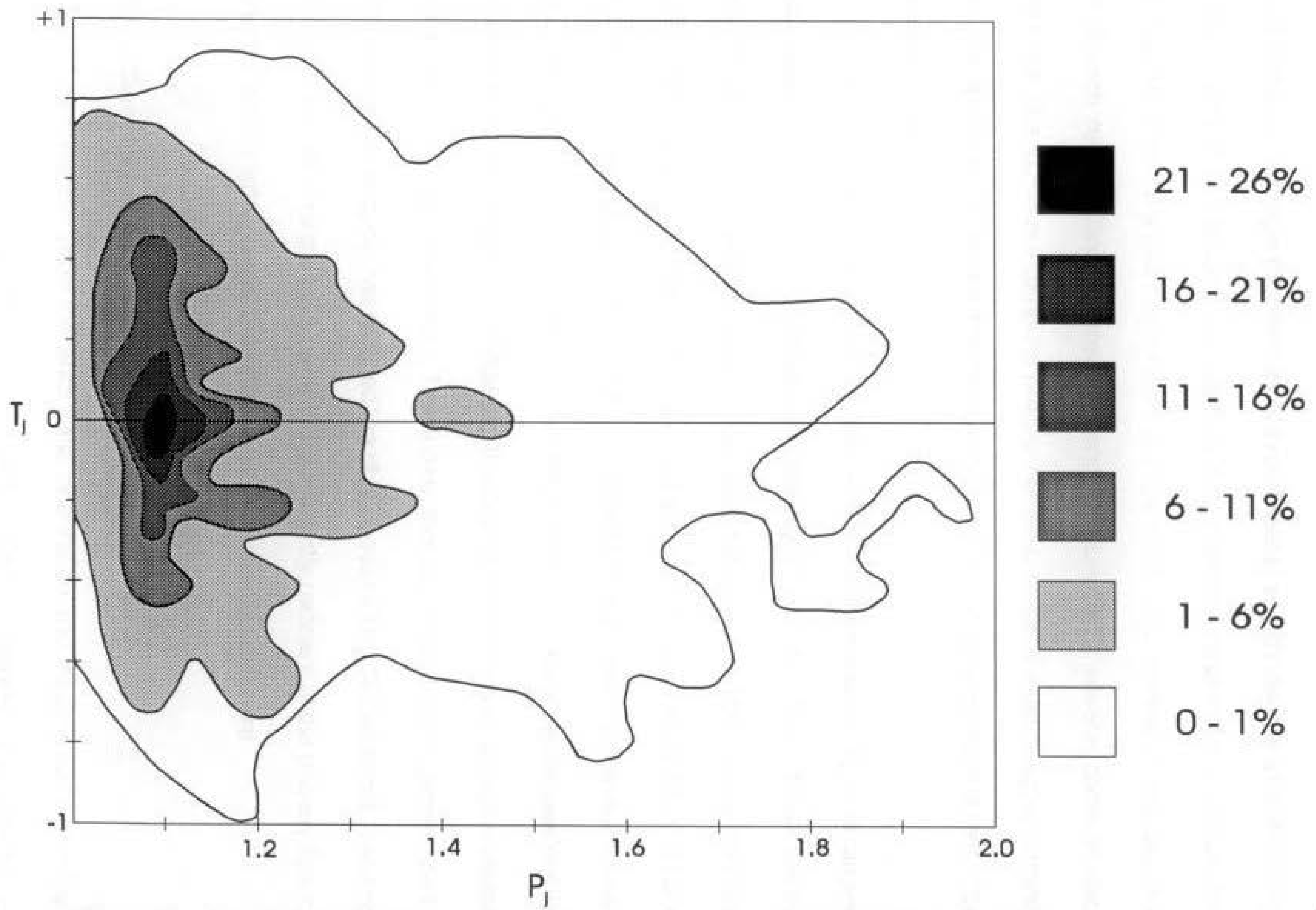

Figure 5-4 Plot of the Jelinek (1981) parameter Pj and Tj for the mean AMS ellipsoid of each sample (n = 418).

parameters, its shape (oblateness or prolateness) and its degree of eccentricity. The Jelinek (1981) shape parameters T_j and eccentricity parameter P_j will be used in this study and the plot can be seen in Figure 5-4. The number of data points is 418,each representing the mean P_j and T_j values from several cores of each sample. The SI298.exe computer program which contours the Jelinek plot currently allows only a maximum number of data points of 500, which explains the use of the sample means.

The AMS ellipsoid is slightly oblate with a shape parameter, T_j, of mean and standard error of 0.12 ± 0.01 and an eccentricity, P_j, of 1.41 ± 0.06. These are the mean parameter values for the sample mean data set (n = 418). The mean and standard error of T_j an P_j for the entire core data set (n = 1170) are 0.12 ± 0.01 and 1.66 ± 0.13, respectively. The tendency of the AMS fabric toward oblateness may also indicate that a primary sedimentary fabric remains, where oblateness results from compaction preferentially flattening the mineral content within a common plane parallel to bedding (S-tectonite). The superimposed tectonic fabric, where the L-fabric is well developed, has reduced the oblateness of the AMS ellipsoid, lowering T_j value, and producing a fabric where S(dominantly remnant of the primary fabric) component is slightly larger than the L(tectonic fabric) component.

5.3 Summary of AMS

The complete list of the AMS data, orientation and magnitude of principal axes, mean susceptibility, P_j and T_j, can be found in APPENDIX B. The AMS fabric is partly tectonic, as will be argued later in Chapter 7. Magnetic foliation planes dip moderately to shallowly east and west, inclined to bedding, while the magnetic lineation predominantly trends N to NNE and S to SSW with a gentle plunge of about 0° to 20°. The ellipsoid is slightly oblate and moderately eccentric, no doubt a result of the remaining primary sedimentary fabric due to compaction.

Chapter 6 - Anisotropy of Anhysteretic Remanent Magnetization (AARM)

6.1 Introduction

The anisotropy of anhysteretic remanent magnetization (AARM) adds a dimension to the analysis of a magnetic fabric by isolating the fabric of the ferromagnetic minerals: those able to acquire a magnetic remanence.

A sample acquires an anhysteretic remanent magnetization (ARM) by exposing it to a decaying alternating field (AF) that randomizes the spin moments. Simultaneously, over at least part of the AF range, a small direct current (DC) field is imposed. This is sometimes called the bias field. Measurements for this study were done using a Sapphire Instruments SI-4 non-tumbling alternating field demagnetizer. In this study, using the laboratory's previous experiences, the AF decayed from a peak intensity of 100 mT and a DC field of 0.1 mT was applied during the decay window of the AF between 60 to 0 mT. The relationship between the remanent magnetization and the applied DC field is expressed by the following equation

$$M_r = k \cdot f(H) \qquad \textbf{Eqn. 5-1}$$

where, M_r is the remanent magnetism, k is a second rank symmetric tensor, and f(H) is a function of the applied DC magnetic field.

6.2 Measurement Procedure

The measuring procedure follows the same Nye's seven orientation scheme used for the AMS measurements (Figure 5-1). First, the sample is demagnetized by an AF decaying from a peak value of 100 mT to zero (AF_{100}) in the first three orthogonal positions of the Nye's scheme. Subsequently the sample is exposed to the AF_{100} superimposed on a DC field in all seven orientations and the ARM intensity is measured after each orientation. The ARM intensity is measured with a JR-5 spinner magnetometer, which has an accuracy of 0.001 mA/m. The seven orientations of the ARM measurements are collected by the computer program Spin98.exe design by Dr. G. J. Borradaile. The data is then transferred to the SI298.exe computer program, also designed by Dr. G. J. Borradaile, which calculates the three principal axes of the anisotropy of ARM ellipsoid, $AARM_{max}$, $AARM_{int}$, and $AARM_{min}$.

6.2.1 Sample Screening Processes

The measurement procedure for determining the AARM is time consuming, with an average time per sample of 20 to 25 min. For this reason, it is more efficient to develop a screening process to identify the samples which will yield a meaningful AARM. Such samples need to carry a ferromagnetic mineral capable of acquiring a remanence, as well as a sufficiently high concentration of this mineral in order for the intensity of the remanence to be measurable by the instrumentation.

The first screening test eliminated the samples with negative low field induced magnetic susceptibility as found from the AMS study. With a negative susceptibility, indicating a diamagnetic bulk response due to calcite, it is unlikely the ferromagnetic concentration will be sufficient, that is if ferromagnetic minerals are even present. Thus, 430 cores were rejected (37% of total cores, leaving 740 measurable cores for the AARM study).

A common way of further screening for an AARM study is to determine the intensity of their natural remanent magnetization (NRM). If the sample yields an NRM intensity greater than 1 mA/m the sample was accepted. This method of screening was used for 20 samples , all of which were accepted. However this process is also time consuming (~ 5 minutes per sample).

Therefore, a more rapid screening process used isothermal remanent magnetization (IRM) as a potential tool for quickly removing unsuitable samples for the AARM study. The procedure entailed applying an IRM of 100 mT (IRM_{100}) in the -x direction (horizontal to the top of the core) using a SI-6 pulse magnetizer and then measuring the intensity of the IRM in that direction with a Molspin spinner magnetometer. A total of 42 samples were given IRM_{100} and produced intensities ranging from 35 to 4269 mA/m. By trial and error it was determined that a minimum IRM_{100} of 40 mA/m was needed in order to produce a sufficiently measurable ARM. AARM was then measured on those samples meeting that criteria (37 samples).

Processing the data revealed suspicious AARM principal directions when compared to AARM principal directions obtained from 20 samples not exposed to the IRM_{100} but selected by the much lengthier NRM intensity selection criterium.

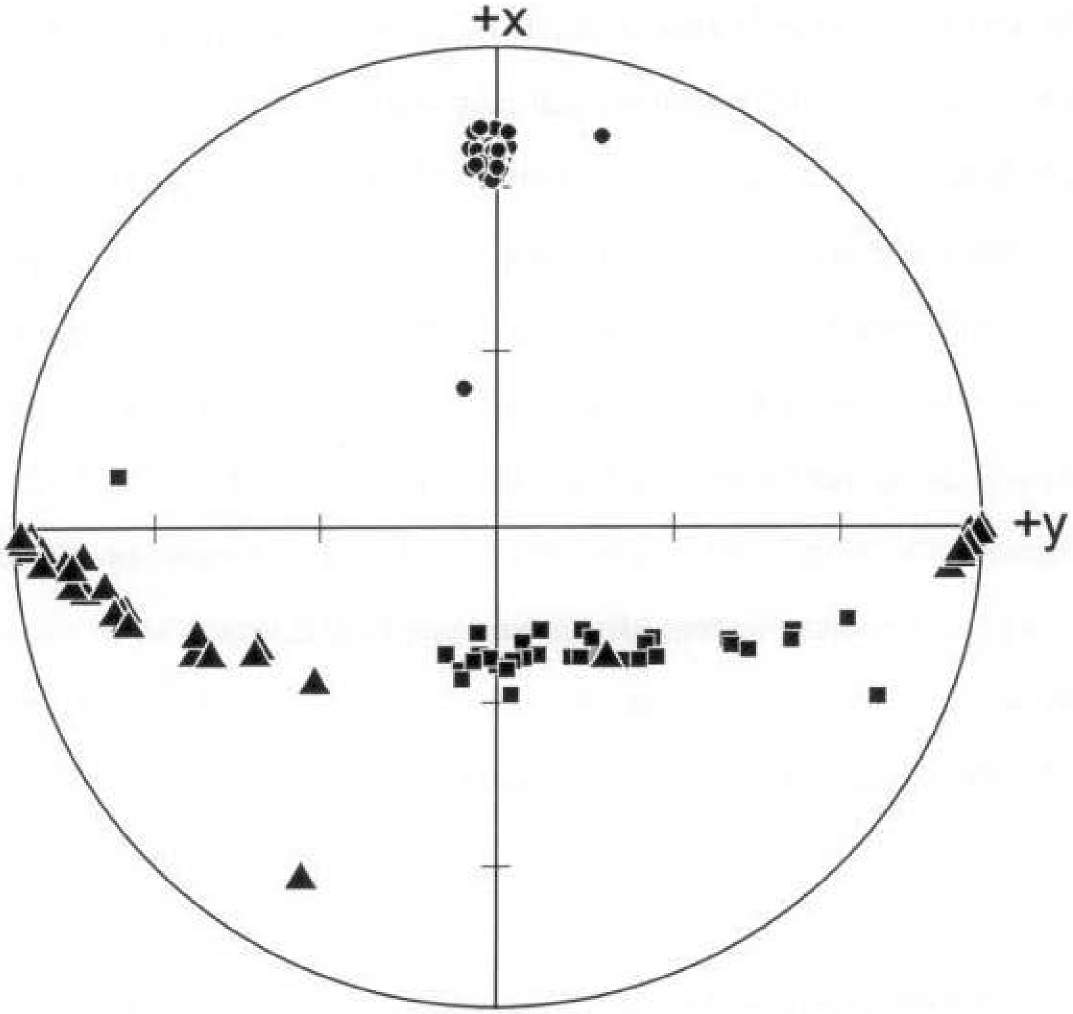

Figure 6-1 Stereographic projection of the suspicious AARM principal directions of the 37 samples exposed to an IRM_{100} in the screening process. Circles = minima axes, triangles = intermediate axes, and squares = maxima axes.

Their AARM minima axes clustered about an axis trending in the x direction and dipping approximately 20 degrees in the lower hemisphere of the stereographic projection (Figure 6-1). AARM maxima and intermediate axes directions formed a girdle striking in the y direction and dipping approximately 70 degrees to the -x direction. These results suggest that the AF_{100} applied in the -x direction is not adequate to clean an applied IRM_{100} along the same direction.

Two samples, FL98237B and FL98238D, were chosen to test what AF maximum peak intensity ($AF_?$) was needed to clean IRM_{100} from these rocks. First, the NRM was measured with a JR-5a spinner magnetometer. Secondly, an IRM_{100} was applied in the x direction followed by a three axes AF_{50} demagnetization and finally measuring the remanent magnetization intensity and direction with the JR-5a spinner magnetometer. This second step was repeated for AF peak intensities of 100, 150, 160, 170, 180, 190, and 200 mT (Table 6-1; steps 1 through 9). Sample FL98238D was cleaned of its IRM_{100} by an AF between 190 and 200 mT. In sample FL98237B, an AF field of 200 mT (the maximum AF field generated by the SI-4 AF demagnetizer) was able to scatter the IRM direction. Since the SI-4 AF demagnetizer could not confidently clean all samples of the imposed IRM, this method was not used.

Table 6-1 Measurements of magnetic remanence orientation and intensity of sample FL98238D in order to clean an applied IRM of 100 mT in the x direction (360/00) (steps 1 - 10) and then cleaning of the thermally acquired self magnetization obtained in step 10 (step 11 - 12).

Step	Treatment	Declination	Inclination	Intensity (mA/m)
1	none (NRM)	352	57	1.15
2	AF demag 50 mT	2	-1	28.93
3	AF demag 100 mT	359	9	0.57
4	AF demag 150 mT	358	2	0.19
5	AF demag 160 mT	7	24	0.10
6	AF demag 170 mT	0	32	0.14
7	AF demag 180 mT	0	10	0.09
8	AF demag 190 mT	355	13	0.12
9	AF demag 200 mT	330	26	0.05
10	***Th demag 100 °C***	***359***	***0***	***230.02***
11	AF demag 50 mT	359	-1	26.50
12	AF demag 200 mT	0	1.5	1.03

Finally, the samples were screened by simply applying an ARM in the one direction and measuring the acquired intensity in the given direction with the Molspin spinner magnetometer. The ARM consisted of an AF_{100} superimposed on the DC field of 0.1 mT through the AF window of 60 to 0 mT. The sample was rejected if the acquired intensity was less than 1 mA/m. This screening process was performed on 269 samples, of which 81 were rejected. Of course, since the AARM principal directions are unknown, the one-step ARM could have been applied in a low-ARM direction. This probably lead to the rejection of some samples for which AARM could have been adequately measured.

The total amount of cores that satisfied my criteria for the AARM study is 201.

6.2.2 A Case of Thermally Acquired Self-Remagnetization

An alternate method to clean the samples of the IRM is by thermal demagnetization. Sample FL98238D (the same sample from above which was cleaned of its IRM by an AF of 200 mT) was again subjected to an IRM_{100} in the x direction. The sample was then heated to 100 °C in a thermal demagnetizer and was maintained at that temperature for 5 minutes before slowly cooling down. Afterwards, the remanent magnetization was measured with the JR-5a spinner magnetometer. The declination and inclination of the remanence was not deflected from orientation of the applied IRM_{100}, however the intensity of the remanence, after thermal demagnetization, was 230 mA/m (step 10 in Table 6-1), where prior to thermal demagnetization the remanence intensity was only 0.05 mA/m (step 9 in

Table 6-1). Such an intensity has not been seen in these samples with AF demagnetization, in fact the largest intensity was 28 mA/m measured on sample FL98238D after AF_{50} demagnetization.

Remagnetization during thermal demagnetization could result from contamination due to inadequate shielding of the furnace from the external earth magnetic field. However, I do not believe this to be the cause of the present observation. The thermal demagnetizer used has a four layer mumetal shield, non-inductively wound furnace with ceramic walls and Al_2O_3 wool insulation. It is a well tested instrument that has produced very good results on numerous other samples of various rock types. Moreover, there has been no evidence of contamination in concurrent routine paleomagnetic studies.

Thermally acquired self-magnetization is rarely seen but has been observed in samples containing pseudo-single domain magnetite. Perhaps, in this case, thermal demagnetization does clean the remanence within the pseudo-single domain magnetite grain while not completely cleaning the trans-domain remanence. During cooling, the uncleaned remanence between domain walls could remagnetize the pseudo-single domain magnetite grains. This self-acquired remagnetization is a soft remanence magnetization and is easily cleaned by a small AF demagnetization. Therefore, in order to determine whether this process occurred to sample FL98238D, the sample was demagnetized at an AF_{50} and AF_{200}. We would expect to obtain similar remanence intensities to those obtained during the first AF demagnetization treatment. Table 6-1(steps 11 and 12) shows that

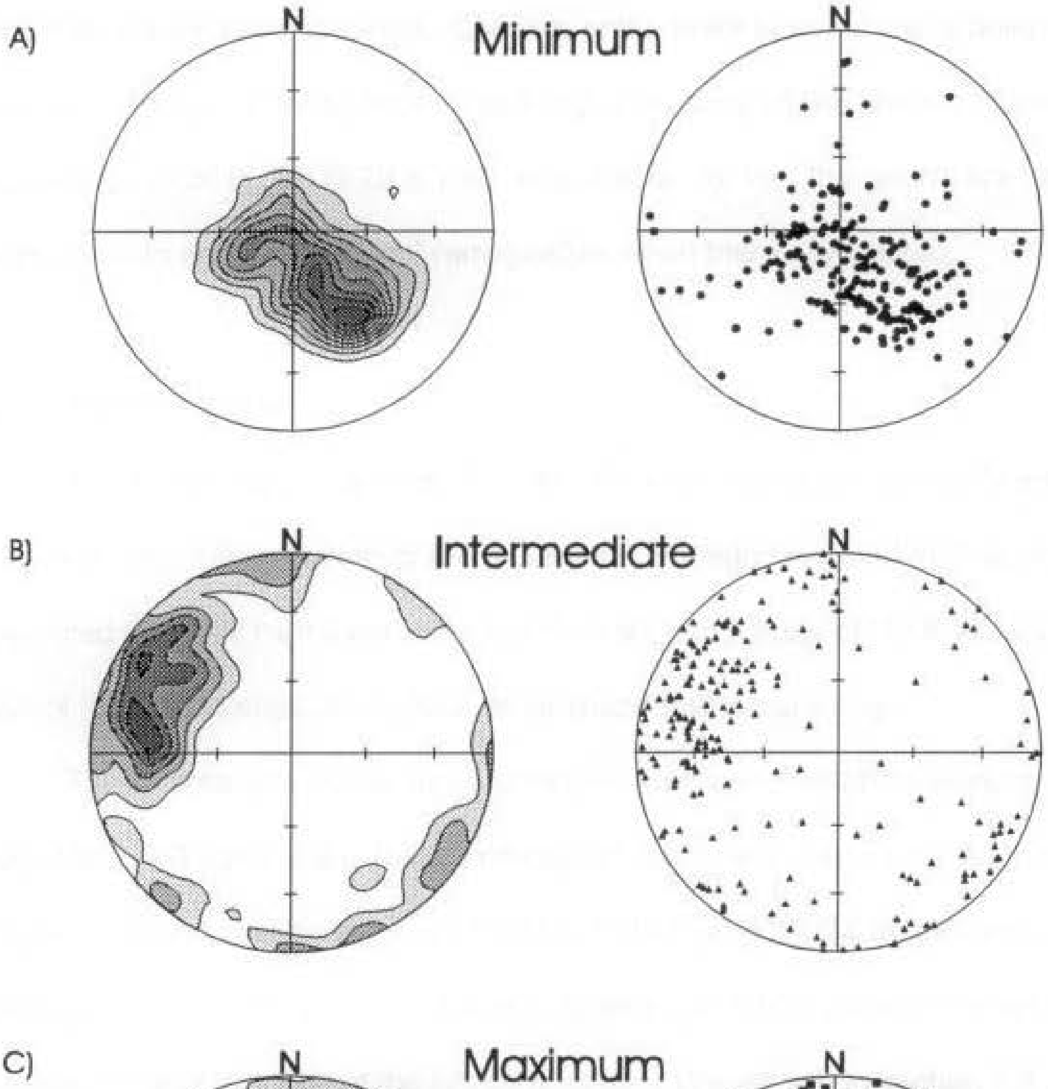

Figure 6-2 Stereographic projection of the three principal axes of the AARM ellipsoid. The number of data points for each projection is 201. The contour interval increase from the expected count of 2.01 per 1% unit area by 2 standard deviation (S = 0.992) up to +14S for the minima, +8S for the intermediate, and +20S for the maxima axes.

expected results were obtained. Consequently, there is evidence to believe the magnetite present in these rocks has a high coercivity of remanence (mean and standard error of H_{cr} is 29.70 ± 1.40; see chapter 3), that the grains are pseudo single domain and they can self-remagnetize when thermally treated.

6.3 AARM Results

The AARM study included 201 cores located throughout the study area. A discussion and interpretation of AARM regional variation is found in Chapter 7. Presented here, will be the overall orientation and magnitude of the three principal axes of the AARM ellipsoid, as well as its shape and eccentricity.

The orientations of the three principal axes are plotted on stereographic projections in Figure 6-2. Peak contouring trend and plunge of the minima, intermediate and maxima axes are 145/48, 279/25 and 022/24 respectively. The $AARM_{min}$ axes are the poles to the AARM foliation, while usually the $AARM_{max}$ represents the orientation of the AARM lineation. We will see in section 7.3.2 that in some areas the AARM fabric is a composite result of the S_0 and the partially overprinted magnetic foliation planes. In these areas, the AARM lineation is represented by the $AARM_{int}$ axes.

6.3.1 Shape and Eccentricity of the AARM Ellipsoid

The AARM ellipsoid is characterized in the same manner that the AMS ellipsoid was described. The Jelinek plot is illustrated in Figure 6-3. The distribution is clearly bimodal. One mode, defined by 114 data points, describes

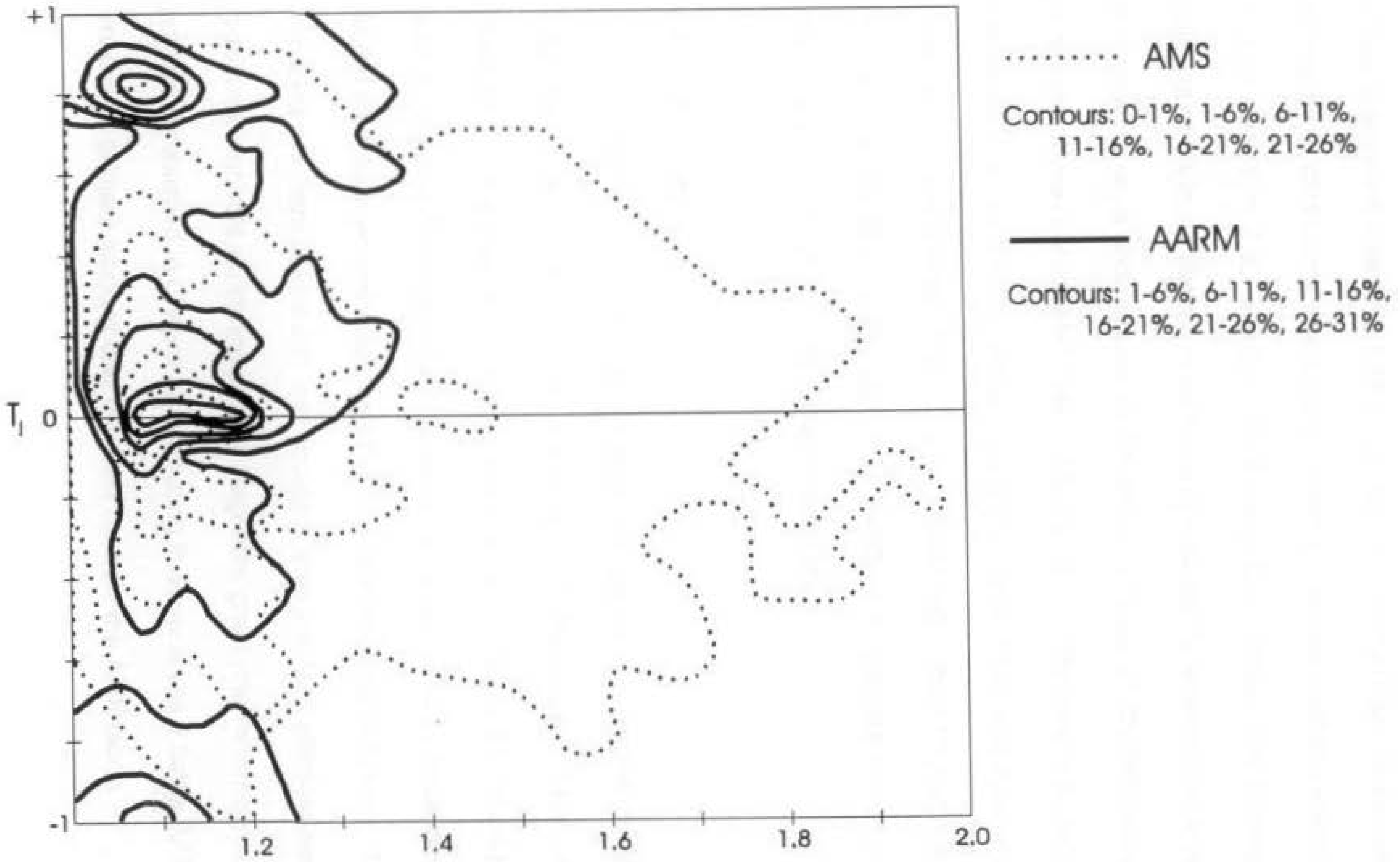

Figure 6-3 Contoured Jelinek (1981) plot of the AARM ellipsoid (thick line) in comparison with the AMS ellipsoid (dotted line). The number of data points for each fabric is 201.

a neutral ellipsoid where P_j = 1.13 ± 0.01 and T_j = 0.10 ± 0.02. The second mode, defined by 67 data points, describes an extremely oblate ellipsoid, where P_j = 1.12 ± 0.01 and T_j = 0.93 ± 0.02. Regionally, both fabrics are homogeneously distributed. A lower degree of eccentricity reflects the absent contribution of the platy clay minerals and the primary sedimentary fabric which dominated the non-tectonic component of the AMS fabric. Magnetite, the ferromagnetic contributor to the AARM fabric is typically considered to have grains that are dimensionally and thus magnetically prolate. Therefore, an oblate fabric, may be interpreted due to tectonic control scattering grain prolate ellipsoids to give an orientation distribution that generates a more strongly oblate AARM fabric.

6.4 Summary

A complete list of the AARM data, orientation and magnitude of principal axes, mean intensities , P_j and T_j, can be found in APPENDIX C. The minima axes cluster to define a foliation plane which dips about 40° to the NE. It will be argued later in Chapter 7 that the AARM lineation is represented in some cases by the AARM maxima axes and elsewhere by the AARM intermediate axes. The AARM ellipsoids are more oblate and less eccentric than the AMS ellipsoid perhaps due to tectonic controls scattering prolate magnetite grain (the ferromagnetic mineral present, established in Chapter 4) producing in some areas a flatter AARM fabric; whereas a primary fabric of clay minerals controls the AMS fabric.

Chapter 7 - Interpretation and Discussion

This chapter will discuss the interpretation of the orientation of cleavage (S_1), AMS and AARM. First, each data set will be approached individually. Secondly, relationships between data sets and tectonic regimes will be examined chronologically.

7.1 Bedding (S_0), Cleavage (S_1) and Vergence

7.1.1 Orientation and Regional Distribution

A complete list of the bedding and cleavage measurements can be found in APPENDIX A. The regional variation of the stylolitic cleavage orientations measured in the field are presented in Figure 7-1. Plotted are the mean measurement at each outcrop where cleavage was present (total of 171 outcrops). The first observation is that S_1 is not parallel to the bedding planes (S_0), which dip gently to the north and south (Figure 7-2). The angular discordance of S_1 and S_0 confirms that the cleavage was not due to diagenetic compaction and cementation. Furthermore, the photograph and line diagram in Figure 7-3 clearly demonstrates bedding stylolites being cut by tectonic stylolites. Note that where S_1 stylolite cuts across the S_0 stylolite, *the S_0 stylolite is displaced by 1.42 cm, indicating that this thickness of* limestone was removed on a single tectonic (S_1) stylolite. Note that the thickness of insoluble residue on the S_1 stylolite between its intersections with the S_0 stylolite is of 0.82 mm and the thickness of the S_0 stylolite outside this zone is 0.25 mm.

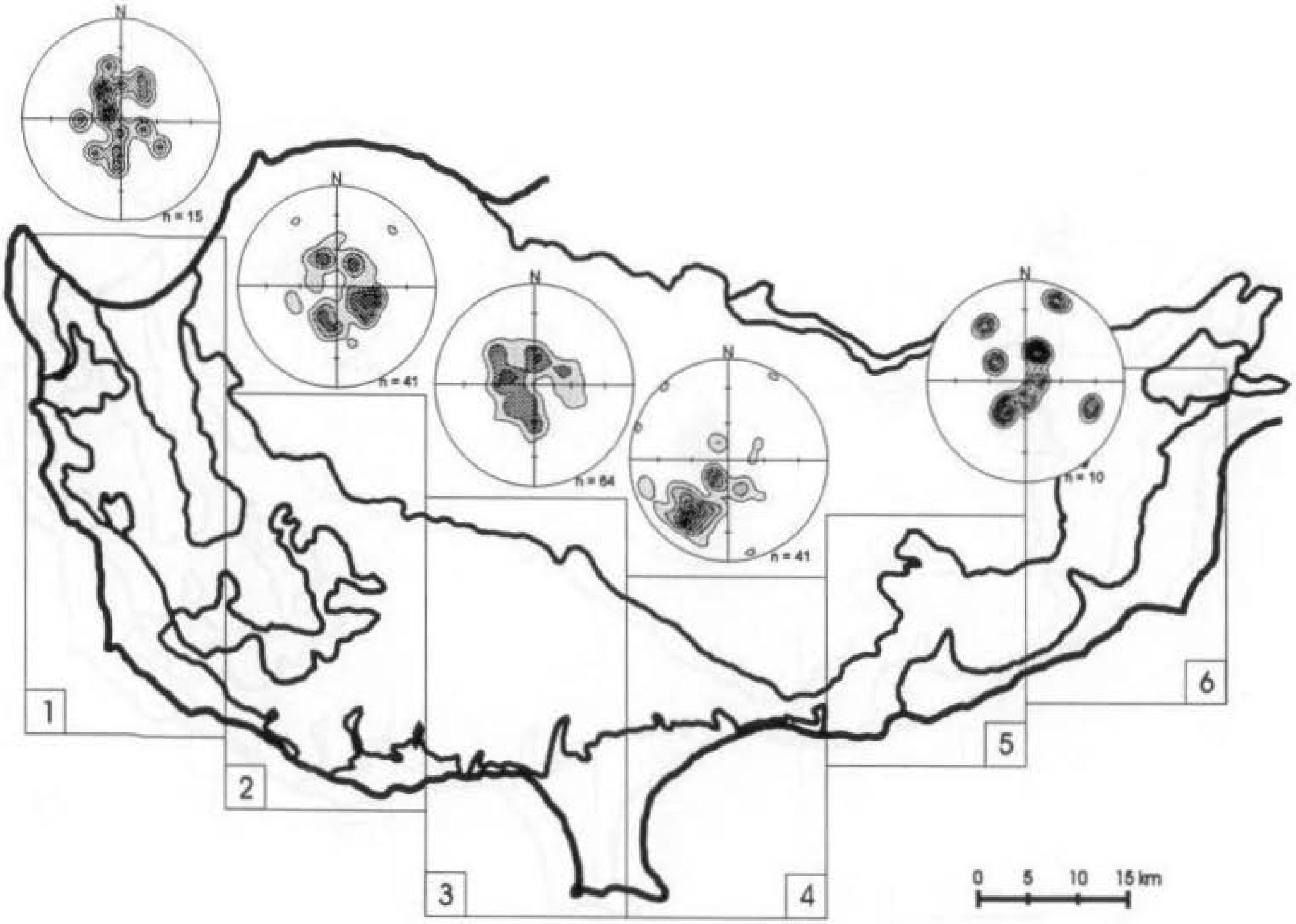

Figure 7-1 Regional variation of stylolitic cleavage (S_1).

Figure 7-2 Regional variation of bedding (S_0).

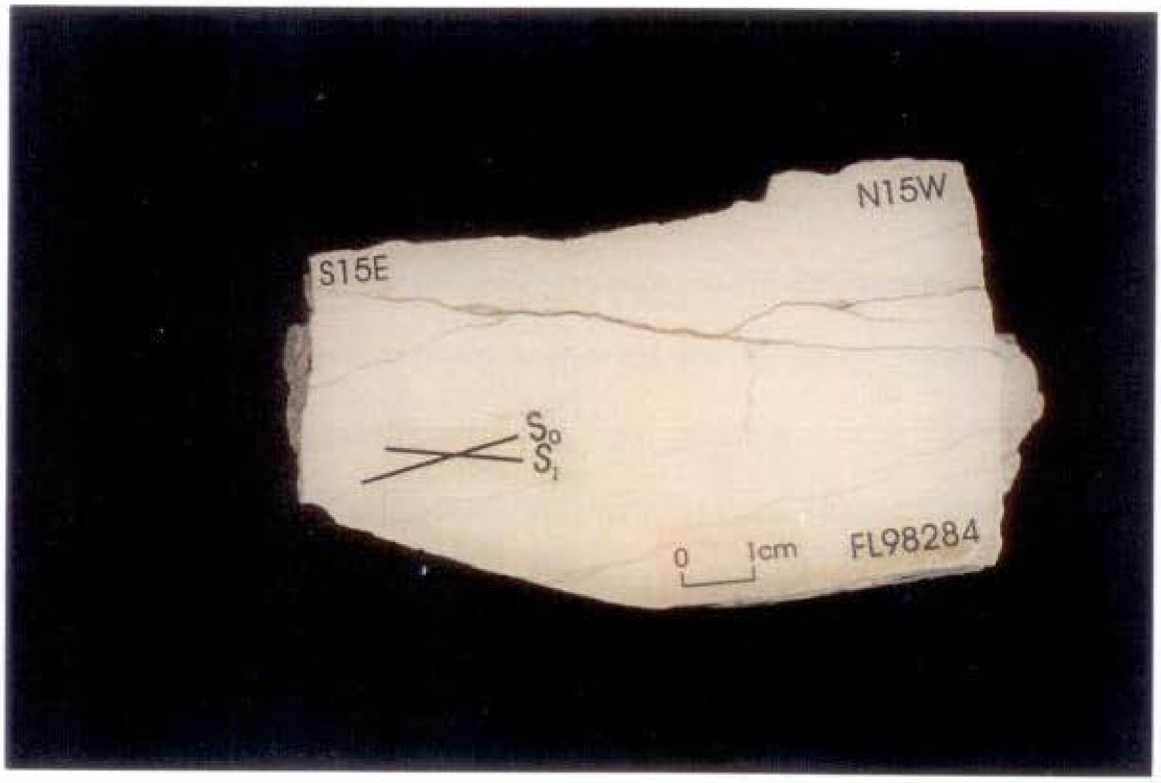

Figure 7-3 Photograph of sample FL98284 and line diagram. The sample was reoriented and a vertical face was cut parallel to 345° azimuth. The tectonic stylolites crosscut the bedding or diagenetic stylolites. The vergence is southerly. 70% of the accumulated insoluble residue is due totectonic pressure solution and only 30 % to diagenetic pressure solution. Furthermore a displacement of 14.66 mm occurred along S_1 due to dissolution. Outcrop location may be found on MAP SHEET A at the back.

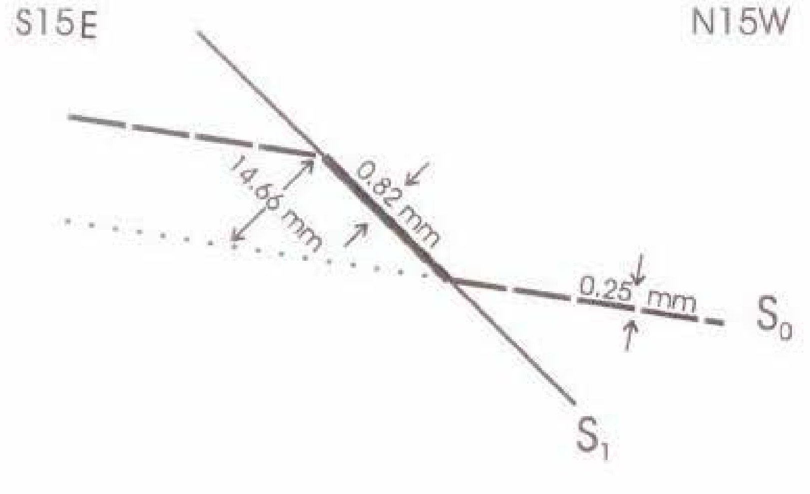

Therefore 70% of the insoluble residue was accumulated during the S_1 tectonic pressure solution event. This defines a ratio of accumulated insoluble residue resulting from tectonic pressure solution relative to diagenetic pressure solution of 2.3 : 1.

The stereographic projections of the poles to the cleavage planes in Zones 1 through 6 illustrates that S_1 has a steeper dip than bedding. Table 7-1 lists the calculated contouring peaks for each zone. All zones have more than one cluster, generally two clusters are present and in Zone 2 there are 4 clusters identified. The dips of the cleavage planes consistently range between 12° and 29°. In Zone 4, there is an additional peak which corresponds to a cleavage dipping at 56°. This cleavage is an exception related to an Early to Middle Miocene compressive tectonic regime which produced the Yeresa fold and thrust belt along with 3 of the

Table 7-1 A list of attitudes of the contouring peaks in each zone. The listed orientation is the trend and plunge of the pole to the principle cleavage plane for the corresponding peak. In brackets the intensity of the peak is given by the multiple of the expected value (E) if the data was distributed homogeneously on the stereographic projection (expected value E is equal to the number of data, n, divided by 100). Also given is the vergence direction defined by each peak.

Zone	Contouring Peaks	Vergence
1	330 / 65 (11.75E) 292 / 78 (11.32E)	NNW WNW
2	111 / 61 (9.90E) 036 / 67 (7.47E) 333 / 66 (7.45E) 204 / 63 (6.88E)	ESE NE NNW SSW
3	286 / 65 (7.31E) 005 / 68 (6.33E)	WNW N
4	215 / 34 (13.10E) 213 / 71 (8.73E)	SSW SSW
5 and 6	023 / 64 (18.58E) 216 / 62 (13.55E)	NNE SW

compressive lineament (Figure 7-4). For the following discussion, the tectonic compression cleavage in Zone 4 will be put aside and considered later in the chapter.

The consistency of the cleavage dips suggests that the strain producing S_1 was approximately coaxial in individual subareas across the region. There is no evidence of rotation of S_1 with progressive strain and together with the stylolitic nature of S_1, suggests a pure shear origin for S_1. Although some fabrics develop with a shear component as transpressive shear, combining pure shear and a shear strain, this does not appear to be the case here (see Figure 2-4 for definition of pure shear, transpressive and the hypothetical simple shear).

In kinematics, vergence characterizes the angular relationship between a certain fabric and the one that preceded it. The common use of vergence relates bedding and cleavage in order to define the direction towards which the fold axes lean. The great variability of the dip direction of the cleavage produces equally variable vergence directions. Figures 7-5, 7-6 and 7-7 are photographs of three samples which all exhibit a different cleavage bedding angle and consequently different intensity or direction of vergence. Note in Figure 7-6 the displacement of bedding stylolites at the base of the oxidized bed, on S_1 stylolites. And in Figure 7-7 note the relative intensities of S_1 and S_0 pressure solution, approximately equal in significance.

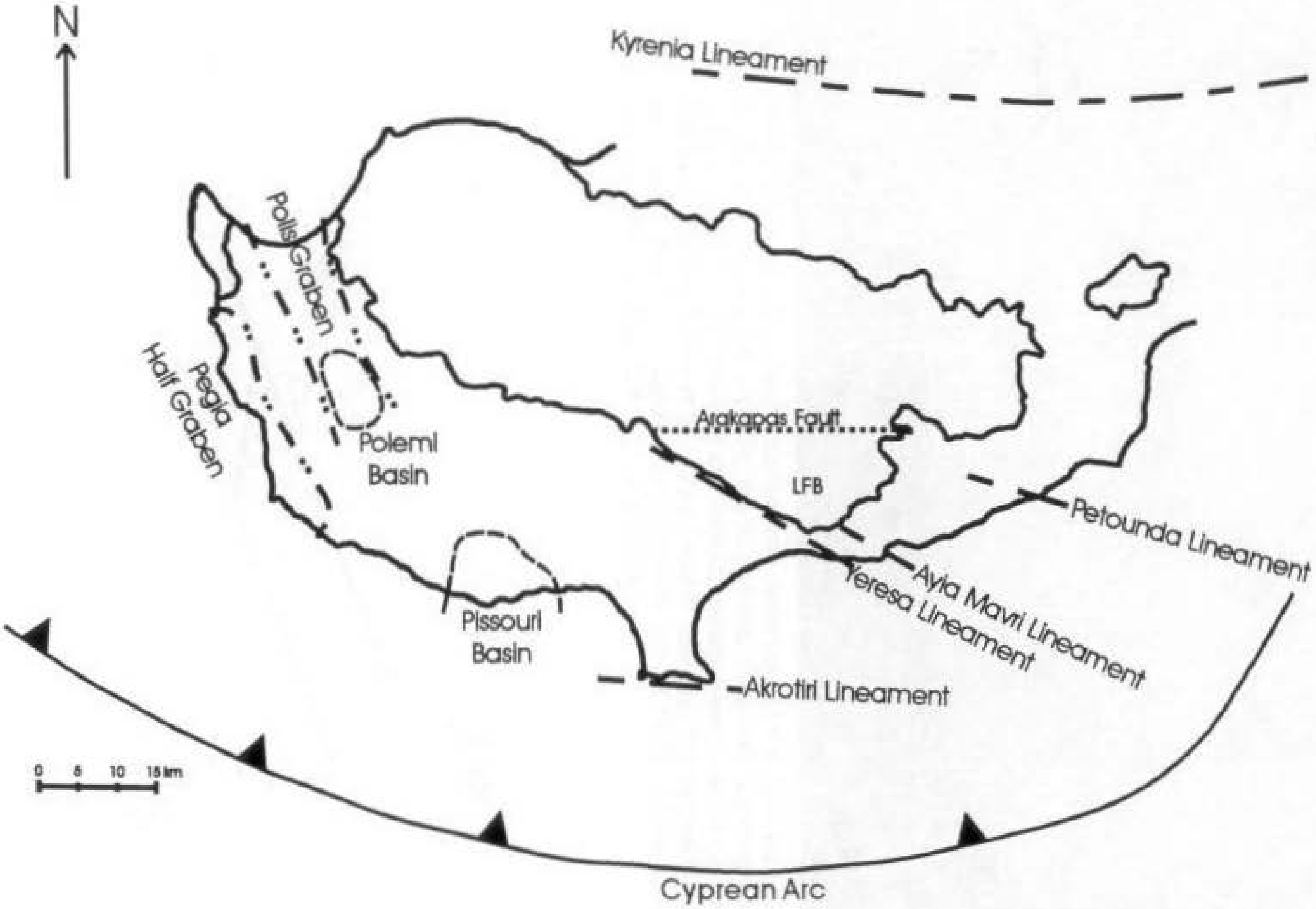

Figure 7-4 Map of Cyprus outlining some of the major structures. LFB = Limassol Forest Block

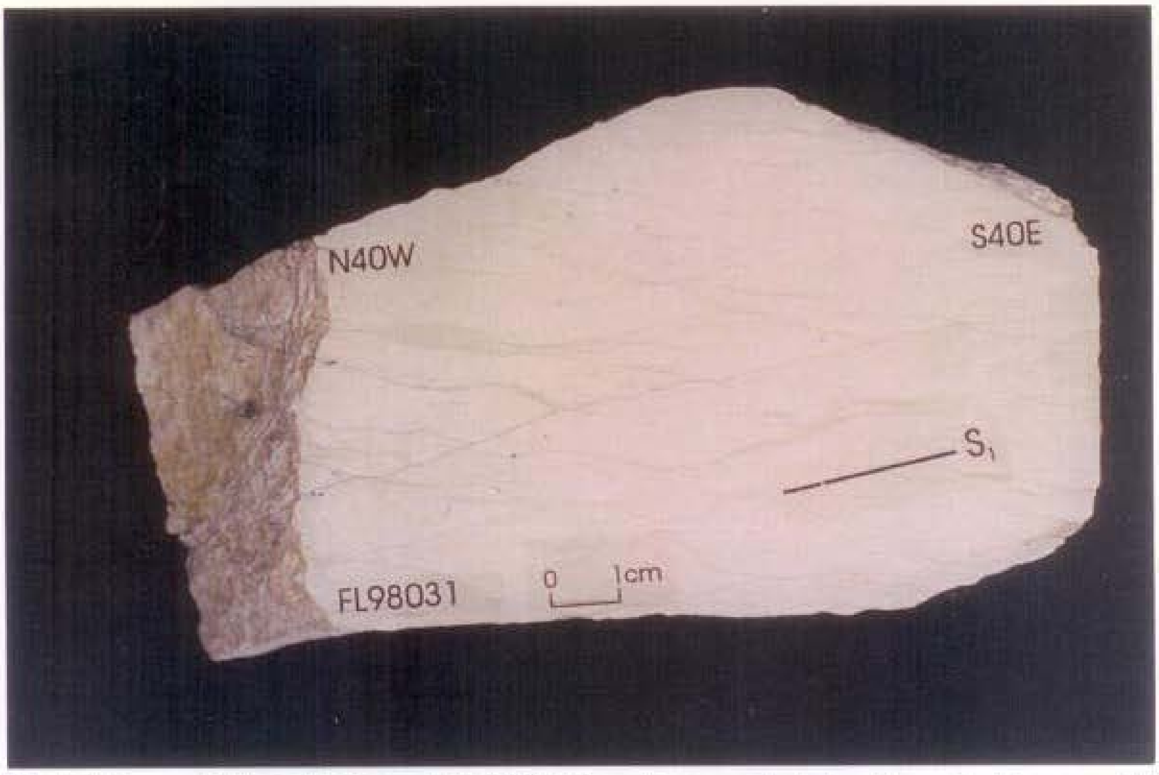

Figure 7-5 Photograph of sample FL98031. Sample was reoriented and a vertical face parallel to 320° azimuth was cut exposing the S_1 stylolitic cleavage. Bedding was not present at this outcrop, however this face cut clearly shows a second consistent stylolitic orientation which is most likely parallel to bedding. It is evident that these are **older** than the S_1 stylolites because they are cut by S_1. Outcrop location may be located on MAP SHEET A at the back.

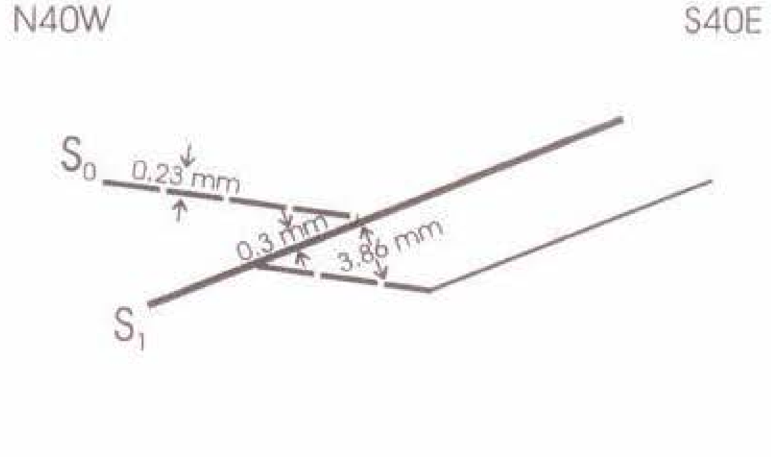

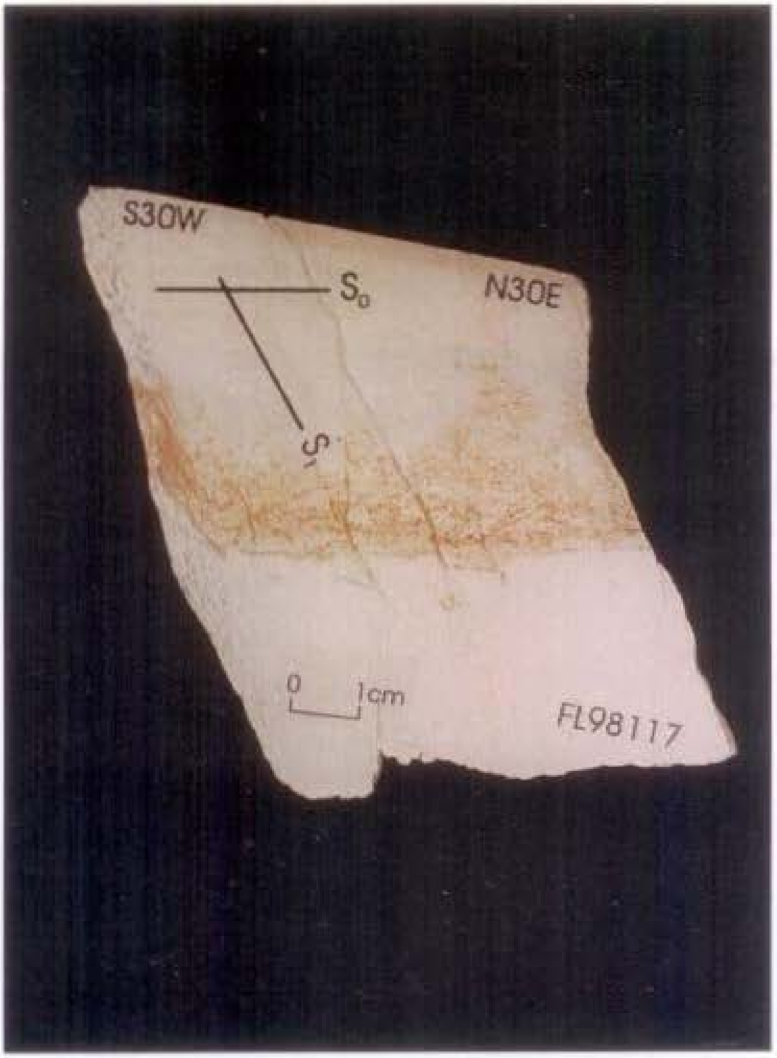

Figure 7-6 Photograph of sample FL98117. Sample was reoriented and a vertical face parallel to 030° azimuth was cut exposing the S_1 stylolitic cleavage. Vergence is in a southwesterly direction. Note the displacement of bedding stylolite at the base of oxidized bed on S_1 stylolites. Outcrop location is indicated on MAP SHEET A at the back.

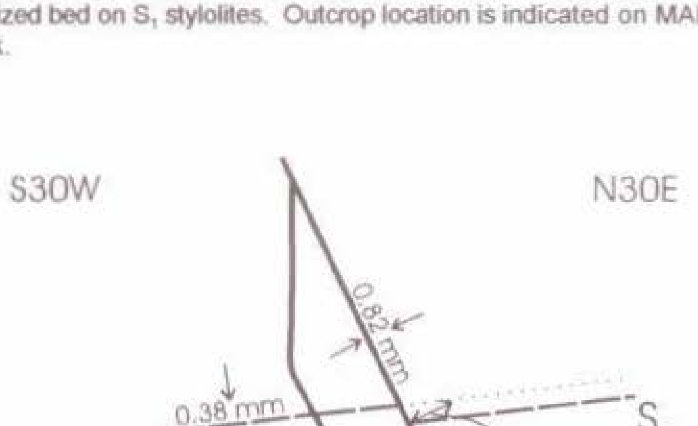

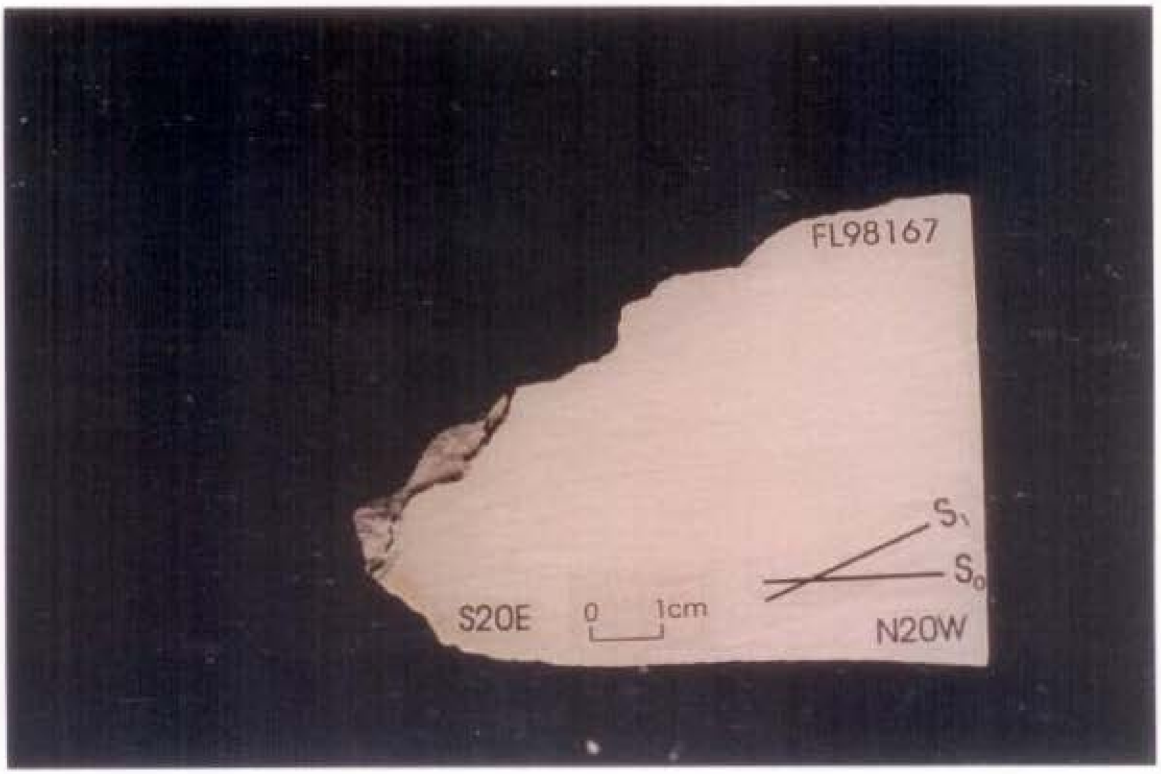

Figure 7-7 Photograph of sample FL98167. Sample was reoriented and a vertical face parallel to 160° azimuth was cut exposing the S_1 stylolitic cleavage. Vergence has a northerly direction. Note the relative intensities of S_1 and S_0 pressure solution, approximately equal in significance. Outcrop location may be found on MAP SHEET A at the back.

In the study area, folds are very gentle and open, but vergence may still be determined indicating the direction of the kinematic movements. Regionally, the vergence directions, and consequently the directions of movement, do not produce a very clear pattern; however it appears there is some preferred orientation to the push directions (Figure 7-8).

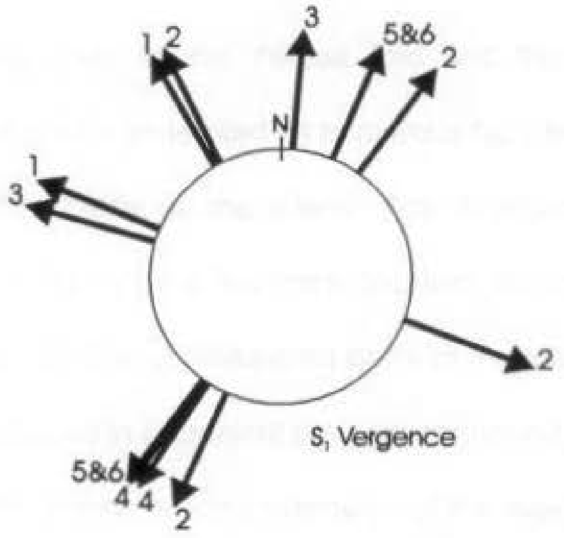

Figure 7-8 Variation in cleavage vergence directions for each zone of the study area (zone is marked by the number at the end of the arrows).

7.1.2 Interpretation

In order to interpret the cleavage vergence, and in later sections the results of the AMS and AARM studies, we must consider the tectonic settings which may have caused instability in the region. Since the deposition of the sedimentary cover, there have been two principal sources of instability for Cyprus. Firstly, the continued uplift of the ophiolite complex with periodical increases in rates of uplift in localized areas such as the Limassol Forest Block (Early Miocene) and Mount

Troodos (Pleistocene). Tectonic activity associated with uplift would include principally gravity sliding of the sediments away from the uplifting mass. The second source of instability is a subduction zone which presently runs south of the island but at the beginning of the Miocene was situated north of the Troodos ophiolite along the structure presently called the Kyrenia lineament (Figure 7-4).

Since the Miocene this active subduction zone produced compressional effects, predominantly seen in the Yeresa fold and thrust belt. Moreover, extensional effects were also generated as numerous fault bounded basins in the south and southwest regions of the island. The southward migration of the subduction zone from its original northern location introduced southwesterly compression in the south and southeastern parts of the island later. Once the subduction zone was located in its present position, continued southward migration of the subduction zone trench caused extension of the overriding northern plate (Figure 7-9). The term supra-subduction tectonics will be used here to describe an area under extension located above a subduction zone.

In Zone 4, where the vergence is to the SSW, we can confidently interpret this southwesterly directed push as evidence of the Early to Middle Miocene localized rapid uplift of the Limassol Forest Block producing the well known fold and thrust belt in the area. This tectonic setting also causes the SW vergence found in Zones 5 and 6. Outcrops yielding SW vergences for this area are located in the southwestern corner of Zone 5, in proximity to the Ayia Mavri lineament. In the Zones 1, 2, 3 and 6, where vergence directions are more scattered, the

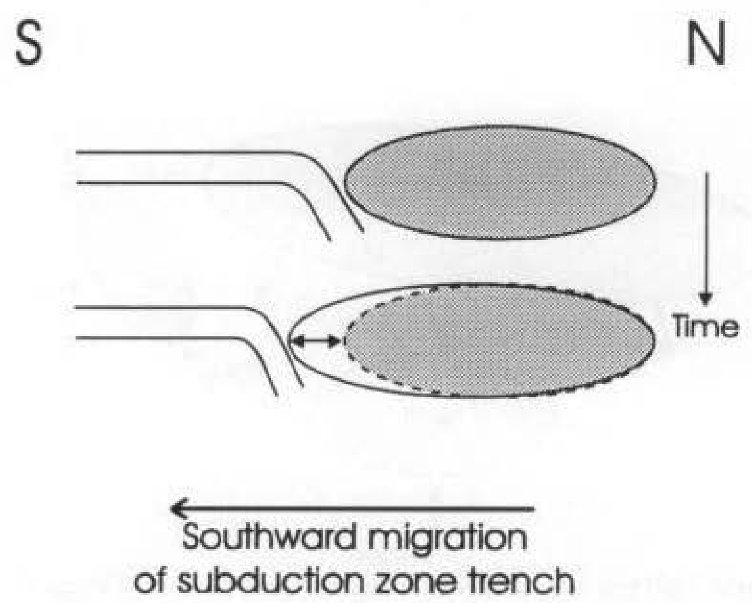

Figure 7-9 Schematic illustration of a supra subduction extensional regime. The overriding plate extends to compensate for the gap caused by southward trench migration.

interpretation is somewhat more intricate.

I believe we can dismiss any explanation directly related to subduction for generating the cleavage in these other zones. Under a compression or extension regime, I would expect a clearly dominant single SW vergence direction much like in Zone 4. Since this is not the case here, I credit gravity sliding, in response to continued regional uplift, as a contributor to the development of the S_1 stylolitic cleavage. If the Troodos ophiolite was the only uplifted or higher elevated region, vergence directions would be consistently away from the ophiolite complex, in the direction of gravity sliding. Therefore, to the west, south and east of the Troodos Complex, vergences would have southwesterly, south and southeasterly directions, respectively. Once again, results illustrated in Figure 7-8 and listed in Table 7-1

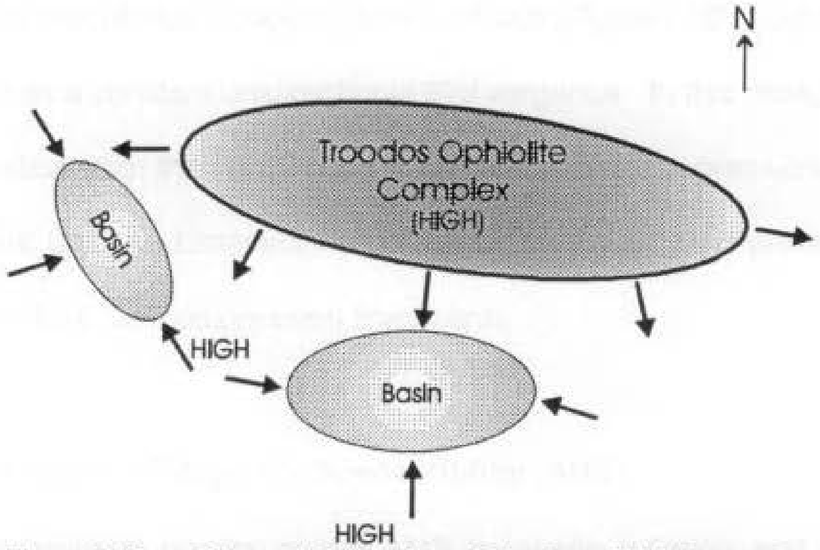

Figure 7-10 Schematic illustration of a basin and high topography which may explain the variable S_1 vergence directions. Black arrows represent the possible vergence directions which could arise from such a topography. Such a model would produce multiple vergence directions, as is the case for the cleavage vergence directions of the study area.

do not entirely agree with this scenario.

Sedimentary facies studies have identified numerous basins in the southerly regions of the island (Orszag-Sperber *et al.*, 1989; Eaton and Robertson, 1993; Stow *et al.*, 1995). These basins must have been surrounded by higher elevated terrain that produced other possible gravity sliding directions, push directions and vergence directions. Further evidence of uneven topography comes from debris flows and slump folds showing displacements from the north to the south and also from the south to the north (Eaton and Robertson, 1993).

I believe the best possible interpretation of the multiple push directions observed across the region comes from a basin filled topography, with several higher elevated terrains as sources of localized gravity sliding, and continued uplift as the mechanism initiating regional gravity sliding (Figure 7-10). Zone 4, being the exception, has a constant unidirectional SW vergence. In this case, a subduction zone migration from the north to the south initiated a compressional front which thrusted the uplifting Limassol Forest Block southward and produced the four WNW-NW / ESE-SE compression lineaments.

7.2 Anisotropy of Magnetic Susceptibility (AMS)

The regional results of the AMS magnetic foliation and lineation are presented in Figures 7-11 and 7-12, respectively. Plotted are the spatial averages calculated at stations located at one kilometer intervals in both the N-S and E-W directions. At each station, the measurements found within a 2.5 km radius are weighted in inverse proportion to their distance away from the station and then averaged. The spatial averaging is performed by Spheristat, a software program designed by Dr. Bob Stesky (APPENDIX B, Figures B-1 and B-2).

7.2.1 AMS Foliation

The AMS foliation, represented by the K_{min} axes of the magnetic susceptibility ellipsoids, is in part tectonic, but retains a strong primary sedimentary fabric component. Everywhere the K_{min} axes, poles to the AMS foliation planes, are nearly perpendicular to bedding. One striking difference between the AMS foliation and bedding planes is the difference in the shape of the clusters of data. The poles to bedding planes forms tightly grouped clusters. The poles to AMS foliation planes form clusters that are slightly dispersed in an E-W direction to form a weak partial

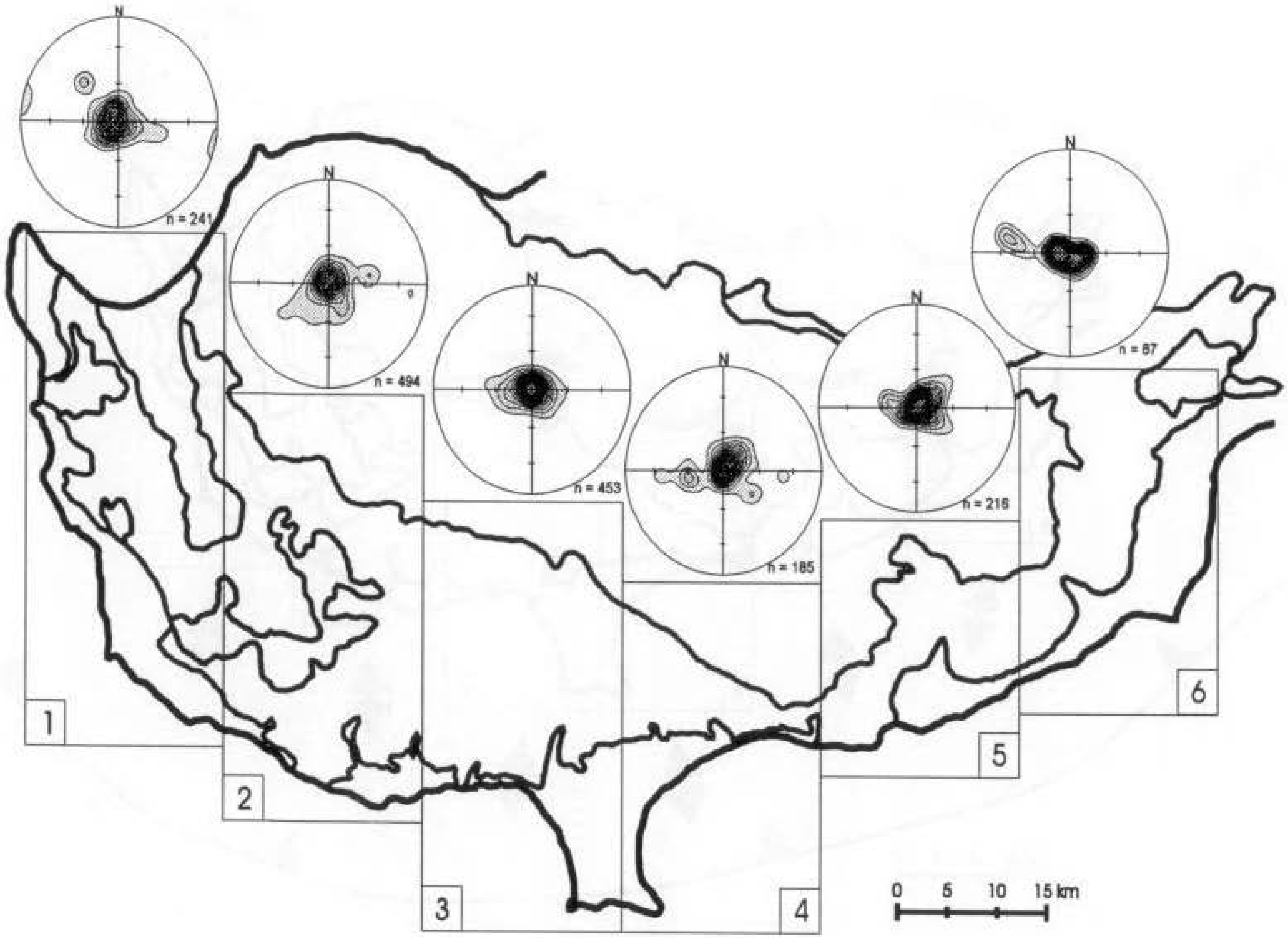

Figure 7-11 Regional variation of AMS foliation.

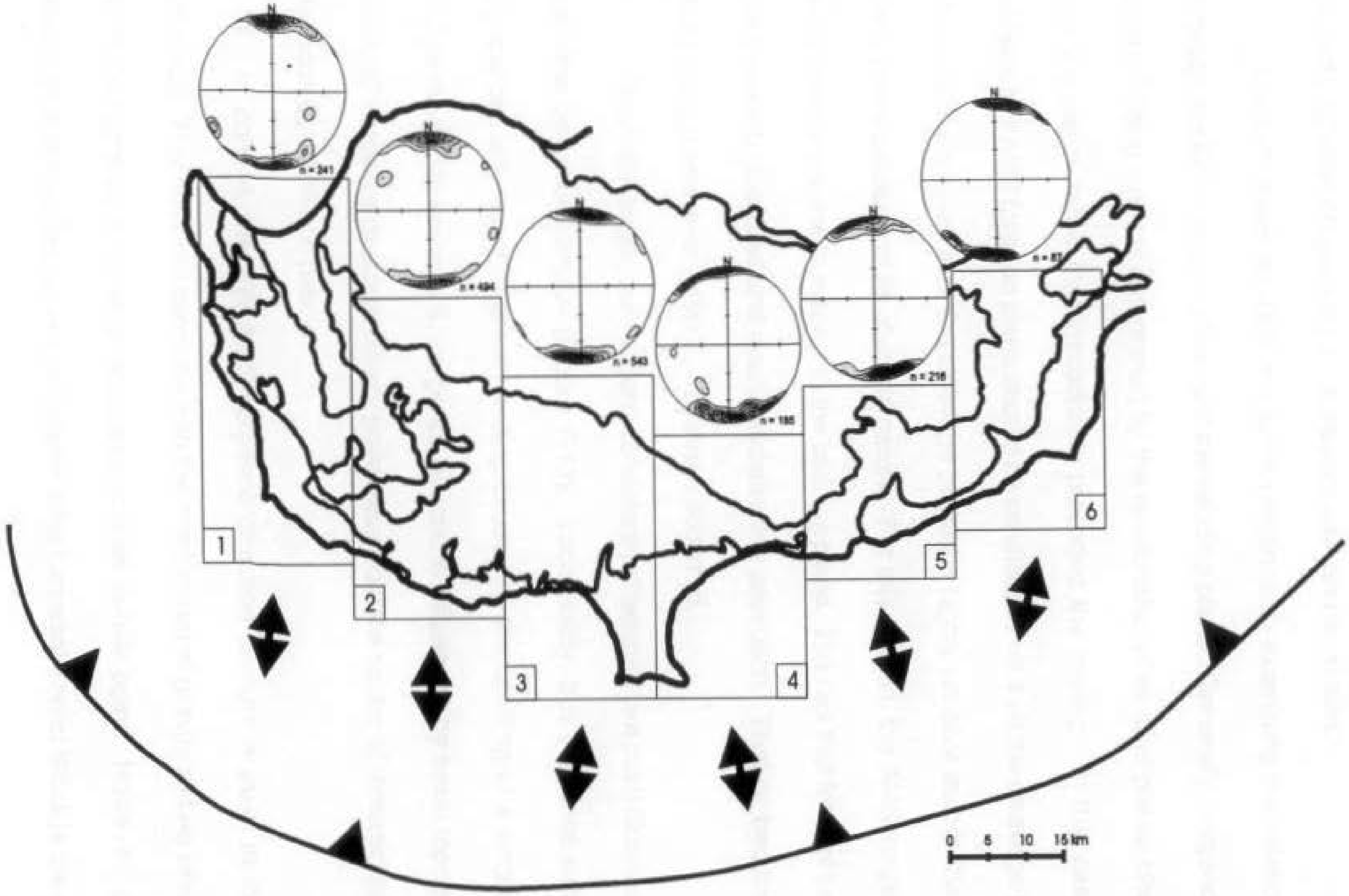

Figure 7-12 Regional variation of AMS lineation. Mean direction of lineation for each zone is indicated by the arrows found beneath the zone box.

girdle, where "zone-axis" defines the lineation. Therefore from a horizontal position, the AMS foliation planes vary by scattered east and west dips.

We can obtain an AMS magnetic vergence by examining the relationship between the AMS foliation plane and the bedding plane. Generally, vergence of a certain folding event is determined by the relationship of its axial planar cleavage with the planar fabric that immediately preceded the folding. In this case, the vergence of AMS foliation plane should be considered *vis à vis* the cleavage plane. However the orientation of the cleavage planes is highly variable across the study area, partly because of its stylolitic nature. For this reason, the AMS vergence is determined always with respect to the bedding plane. The fact that folds of bedding are generally subdued and open validates this approach. That is, bedding was essentially planar even after F_1 / S_1 event occurred.

The AMS vergence directions consistently characterize a push directed away from the ophiolite complex (Figure 7-13). Tectonically, this vergence pattern is compatible with regional gravity sliding caused by the uplifting of a single area. Unlike the highly variable S_1 vergence directions influenced by basin topography, the AMS vergence direction clearly point away from the center of tectonic uplift, the Troodos ophiolite complex.

In Zone 4, the SW AMS vergence direction favours a push in the SW direction. This does not correlate with the mechanism of gravity sliding where the Troodos ophiolite complex is the tectonic uplift center point. However, gravity sliding may still be the active mechanism if the Limassol Forest Block is the center

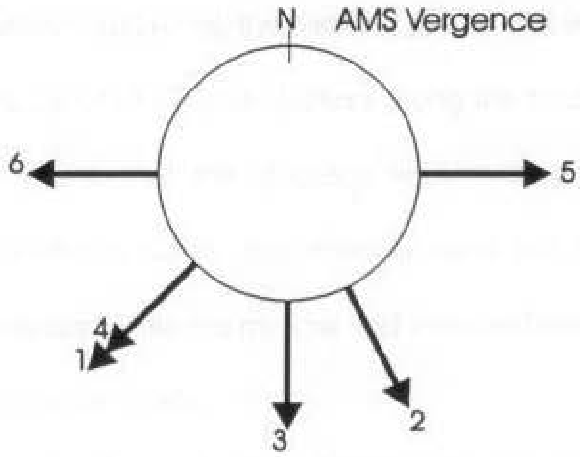

Figure 7-13 Variation in AMS vergence directions, with respect to bedding, for each zone of the study area (zone is marked by the number at the end of the arrows).

point of tectonic uplift. Additional evidence will be given later relating the AMS vergence to the Early to Middle Miocene tectonic uplift of the Limassol Forest Block. Therefore, like the other regions, gravity sliding can explain AMS vergence direction obtained in this zone but the source driving the gravity sliding, in zone 4, is different from that of the other regions.

7.2.2 AMS Lineation

The AMS lineation is represented by the K_{max} axes of the magnetic susceptibility ellipsoids. A primary sedimentary fabric with no tectonic overprint and no strong current alignment should have well clustered minima axes perpendicular to the bedding plane and maxima and intermediate axes scattered along the bedding plane. A primary sedimentary fabric which is partly overprinted by a tectonic fabric will also have minima axes clustered normal to the bedding and maxima and intermediate axes along the bedding plane. However, the maxima and intermediate axes will form two distinct clusters along the bedding instead of being scattered. In the event that the primary sedimentary fabric is completely overprinted by the tectonic fabric, the maxima axes are well clustered in the magnetic lineation direction while the minima and intermediate axes form elongated clusters defining a common plane.

The AMS results for the study area define a clear magnetic lineation from the cluster of K_{max} axes which lies within the bedding plane or AMS foliation plane. The K_{int} axes also form a cluster within the plane of bedding or foliation. Therefore, following the statements mentioned above, it can be said that the AMS fabric is in part tectonic, where K_{max} axes represent the AMS lineation.

The mean AMS magnetic lineation directions can be seen at the bottom of each zone box in Figure 7-12. In each zone, the lineation is similar to the corresponding AMS vergence direction. The lineation directions are more or less all directed N-S with a slight deviation towards the AMS vergence direction of that zone. Zone 4 ,however, does not follow the trend. The compressional front seems to be the dominant tectonic influence in this zone. Therefore, it is not surprising the magnetic lineation direction deviates from the average N-S direction to a NNW-SSE direction. This is an attempt to align the K_{max} axes perpendicular to the compression direction. The angular deviation of the magnetic lineation, away from the N-S direction, in all zones is subtle because of the incomplete overprint of the primary sedimentary fabric at these low strains.

Two possible tectonic situations could have produced the observed magnetic lineations. The first takes into account the similar orientations between the AMS vergence and the AMS lineation. If gravity sliding away from an uplifting Troodos ophiolite complex produced the AMS fabric, then the magnetic lineation represents the general direction of gravity sliding. The subtle change in orientation from Zone 1 to Zone 6 agrees with this first possibility.

This second hypotheses considers supra subduction extension as the tectonic regime responsible for the AMS regional magnetic lineation pattern. As mentioned earlier, extension within the overriding plate occurs in order to compensate for the gap produced by the backward migrating subduction zone trench (Figure 7-9). Backward migration of a trench ('roll-back') seems to be the result of a subducting oceanic crust which is older, colder and consequently denser than the mantle it is penetrating (Le Pichon and Angelier, 1981). The Hellenic Trench, which is the westward continuation of the Cyprean Arc, has also been reported by LePichon and Angelier (1981) to have undergone 'roll-back' at a rate (dR/dt) of 10-20 cm/yr. They determined the rate by examining the relative motions of Africa, Europe and Turkey. Robertson (1990) states that during the Miocene (~22 to 6 Ma) northward underthrusting (subduction) along the Cyprean Arc was never extensive and at the most 500 km was consumed. From this information I have calculated the subduction rate (dS/dt) along the Cyprean arc for the Miocene, obtaining a rate of ~3 cm/yr. The relationship between the rate of 'roll-back' or retreat (dR/dt) and the rate of subduction (dS/dt) (see Figure 7-14) can be of three

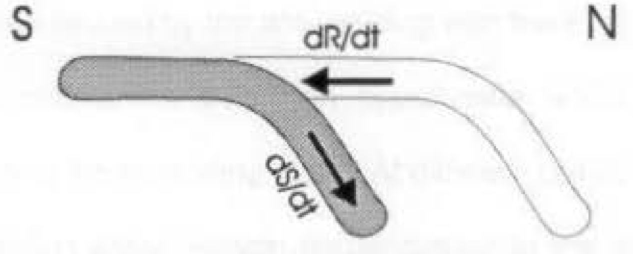

Figure 7-14 Schematic diagram illustrating the relationship between the rate of 'roll-back' or retreat (dR/dt) and the rate of subduction (dS/dt).

types. These include scenarios where dS/dt = dR/dt, dS/dt > dR/dt, and dS/dt < dR/dt.

The first case, where dS/dt = dR/dt, would produce a tectonically stagnant situation. That is, neither compression or extension would occur. When compressive deformation (folding, mountain building) occurs at a plate boundary, dS/dt > dR/dt. The third scenario, describes a situation where dS/dt < dR/dt and extension deformation (normal faulting, basin formation) is favoured. If we relate the calculated subduction rate of the Cyprean Arc, for the Miocene period, of 3 cm/yr to the rate of retreat of 10 - 20 cm/yr along the Hellenic Arc quoted by LePichon and Angelier (1981), with the assumption that dR/dt along the Cyprean Arc would be similar, tectonic extension would be the favored scenario with dS/dt <<dR/dt.

Once started, backward migration of a trench should only cease when the denser lithosphere has been entirely consumed or when the arc collides with a continental crust (Lonergan and White, 1997). In the case of the Cyprean arc, Early Pliocene termination of the southward migrating trench and slower subduction rates may have been caused by the arc colliding with the Eratosthene Seamount.

The supra subduction extension hypotheses would produce variable extension directions in the overriding plate. At different position along the trench, the extension direction would remain perpendicular to the strike of the trench. Figure 7-11 illustrates the relationship between the regional magnetic lineation and the shape of the Cyprean Arc. The sympathy between the two (including Zone 4) validates this second possible tectonic situation.

7.2.3 Summary of AMS Fabric

In Chapter 3 the magnetic mineralogy controlling the AMS fabric was identified as calcite and quartz where the bulk susceptibility is negative, and clays where the bulk susceptibility is positive. Within the present chapter, the AMS fabric has been defined by its foliation, lineation, and vergence with respect to bedding.

Two tectonic situations have been suggested for the formation of the AMS fabric. The first describes gravity sliding away from the uplifting Troodos ophiolite complex. Both its vergence and AMS lineation direction are compatible with this situation. The second situation describes supra-subduction extension in response to southwards migration of the trench. Once again, lineation (exception in zone 4) and vergence (exceptions in Zone 4 and 6) directions agree with this second possible situation.

The apparent lack of compatibility of the AMS foliation plane orientations with either situations, is most likely due to weak strain having insufficiently overprinted the bedding. There are developmental stages involved in transforming a completely primary sedimentary fabric into a completely tectonic fabric in a sedimentary rock as was discussed earlier in section 7.2.2. It appears that the primary fabric component (bedding) is too strong for strain or recrystallization to align the K_{min} axes. However, I am under the impression that the E-W dispersion of the poles to foliation is a move towards K_{min} and K_{int} defining a common plane normal to the extension direction as the zone axis. Even if this is the case, we are no closer deciding between the two hypotheses since extension would be in nearly identical directions in both situation.

7.3 Anisotropy of Anhysteretic Magnetic Remanence (AARM)

The regional results of the AARM magnetic foliation and lineation are presented in Figures 7-15 and 7-16, respectively. Plotted are the spatial averages calculated at stations located at one kilometer intervals in both the N-S and E-W directions. At each station, the measurements found within a 2.5 km radius are weighted in inverse proportion to their distance away from the station and then averaged. The spatial averaging is performed by Spheristat, a software program designed by Dr. Bob Stesky (APPENDIX C, Figure C-1 and C-2).

7.3.1 AARM Foliation

The AARM foliation planes, represented by the minimum axes of the anhysteretic remanence ellipsoids, are consistently oriented throughout the study area. Zone 4 defines a different foliation direction. The poles to foliation cluster in the southeast quadrant, in Zones 1, 2, and 3, illustrating a foliation plane dipping

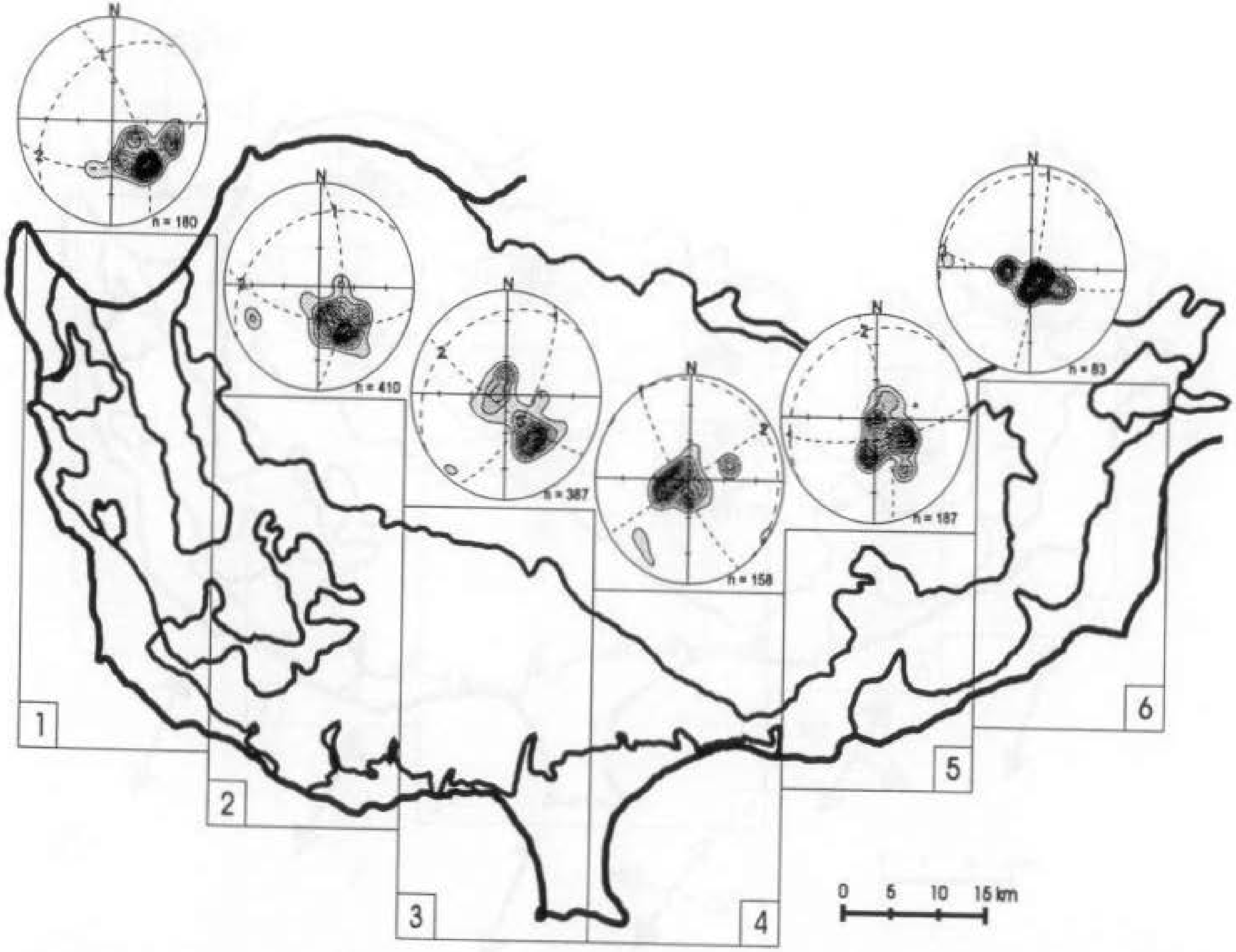

Figure 7-15 Regional variation of the AARM foliation. Superimposed on the stereographic projections are the principal directions (maximum = 3, intermediate = 2, minimum = 1) and principal planes of the contoured data.

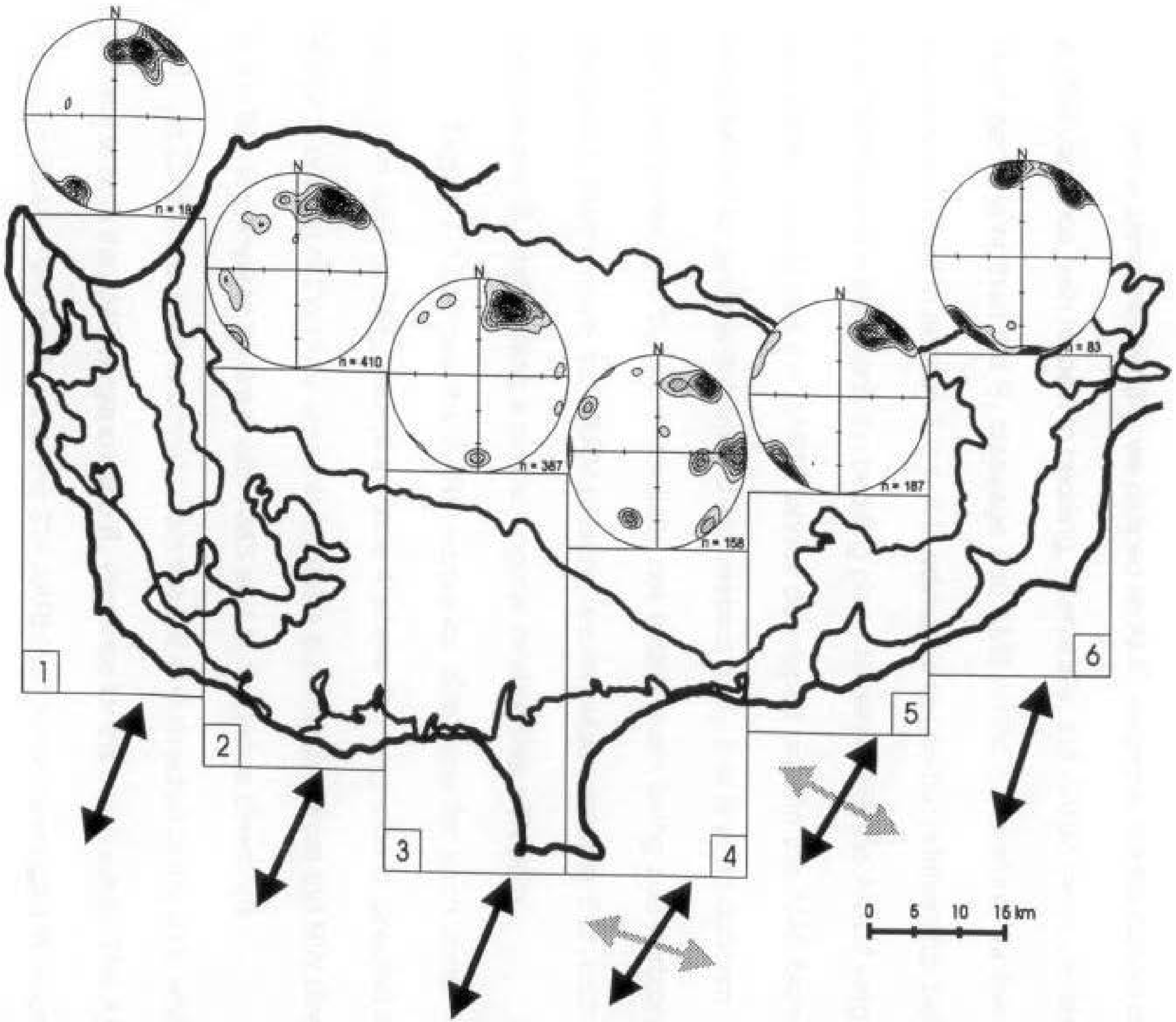

Figure 7-16 Regional variation of the AARM lineation directions. Mean direction for each zone is indicated by the arrow found beneath the zone box. Black arrows represent a composite lineation. Grey arrows represent a compression lineation.

~45° to the NW. Zone 4 has a foliation plane dipping to the NE by ~15°. Zones 5 and 6, to the east of the study area, define average foliation planes with much shallower dips than in the first three zones to the west, of 25° and 10° respectively.

In the same manner that we defined an AMS vergence, we can determine the AARM vergence, with respect to bedding. Generally, the AARM fabric develops at least partly later than the S_1 cleavage and AMS fabric. Therefore, for the same reasons discussed in section 7.2.1, it is advisable to use the relationship between the AARM foliation plane and the bedding plane to determine the AARM vergence. It is most unlikely that the AARM fabrics developed prior to the AMS fabric, but since AARM vergence is determined with respect to S_0, this is of no concern. AMS foliation planes and S_0 are essentially not folded, both being sub-horizontal to horizontal. Furthermore, the AARM foliation is everywhere steeper than both AMS foliation and S_0 maintaining a similar angular relationship with both.

Figure 7-17 shows the AARM vergence directions for each zone. They range from ESE to SSE, except in Zone 4 where the vergence is directed to the WSW. For most of the study area this implies a push coming from the NW directed to the SE, in complete contrast with AMS and S_1 vergence directions.

In Zone 4 the push is coming from the NE and directed to the SW, which is identical to both the AMS vergence and S_1 vergence for the same area. The AARM magnetic lineation will confirm that the SW AARM vergence developed in response to a localized NE-SW maximum compression direction, continued from the time of S_1 and AMS development.

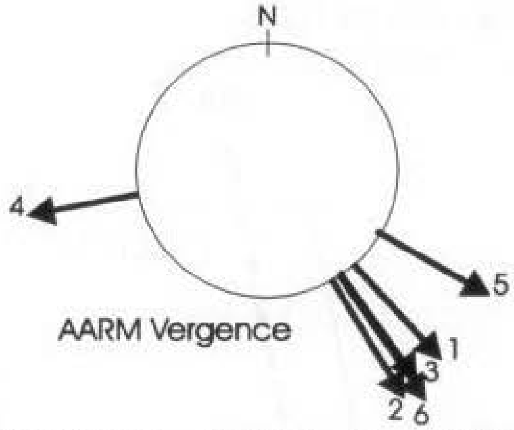

Figure 7-17 Variation in AARM vergence directions across the study area. The corresponding zone is indicated by the number at the end of the arrows.

7.3.2 AARM Lineation

The AARM lineation, represented by the maximum axes of the anhysteretic remanence ellipsoid, is every where directed dominantly to the NE. This is a composite fabric between AARM foliation and S_0, caused by the AARM vergence, where $AARM_{max}$ axes represents the intersection lineation between S_0 and AARM foliation. Since S_0 is nearly horizontal, the intersection lineation is shallow dipping and trends parallel to the strike of the AARM foliation planes (Figures 7-18). Consequently, the AARM fabric, of most of the study area, is not *purely* tectonic.

Zones 4 and 5 have two distinct magnetic lineation directions. One is oriented NE and SW, coinciding with the composite fabric developed everywhere else. The other (grey arrows in Figure 7-16) has an ESE and WNW orientation. Samples exhibiting these extension directions are found in proximity to the Yeresa and Ayia Mavri lineament. We have already interpreted the AARM foliation and

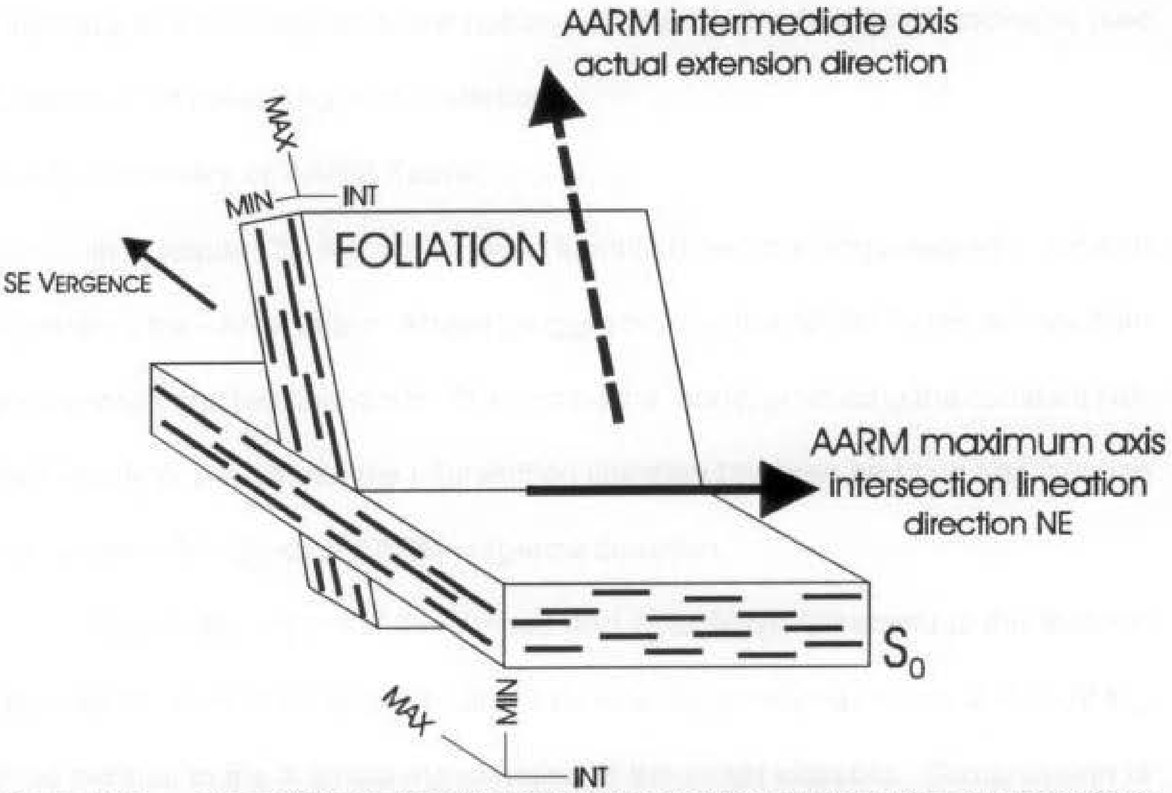

Figure 7-18 Schematic illustration of the development of the AARM lineation composite fabric. The intermediate axes of the AARM 'subfabrics' for bedding and foliation planes are parallel, combining to produce the overall longest axes of the combined fabrics. Therefore, the regionally constant NE directed AARM lineation is of tectonic origin, but does not directly indicate the extension direction.

vergence in Zone 4 as a result of a locally different compression direction. The same compressional event also developed distinct S_1 cleavage and AMS fabric orientations within these zones.

Close observations of the S_1, AMS and AARM vergence directions for Zone 4, indicate that there is a systematic clockwise rotation of the vergence directions from the younger S_1 vergence to the older, or later developed, AARM vergence. The azimuth of vergence direction rotate as follows: 213° for S_1 vergence, 225° for AMS vergence, and 258° for AARM vergence. Such a relationship indicates that the strain responsible for the compressional regime in this isolated area was markedly of a non-coaxial shear nature with the crust rotating anticlockwise (see Chapter 1 for paleomagnetic evidence).

7.3.3 Summary of AARM Fabric

In Chapter 3, magnetite was identified as the ferromagnetic mineral controlling the AARM fabric. Above I suggested that the AARM fabric defines both a composite and tectonic fabric. The composite fabric, producing the constant NE-SW lineation, represents the intersection lineation between bedding and foliation caused by a SE directed AARM vergence direction.

Only in the region of the Yeresa and Ayia Mavri lineament is the tectonic fabric interpreted as the direct result of a tectonic compressive regime with $AARM_{max}$ axes parallel to the X stretching direction of the strain ellipsoid. Compression is preferred because the lineation direction is parallel to the strike of the foliation (the X direction) and parallel to a lineament produced by compression.

7.4 Chronology Interpretation

In the previous section I identified the S_1 cleavage as being tectonic, the AMS fabric as tectonic in some areas and diagenetic in others whereas the AARM fabric is a composite fabric where the true extension direction is represented by the $AARM_{int}$ axes except in one well defined region where the extension direction is represented by the conventional $AARM_{max}$ axes. In this concluding section, I will clarify the chronology of various tectonic events, that affected Cyprus since the deposition of the Troodos Sedimentary Cover. This in turn, will reveal a relative time frame for the development of the various fabrics.

By the Miocene period, both the Lefkara Formation and Pakhna Formation had been deposited on top of the Troodos ophiolite, which began emerging from the ocean in the early stages of the Miocene (Robertson, 1977). The first significant tectonic event to affect the sedimentary cover occurred during the Early Miocene in the vicinity of the Limassol Forest in response to renewed subduction. Payne and Robertson (1995) suggest that the subduction zone, initially located north of the Troodos ophiolite complex along the present Kyrenia lineament, jumped southward to form the Cyprean Arc south of the island. Under a compressive regime, the Limassol Forest block was similarly thrusted southwards producing the Yeresa fold and thrust belt along the southwest margin of the block. Furthermore, three other lineaments were formed during the compressive regime: the Akrotiri lineament (south of the Akrotiri peninsula), the Ayia Mavri lineament (south-east of the Limassol Forest block), and the Petounda lineament (east near Petounda point) (Eaton and Robertson, 1993) (Figure 7-4).

All four structures trend roughly NW-SE resulting from a maximum compression directed NE-SW. Of the four structures, the Yeresa fold and thrust belt and the Ayia Mavri lineament are included within the present study area. The Yeresa Fold and thrust belt deformation is characterized by south verging folds and a well developed axial plane cleavage (Morel, 1960). Cleavage plane orientations measured for the present study are in agreement (Figure 7-1: the stereographic projection of the poles to cleavage planes for Zone 4). The axial plane cleavage defines a southwesterly vergence, parallel to the maximum compression direction, supporting a push from the north to the south due to rapid and isolated uplift of the Limassol Forest block during the Early Miocene.

Further evidence of the compressive event can be seen in the magnetic fabric, defined by both the anisotropy of magnetic susceptibility and the anisotropy of anhysteretic magnetization, of samples in Zones 4 and 5 in the vicinity of the Yeresa and Ayia Mavri lineament.

The vergence direction of both AMS and AARM, in Zone 4, are to the SW, parallel to the maximum compression direction. Furthermore, the AARM magnetic lineation in these areas clearly trend NW-SE, or parallel to the lineaments' trend and perpendicular to the maximum compression direction (Figure 7-16).

Commencing during the later stages of the Late Miocene, following the short period of intense localized compression, the island of Cyprus was subjected to an extensional regime of tectonic activities. Numerous studies observing fault planes, slickensides, and extensional joint surfaces cutting through the Troodos sedimentary cover have defined two extension directions since the late Miocene *until the present* (Lapierre *et al.*, 1988, Grand *et al.*, 1993: ophiolite complex and sedimentary cover of southern Cyprus; Orsag-Sperber *et al.*, 1989, Eaton and Robertson, 1993: southern Cyprus sedimentary cover; Payne and Robertson, 1995: West Cyprus sedimentary cover). Miocene and older sedimentary units in the Polis graben area (SW Cyprus) are cut by faults and extensional joints trending 140°-160° / 320°- 340° that correlate with a maximum extension direction of 60°/240°.

This period of extension has been associated with a supra-subduction extension regime by Payne and Robertson (1995). An increased rate of subduction perhaps linked to a change in convergence orientation between the African plate and the Eurasian plate caused the overriding slab to extend, filling the gap left by a trench migrating southward ('rolling-back'). Such a scenario would create an extensional fabric in the overriding slab sympathetic to the shape of the arc. Maximum extension direction would be perpendicular to the strike of the arc for the adjoining area. From the discussion in section 7.2.2, the AMS fabric may very well be expressing this tectonic event.

By Early Pliocene, slower subduction rates resumed and trench roll-back ceased, ending the supra-subduction related extensional regime. However extension during the Pliocene continued in a slightly different orientation forming to the west the Pegia half-graben (Payne and Robertson, 1995), the Polemi basin (an extension to the Polis graben) and to the south the Pissouri basin (Orszag-Sperber *et al.*, 1989) (Figure 7-4). Paleogene, Miocene and Quaternary sedimentary rock units, predominantly in the south and southwestern parts of Cyprus, are cut by younger faults and extensional joints trending 100°-130° / 280°-310° which correlates to a maximum extension direction of 025° / 205°. The $AARM_{int}$ axes, true extension direction in AARM composite fabric is clearly oriented parallel to the strike of these younger faults. Normally, we would expect to have crystallographic alignment of magnetite grains parallel to the maximum extension in an extensional regime instead of perpendicular to it, as is the case here.

Table 7-2 Summary of the relative chronology of the various fabrics studied.

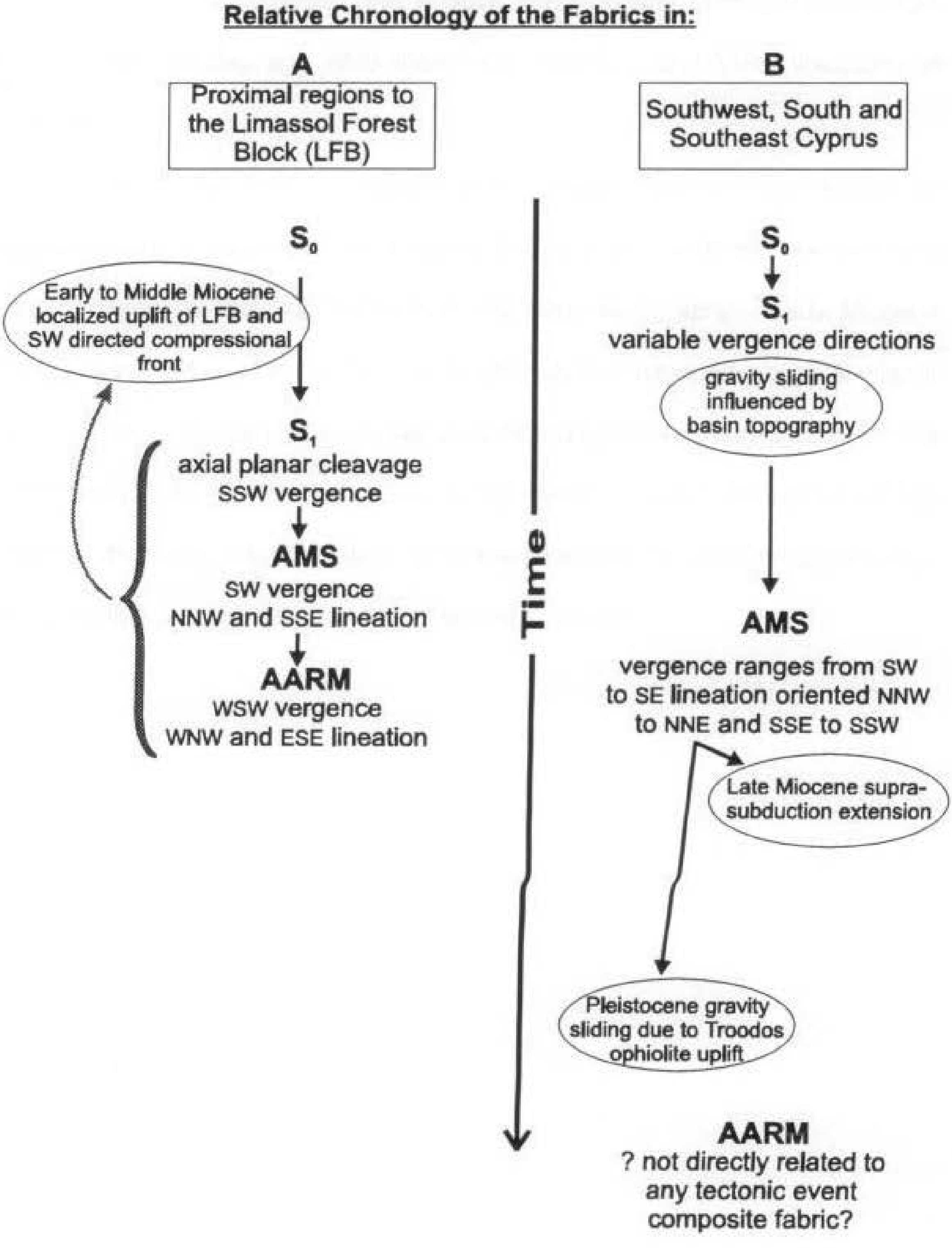

7.5 Summary

Table 7-2 summarizes the relative chronological relationship between bedding, stylolitic cleavage, AMS lineation and foliation, and AARM lineation and foliation.

Shortly after the deposition and probably during later stages of sedimentation, S_1 cleavage was acquired due to gravity sliding of sediments in various directions resulting from basin and ridge topography. Early Miocene compression in the Limassol Forest Block region developed an axial planar cleavage verging to the SW, as well as an AMS and AARM vergence directed to the SW. Finally, Late Miocene supra-subduction extension is expressed by the AMS lineation. However, the AMS fabric could also potentially express Pleistocene age gravity sliding due to localized uplift of Mount Troodos.

Chapter 8 - Conclusions

This thesis sought to define the magnetic fabric of the Troodos ophiolite circum sedimentary succession and subsequently interpret the results to shed extra light on the established tectonic evolution of Cyprus. In the literature, the magnetic fabric of Cyprus rocks has only been previously tackled by Tauxe *et al.* (1998) who studied the AMS of dikes. Additionally, bedding and stylolitic cleavage data, was collected in the field and was coupled with the magnetic fabric results.

The study incorporated predominantly samples from the Lefkara and Pakhna Formations (Miocene and older sediments) of the sedimentary succession with some sedimentary rock samples of Pliocene and younger age. Tectonic activity affecting the sedimentary succession include (Chapter 1):

- the later stages of a 90 degree counterclockwise rotation of the Troodos Microplate which terminated in Early Eocene time,
- Early Miocene age localized uplift and southwestward thrusting of the Limassol Forest Block (LFB),
- Miocene jump of the subduction zone from a position north of the island to a position south of the island. Continued 'roll-back' or migration southward has been postulated (Chapter 7), and
- Pleistocene age localized uplift of the Troodos ophiolite complex.

It is within these tectonic settings and mechanisms that the observed petrofabric and magnetic fabric of this sample suite were interpreted.

The goal of this study, relating rock fabric to tectonics, could not be reached if petrofabrics alone were being interpreted. On an outcrop scale, portions of the study area appear completely undeformed (i.e. no folding, no cleavage). Magnetism and magnetic anisotropy is an inherent property of all material and provides an extra dimension to fabric studies, making tectonic interpretation of apparently undeformed rocks possible and of deformed rocks without conventional strain markers (Chapter 2 and 3).

Interpreting magnetic fabric does require a certain knowledge of the samples' mineralogy. Within Chapter 4, evidence and discussion of the diamagnetic, paramagnetic and ferromagnetic contributors were presented. Both low-field and high-field susceptibility identified that diamagnetic minerals were an important mineralogical fraction of the samples, where AMS measurements yielded negative mean susceptibilities in 37% of the samples (n=1170) and Micromag results identified diamagnetic matrix in ~12% of the samples (n =170). The range of mean low-field susceptibility further suggested that calcite and quartz were the diamagnetic minerals present. Paramagnetic contributors are in most cases clays, given the pelagic nature of most of the sample suite. Sedimentary samples which *formed in shallower waters, and more proximal distances to eroding land, may have* terrigenous clasts derived from the ophiolitic terrain contributing to the samples paramagnetic fraction.

Hysteresis loop properties determined that the ferromagnetic contributor was pseudo-single domain magnetite. Micromag results indicated that the ferromagnetic content contributed more than 50 % of the susceptibility in 71% of the samples (n=170), however mean low-field susceptibility values would indicate that magnetite makes up less 0.1% of the cores volume (see Table 4-3) in almost the entire sample suite. Therefore, interpretation of the AMS fabric will reflect the preferred crystallographic orientation of the clay minerals whereas interpretation of the AARM fabric will reflect the preferred dimensional orientation of the magnetite grains.

Table 8-1 summarizes the petrofabric and magnetic fabric characteristics presented in Chapters 5, 6, and 7.

Table 8-1 Summary of study's petrofabric and magnetic fabric results.

<table>
<tr><th colspan="2">Characteristic</th><th>S_1</th><th>AMS</th><th>AARM</th></tr>
<tr><td rowspan="6">Vergence</td><td>zone 1</td><td>NNW, WNW</td><td>SW</td><td>SE</td></tr>
<tr><td>zone 2</td><td>ESE, NE, NNW, SSW</td><td>SE</td><td>SE</td></tr>
<tr><td>zone 3</td><td>WNW, N</td><td>S</td><td>SE</td></tr>
<tr><td>zone 4</td><td>SSW</td><td>SW</td><td>WSW</td></tr>
<tr><td>zone 5</td><td rowspan="2">SW, NNE</td><td>E</td><td>ESE</td></tr>
<tr><td>zone 6</td><td>W</td><td>SE</td></tr>
<tr><td colspan="2">magnetic lineation</td><td></td><td>NNW to NNE and SSE to SSW</td><td>WNW ($AARM_{int}$: throughout)
WNW and ESE (zone 4 and 5)</td></tr>
<tr><td colspan="2">magnetic foliation</td><td></td><td>nearly horizontal, dips east and west</td><td>dips 45° to the NW</td></tr>
<tr><td colspan="2">P_j</td><td></td><td>1.66 ± 0.13</td><td>Mode 1- 1.13 ± 0.01
Mode 2- 1.12 ± 0.01</td></tr>
<tr><td colspan="2">T_j</td><td></td><td>0.12 ± 0.01</td><td>Mode 1- 0.10 ± 0.02
Mode 2- 0.93 ± 0.02</td></tr>
</table>

The interpretation and discussion of these results are found in Chapter 7, where Table 7-2 summarizes the relative chronology of the S_1, AMS and AARM fabrics and the mechanisms which possibly generated them. A history is outlined for both the island as a whole and the region of the Yeresa fold and thrust belt.

Proximally to the Limassol Forest Block, the fabrics developed during a single tectonic event (Early to Middle Miocene) which uplifted and thrusted the Limassol Forest Block southwestward creating the Yeresa Fold and thrust belt and three other compressional lineament. S_1, AMS and AARM vergence all indicate a tectonic push directed to the SW. It is an accepted view that S_1 would be the first fabric to develop and that AMS and subsequently AARM would follow. Given the relative time of formation and the apparent anticlockwise rotation of the vergence direction in this area, I concluded that the deformation was possibly produced by non-coaxial strain.

The fabric developed in other regions of the island seem dominantly influenced by gravity sliding. A basin topography was suggested to explain the highly variable S_1 vergence directions. AMS vergence and magnetic lineation yielded much more consistent orientations, which have been interpreted in two ways. The first associates the AMS to supra-subduction extension due to a southward migrating subduction zone during the Miocene (section 7.2.2). *Secondly, the fabric may also be interpreted as expressing a Pleistocene age* localized tectonic uplift of the Troodos ophiolite complex. Since the studies rock samples range in age between Late Cretaceous and Pliocene, samples younger than Miocene age could not express a fabric of supra-subduction extension, and therefore if older samples developed fabric associated with this event, two AMS fabric should be identifiable. Unfortunately, in this case, the fabric produced by supra-subduction extension and that produced by gravity sliding, due to tectonic uplift of the Troodos ophiolite complex, would result in similar AMS expressions.

The AARM fabric, away from the Limassol Forest Block, is a composite fabric where the magnetic lineation (WNW; Chapter 6) is not expressed by the maximum axes of the AARM ellipsoid but instead by the intermediate axes. The maximum axes represent the intersection lineation between the AARM foliation plane and S_o. The association of the composite AARM fabric to a tectonic event was not established.

References

Allerton, S. and Vine, F. J., 1991, Spreading evolution of the Troodos ophiolite, Cyprus: *Geology*, 19: 637-640.

Allerton, S. and Vine, F. J., 1987, Spreading structure of the Troodos ophiolite, Cyprus: Some paleomagnetic constraints: *Geology*, 15: 593-597.

Alvarez, W., Engelder, T., and Geiser, P. A., 1978. Classification of solution cleavage in pelagic limestones. *Geology*, 6: 263-266.

Balsley, J. R., and Buddington, A. F., 1960, Magnetic susceptibility anisotropy and fabric of some Adirondack granites and orthogneisses. *American Journal of Science*, 258A: 6-20.

Ben-Avraham, Z. and Nur, A., 1986, Collisional processes in the Eastern Mediterranean: *Geologische Rundschau*, 75: 209-217.

Berthé, D., Choukroune, P. and Jegouza, P., 1979, Orthogneiss, mylonite and noncoaxial deformation of granites: the example of the South Armorican shear zone: *Journal of Structural Geology*, 1: 31-42.

Blome, C.D. and Irwin, W.P., 1985, Equivalent radiolarian ages from ophiolitic terranes of Cyprus and Oman: *Geology*, 13: 401-404.

Borradaile, G.J., 1991, Correlation of strain with anisotropy of magnetic susceptibility (AMS): *Pure and Applied Geophysics*, 135: 15-29.

Borradaile, G.J., 1988, Magnetic susceptibility, petrofabrics and strain: *Tectonophysics*, 156: 1-20.

Borradaile, G.J. 1979. Strain study of the Caledonides in the Islay region, SW Scotland: implications for strain histories and deformation mechanisms in greenschists. *J. Geol. Soc. (London)*, 136, 77-88.

Borradaile, G.J. & Henry, B., 1997, Tectonic applications of magnetic susceptibility and its anisotropy: *Earth Science Reviews*, 42: 49-93.

Borradaile, G. J. and Dehls, J. F., 1993, Regional kinematics inferred from magnetic subfabrics in Archean rocks of Northern Ontario, Canada: *Journal of Structural Geology*, 15: 887-894.

Borradaile, G. J.,Werner, T., Dehls, J. F., and Spark, R. N., 1993a, Archean Regional transpression and Paleomagnetism in Northwestern Ontario, Canada: *Tectonophysics*, 220: 117-125.

Borradaile, G. J., Chow, N. and Werner, T., 1993b, Magnetic hysteresis of limestones: facies control?: *Physics of the Earth and Planetary Interiors*, 76: 241-252.

Borradaile, G. J. and Spark, R. N., 1991, Deformation of the Archean Quetico-Shebandowan subprovince boundary in the Canadian Shield near Kashabowie, northern Ontario: *Canadian Journal of Earth Science*, 28: 116-125.

Borradaile, G. J., Keeler, W., Alford, C and Sarvas, P., 1987, Anisotropy of Magnetic susceptibility of some metamorphic minerals: *Physics of the Earth and Planetary Interiors*, 48: 161-166.

Borradaile, G. J., 1985, Tectonic strain determined from pillow selvages: accuracy and the cut-effect: *Canadian Journal of Earth Science*. 10: 1548-1552.

Borradaile, G. J. and Mothersill, J. S., 1984, Coaxial deformed and magnetic fabrics without simply correlated magnitudes of principal values:*Physics of the Earth and Planetary Interiors*, 35: 294-300.

Borradaile, G. J. and Stupavsky, M., 1995. Anisotropy of magnetic susceptibility: Measurement schemes. *Geophysical Research Letters*, 22: 1957-1960.

Borradaile, G. J., Bayly, M. B., and Powell, C. Mc A., 1982, Atlas of Deformational and Metamorphic Rock Fabrics. Springer-Verlag, New York, 551 pages.

Butler, R.F., 1992, *Paleomagnetism: Magnetic Domains to Geologic Terranes*, Blackwell Scientific Publications, Boston, 319 pp.

Cahn, R. W., 1970, Recovery and recrystallization, In: R. W. Cahn (Editor) Physical Metallurgy, Elsevier: 1129.

Cañón-Tapia, E., 1994, Anisotropy of Magnetic Susceptibility Parameters: Guidelines for their Rational Selection: *PAGEOPH*, 142: 365-382.

Carmichael, R. S., 1982, Magnetic Properties of Minerals and Rocks. In: CRC handbook of Physical Constants for Rocks, Boca Raton, Florida: 229-287.

Clube, T. M. M. and Robertson, A. H. F., 1986, The paleorotation of the Troodos microplate, Cyprus, in the Late Mesozoic - Early Cenozoic plate tectonic framework of the Eastern Mediterranean: *Surveys in Geophysics*, 8: 375-437.

Cogné, J.-P., and H. Perroud, 1988, Anisotropy of magnetic susceptibility as a strain gauge in the Flamanville granite, NW France: *Physics of the Earth and Planetary Interiors*, 51: 264-270.

Davis, G. H., 1984, *Structural Geology of Rocks and Regions*, John Wiley & Sons, 492 pp.

Day, R., Fuller, M. D. and Schmidt, V.A. 1977. Hysteresis properties of titanomagnetites: grain size and compositional dependence. *Physics of the Earth and Planetary Interiors*, 13: 260-267.

Dewey, J. F., Pittman, W.C., Ryan, W. B. F. and Bonnin, J., 1973, Plate tectonics and the evolution of the Alpine system: *Geological Society of America Bulletin*, 84: 3137-3180.

Dilek, Y., Thy, P., Moores, E.M. and Ramsden, T. W., 1990, Tectonic evolution of the Troodos ophiolite within the Tethyan framework: *Tectonics*, 9: 811-823.

Drury, M. R. and Urai, J. L., 1990, Deformation related recrystallization processes: *Tectonophysics*, 172: 235-253.

Dunlop, D. P. and Özdemir, Ö., 1997, *Rock magnetism: fundamentals and frontiers*, Cambridge University Press, 573 pp.

Eaton, S., and Robertson, A., 1993, The Miocene Pakhna Formation, southern Cyprus and its relationship to the Neogene tectonic evolution of the Eastern Mediterranean. *Sedimentary Geology*, 86: 273-296.

Etheridge, M. A. and Hobbs, B. E., 1974, Chemical and deformational controls on recrystallization of mica: *Contributions to Mineralogy and Petrology*, 43: 111-124.

Flinn, D., 1965, On the symmetry principle and the deformation ellipsoid. *Geol. Mag.*, 102: 36-45.

Follows, E. J. and Robertson, A. H. F., 1990, Sedimentology and structural setting of the Miocene reefal limestones in Cyprus, in *Troodos '87, Ophiolite and Oceanic Lithosphere*. Cyprus Geological Survey Department, p. 207-216.

Gass, I. G., 1990, Ophiolites and oceanic lithosphere, in *Troodos '87, Ophiolite and Oceanic Lithosphere*. Cyprus Geological Survey Department, p. 1-10.

Gottsein, G. and Mecking, H., 1985, Recrystallization, In: H. R. Wenk (Editor), Preferred orientation in Deformed Metals and Rocks: An Introduction to Modern Texture Analysis: 183-218.

Graham, J. W., 1954, Magnetic anisotropy, an unexploited petrofabric element: *Bulletin of the Geological Society of America*, 65: 1257-1258.

Grand, T., Lapierre, H., Mascle, G. H., Ohnenstetter, M. and Angelier, J., 1993, Superimposed tectonics of the Cyprus ophiolitic massifs: *Tectonics*, 12: 93-101.

Griggs, D. J., 1967, Hydrolitic weakening of quartz and other silicates: *Geophysical Journal of the Royal Astronomical Society*, 14: 19-31.

Groves, G. W. and Kelly, A., 1969, Change of shape due to dislocation climb: *Philosophical Magazine*, 19: 977-986.

Hay, R. and Evans, B., 1987, Chemically induced migration in low and high angle calcite grain boundaries: *Acta Metall.*, 34: 2049-2062.

Hobbs, B.E., 1968, Recrystallization of single crystals of quartz: *Tectonophysics*, 6:353-401.

Hobbs, B. E., Means, W. D. and Williams, P. F., 1976, *An Outline of Structural Geology*, John Wiley & Sons, 571 pp.

Hrouda, F, 1986, The effect of quartz on the magnetic susceptibilty of quartzite: *Stud. Geoph. Geod.*, 30: 39-45.

Hrouda, F., 1982, Magnetic anisotropy of rocks and its application in geology and geophysics: *Geophysical Surveys*, 5: 37-82.

Hrouda, F. Chlupacova, M. and Rejl, L. 1971 The mimetic fabric of magnetite in some foliated granodiorites, as indicated by magnetic anisotropy. *Earth and Planetary Science Letters*, 11,381-384.

Jelinek, V., 1981, Charaterization of the magnetic fabric of rocks: *Tectonophysics*, 79: 63-67.

Kempler, D. and Ben-Avraham, Z., 1987, The tectonic evolution of the Cyprean Arc: *Annales Tectonicae*, 1: 58-71.

Khan, M. A., 1962. Anisotropy of magnetic susceptibility of some igneous and metamorphic rocks, *J. Geophys. Res.*, 67, 2873-2885.

Knopf, E. B. and Ingerson, E., 1938, Structural Petrology: *Geological Society of America*, Memoir 6, 270 pp.

Lapierre, H, Angelier, J., Cogné, X., Grand, T. and Mascle, G., 1988, Tectonique superposée de la zone de faille d'Arakapas (Massif de Troodos, Chypre): *Geodinamica Acta*, 2-4: 197-206.

Le Pichon, X., and Angelier, J., 1981, The Aegean Sea. *Philos. Trans. R. Soc. London, Ser. A.*, 300: 357-372.

Livermore, R.A. and Smith, A.G., 1984, Some boundary conditions for the evolution of the Mediterranean region, in Stanley, D.J. and Wezel, F.-C. (Editors): *Geological evolution of the Mediterranean Basin*, Springer-Verlag: 83-100.

Lonergan, L., and White, N., 1997, Origin of the Betic-Rif mountain belt. *Tectonics*, 16: 504-522.

Lowrie, W., and F. Heller, 1982. Magnetic properties of marine limestones, *ReGeophys. Space Phys.*, 20, 171-192.

McCallum, J. E. and Robertson, A. H. F., 1990, Pulsed uplift of the Troodos Massif - evidence from the Plio-Pleistocene Mesaoria basin, in *Troodos '87, Ophiolite and Oceanic Lithosphere*. Cyprus Geological Survey Department, *p.* 217-230.

McClay, K. R., 1977, Pressure Solution and Coble Creep in rocks and minerals: a review, *Journal of the Geological Society of London*. 134: 57-70.

Miyashiro, A., 1973, The Troodos ophiolite complex was probably formed in an island arc: *Earth and Planetary Science Letters*, 19: 218-224.

Moores, E.M., Robinson, P.T., Malpas, J. and Xenophontos, C., 1984, A model for the origin of the Troodos Massif, Cyprus and other mid-east ophiolites: *Geology*, 12: 500-503.

Morel, S. W., 1960, The geology and mineral resources f the Apsiou-Akrotiri area. *Mem. Geol. SurDept. Cyprus, no. 7: 51-88.*

Murton, B.J., 1990, Was the Southern Troodos transform fault a victim of microplate rotation?, in *Troodos '87, Ophiolite and Oceanic Lithosphere*. Cyprus Geological Survey Department, p. 87-98.

Nagata, T., 1961. Rock Magnetism, 2nd, 350 pp., Maruzen, Tokyo.

Néel, L., 1955, Some theoretical aspects of rock magnetism: *Suppl. Philosophical Magazine*, 4: 194-242.

Nicolas, A., and Poirier, J. P., 1976, Crystalline Plasticity and Solid State Flow in Metamorphic Rocks, John Wiley & Sons, Toronto, 444 pages.

Nye, J. F., 1957, The physical properties of crystals. Clarendon Press, Oxford. 322pp.

O'Reilly, W., 1984, Rock and Mineral Magnetism, Chapman and Hall, New York, 220 pages.

Orsag-Sperber, F., Rouchy, J. M., and Elion, P., 1989, The sedimentary expression of regional tectonic events during the Miocene-Pliocene transition in the southern Cyprus basins. *Geol. Mag.*, 136: 291-299.

Owens, W.H. 1974 Mathematical model studies on factors affecting the magnetic anisotropy of deformed rocks. *Tectonophysics*, 24, 115-131.

Park, R. G., 1989, *Foundations of Structural Geology*, 2nd Edition, Blackie Academic & Professional, 148 pp.

Payne, A. S., and Robertson, A. H. F., 1995, Neogoene supra-subduction zone extension in the Polis graben system, west Cyprus. *J. Geol. Soc. (London)*, 152: 613-628.

Pierce, J. A., Lippard, S.J. and Roberts, S., 1984, Characteristic and tectonic significance of supra-subduction zone ophiolites: *Geological Society of London Special Publications*, No. 16: 77-96.

Poirier, J-P., 1985, Creep of Crystals: High-temperature deformation processes in metals, ceramics and minerals, Cambridge University Press, New York, 260 pages.

Powell, C. Mc A., 1979, A morphological classification of rock cleavage: *Tectonophysics*. 58: 21-34.

Price, N. J., 1975, Rates of deformation: *Journal of the Geological Society of London*. 131: 553-575.

Ramsay, J. G. 1967. Folding and Fracturing of Rocks. McGraw-Hill, New York, 578pp.

Ramsay, J. G., and Huber, M. I., 1983, The Techniques of Modern Structural Geology: Strain Analysis, Academic Press, Toronto, volume 1, 307 pages.

Rathore, J. S., 1980, The magnetic of some slates from the Borrowdale Volcanic Group in the English Lake District and their correlations with strain: *Tectonophysics*, 67: 207-20.

Rees, A.I., 1966. The effect of the depositional slopes on the anisotropy of magnetic susceptibility of laboratory deposited sands. *J. Geol.*, 74: 856-867.

Robertson, A. H. F., 1990, Tectonic evolution of Cyprus, in *Troodos '87, Ophiolites and Oceanic Lithosphere*. Cyprus Geological Survey Department, p. 235-250.

Robertson, A. H. F., 1977, Tertiary uplift history of the Troodos massif, Cyprus: *Geological Society of America Bulletin*, 88: 1763-1772.

Robertson, A. H. F. and Woodcock, N.H., 1979, Mamonia Complex, southwest Cyprus: Evolution and emplacement of a Mesozoic continental margin: *Geological Society of America Bulletin, Part I*, 90: 651-665.

Robertson, A. H. F. and Woodcock, N.H., 1986, The geological evolution of the Kyrenia Range: a critical lineament in the Eastern Mediterranean, in Reading, H.G., Watterson, J. and White, S. H. (Editors), Major crustal lineaments and their influence on geological history of the continental lithosphere: *Philosophical Transactions of the Royal Society of London*, A317: 141-171.

Robinson, P. T. and Malpas, J., 1987, The Troodos ophiolite of Cyprus: New perspective on its origin and emplacement, in *Troodos '87, Ophiolites and Oceanic Lithosphere*. Cyprus Geological Survey Department, p. 13-26.

Rochette, P., Jackson, M. and Aubourg, C., 1992, Rock magnetism and their interpretations of the anisotropy of magnetic susceptibility: *Reviews in Geophysics*. 30: 209-226.

Rotstein, Y., 1984, Counterclowise rotation of the Anatolian Block: *Tectonophysics*, 108: 71-91.

Rutter, E. H., 1976, The kinetics of rock deformation by pressure solution: *Philosophical Transactions of the Royal Society of London*. A283: 203-219.

Stacey, F. D., Joplin, G., and Lindsay, J., 1960, Magnetic anisotropy and fabric of some foliated rocks from SE Australia. *Geophysica Pura Appl.*, 47: 30-40.

Staudigel, H., Gillis, K. , and Duncan, R., 1986, K/Ar and Rb/Sr ages of celadonites from Troodos ophiolite, Cyprus: *Geology*, 14: 72-75.

Stow, D. A. V., Braakenburg, N. E., and Xenophontos, C., 1995, The Pissouri Basin fan-delta complex, southwestern Cyprus. *Sedimentary Geology*, 98: 245-262.

Tarling, D. H. and Hrouda, F., 1993, *The magnetic anisotropy of rocks*. Chapman and Hall, 217pp.

Tauxe, L., Gee, J. S. and Staudigel, H., 1998, Flow directions in dikes from anisotropy of magnetic susceptibility data: The bootstrap way: *Journal of Geophysical Research*. 103, 17:775-790.

Urai, J. L., Means, W. D. and Lister, G. S., 1986, Dynamic recrystallization of minerals: *Geoph. Monogr., Am. Geophys. Union*, 36: 161-199.

Urrutia-Fucugauchi, J., 1980, Paleomagnetic studies of Mexican rocks. Ph.D. thesis, University of Newcastle upon Tyne, 689 pages.

Voight, W. and Kinoshita, S. 1907 Bestimmung absoluter Werte von Magnetisierungszahlen, insbesondere fur Kristalle. *Annalen der Physik*, 24: 492-514.

Werner, T. and Borradaile, G. J., 1996, Paleoremanence dispersal across a *transpressional Archean terrain: Deflection by anisotropy or by late* compression?: *Journal of geophysical Research*, 101: 5531-5545.

Wood, D. S., Oertel, G., Singh, J. and Bennett, H. F., 1976, Strain and anisotropy in rocks: *Philosophical Transactions of the Royal Society of London*, A283: 27-42.

Appendix A

Bedding and Cleavage Data

Table A-1 Field Data

	Coordinates			Bedding		Cleavage		
Outcrop	Northing	Easting	Sample #	Strike	Dip	Strike	Dip	Type of Cleavage
4	3847937	524660	FL98003	24	17	112	74	stylolitic
				356	14	113	75	stylolitic
5	3846302	507713	FL98004	297	49	284	72	stylolitic
			FL98005	300	54	289	69	stylolitic
				302	46	290	84	stylolitic
6	3846241	507764	FL98006	290	39	294	49	stylolitic
				295	43	284	45	stylolitic
						256	30	stylolitic
						318	48	stylolitic
7	3846004	507790	FL98007	176	19	295	50	stylolitic
				184	35	285	76	stylolitic
				198	19	274	59	stylolitic
						302	52	stylolitic
				186	2	288	56	stylolitic
						286	62	stylolitic
						277	50	stylolitic
8	3845760	507846	FL98008	26	5	300	54	stylolitic
			FL98009	65	15	300	50	stylolitic
				56	12	308	56	stylolitic
						308	60	stylolitic
9	3845714	508191	FL98010	86	22	292	55	stylolitic
						305	57	stylolitic
						298	58	stylolitic
						296	56	stylolitic
10A	3845770	508474	FL98011	320	86	313	74	stylolitic
			FL98012	300	90	302	42	stylolitic
				132	56	276	41	stylolitic
10B	3845770	508474	FL98013	234	39	301	38	stylolitic
				128	46	304	38	stylolitic
				124	18			stylolitic
11	3845859	508529	FL98014			318	39	stylolitic
						313	54	stylolitic
12	3845847	508559	FL98015	54	44	304	46	stylolitic
13	3845741	508435	FL98016	330	62	322	42	stylolitic
			FL98017	322	46	319	41	stylolitic
						316	39	stylolitic
14	3845532	508458	FL98018			316	69	stylolitic
			FL98019			310	69	stylolitic
						306	43	stylolitic
15	3845428	508545	FL98020	125	49	294	28	stylolitic
				121	49	295	15	stylolitic
				120	51			
16	3844799	508234	FL98021	99	27	306	19	stylolitic
				94	14			
				94	15			
				100	12			
				111	16			
17	3844655	508013	FL98022	102	22			
				103	30			
				108	20			

Table A-1 Field Data

Outcrop	Coordinates Northing	Easting	Sample #	Bedding Strike	Dip	Cleavage Strike	Dip	Type of Cleavage
				99	24			
18	3844559	508056	FL98023	108	34	298	15	stylolitic
			FL98024	98	25	315	9	stylolitic
				102	20	332	26	stylolitic
19	3844525	507849	FL98025	72	23			
			FL98026	70	15			
20	3843069	511336	FL98027	110	32	70	18	stylolitic
				80	10	40	20	stylolitic
21	3842819	511293	FL98028 A + B	52	30			
22	3843743	511738	FL98029	302	44	336	41	stylolitic
						318	50	stylolitic
						326	33	stylolitic
23	3843551	511700	FL98030	132	10	336	32	stylolitic
				172	15	348	16	stylolitic
						314	18	stylolitic
						292	5	stylolitic
						312	10	stylolitic
24	3843239	511721	FL98031			243	22	stylolitic
						235	22	stylolitic
						218	27	stylolitic
25	3842722	511208	FL98032	75	26	272	20	stylolitic
						308	24	stylolitic
						286	18	stylolitic
						275	22	stylolitic
26	3844508	502646	FL98033	331	15			
				327	9			
				348	10			
27	3849459	502255	FL98034	72	60	253	24	stylolitic
				82	49			
				80	45			
28	3849151	502799	FL98035	96	51	118	84	stylolitic
			FL98036	98	51	120	84	stylolitic
				99	52			
				94	54			
29	3849110	502852	FL98037	90	31			
				76	35			
				110	35			
				99	40			
30	3848930	502461	FL98038	109	20			
				108	20			
				102	20			
				119	18			
31	3848582	502545	FL98039	104	15			
				172	16			
				170	8			
32	3848308	502381	FL98040	25	5			
				158	9			
				140	0			
33	3848146	502398	FL98041	123	4			

Outcrop	Coordinates Northing	Easting	Sample #	Bedding Strike	Dip	Cleavage Strike	Dip	Type of Cleavage
				131	9			
				96	13			
34	3848112	501296	FL98042	125	0			
				285	3			
				178	3			
35	3842475	501577	FL98043	76	10			
36	3843264	501319	FL98044	126	5			
				120	10			
37	3845302	499949	FL98045	10	14			
			A + B	4	10			
38	3846705	498977	FL98046	102	6			
				86	9			
39	3846860	498679	FL98047	124	6	48	86	stylolitic
				102	8			
40	3847025	498678	FL98048	31	1			
			FL98049	74	4			
				44	4			
41	3847304	498919	FL98050	158	7	259	79	stylolitic
				165	2	254	90	stylolitic
				350	2	256	81	stylolitic
42	3847793	499022	FL98051	78	5			
				352	1			
				118	1			
43	3850360	499968	FL98052	114	62	139	28	stylolitic
			FL98053	118	61	169	29	stylolitic
						146	29	stylolitic
44	3850910	499887	FL98054	274	84	323	38	stylolitic
				302	71	330	55	stylolitic
						335	54	stylolitic
45	3849502	529190	FL98055	314	4			
				234	5			
46	3851391	529819	FL98056	301	0			
				136	4			
			FL98057	13	9			
				18	8			
47	3852076	529569	FL98058	10	6	196	59	stylolitic
				25	9	194	57	stylolitic
				34	12	216	66	stylolitic
48	3852150	529163	FL98059	46	9	44	90	stylolitic
				48	7	60	43	stylolitic
						54	39	stylolitic
49	3852513	528236	FL98060	347	12			
				335	11			
50	3852442	527241	FL98061	256	11			
				257	8			
				244	10			
51	3853610	526160	FL98062	260	2			
				331	5			
52	3854584	525357	FL98063	26	14			
				12	13			

Table A-1 Field Data

	Coordinates			Bedding		Cleavage		
Outcrop	Northing	Easting	Sample #	Strike	Dip	Strike	Dip	Type of Cleavage
53	3855289	524638	FL98064	125	41			
				119	45			
54	3855260	525397	FL98065	199	9			
				101	11			
				66	12			
55	3855736	527182	FL98066	124	14			
				63	22			
				84	18			
56	3861640	546700	GBFL001	356	16	180	10	stylolitic
57	3861750	545850	GBFL002	53	6			
58	3863000	544100	GBFL003	20	7			
59	3862300	543640	GBFL004					
60	3863050	542420	GBFL005	198	14			
61	3866340	545600	GBFL006	36	24			
62	3865500	548380	GBFL007	90	7	266	15	stylolitic
63	3864980	549900	GBFL008	20	3	312	36	stylolitic
				105	7	295	32	stylolitic
64	3858820	527850	GBFL009	140	32			
65	3853393	532861	FL98067	77	29			
66	3853684	533286	FL98068	78	29			
				83	27			
				88	25			
67	3853932	532970	FL98069	71	14			
				56	15			
				81	14			
68	3854132	532583	FL98070	118	11			
				130	15			
				99	10			
69	3854337	532312	FL98071	206	7			
				222	5			
70	3854612	532039	FL98072	70	9			
				76	9			
71	3854887	531671	FL98073	72	10			
				66	14			
72	3854931	531541	FL98074	32	14			
73	3855131	531078	FL98075	74	30			
				69	20			
74	3855113	530831	FL98076	59	55			
				60	55			
				60	55			
75	3855434	530361	FL98077	94	12			
			FL98078	106	14			
76	3855837	530017	FL98079	56	8			
				78	8			
77	3856421	529901	FL98079	50	15			
				98	12			
78	3856771	529612	FL98081	68	12			
				51	11			
79	3857108	529104	FL98082	8	14			
				11	25			

Outcrop	Coordinates Northing	Easting	Sample #	Bedding Strike	Dip	Cleavage Strike	Dip	Type of Cleavage
80	3856493	528292	FL98083	301	6			
				306	15			
81	3856525	528556	FL98084	53	17			
				21	22			
82	3856420	528855	FL98085	42	21			
				71	31			
83	3856880	528627	FL98086	275	4			
				229	10			
				199	8			
84	3864259	550621	GBFL010	40	6			
85	3851003	496704	FL98087	232	21			
86	3850846	496397	FL98088	64	16			
				67	16			
87	3850611	496535	FL98089	82	14			
				89	10			
88	3850163	496865	FL98090	34	14			
				39	10			
89	3849509	496962	FL98091	81	5			
				86	5			
90	3848127	496956	FL98092	15	7			
				33	4			
91	3847540	496983	FL98093	101	11			
				84	8			
92	3846575	497269	FL98094	65	3			
				64	8			
				16	3			
93	3844816	497936	FL98095	117	10			
				111	5			
94	3844673	498575	FL98096	118	12			
				124	8			
95	3844006	498581	FL98097	108	16			
				84	20			
96	3843645	498885	FL98098	63	7			
				80	14			
97	3842967	498901	FL98099	153	4			
				224	3			
98	3842513	498861	FL98100	24	5			
99	3851978	490941	FL98101	145	40			
				146	42			
				151	55			
100	3854813	489940	FL98102	39	23			
				24	16			
				346	17			
				66	14			
101	3855783	489580	FL98103	92	12			
				66	11			
102	3855927	489549	FL98104	56	14			
				4	10			
103	3856094	489345	FL98105	61	12	32	76	spaced cleavage (jointing)
				95	14	16	76	spaced cleavage (jointing)

Table A-1 Field Data

Outcrop	Coordinates Northing	Coordinates Easting	Sample #	Bedding Strike	Bedding Dip	Cleavage Strike	Cleavage Dip	Type of Cleavage
104	3855848	489824	FL98106	107	5	10	84	spaced cleavage (jointing)
				93	2	14	89	spaced cleavage (jointing)
105	3856106	490038	FL98107	131	15	86	10	stylolitic
106	3856215	489753	FL98108	106	27			
				96	20			
107	3856769	489552	FL98109	210	23			
				219	21			
108	3857419	486310	FL98110	67	25			
			FL98111	65	26			
109	3846318	507645	FL98112	277	39	313	69	stylolitic
			FL98113	271	32	315	68	stylolitic
				291	64	314	71	stylolitic
						322	64	stylolitic
						318	40	stylolitic
						303	36	stylolitic
						289	40	stylolitic
						310	50	stylolitic
110	3846047	507758	FL98114			253	40	stylolitic
						292	40	stylolitic
						286	40	stylolitic
111	3845872	507670	FL98115	121	20	298	60	stylolitic
				121	15	318	56	stylolitic
						303	52	stylolitic
112	3845840	507665	FL98116	102	34	305	62	stylolitic
						311	76	stylolitic
113	3845734	507812	FL98117	60	15	303	60	stylolitic
				52	13	298	70	stylolitic
						304	60	stylolitic
114	3845598	507825	FL98118	73	25	304	65	stylolitic
				86	25	301	56	stylolitic
				72	22			
115	3845037	507577	FL98119	129	15	290	70	stylolitic
				148	20	295	66	stylolitic
						292	60	stylolitic
116	3845091	507445	FL98120	115	24	302	74	stylolitic
						290	60	stylolitic
						301	69	stylolitic
117	3844716	507692	FL98121	131	10	312	63	stylolitic
				134	8	344	45	stylolitic
				116	5	331	53	stylolitic
118	3844767	507586	FL98122	90	8	330	74	stylolitic
				70	11	318	64	stylolitic
				92	14	358	83	stylolitic
						360	70	stylolitic
119	3844594	507588	FL98123	92	5	348	84	stylolitic
				72	15	336	76	stylolitic
				70	13			
120	3844588	507574	FL98124	94	25	332	78	stylolitic
				86	29	315	70	stylolitic
				107	29			

Table A-1 Field Data

Outcrop	Coordinates Northing	Easting	Sample #	Bedding Strike	Dip	Cleavage Strike	Dip	Type of Cleavage
121	3844454	507608	FL98125	97	19	20	89	stylolitic
				85	14	16	83	stylolitic
122	3842814	507713	FL98126	67	10			
			FL98127	22	10			
				46	8			
123	3845484	497096	FL98128	72	8	235	83	spaced cleavage (jointing)
			FL98129	81	6	228	78	spaced cleavage (jointing)
				64	14	226	86	spaced cleavage (jointing)
						227	83	spaced cleavage (jointing)
						244	85	spaced cleavage (jointing)
						240	85	spaced cleavage (jointing)
124	3845555	496998	FL98130	91	8	247	84	spaced cleavage (jointing)
				337	0	240	80	spaced cleavage (jointing)
				93	5	234	88	spaced cleavage (jointing)
						246	80	spaced cleavage (jointing)
125	3845708	496665	FL98131	90	2	239	80	spaced cleavage (jointing)
				77	9	236	88	spaced cleavage (jointing)
				106	10	223	89	spaced cleavage (jointing)
						243	85	spaced cleavage (jointing)
126	3845783	496524	FL98132	93	2	227	86	spaced cleavage (jointing)
				300	5	326	78	spaced cleavage (jointing)
				232	1	344	86	spaced cleavage (jointing)
						346	86	spaced cleavage (jointing)
127	3845831	496113	FL98133	99	10	335	84	spaced cleavage (jointing)
			FL98134	87	11	326	89	spaced cleavage (jointing)
				80	15	326	80	spaced cleavage (jointing)
						245	85	spaced cleavage (jointing)
						230	90	spaced cleavage (jointing)
						239	89	spaced cleavage (jointing)
						230	88	spaced cleavage (jointing)
128	3845979	496231	FL98135	71	7	240	81	spaced cleavage (jointing)
				85	8	245	84	spaced cleavage (jointing)
						250	86	spaced cleavage (jointing)
						280	54	stylolitic
						265	53	stylolitic
129	3846179	495940	FL98136	82	8	240	90	spaced cleavage (jointing)
				91	8	280	76	spaced cleavage (jointing)
130	3846347	495675	FL98137	360	3	260	32	stylolitic
				93	10	274	34	stylolitic
131	3846734	495446	FL98138	128	6	340	80	spaced cleavage (jointing)
			FL98139	117	8	349	87	spaced cleavage (jointing)
132	3846879	495347	FL98140	120	8	346	88	spaced cleavage (jointing)
				106	13	345	85	spaced cleavage (jointing)
				110	7	8	84	spaced cleavage (jointing)
133	3846879	495347	FL98141	80	2	358	86	spaced cleavage (jointing)
				104	4	179	89	spaced cleavage (jointing)
				94	6	175	85	spaced cleavage (jointing)
						181	88	spaced cleavage (jointing)
134	3847364	494989	FL98142	71	4	255	89	spaced cleavage (jointing)
				108	4	248	88	spaced cleavage (jointing)

Table A-1 Field Data

Outcrop	Coordinates Northing	Easting	Sample #	Bedding Strike	Dip	Cleavage Strike	Dip	Type of Cleavage
				59	11	250	83	spaced cleavage (jointing)
135	3847397	494411	FL98143	50	8			
				144	11			
				122	11			
136	3847269	499088	FL98144	150	7			
				95	5			
				127	8			
137	3847158	494021	FL98145	230	6			
			FL98146	112	13			
				215	40			
				223	33			
				226	44			
				221	52			
				226	70			
				216	76			
138	3846643	493428	FL98147	58	10	45	86	spaced cleavage (jointing)
				64	5	222	86	spaced cleavage (jointing)
						240	89	spaced cleavage (jointing)
139	3846641	492921	FL98148	136	10			
				87	7			
				96	4			
				110	8			
140	3838655	494008	FL98149	203	5			
				245	2			
141	3838315	492143	FL98150	8	5			
				47	3			
142	3838058	488871	FL98151	310	5			
				274	7			
				350	10			
143	3839860	487047	FL98152	137	9	283	86	spaced cleavage (jointing) in chalks
				147	2	286	85	spaced cleavage (jointing) in chalks
						322	42	stylolitic
144	*3839813*	*485703*	*FL98153*	*54*	*5*			
				224	3			
145	3839336	484642	FL98154	194	3	264	38	stylolitic
			FL98155	216	11			
			FL98156					
146	3837415	481937	FL98157	112	9	315	10	stylolitic
				130	6			
				149	7			
147	3837939	479151	FL98158		horz.			
			FL98159					
148	3837860	475223	FL98160	86	10	45	31	stylolitic
			FL98161	66	7	62	24	stylolitic
149	3837771	473189	FL98162	98	10			
				30	4			
				82	10			
150A	3837972	473081	FL98163	94	6	66	66	stylolitic
						45	70	stylolitic
						59	58	stylolitic

Table A-1 Field Data

	Coordinates			Bedding		Cleavage		
Outcrop	Northing	Easting	Sample #	Strike	Dip	Strike	Dip	Type of Cleavage
150B	3836687	470505	FL98134	325	6	182	24	stylolitic
			FL98135	204	15	204	47	stylolitic
151	3836443	469359	FL98166	302	5	45	20	stylolitic
				328	9	83	43	stylolitic
						48	11	stylolitic
152	3835262	467671	FL98167	171	8	58	31	stylolitic
			FL98168	166	4	86	17	stylolitic
				142	5			
153	3835479	467088	FL98169	331	25	310	28	stylolitic
				346	28	294	30	stylolitic
154	3836222	466468	FL98170	256	26	159	55	S2 (stylolitic)
				230	22	114	86	S2 (stylolitic)
						134	63	S2 (stylolitic)
						54	80	S1 spaced cleavage (jointing) cuts S2
						42	80	S1 spaced cleavage (jointing) cuts S2
155	3836044	489657	FL98171	98	5			
156	3836363	489372	FL98172	354	6	312	53	stylolitic
						316	50	stylolitic
						300	50	stylolitic
157	3837089	486410	FL98173		horz.	70	51	stylolitic
158	3836740	484068	FL98174	116	10	108	44	stylolitic
						103	52	stylolitic
159	3837126	483453	FL98175	42	3	160	46	stylolitic
						134	44	stylolitic
160	3837957	484309	FL98176	233	1	55	35	stylolitic
				42	2	82	36	stylolitic
161	3836978	483111	FL98177	126	10	8	26	stylolitic
			FL98178	29	1			
162	3835796	468256	FL98179	9	10	214	25	stylolitic
			FL98180	352	3	9	13	stylolitic
				11	10			
163	3837178	463819	FL98181	132	10	256	35	stylolitic
			FL98182			310	35	stylolitic
164	3842253	463594	FL98183	152	15			
165	3842440	463883	FL98184	22	14			
				22	15			
166	3842698	464633	FL98185	205	7			
				166	20			
167	3843092	465260	FL98186	48	4			
				146	12			
168	3843248	466811	FL98187	321	12	270	36	stylolitic
				344	20			
169	3844612	468071	FL98188	354	15			
170	3844896	469215	FL98189					
171	3845359	470448	FL98190	218	2	224	36	stylolitic
172	3845622	471439	FL98191	234	28			
				236	26			
				218	20			
173	3847322	473074	FL98192	15	1	285	40	stylolitic
174	3847853	474235	FL98193			199	21	stylolitic

Table A-1 Field Data

Outcrop	Coordinates		Sample #	Bedding		Cleavage		Type of Cleavage
	Northing	Easting		Strike	Dip	Strike	Dip	
						184	50	stylolitic
175	3848564	475170	FL98194	100	5	292	22	stylolitic
				92	1			
176	3849525	476037	FL98195	79	10			
				98	10			
177	3850651	476326	FL98196	243	2	155	40	stylolitic
				352	5	158	24	stylolitic
178	3851419	477602	FL98197	66	0			
				317	5			
				62	15			
179	3851837	478564	FL98198	215	28			
180	3852445	479452	FL98199	182	5			
				106	12			
181	3839371	491026	FL98200	354	10			
				348	5			
182	3840419	490113	FL98201	250	5			
183	3841340	490098	FL98202	122	1	62	33	stylolitic
				88	4	88	26	stylolitic
184	3842847	489860	FL98203			328	35	stylolitic
						304	29	stylolitic
185	3844476	488807	FL98204	138	5	26	35	stylolitic
186	3846374	486221	FL98205	8	6			
187	3846714	485654	FL98206	78	10			
				70	3			
188	3847502	484850	FL98207	50	3	306	23	stylolitic
						310	29	stylolitic
189	3848709	484592	FL98208	62	10	352	45	stylolitic
						2	29	stylolitic
190	3849597	484004	FL98209	151	5	260	13	stylolitic
191	3850249	483389	FL98210	92	7	147	16	stylolitic
				106	5	150	27	stylolitic
192	3850413	482399	FL98211	121	8	100	21	stylolitic
				133	3	122	31	stylolitic
						110	23	stylolitic
193	3851037	481200	FL98212	107	10	94	24	stylolitic
				99	9	119	36	stylolitic
194	3851618	480922	FL98213	104	11	205	20	stylolitic
				75	10	167	20	stylolitic
195	3852065	481041	FL98214	79	11	23	55	stylolitic
				303	20	43	54	stylolitic
				226	24	35	35	stylolitic
196	3850217	481762	FL98215	12	20	43	45	stylolitic
197	3849676	481533	FL98216	74	10	48	34	stylolitic
						49	29	stylolitic
198	3849172	481383	FL98217	30	6	51	45	stylolitic
						46	41	stylolitic
199	3848433	481477	FL98218	118	7	198	45	stylolitic
200	3847673	481254	FL98219	88	6	226	29	stylolitic
						290	35	stylolitic
201	3846092	480339	FL98220	340	30			

	Coordinates			Bedding		Cleavage		
Outcrop	Northing	Easting	Sample #	Strike	Dip	Strike	Dip	Type of Cleavage
202	3843903	480111	FL98221	358	13			
				66	5			
203	3842511	479742	FL98222	70	5			
204	3841925	479638	FL98223	241	1			
205	3840869	478597	FL98224	141	11			
206	3839065	478406	FL98225	84	10			
207	3840536	494153	FL98226	303	11	322	44	stylolitic
208	3841343	493183	FL98227	85	4	158	52	stylolitic
				130	8	168	69	stylolitic
						180	51	stylolitic
209	3842115	493364	FL98228	148	13	155	34	stylolitic
						150	25	stylolitic
210	3842741	492773	FL98229	12	5	167	59	stylolitic
						183	36	stylolitic
211	3842922	492235	FL98230	14	10	20	33	stylolitic
212	3843861	492351	FL98231	60	5	332	30	stylolitic
				31	6			
213	3844565	492617	FL98232	45	5	310	29	stylolitic
				121	4			
214	3845715	492404	FL98233	74	5	271	33	stylolitic
						282	40	stylolitic
215	3846550	491806	FL98234	43	6	7	28	stylolitic
						347	26	stylolitic
216	3847182	491121	FL98235	160	5	286	26	stylolitic
						294	21	stylolitic
						298	40	stylolitic
217	3847356	491888	FL98236	345	4	13	20	stylolitic
						12	10	stylolitic
						20	34	stylolitic
						30	24	stylolitic
218	3847019	492281	FL98237	120	8	36	40	stylolitic
219	3847275	491572	FL98238	85	10			
220	3848215	491436	FL98239	345	4	133	8	stylolitic
						178	40	stylolitic
						164	29	stylolitic
221	3848712	490936	FL98240	56	8	104	13	stylolitic
						96	10	stylolitic
222	3849639	490008	FL98241	138	12			
				175	9			
				156	9			
223	3850396	489979	FL98242	44	5	20	20	stylolitic
				16	7			
224	3852950	487920	FL98243	98	11			
225	3852838	487811	FL98244	347	6	20	26	stylolitic
				348	8			
226	3852613	486880	FL98245	95	6	2	10	stylolitic
227	3851892	486643	FL98246	81	5	20	15	stylolitic
228	3851431	486434	FL98247	95	4	132	21	stylolitic
229	3851204	486149	FL98248	121	4	43	24	stylolitic
				68	8	42	13	stylolitic

	Coordinates			Bedding		Cleavage		
Outcrop	Northing	Easting	Sample #	Strike	Dip	Strike	Dip	Type of Cleavage
						45	14	stylolitic
230	3850751	485832	FL98249	94	5	106	15	stylolitic
						100	10	stylolitic
						72	19	stylolitic
						90	35	stylolitic
231	3850271	485229	FL98250	99	6			
232	3849594	484646	FL98251	79	5	94	29	stylolitic
			FL98252					
233	3849181	484552	FL98253	164	6	18	25	stylolitic
						193	19	stylolitic
234	3841947	459400	FL98254	38	10			
235	3842926	460941	FL98255	82	14			
				70	16			
				76	15			
236	3843319	461842	FL98256	254	11			
				38	10			
237	3843535	463075	FL98257	105	25	94	41	stylolitic
				102	29			
238	3852590	474566	FL98258	52	3			
			FL98259	27	16			
239	3853136	474579	FL98260	333	10	302	15	stylolitic
			FL98261			294	21	stylolitic
				344	30	282	14	stylolitic
240	3853947	475221	FL98262	30	5	195	10	stylolitic
				43	15			
241	3858552	478665	FL98263	95	16	250	20	stylolitic
				96	32		30	stylolitic
242	3858801	479195	FL98264	240	9	182	11	stylolitic
				76	15	218	19	stylolitic
						163	40	stylolitic
243	3858598	480055	FL98265	125	7	325	14	stylolitic
244	3857874	482894	FL98266	188	9	276	50	stylolitic
				339	10			
245	3856847	482331	FL98267	217	34			
				218	40			
246	3855893	482269	FL98268	356	6	340	25	stylolitic
				339	6	337	19	stylolitic
						312	23	stylolitic
						334	20	stylolitic
247	3854619	482280	FL98269	238	5			
248	3853354	481579	FL98270	95	4	357	40	stylolitic
						353	21	stylolitic
249	3852972	479232	FL98271	101	10	272	35	stylolitic
250	3853891	478898	FL98272	168	6	193	45	stylolitic
						218	19	stylolitic
251	3854789	479207	FL98273	138	2	160	35	stylolitic
252	3855670	479077	FL98274	130	10	180	36	stylolitic
				35	4			
253	3855879	478561	FL98275	70	11	37	35	stylolitic
				68	10	40	34	stylolitic

Table A-1 Field Data

	Coordinates			Bedding		Cleavage		
Outcrop	Northing	Easting	Sample #	Strike	Dip	Strike	Dip	Type of Cleavage
						35	43	stylolitic
254	3856701	478269	FL98276	37	34			
				38	30			
255	3856833	477826	FL98277	103	5	202	30	stylolitic
						218	25	stylolitic
						182	50	stylolitic
256	3856724	477053	FL98278	298	15	300	29	stylolitic
257	3857177	475178	FL98279	89	13	116	26	stylolitic
258	3857404	475118	FL98280	302	14	114	42	stylolitic
						115	24	stylolitic
						131	30	stylolitic
259	3857670	473832	FL98281	279	12			
				258	13			
260	3854594	471199	FL98282	232	8	71	19	stylolitic
				358	4			
261	3854027	471365	FL98283	278	10	250	50	stylolitic
			FL98284			258	48	stylolitic
262	3852857	470266	FL98285	42	8			
			FL98286					
263	3850032	466538	FL98287	72	27	225	20	stylolitic
264	3849534	465813	FL98288	335	15	236	30	stylolitic
						218	39	stylolitic
265	3846154	463102	FL98289	20	20			
				16	10			
266	3842359	459795	FL98290	149	10			
267	3842534	458685	FL98291	322	7			
268	3846137	458783	FL98292	45	30			
269	3846000	459253	FL98293	10	20	3	30	stylolitic
				10	18	336	43	stylolitic
						343	44	stylolitic
270	3848388	460886	FL98294	285	18	33	37	stylolitic
			FL98295			52	28	stylolitic
271	3848945	460364	FL98296	278	20	213	48	stylolitic
						235	22	stylolitic
272	3849302	460542	FL98297	82	16	147	33	stylolitic
						144	32	stylolitic
						108	26	stylolitic
273	3849879	460670	FL98298	4	13	256	15	spaced cleavage (jointing)
						355	56	spaced cleavage (jointing)
274	3850384	460417	FL98299	177	10	14	22	stylolitic
275	3851422	459916	FL98300	52	13	77	35	stylolitic
				5	10			
276	3850822	458888	FL98301	320	14			
277	3850071	458666	FL98302	250	10	338	44	stylolitic
				198	15	325	34	stylolitic
278	3849544	458688	FL98303	210	30			
			FL98304					
279	3854529	462776	FL98305	205	7			
				215	20			
				164	5			

Table A-1 Field Data

	Coordinates			Bedding		Cleavage		
Outcrop	Northing	Easting	Sample #	Strike	Dip	Strike	Dip	Type of Cleavage
280	3855032	463100	FL98306	146	10	132	18	stylolitic
				200	8	125	20	stylolitic
281	3855442	463667	FL98307	148	10			
282	3859432	465364	FL98308	325	8	198	30	stylolitic
283	3860760	464810	FL98309	64	5			
284	3861184	464853	FL98310	335	5	240	21	stylolitic
285	3861789	465004	FL98311	359	40	2	16	stylolitic
286	3863086	465187	FL98312	60	15	175	23	stylolitic
						223	25	stylolitic
287	3864318	466279	FL98313	60	25			
			FL98314	60	24			
				58	30			
288	3860682	464565	FL98315	320	16	202	16	stylolitic
289	3859396	464787	FL98316	293	28	266	31	stylolitic
290	3859555	461353	FL98317	70	15			
291	3859642	460704	FL98318	132	16	148	19	stylolitic
				134	16			
292	3859323	460223	FL98319	130	24			
				125	16			
293	3856679	457034	FL98320	25	6	66	18	stylolitic
						6	7	stylolitic
294	3853559	450343	FL98321	320	30	275	40	stylolitic
				300	27			
295	3854003	451239	FL98322	186	4			
				333	5			
296	3854807	451438	FL98323	146	5			
				299	5			
297	3855423	451497	FL98324	312	12			
298	3853893	453613	FL98325	286	9			
				128	3			
299	3853421	453726	FL98326	267	20			
300	3853005	454292	FL98327	321	4	271	11	stylolitic
				292	4			
				16	22			
301	3856273	451685	FL98328	54	20	77	45	stylolitic
302	3856634	452423	FL98329	28	6	352	35	stylolitic
				28	12	3	32	stylolitic
303	3857463	452473	FL98330					
304	3858266	452740	FL98331	321	9	54	46	stylolitic
				287	9	48	20	stylolitic
						59	10	stylolitic
305	3859494	452649	FL98332	32	20			
306	3861226	451767	FL98333	90	6			
				50	4			
307	3861940	449963	FL98334	352	36			
				352	45			
308	3862528	449102	FL98335	346	11			
				2	18			
309	3863331	448247	FL98336	84	6	118	39	stylolitic
310	3863250	447145	FL98337	336	69			

	Coordinates			Bedding		Cleavage		
Outcrop	Northing	Easting	Sample #	Strike	Dip	Strike	Dip	Type of Cleavage
				4	57			
311	3862728	446160	FL98338	100	10	106	24	stylolitic
						82	29	stylolitic
312	3862437	445396	FL98339	72	15	278	26	stylolitic
313	3861900	444029	FL98340	150	3	213	39	stylolitic
				194	10			
				188	25			
314	3861814	442806	FL98341	340	4	137	25	stylolitic
				139	14	128	31	stylolitic
				286	6			
315	3861113	442139	FL98342	344	1			
				128	0			
316	3860626	443075	FL98343	165	1	56	35	stylolitic
						66	24	stylolitic
317	3834593	474294	FL98344	354	35			
				17	26			
318	3848077	492300	FL98345	140	3			
				25	5			
319	3848853	492265	FL98246	69	10			
				123	10			
320	3854248	492445	FL98347	295	24	80	25	stylolitic
						98	16	stylolitic
						95	30	stylolitic
						90	40	stylolitic
321	3854538	491855	FL98348	115	17	296	30	stylolitic
				72	20	252	45	stylolitic
						288	5	stylolitic
322	3855115	491610	FL98349	110	15	276	15	stylolitic
				88	13			
323	3840800	505200	FL98350	260	14			
324	3841068	505357	FL98351	65	10			
				116	7			
325	3841591	508681	FL98352	72	5			
				87	5			
326	3841297	511693	FL98353	59	10			
327	3842260	512394	FL98354	100	35	65	20	stylolitic
				94	28	62	6	stylolitic
328	3840913	512703	FL98355	92	5			
329	3865568	448443	FL98356	213	10			
330	3864907	448676	FL98357	142	15	200	20	stylolitic
				144	7			
331	3865239	448957	FL98358	330	10			
332	3866560	449166	FL98359	148	7	308	37	stylolitic
				290	15	308	33	stylolitic
333	3867889	449674	FL98360	268	6			
334	3869361	450218	FL98361	148	7			
335	3869882	450332	FL98362		horz.			
336	3875068	446218	FL98363	180	6			
			FL98364	140	7			
337	3872516	445626	FL98365	178	8			

Table A-1 Field Data

Outcrop	Coordinates Northing	Easting	Sample #	Bedding Strike	Dip	Cleavage Strike	Dip	Type of Cleavage
338	3871152	445731	FL98366	270	9	344	12	stylolitic
				318	26	27	10	stylolitic
339	3866855	445433	FL98367	62	12			
340	3865355	446835	FL98368	139	11			
341	3837963	471439	FL98369	66	8			
				60	7			
342	3841124	471423	FL98370	27	9			
				142	8			
				153	8			
343	3841679	474531	FL98371	56	20			
			FL98372					
344	3842015	517144	FL98001	28	12	245	36	stylolitic
			FL98002	61	29	248	24	stylolitic
			FL98373					
			FL98374					
345	3840987	521374	FL98375	100	5			
346	3840479	521226	FL98376	88	18	310	20	stylolitic
						304	27	stylolitic
347	3841713	521086	FL98377	86	7			
348	3842584	523766	FL98378	108	20			
349	3840672	524593	FL98379	84	7	120	28	stylolitic
						114	42	stylolitic
350	3841779	525203	FL98380	288	16			
351	3842950	525500	FL98381	325	14	32	33	stylolitic
						29	25	stylolitic
352	3846981	527531	FL98382	45	12	110	26	stylolitic
			FL98383	112	10			
353	3848096	527100	FL98384	145	3			
354	3849416	526365	FL98385	130	40			
			FL98386	216	36			
				206	36			
				208	40			
355	3848136	526481	FL98387	219	10			
356	3847894	525957	FL98388	54	20			
357	3847663	525144	FL98389	300	4			
				120	8			
358	3847867	524444	FL98390	25	13	162	14	stylolitic
						118	27	stylolitic
						74	26	stylolitic
359	3847652	522101	FL98391	20	5			
				14	20			
1*	3844700	500540	CY9701	345	17	180	20	stylolitic
2*	3844950	499550	CY9702	180	12			
3*	3847180	495020	CY9703	112	16			
4*	3846875	492570	CY9704					
5*	3850500	492425	CY9705					
6*	3851450	492500	CY9706	152	12			
7*	3855025	492150	CY9707	60	17			
8*	3856300	492320	CY9708	84	18	75	20	stylolitic
9*	3856590	487900	CY9709	90	24			

Table A-1 Field Data

	Coordinates			Bedding		Cleavage		
Outcrop	Northing	Easting	Sample #	Strike	Dip	Strike	Dip	Type of Cleavage
			CY9710	102	66			
10*	3854020	488020	CY9711	120	34	290	16	stylolitic
11*	3854550	486580	CY9712	72	10			
			CY9713	291	86			
12*	3853200	484775	CY9714	60	15			
13*	3851075	484150	CY9715	58	10			
14*	3837700	491800	CY9721	115	8			
15*	3840000	485850	CY9722	115	5			
16*	3836525	466600	CY9723	285	15			
17*	3836800	466100	CY9724	118	10			
18*	3840525	460850	CY9725	120	80			
			CY9726	85	52			
			CY9727A	130	28			
19*	3853520	450600	CY9727B	298	40			
20*	3855825	451600	CY9728	300	10			
21*	3857450	452620	CY9729	340	18			
22*	3859400	452810	CY9730	25	16			
			CY9731					
23*	3864700	447175	CY9732	165	9			
34*	3879650	508975	CY9748	111	65			
35*	3878700	510000	CY9749	310	28			
			CY9750	90	10			
36*	3878200	517900	CY9751		horz.			
37*	3843100	499050	CY9752	88	8			
43*	3845650	507600	CY9766	104	15	316	70	stylolitic

Appendix B

Anisotropy of Magnetic Susceptibility Data
(AMS)

Table B-1 AMS Data

		Minimum		Intermediate		Maximum				
Outcrop	Sample #	Decln.	Incln.	Decln.	Incln.	Decln.	Incln.	Kmean	Pj	Tj
4	FL98003A	113.9	60.3	356.6	14.6	259.6	25.2	-5	1.214	-0.417
	FL98003B	148.6	73.4	37.5	6.1	305.8	15.4	0	4.993	0.1
	FL98003C	293.7	30.4	40.4	26.1	163.2	47.9	1	2.323	0.855
5	FL98004A	234.7	67.9	139.9	1.9	49.1	22	4	1.303	0.502
	FL98005A	242.8	79.5	344.8	2.2	75.2	10.3	33	1.04	-0.377
	FL98005B	45.1	67.3	179	16.2	273.6	15.5	46	1.035	0.258
	FL98005C	62.7	36.4	207.3	47.9	318.6	18.2	36	1.028	-0.194
	FL98005D	146.7	81	39.4	2.7	308.9	8.6	35	1.019	-0.139
6	FL98006A	215.5	70	73.3	16	339.9	11.6	4	1.177	0.46
	FL98006B	346.5	53.9	118	25.8	220.1	23.4	7	1.167	0.042
7	FL98007B	184.6	79.6	32.3	9.2	301.5	4.7	2	1.602	0.815
	FL98007C	227.5	60.5	357.4	20	95.3	20.8	1	2.864	0.576
8	FL98008A	99.4	77.2	274.6	12.7	4.8	1	2	1.686	0.483
	FL98008B	283.4	55.6	31.8	12.2	129.5	31.6	2	2.101	0.241
	FL98008C	144.4	76.1	344.3	13.1	253.3	4.6	0	1.387	0.401
	FL98009A	223.9	53.2	90.6	27.1	348.1	22.8	0	4.356	0.415
9	FL98010A	207.3	50.1	33.7	39.8	301.1	3.1	6	1.057	0.995
	FL98010B	327.1	84.1	191.2	4.3	100.9	4.1	11	1.065	0.158
10A	FL98011A	349.2	37.8	203.1	46.9	93.4	17.6	-3	1.392	-0.547
	FL98011B	23.2	7.5	141.9	74.7	291.4	13.32	-3	1.209	0.69
	FL98012A	95.2	78.1	242.9	10.1	334.1	6.2	0	2.362	-0.043
10B	FL98013A	34.2	66.8	164.6	15.5	259.4	16.8	0	16.228	0.734
	FL98013B	40.4	85.6	160.7	2.2	250.9	3.8	-1	1.554	-0.415
	FL98013C	214.8	63.7	92.4	14.8	356.5	21.3	-1	1.387	0.401
11	FL98014A	206.3	64.5	32.9	25.4	301.7	2.5	4	1.13	0.03
	FL98014B	220.5	39.2	97	34.1	341.6	32.3	6	1.084	0.219
12	FL98015A	334	48.4	123	37.2	225.4	15.8	5	1.186	-0.296
	FL98015B	82.2	46.2	321.1	26.4	213	32.1	10	1.077	0.267
13	FL98016A	41	25.8	185.3	59.2	303.2	15.6	16	1.099	-0.586
	FL98016B	99	79.4	271.4	10.5	1.6	1.4	18	1.091	-0.724
	FL98017A	203.2	65.8	71.1	16.8	335.8	16.9	8	1.131	0.03
	FL98017B	119.5	42.1	329.9	43.6	224.3	15.8	4	1.146	0.362
14	FL98018A	180	71.6	36.3	15	303.5	10.4	3	1.403	-0.62
	FL98018B	243.6	18.4	29.6	68.2	149.8	11.4	0	1.575	0.112
	FL98019A	71.6	19.1	283.6	67.8	165.5	10.9	4	1.655	0.22
	FL98019B	254.7	30.8	97.2	57.1	350.9	10.3	3	1.262	-0.516
15	FL98020A	270	71.6	21.4	6.9	113.6	17	68	1.02	-0.536
	FL98020B	37.9	87.4	268.3	1.6	178.2	2	84	1.098	-0.564
16	FL98021A	339.3	28.8	229.2	32.1	101.6	44.2	-12	1.107	-0.052
	FL98021B	119.9	68.8	294.8	21.1	25.5	1.7	-12	1.055	0.673
17	FL98022A	278.5	29.2	21.8	22.5	143.4	51.7	-8	1.048	0.011
	FL98022B	238.6	58.3	90.6	27.7	352.9	14.3	-8	1.084	0.0162
18	FL98023A	43.8	59.6	159.2	14.1	256.4	26.3	-2	1.319	-0.075
	FL98023B	338.9	63.7	136.6	24.6	230.7	8.8	-9	1.086	-0.705
	FL98023C	146.7	79.8	263.4	4.6	354.1	9.1	-3	1.242	0.054
	FL98024A	74.8	58.7	322.7	12.9	225.7	28	18	1.21	-0.62
	FL98024B	60.3	42.6	265.7	44.5	162.6	13	26	1.092	0.648

		Minimum		Intermediate		Maximum				
Outcrop	Sample #	Decln.	Incln.	Decln.	Incln.	Decln.	Incln.	Kmean	Pj	Tj
	FL98024C	214.1	69.8	353.5	15.6	87.1	12.5	15	1.071	-0.074
19	FL98025A	247.8	60.3	146.3	6.4	52.8	28.8	19	1.065	-0.32
	FL98025B	261.6	83.8	17.7	2.5	107.9	6.4	21	1.034	0.435
	FL98026A	241	83.5	355.1	2.7	85.4	5.9	5	1.216	0.138
	FL98026B	138.7	66.7	243	6.1	335.5	22.4	6	1.206	-0.031
20	FL98027A	82.9	16	187.5	41.4	336.7	44.3	12	1.073	-0.094
	FL98027B	293.7	41.5	27.6	4.5	122.6	48.1	16	1.061	0.214
	FL98027C	240.2	42.3	119.3	29.4	7.3	33.6	14	1.066	0.126
	FL98027D	276.4	25.8	95.3	64.2	186.2	0.4	13	1.154	-0.23
21	FL98028A	229.4	30.5	102	45.9	338	28.4	-20	1.043	0.754
	FL98028B	254.9	58.2	94	30.4	359	8.6	-18	1.084	0.584
22	FL98029A	82.1	20.2	231.4	66.9	348	10.8	-7	1.13	0.141
	FL98029B	108	5.2	343.1	81	198.7	7.4	-7	1.105	0.167
	FL98029C	152	50.2	306.5	36.9	46.3	12.8	-6	1.126	0.277
	FL98029D	1.6	68.3	213	18.8	119.3	10.5	-7	1.12	-0.224
23	FL98030A	277.1	5.1	25	73.9	185.7	15.2	3	1.245	-0.689
	FL98030B	256.5	40.4	19.1	32.4	133.3	32.8	3	2.037	-0.514
24	FL98031A	165.4	59.7	23	24.8	285.3	16.2	5	1.146	0.175
	FL98031B	87.2	41.2	308.9	40.5	198.3	22.4	2	1.635	-0.046
25	FL98032A	318.5	68.9	87.4	13.6	181.3	15.8	13	1.118	0.357
	FL98032B	89.2	68.7	215.8	13.1	309.8	16.5	16	1.087	0.552
26	FL98033A	319.3	61.7	111	25.4	206.7	11.7	4	1.189	-0.394
	FL98033B	78.8	65.1	266.2	24.7	174.9	2.8	1	3.574	0.288
	FL98033C	307.3	79.2	92.3	8.9	183.3	6.1	-1	9.656	0.41
27	FL98034A	309.4	46	131.1	44	40.3	0.9	11	1.157	0.16
	FL98034B	125	77.3	287.6	12.1	18.3	3.7	13	1.092	-0.812
28	FL98035A	293.3	59.1	63.2	21	162	21.6	14	1.035	-0.192
	FL98035D	31	15.2	265	65.2	126.4	19.1	17	1.124	-0.479
	FL98035B	269.1	2.6	5.6	67.8	178	22	14	1.116	-0.225
	FL98035C	53.5	61.6	236.1	28.3	145.5	1.1	21	1.052	0.804
	FL98036A	332.6	12.1	75.8	46.7	232	40.7	10	1.092	-0.09
	FL98036B	26.9	76.5	208.6	13.5	118.5	0.4	14	1.062	0.756
29	FL98037A	87.6	52.6	194.8	12.8	293.8	34.4	-15	1.098	-0.044
	FL98037B	167.7	5.8	69.5	54.8	261.7	34.6	-17	1.034	0.34
	FL98037C	289.4	55.8	86.9	32.1	183.6	10.5	-16	4.057	-0.098
30	FL98038A	54.7	5.7	305.3	73.4	146.3	15.5	8	1.116	-0.537
	FL98038B	174.3	69.9	288.4	8.5	21.2	18.1	8	1.185	0.183
31	FL98039A	85.4	71.3	263.7	15.9	353.9	0.6	8	1.121	-0.537
	FL98039B	71	15.1	228.9	73.7	339.4	5.8	5	1.231	-0.225
32	FL98040A	143.3	78.8	250.5	3.3	341.1	10.7	4	1.204	-0.065
	FL98040B	354.2	68.5	219	15.6	124.9	14.4	7	1.085	0.677
33	FL98041A	337.4	3.4	72	53.2	244.8	36.6	-12	1.1	0.023
	FL98041B	49	45.3	218.3	44.2	313.6	5.4	-12	1.059	0.156
34	FL98042A	200	11.9	33.7	77.8	291.5	2.6	-13	1.114	-0.702
	FL98042B	73.3	46.3	281.4	40.2	178.8	14.4	-6	1.096	0.023
	FL98042C	176.4	74.9	31.5	12.5	299.6	8.4	3	1.314	-0.134
35	FL98043A	92.6	79.2	262.7	10.6	353	1.8	156	1.036	0.524

Table B-1 AMS Data

		Minimum		Intermediate		Maximum				
Outcrop	Sample #	Decln.	Incln.	Decln.	Incln.	Decln.	Incln.	Kmean	Pj	Tj
	FL98043B	290.3	73.5	61.4	11	153.8	12.1	175	1.032	0.15
36	FL98044A	167.8	87.6	265.6	0.3	355.6	2.4	217	1.023	0.784
	FL98044B	51.2	61.3	314.2	3.8	222.2	28.4	179	1.059	-0.531
37	FL98045A	140.2	25.3	289.7	61.3	44.1	12.7	19	1.123	-0.102
	FL98045B	90	59	226.3	23.4	324.9	19	17	1.04	-0.134
38	FL98046A	95.6	65.3	229.9	17.8	325.4	16.5	20	1.041	-0.241
	FL98046B	307.4	68.3	104.4	20.1	197.2	7.8	21	1.059	0.51
	FL98046C	14.6	80.8	230.5	7.5	139.8	5.3	26	1.075	0.279
39	FL98047A	74.3	41.7	231.2	45.9	333.6	11.7	17	1.07	0.348
	FL98047B	229.9	69.6	69.2	19.3	337	6.2	19	1.068	0.511
	FL98047C	200.9	79.4	326.8	6.2	57.7	8.5	22	1.047	0.606
	FL98047D	121.3	57.8	252.2	22.4	351.7	21.9	18	1.062	-0.076
40	FL98048A	341.1	80.3	88.3	2.9	178.7	9.3	31	1.065	0.485
	FL98048B	305.1	82.6	159.1	6.1	68.7	4.1	33	1.052	0.509
	FL98049A	71.8	53.9	217.2	30.9	317.5	16.7	35	1.059	-0.389
41	FL98050A	20.2	83.9	252.1	3.8	161.8	4.8	-5	1.167	0.148
	FL98050B	327.1	65	77.9	9.4	171.9	23	-3	1.174	-0.646
42	FL98051A	186.3	5.3	93.3	29.7	285.4	59.7	-6	1.138	-0.477
	FL98051B	134.6	60.6	277.2	24.1	14.4	15.8	-5	1.206	-0.418
	FL98051C	323.3	41.3	157	47.9	59.4	6.8	-5	1.249	0.322
43	FL98052A	20.8	12.4	148.4	70.1	287.4	15.3	34	1.037	0.506
	FL98052B	40	15.8	219	74.2	309.9	0.3	34	1.037	-0.662
	FL98052C	44.3	74.7	182.1	11.4	274.2	10	32	1.021	-0.138
	FL98053A	34	64.1	239.9	23.6	145.5	10.1	-5	1.17	-0.073
	FL98053B	105.3	35.8	273.6	53.6	11.2	5.6	-4	1.291	0.153
44	FL98054A	222.4	5.7	321.1	56.7	128.7	32.7	44	1.055	-0.238
	FL98054B	222.1	57.1	97.1	20.3	357.3	24.7	25	1.063	0.015
45	FL98055A	55.2	38.8	241.3	51	147.6	3	13	1.0037	-0.192
	FL98055B	243.2	73.5	74.1	16.2	343.2	3	16	1.071	0.467
46	FL98056A	229.5	75	53.8	14.9	323.5	1.1	12	1.105	-0.052
	FL98056B	334.1	79	219.8	4.6	129	10	10	1.06	-0.659
	FL98056D	133.5	68.8	283.3	18.5	16.6	9.9	-6	1.098	0.023
	FL98057A	288.1	78.7	74.2	9.5	165.3	6.2	13	1.101	-0.208
	FL98057B	48.7	56.7	230.9	33.3	140.3	1	16	1.098	-0.178
	FL98057C	196.7	55.4	70.3	22.3	329.3	25	19	1.037	0.151
47	FL98058A	117.3	85.9	273.3	3.8	3.5	1.7	23	1.051	0.012
	FL98058B	257.4	63.4	65	26.1	157.5	5	21	1.053	-0.078
	FL98058C	264.4	79.7	93.8	10.2	3.5	1.6	20	1.092	0.242
48	FL98059A	286.4	85.9	69.6	3.3	159.7	2.5	26	1.075	0.885
	FL98059B	199.2	61.6	10.5	28.1	102.4	3.7	22	1.042	0.342
49	FL98060A	251.6	82.5	71.6	7.5	153.2	8.8	11	1.106	0.808
	FL98060B	306	60	136	29.6	43.5	4.3	14	1.108	0.092
50	FL98061B	161.4	75.9	14.3	11.9	282.7	7.4	-7	1.56	-0.701
51	FL98062A	248.8	74.7	75.5	15.2	345	1.7	4	1.328	0.233
	FL98062B	283.8	60	92.8	29.5	185.5	4.7	4	1.189	-0.468
52	FL98063A	209.1	25.2	64.5	60	306.5	15.2	5	1.207	-0.571
	FL98063B	345.8	70.9	93.1	5.9	185	18.1	4	1.237	0.378

Table B-1 AMS Data

		Minimum		Intermediate		Maximum				
Outcrop	Sample #	Decln.	Incln.	Decln.	Incln.	Decln.	Incln.	Kmean	Pj	Tj
53	FL98064A	54.9	44.6	258.2	43	156.9	11.9	-14	1.215	-0.76
	FL98064B	78.5	44.4	270	45	174.2	5.8	-12	1.058	-0.129
	FL98064C	317.8	53.3	93.5	28.1	195.7	21.6	-12	1.087	-0.383
54	FL98065A	146.1	61	294.7	25.4	31.1	13.2	47	1.061	-0.764
	FL98065B	201.6	54.8	54.3	30.7	314.8	15.5	48	1.035	0.506
55	FL98066A	23.7	80.1	256.5	6	165.6	7.8	0	10.747	0
	FL98066B	185.6	83.1	295.9	2.4	26.2	6.4	0	5.372	0.563
56	GBFL001A	295.1	42.9	72.1	38.2	181.7	23.1	-11	1.083	0.757
	GBFL001B	278.8	16.7	65.4	70.2	185.6	10.3	-10	1.137	0.108
	GBFL001C	282.2	31.2	116.8	58	16.2	6.6	-11	1.134	0.707
57	GBFL002A	114.1	62.4	280.1	26.9	13	5.7	10	1.118	0.298
	GBFL002B	176.5	81.6	300.9	4.8	31.5	6.9	7	1.476	0.745
	GBFL002C	222.1	60	122.6	5.4	29.5	29.4	8	1.143	0.479
58	GBFL003A	96	83.4	353.3	1.4	263.2	6.4	22	1.065	0.015
	GBFL003C	288.4	65.1	48.9	13.2	144	20.7	25	1.126	-0.376
	GBFL003D	283.7	74.7	95.7	15.2	186.3	2	21	1.074	0.217
59	GBFL004A	30.2	78.3	287.1	2.7	196.5	11.4	7	1.208	-0.02
	GBFL004B	147.8	62.3	270.3	15.7	6.9	22.2	9	1.174	0.106
	GBFL004C	100.2	82.1	265	7.6	355.3	2	6	1.212	0.275
60	GBFL005A	118.7	71	305	18.9	214.3	1.9	11	1.151	0.492
	GBFL005B	32.4	82.2	168.8	5.7	259.4	5.4	15	1.168	0.91
	GBFL005C	92.7	72.8	284	16.1	193	3.1	13	1.136	0.642
61	GBFL006A	241.9	76.1	71	13.7	340.5	2.1	16	1.12	-0.344
	GBFL006B	307.6	74.8	114.2	14.8	205.1	3.4	14	1.119	0.275
62	GBFL007A	233.2	78.3	89.1	9.6	357.9	6.8	16	1.108	0.518
	GBFL007B	126.6	60.1	274.2	8.4	4.9	5.3	19	1.06	0.465
63	GBFL008A	270	71.6	36.2	11.1	129.1	14.5	-5	1.133	-0.404
	GBFL008B	298.7	63.2	81.7	21.9	177.7	14.6	-4	1.41	0.452
	GBFL008C	140.3	50.2	293	36.5	33.4	13.6	-4	1.212	-0.205
64	GBFL009A	17.3	81.5	247.1	5.5	156.5	6.4	-3	1.464	0.094
65	FL98067A	145.2	24.1	247.1	24.9	17.1	54.1	4	1.306	-0.025
	FL98067B	126.4	15.7	19.5	45.9	229.9	39.8	6	1.297	-0.451
66	FL98068A	37.9	57.9	174.7	24.6	274	19.3	-6	1.247	0.47
	FL98068B	116.3	74.9	282.7	14.7	13.6	3.4	-7	1.315	0.789
67	FL98069A	235.8	62	142.5	1.7	51.6	27.9	11	1.073	0.512
	FL98069B	107.5	84.6	267.1	5.1	357.2	1.9	5	1.239	-0.286
68	FL98070A	198.4	85.1	287.8	3.3	18.4	4.9	7	1.201	0.187
	FL98070B	141.7	75.4	285.5	11.9	17.3	8.4	9	1.256	0.444
69	FL98071A	119.8	61.1	302.9	28.8	212.2	1.3	7	1.174	0.528
	FL98071B	47.5	81.5	306.8	1.6	216.6	8.3	16	1.097	0.586
	FL98071C	264.9	30.6	104.8	57.8	0.2	9	2	1.505	0.189
70	FL98072A	192.6	85.8	51.7	3.2	321.5	2.6	9	1.136	0.36
	FL98072B	72.8	61.9	239.6	27.5	332.4	5.5	9	1.083	0.444
	FL98072C	62.5	74.8	252.6	15	161.9	2.5	7	1.15	-0.241
	FL98072D	53.8	25.9	265.8	60.2	150.6	13.7	7	1.125	0.14
71	FL98073A	172.8	20.5	26.6	65.8	267.5	12.3	-20	1.086	0.312
	FL98073B	242.9	61.7	141.5	6	48.4	27.5	-3	1.591	0.305

Table B-1 AMS Data

		Minimum		Intermediate		Maximum				
Outcrop	Sample #	Decln.	Incln.	Decln.	Incln.	Decln.	Incln.	Kmean	Pj	Tj
	FL98073C	88.1	15.7	336.5	52.6	188.6	32.9	-8	1.092	-0.705
	FL98073D	356.8	86.3	100.1	0.8	190.1	3.6	-17	1.226	-0.447
72	FL98074A	149.5	61.6	318.5	28	51	4.6	-6	1.274	-0.589
	FL98074B	92.1	76.9	222.7	8.6	314.2	9.8	-10	1.105	0.42
73	FL98075A	115.1	66.8	290.4	23.1	21.2	1.7	-2	1.735	-0.392
	FL98075B	245.2	79.6	87.2	9.7	356.5	3.8	13	1.124	0.488
74	FL98076A	10.4	7.2	117.6	66.9	277.5	21.9	20	1.032	-0.663
	FL98076B	122.8	84.7	276.5	4.8	6.7	2.3	20	1.041	0.259
75	FL98077A	90.9	12.6	311.7	73.5	183.3	10.4	-7	1.261	0.656
	FL98077B	52.6	77.7	272.1	9.6	180.8	7.7	-8	1.145	0.303
	FL98078A	242.6	22.1	65.9	67.9	333.1	1.2	0	20.174	0.575
	FL98078B	125.3	73.2	15.2	5.9	283.5	15.7	-2	1.763	0.392
76	FL98079A	102.3	78.2	203.3	2.3	293.8	11.6	10	1.06	0.014
	FL98079B	54.8	42.4	232.4	47.6	323.7	1.2	11	1.272	0.285
	FL98079C	142.8	65.7	283.3	19.2	18.4	14.3	10	1.05	0.607
77	FL98080A	334.1	74.1	242.3	0.5	152.2	15.9	-22	1.027	-0.328
	FL98080B	73.1	48.3	273.9	39.8	175.1	10.5	-20	1.179	0.408
78	FL98081A	208	56.3	91.5	16.5	352.3	28.4	24	1.43	-0.18
	FL98081B	334.7	63.4	228.7	7.8	135	25.2	-2	2.474	0.268
79	FL98082A	166.1	72	313.6	15.3	46.2	9.2	23	1.14	0.128
	FL98082B	129.4	66.4	258.7	15.5	353.7	17.4	26	1.068	0.308
	FL98082C	303.7	81.6	24.3	0	123.7	8.4	21	1.103	0.997
80	FL98083A	102.4	81.6	265	8	355.4	2.5	10	1.212	0.095
	FL98083B	230.8	86.2	103.9	2.3	13.8	3	15	1.13	0.663
81	FL98084A	55.7	79.6	283.3	7.1	192.3	7.6	33	1.043	0.437
	FL98084B	305.6	80.4	43.4	1.3	133.6	9.6	44	1.056	0.659
	FL98084C	7.3	80.3	105.5	1.4	195.7	9.6	34	1.052	0.755
82	FL98085A	28.9	65.3	211.9	24.6	121.4	1.1	13	1.123	0.153
	FL98085B	212.2	84.9	327.9	2.2	58.1	4.6	20	1.065	0.092
83	FL98086A	252.3	80.9	73.7	9.1	343.7	0.2	15	1.161	0.337
	FL98086B	235	76	32.2	12.9	123.4	5.2	20	1.051	0.41
84	GBFL010A	241.2	55.3	100.3	28.3	360	18.4	6	1.145	0.144
	GBFL010B	37	80.4	257	7.4	166.2	6.1	12	1.085	0.02
	GBFL010C	335.7	77.9	86.6	4.4	177.5	11.3	10	1.128	0.521
85	FL98087A	225.1	36	341.9	31.9	100.8	37.8	-15	2.24	-0.308
	FL98087B	39.9	63.8	230.4	25.8	138.4	4.2	-17	1.077	-0.657
86	FL98088A	92.7	51.4	275.9	38.5	184.7	1.6	-15	1.227	0.503
	FL98088B	66.5	40.8	303.4	32.3	189.8	32.4	-13	1.078	0.217
87	FL98089A	141.7	48.4	299.8	39.4	39	11	-8	1.356	0.038
	FL98089B	141.3	54.2	355.9	30.7	255.7	16.6	-11	1.073	-0.234
88	FL98090A	78.9	76.3	286.6	12.1	195.3	6.2	4	1.456	0.026
	FL98090B	262.4	65.1	106.4	23	12.5	9.1	2	1.529	-0.097
	FL98090C	270	71.6	94.2	18.4	3.8	1.3	12	1.174	-0.882
	FL98090D	172.5	39.4	329.4	48.2	72.8	11.7	11	1.23	-0.55
89	FL98091A	20.8	73.6	114.9	1.2	205.3	16.3	10	1.109	-0.066
	FL98091B	238.1	57.3	94.3	27.4	355.5	16.5	10	1.138	-0.516
	FL98091C	274.6	66.3	82.6	23.3	174.5	4.4	9	1.357	-0.335

Table B-1 AMS Data

		Minimum		Intermediate		Maximum				
Outcrop	Sample #	Decln.	Incln.	Decln.	Incln.	Decln.	Incln.	Kmean	Pj	Tj
90	FL98092B	251.1	77.9	83.1	11.9	352.6	2.4	1	2.688	-0.296
91	FL98093A	160.1	81.3	289.8	5.6	20.5	6.7	16	1.076	0.018
	FL98093B	234.2	60.4	121	12.6	24.7	26.3	14	1.112	0.726
	FL98093C	45.8	65.9	272.2	17.1	177	16.4	15	1.08	0.019
	FL98093D	250.7	72.3	49.2	17.1	141.1	6.1	12	1.106	-0.052
92	FL98094A	107.7	55.5	242.3	25.8	343.1	21.3	3	1.7	0.006
	FL98094B	130.2	43.4	235.1	15.2	339.6	42.6	3	1.559	0.759
	FL98094C	316.2	83	106	6.1	196.4	3.5	6	1.293	-0.19
93	FL98095A	302	52.6	97	34.7	195.6	12.2	12	1.055	-0.13
	FL98095B	355.1	10	238.9	68.3	88.6	19.1	8	1.577	0.284
	FL98095C	174.2	71.5	267.8	1.2	358.3	18.4	11	1.234	-0.287
94	FL98096A	107.4	22.5	326.5	62	204.2	15.9	9	1.123	-0.62
	FL98096B	327.2	36	141.3	53.9	235.1	2.8	9	1.265	-0.89
95	FL98097A	249.8	72.8	109	13.5	16.4	10.5	17	1.046	-0.24
	FL98097B	115.9	57.3	321.7	30	224.8	11.7	20	1.12	-0.527
	FL98097C	102.8	61.6	248.7	24.1	345.1	14.1	22	1.034	0.718
	FL98097D	224.2	60	26.9	28.9	121	7.5	18	1.063	-0.443
96	FL98098A	282.4	54	126.6	33.6	28.8	11.6	39	1.082	0.18
	FL98098B	169.7	47.7	356.3	42.1	263.3	3.3	57	1.039	-0.264
97	FL98099A	262.5	72.2	123.8	13.6	31	11.3	18	1.039	0.152
	FL98099B	135.1	10.3	22.6	64.5	229.6	23.1	3	1.772	-0.307
98	FL98100A	106.9	70.7	272	18.7	3.5	4.6	47	1.038	0.231
	FL98100B	254	29.3	102.1	57.6	351.3	12.7	35	1.025	-0.105
99	FL98101A	206.5	48.4	85.9	24.3	339.8	31.4	-14	1.092	0.824
	FL98101B	250.4	53.9	103.9	31.3	3.8	16.1	-13	1.107	0.405
100	FL98102A	302.2	20.9	188.6	46.3	48.5	36.3	-18	1.132	0.074
	FL98102B	128.9	31.9	14.7	33.3	250.8	40.3	-18	1.063	-0.443
	FL98102C	269.4	69.4	73.7	19.9	165.6	5.1	-18	1.072	-0.215
101	FL98103A	168.6	26.9	49.8	43.5	279	34.6	6	1.115	-0.117
	FL98103B	123.6	34.4	309	55.4	215.3	2.5	2	1.556	-0.477
	FL98103C	253.4	52.7	91.4	36	355	8.7	2	2.521	0.851
102	FL98104A	131.3	4.2	41	4.1	267.2	84.1	-8	1.192	-0.023
	FL98104B	194.3	64.5	333.2	19.7	68.8	15.4	-9	1.044	0.507
	FL98104C	267.2	59.2	118	27.1	21	13.5	-8	1.067	-0.59
	FL98104D	297.5	22.1	139.1	66.4	30.7	7.8	-8	1.171	0.564
103	FL98105A	279.2	7.6	69.4	81.3	188.7	4.3	-12	1.064	0.015
	FL98105B	48	23.7	241.2	65.7	140.2	4.9	-14	1.108	0.092
104	FL98106A	80.7	72.7	259.5	17.3	349.6	0.3	-7	1.272	0.112
	FL98106B	144.8	54.1	335.5	35.4	241.9	5.1	-8	1.182	-0.395
105	FL98107A	100.2	55.3	263.7	33.5	358.9	7.8	-9	1.144	0.523
	FL98107B	175.4	76.7	316.1	10.6	49.6	7.9	-4	1.425	0.559
106	FL98108A	214.6	56.8	116.2	5.4	22.7	32.6	25	1.068	0.075
	FL98108B	343.7	85.4	242.2	0.9	152.2	4.6	42	1.078	0.611
107	FL98109A	105.8	34.4	284.2	55.6	15.3	0.7	-13	1.101	0.253
	FL98109B	276.3	33.5	124.3	53.1	15.6	13.6	-14	1.058	-0.2237
108	FL98110A	46.4	30.8	297.4	28.6	173.7	45.5	-11	1.188	0.095
	FL98110B	91	53.3	231.5	29.9	333	19.3	-10	1.268	-0.635

Table B-1 AMS Data

		Minimum		Intermediate		Maximum				
Outcrop	**Sample #**	**Decln.**	**Incln.**	**Decln.**	**Incln.**	**Decln.**	**Incln.**	**Kmean**	**Pj**	**Tj**
	FL98111A	114.2	46.2	297.9	43.7	206.1	1.9	-3	1.219	0.375
	FL98111B	325.3	49.3	119.8	37.9	220	12.9	-2	9.128	0.634
109	FL98113A	316.4	36.3	149.5	52.9	51.1	6.4	-11	2.531	-0.85
	FL98113B	120.2	68.2	313.8	21.2	222	4.7	-7	1.167	-0.299
110	FL98114A	143.5	84.8	244.7	1	334.8	5.1	16	1.28	0.849
	FL98114B	288.5	78.8	43.6	4.8	134.4	10.1	16	1.1	-0.228
111	FL98115A	100.6	50.9	279.9	39.1	10.2	0.3	2	1.392	-0.029
	FL98115B	66.8	57.6	225.8	30.6	321.5	9.5	4	1.232	0.052
	FL98115C	236.9	72.6	6.9	11.4	99.6	13	3	2.788	0.338
	FL98115D	246.6	80.5	77.1	9.4	346.8	1.7	4	1.484	-0.281
112	FL98116A	177	36.5	50.3	38.9	292.4	30.1	8	1.49	0.666
	FL98116B	232.5	59.8	19.9	26.1	116.9	14.1	6	1.226	-0.093
	FL98116C	9.3	79.9	188.1	10.1	278.2	0.2	5	2.056	0.803
113	FL98117A	233.9	67.6	355.8	12.3	90	18.4	5	1.2	0.372
	FL98117B	41.3	55.3	132.4	0.8	222.9	34.7	6	1.556	-0.591
114	FL98118A	275.2	9.1	120.4	80	5.8	4.2	19	1.08	-0.452
	FL98118B	233.5	80.8	23.5	8	114.2	4.5	22	1.224	0.116
	FL98118C	265.7	48.2	39.9	32	146	24	17	1.125	-0.274
115	FL98119A	198.4	52.4	113.3	5.1	18.4	37.6	15	1.034	-0.595
	FL98119B	280.7	67.2	39.7	11.5	133.7	19.4	17	1.126	-0.016
	FL98119C	264.8	53.1	37.8	36.9	356.7	1.5	14	1.075	0.414
116	FL98120A	198.9	72.5	53.1	14.6	320.7	9.4	2	13.362	0.503
	FL98120B	241.2	7.4	15.8	79.6	150.3	7.4	1	10.555	0.334
117	FL98121A	257.7	22.8	90.3	66.7	349.6	4.7	-18	1.235	0.208
	FL98121B	82.1	60.2	258.6	29.8	349.5	1.5	-17	1.03	0.604
	FL98121C	88.9	32.8	257.5	56.7	355.5	5.2	-17	1.076	0.248
	FL98121D	259.4	35	78.3	55.8	169.1	0.9	-17	1.114	0.774
118	FL98122A	90.4	41.3	331.7	28.7	218.8	35.3	-22	1.255	0.617
	FL98122B	130.3	27.1	35.3	9.7	287.4	60.9	-22	1.028	-0.328
	FL98122C	30.9	82.5	265.9	4.3	175.4	6.1	-21	1.053	-0.261
	FL98122D	96.5	54.3	259.8	34.5	355.3	8	-21	1.043	-0.325
119	FL98123A	240.5	44	72	45.4	336.1	5.8	-25	1.231	0.592
	FL98123B	170.6	32.8	70.1	15.8	318.2	52.7	-25	1.02	0.204
	FL98123C	102.5	16.5	241.7	68.6	8.5	13.2	-25	1.041	-0.392
120	FL98124A	12.8	54.2	130.8	18.7	231.7	29.3	2	1.77	0.84
	FL98124B	290.6	55.8	98.7	33.7	192.4	5.5	8	1.138	0.301
	FL98124C	195.2	60.7	60.7	21.5	322.9	19	5	1.615	-0.304
121	FL98125A	265.5	78.1	110.6	10.5	19.7	5	-16	1.057	-0.098
	FL98125B	84.6	77.5	284.4	11.8	193.5	4.1	-18	1.072	0.675
	FL98125C	245.7	5.1	97	84	336	3.1	-15	1.061	-0.321
	FL98125D	8.9	66.4	199.3	23.3	107.7	3.8	-18	1.085	-0.047
122	FL98126A	159.2	1.4	61.8	79.1	249.5	10.8	22	1.038	-0.494
	FL98126B	299.8/	7	46.4	66.8	207	22	38	1.038	0.435
	FL98127A	300.9	67.8	129	23.9	37.8	4.6	-4	1.232	0.795
	FL98127B	153.4	61.8	270.5	13.7	6.8	24.2	-4	1.201	-0.207
	FL98127C	227	67.5	2.9	16.6	97.4	14.8	-4	1.236	-0.52
	FL98127D	66.5	5	186.9	80.1	335.8	8.5	-6	1.277	0.86

		Minimum		Intermediate		Maximum				
Outcrop	Sample #	Decln.	Incln.	Decln.	Incln.	Decln.	Incln.	Kmean	Pj	Tj
123	FL98128A	70.5	45.4	317.2	21.4	210.1	36.9	8	1.103	0.517
	FL98128B	281.4	20	66.3	66	186.7	12.7	9	1.177	0.04
	FL98128C	227.3	51	55.9	38.7	322.5	4.2	10	1.321	-0.175
	FL98129A	271	68	119.5	19.6	26	9.7	-7	1.191	-0.468
	FL98129B	4.7	32.4	248.5	34.9	124.9	38.5	-5	9.052	0.714
	FL98129C	305.3	74.6	176.5	9.8	84.4	11.8	-3	1.262	-0.516
124	FL98130A	149.2	44.7	52.3	6.9	315.5	44.5	-3	1.248	-0.384
	FL98130B	69.8	79.5	230.2	9.9	320.8	3.5	-2	1.382	0.08
125	FL98131A	104.3	1.5	11.8	59.3	195.2	30.7	9	1.051	-0.188
	FL98131B	112.3	48.7	360	18.4	256.3	35.4	9	1.063	0.996
	FL98131C	176.8	51.3	332.7	36.2	71.6	11.9	9	1.104	-0.312
126	FL98132A	196.8	28.2	344.5	57	100.1	15.7	7	1.333	0.393
	FL98132B	213.6	38.6	89.6	35	333.6	32	4	2.129	-0.406
127	FL98133A	109.4	67	323.2	19.4	229	11.9	1	8.283	0.424
	FL98133B	182.4	72.8	299.6	8.1	31.8	15.1	1	6.958	0.104
	FL98134B	10.4	16.9	276.2	13.5	149.4	68.1	-3	1.111	0.026
	FL98134C	336.7	59.1	206.8	21	108	21.6	-2	1.239	-0.149
	FL98134D	249.1	59.1	58.1	30.4	151	4.8	-2	1.455	0.471
128	FL98135B	93.8	68.5	261.1	21	352.8	4.3	13	1.071	0.348
	FL98135C	314.4	53.4	97	30.5	198.2	18.2	16	1.05	0.012
129	FL98136A	113.2	76.4	287.7	13.5	18	1.2	13	1.093	0.352
	FL98136B	10.4	82.7	252.5	3.4	162.2	6.4	15	1.4	0.342
130	FL98137A	331.6	63.6	70.4	4.3	162.5	26	9	1.131	0.3
	FL98137B	82.5	72.9	288.1	15.5	196.1	7	9	1.092	-0.484
	FL98137C	115.1	81.4	260.5	7.1	351.1	4.8	2	1.699	0.217
131	FL98138A	83.1	76.8	273.9	12.9	183.3	2.4	10	1.204	-0.361
	FL98138B	70.7	44.7	228.7	43.1	329.4	11.2	7	1.162	-0.615
	FL98138C	301.2	70.9	83.5	15.3	176.6	11.1	9	1.131	0.653
	FL98139A	337.1	73.5	195.7	13	103.4	10	8	1.096	0.724
	FL98139B	254	75.7	107.2	12	15.5	7.6	8	1.419	-0.23
132	FL98140A	260.4	65.8	142.1	12	47.5	20.7	8	1.089	-0.122
	FL98140B	301.9	55.2	110.2	34.2	204	5.5	5	1.129	-0.113
133	FL98141A	150.3	27.4	56.9	6.6	314.5	61.7	-3	1.218	-0.389
	FL98141B	16.8	80.9	265	3.4	174.5	8.5	-2	1.594	-0.41
	FL98141C	48.7	73.9	251.7	14.8	160.1	6	3	1.401	-0.084
134	FL98142A	33.6	75.8	257.1	10.4	165.4	9.6	24	1.072	-0.042
	FL98142B	93.2	74.7	208.9	6.8	300.5	13.7	31	1.043	0.24
135	FL98143A	125	64.9	252.4	15.9	348	18.9	5	1.185	-0.527
136	FL98144A	43.3	66.3	257	20	162.5	12.1	0	2.207	-0.256
	FL98144B	65.3	76.6	288.1	9.9	196.5	8.9	0	8.826	0.821
137	FL98145A	136.3	57.8	273	24.6	12.3	19.4	0	8.826	0.82
	FL98145B	11.7	70.3	253.1	9.7	160.1	16.9	-1	1.735	0.323
	FL98146A	158.2	69.6	253.7	2.1	344.5	20.3	-1	2.028	0.256
	FL98146B	193.2	60.4	304.5	11.7	40.5	26.8	-2	2.629	0.934
138	FL98147A	356.9	65	101.1	6.5	194.1	24	21	1.053	-0.078
	FL98147B	184.7	66.9	289.8	6.3	22.4	22.2	18	1.046	0.508
	FL98147C	270	71.6	56.3	15.5	149	9.7	15	1.075	0.108

		Minimum		Intermediate		Maximum				
Outcrop	Sample #	Decln.	Incln.	Decln.	Incln.	Decln.	Incln.	Kmean	Pj	Tj
	FL98147D	212.7	74.7	48.8	14.8	317.7	4.1	18	1.093	-0.484
139	FL98148A	316.1	38.9	105.5	46.9	213	15.7	12	1.091	-0.438
	FL98148B	102.3	38.6	342.8	31.6	226.9	35.4	16	1.097	-0.178
	FL98148C	243	76.2	61.6	13.8	151.6	0.3	15	1.134	0.496
	FL98148D	331.2	81.2	138.6	8.6	228.9	1.9	14	1.1	0.023
140	FL98149A	50.2	68.7	279.2	14.3	185.1	15.4	23	1.039	0.12
	FL98149B	303.7	84.6	42.1	0.8	132.2	5.4	26	1.347	0.437
	FL98149C	331.8	83.9	94.4	3.3	184.7	5.1	33	1.037	0.341
	FL98149D	335.1	68.8	187.8	18.1	94.3	10.7	29	1.067	0.566
141	FL98150A	307.4	41.3	188.9	28.5	76.2	35.5	-31	1.029	0.339
	FL98150B	312.5	11.9	217.9	20.8	70.5	65.8	-30	1.061	0.878
	FL98150C	200.2	44.4	105.5	4.8	10.7	45.2	-31	1.019	0.337
	FL98150D	206.4	49.8	336.7	28.7	81.9	25.6	-31	1.022	0.148
142	FL98151A	241.2	67	333.1	0.8	63.5	23	12	1.174	0.237
	FL98151B	70.8	75.1	297.1	10.4	205.2	10.6	9	1.282	0.584
	FL98151C	310.3	79.2	119.9	10.7	210.3	1.9	12	1.116	0.407
143	FL98152A	11.2	76.7	246.4	7.7	154.9	10.8	39	1.043	0.631
	FL98152B	195.6	86.7	71.7	1.9	341.7	2.8	32	1.047	-0.056
144	FL98153A	78.5	71.6	271.6	18	180.3	3.9	5	1.249	-0.604
	FL98153B	163.5	82.6	49.4	3	319	6.6	3	1.395	0.999
	FL98153C	272.6	6	22.7	73.1	180.9	15.7	6	1.328	-0.478
	FL98153D	306.9	71	75.6	12.2	168.7	14.4	3	1.393	-0.009
145	FL98154A	201.8	76.7	64.6	9.8	333.1	8.8	16	1.089	-0.122
	FL98154B	232.2	77.1	31.3	12.1	122.3	4.4	29	1.055	0.606
	FL98154C	264.9	63.4	135.3	17.7	38.9	19.2	15	1.113	0.151
	FL98154D	235.1	66.7	125.3	8.3	32	21.6	29	1.117	-0.352
	FL98155A	60.6	43.5	158.5	8.2	256.9	45.3	0	2.317	0.38
	FL98155B	285.1	79.3	47.4	5.8	138.3	9	0	19.358	0.474
	FL98155D	176.2	30.3	327.1	55.6	77.9	13.6	0	3.879	-0.214
	FL98156A	137.8	71.5	33.1	4.8	301.6	17.8	14	1.095	0.678
	FL98156B	328.8	70.9	186.5	15.3	93.4	11.1	16	1.075	0.646
	FL98156C	355.4	66.6	96.1	4.6	188	22.8	13	1.107	0.308
	FL98156D	301.1	67.9	50.4	7.7	143.3	20.6	16	1.06	0.656
146	FL98157A	290.2	71.5	99.1	18.2	190.2	3.3	27	1.068	0.237
	FL98157B	108.4	43.5	347.9	28.2	237.1	33.4	23	1.027	-0.664
147	FL98158A	93.6	84.6	280.4	5.3	190.4	0.6	38	1.032	0.34
	FL98158B	132.7	84.4	297.2	5.4	27.3	1.5	39	1.034	0.835
	FL98159A	160	72.8	274	7.2	6	15.5	35	1.019	0.147
	FL98159B	91.6	87.4	288.8	2.5	198.8	0.8	37	1.176	0.826
148	FL98160A	94.2	76.4	245.4	11.9	336.7	6.4	25	1.076	0.07
	FL98160B	230.8	78.9	90.2	8.6	359.1	6.9	25	1.085	0.162
	FL98161A	322.4	82.4	88.6	4.5	179.1	6.1	26	1.056	0.298
	FL98161B	237.9	32.4	5.1	43.6	127.2	29.2	27	1.119	0.226
149	FL98162A	227.3	50.5	16	35.2	117.4	15.7	-9	1.043	0.101
150B	FL98165A	239.3	71.5	93.2	15.5	0.4	9.8	94	1.022	-0.043
151	FL98166A	3.3	74.8	243.6	7.6	151.8	13	38	1.073	0.55
	FL98166B	23.3	40.4	143.4	30.5	257.4	34.6	39	1.062	0.181

Outcrop	Sample #	Minimum Decln.	Minimum Incln.	Intermediate Decln.	Intermediate Incln.	Maximum Decln.	Maximum Incln.	Kmean	Pj	Tj
	FL98166C	184.1	88	54.5	1.3	324.4	1.5	33	1.078	0.746
152	FL98167A	68.6	83.4	289.1	5	198.7	4.2	26	1.078	-0.182
	FL98167B	322.7	55.8	92.2	23.4	193.1	23.4	23	1.158	-0.5
	FL98167C	204.7	74.2	62.7	12.6	330.6	9.4	24	1.086	0.488
	FL98168A	39.8	77	192	11.6	283.2	5.9	25	1.111	0.283
	FL98168B	30.3	68.3	174.6	17.9	268.5	11.9	28	1.106	0.643
	FL98168C	329.4	76.3	215.6	5.6	124.4	12.4	26	1.086	0.291
153	FL98169A	156.7	72.9	269.3	6.7	1.2	15.7	24	1.057	0.547
	FL98169B	248.2	86.8	92.3	2.9	2.2	1.3	18	1.098	-0.154
	FL98169C	142.9	68.4	277	15.4	11.1	14.8	20	1.12	-0.103
154	FL98170A	0.5	61.8	212.9	24.4	116.7	13.3	10	1.129	0.359
	FL98170B	234	38.4	73.5	49.9	331.8	9.7	14	1.08	-0.072
155	FL98171A	84.6	21.8	249	67.4	3.52.4	5.5	-16	1.13	0.788
	FL98171B	95.6	41	293.3	47.7	193.4	8.9	-17	1.062	0.609
	FL98171C	268.9	29	134.9	51.4	12.6	23.1	-19	1.027	0.604
156	FL98172B	170.2	71.6	49.2	9.4	316.5	15.4	-1	3.039	-0.397
157	FL98173A	287.1	49.4	119.8	39.9	24.5	6.3	11	1.109	0.474
	FL98173B	285.7	57.4	76.9	29.3	174.4	13.1	12	1.077	0.129
	FL98173C	217.2	73.2	64.6	15	332.6	7.4	8	1.138	0.619
	FL98173D	200.9	44	80.1	27.9	329.9	33.1	9	1.073	-0.658
158	FL98174A	162.1	86.9	32.2	2	302.1	2.3	14	1.087	-0.485
	FL98174B	275.5	49.7	56.5	33.4	160.3	19.9	13	1.11	-0.118
159	FL98175A	113.2	28.8	308.1	60.4	206.7	6.4	-16	1.025	-0.496
	FL98175B	272.3	40.1	17.8	17.6	128.1	44.7	-15	1.221	0.246
	FL98175C	318.9	3.9	54.4	54.5	226.1	35.2	-15	1.196	0.776
160	FL98176A	16.9	64.8	225.5	22.5	130.9	10.9	26	1.057	-0.708
	FL98176B	68.1	81.3	302.3	5.1	211.6	7	17	1.076	0.676
	FL98176C	42.2	62.7	182.6	21.7	279	15.7	33	1.036	-0.326
	FL98176D	342.6	54.7	200.4	29.2	99.9	18	16	1.049	0.012
161	FL98177A	126.1	10.2	346.7	76.6	217.7	8.5	-3	1.133	1.001
	FL98177B	259.6	67.1	51.8	20.5	145.5	9.8	5	1.395	0.669
	FL98178A	121	34.4	342.7	47.4	226.9	21.8	1	1.626	0.431
	FL98178B	28.3	30.7	263.3	44	138.7	30.4	0	21.114	0.665
162	FL98179A	140.7	65.1	236.4	2.6	327.6	24.7	-11	1.087	-0.18
	FL98179B	96.3	23.8	290.3	65.5	188.7	5.3	-13	1.094	0.648
	FL98180A	195	31.4	61.5	48.4	300.9	24.3	-12	1.119	0.557
	FL98180B	256.8	57.3	156.9	6.3	63	31.9	-14	1.081	-0.255
163	FL98181A	235.7	63.4	82.9	24	348.1	10.8	0	2.866	-0.088
	FL98181B	114	63.4	19.1	2.4	287.9	26.5	5	1.504	0.386
	FL98182A	141.6	41.5	290.9	44.2	36.9	15.9	9	1.211	0.336
164	FL98183A	61.9	72.7	320.4	3.5	229.4	16.9	386	1.029	0.589
	FL98183B	39.2	69.9	266	14.1	172.4	14	413	1.036	0.81
	FL98183C	83.8	74	339.7	4	248.6	15.5	388	1.026	0.479
	FL98183D	89.4	85.2	302.2	4.1	212	2.6	350	1.035	0.872
165	FL98184A	258.3	29.1	164.2	7.5	61.2	59.7	7	1.137	-0.169
	FL98184B	258.5	41.3	113.9	42.9	5.7	18.6	-4	1.302	0.836
	FL98184C	277.3	52.5	168.2	14.1	68.4	33.9	83	1.053	-0.033

Table B-1 AMS Data

		Minimum		Intermediate		Maximum				
Outcrop	Sample #	Decln.	Incln.	Decln.	Incln.	Decln.	Incln.	Kmean	Pj	Tj
166	FL98185A	272.9	75.9	152.3	7.1	60.7	12.3	71	1.026	0.767
	FL98185B	49.8	60.8	256.6	6.5	160.9	11.4	68	1.03	0.406
	FL98185C	8.8	84.1	171.8	5.7	262	1.7	64	1.035	0.718
167	FL98186A	152.6	6.5	57.4	38.9	250.6	50.3	49	1.079	-0.657
	FL98186B	170.5	64.1	23.1	22.2	287.9	12.6	48	1.032	0.472
	FL98186C	29.4	71.1	282.2	5.8	190.3	17.9	48	1.088	-0.151
168	FL98187A	130.8	0.2	40.7	9.5	222.1	80.5	12	1.083	0.416
	FL98187B	333.8	53.6	65.5	1.3	156.5	36.4	12	1.942	0.544
	FL98187C	203.5	32	84.5	37.8	320.4	35.8	12	1.271	-0.328
169	FL98188A	112.8	4.1	21	23.9	212	65.8	17	1.175	0.39
	FL98188B	295.2	69.1	159.6	15.2	65.7	13.9	12	1.253	0.335
170	FL98189A	259	25.1	46.8	61	162.6	13.5	8	1.099	-0.483
171	FL98190A	194.3	32.9	70.1	41	307.7	31.6	14	1.108	-0.176
	FL98190B	149.8	72	311.5	17.1	43.1	5.3	7	1.199	0.272
172	FL98191A	137.5	56.2	303.3	33	37.6	6.6	38	1.037	-0.278
	FL98191B	199.3	63.2	340.7	21.5	76.9	15.1	34	1.123	-0.274
173	FL98192A	113.4	35	250	46	6.1	23	-2	2.915	0.435
	FL98192B	52.5	41.3	215.4	47.5	314.9	8.6	2	3.213	0.494
174	FL98193A	30	51	238.4	35.5	138.1	14.1	7	1.312	0.423
	FL98193B	277.3	7.9	165	69.8	9.9	18.5	6	1.195	-0.42
	FL98193C	290.9	69.2	145.9	17.3	52.4	11.2	1	1.527	0.506
175	FL98194A	179	65.9	21.7	22.4	288.2	8.4	5	1.245	0.144
	FL98194B	117.2	73.2	260.8	13.7	353.2	9.6	2	1.512	-0.311
176	FL98195A	117.2	4	16.4	69.5	208.6	20	16	1.078	-0.487
	FL98195B	109.4	20.8	233.3	55.7	8.8	25.9	14	1.0055	-0.238
	FL98195C	266.4	74.9	121.5	12.5	29.6	8.4	13	1.077	-0.183
177	FL98196B	208.9	68.9	306.5	2.9	37.6	20.9	7	1.215	0.57
	FL98196C	320	63.3	101.3	21.4	197.4	15.1	6	1.123	0.029
179	FL98198A	57.5	80.6	165.3	2.9	255.8	8.9	23	1.0047	0.283
	FL98198B	82.2	51	330.2	16.9	228.4	33.9	26	1.938	0.126
180	FL98199A	265.8	82.9	79.5	7	169.6	0.8	27	1.037	0.208
	FL98199B	344.7	18.8	93.4	43.3	237.6	40.7	25	1.235	0.256
	FL98199C	145.2	10	288.3	77.5	53.9	7.3	27	1.061	-0.49
181	FL98200A	136.6	87.1	121	45.8	313.7	86.8	-15	1.303	0.065
	FL98200B	269.3	50.9	99	38.7	5.5	5	-17	1.136	0.122
	FL98200C	100.7	49.1	272.5	40.6	6	4	-15	1.121	-0.389
182	FL98201A	145.9	72	272.3	10.9	5.1	14.2	-1	3.468	-0.562
	FL98201B	257.2	17.3	138.6	56.9	356.4	27.2	-14	1.051	0.155
183	FL98202A	235.3	60.5	129.5	8.8	34.8	28	24	1.056	-0.53
	FL98202B	238.9	47.3	42.3	41.5	139.8	8.4	21	1.054	-0.629
	FL98202C	160.4	79	293.1	7.5	24.2	8	17	1.087	-0.046
184	FL98203A	275.4	66.6	92.1	23.3	182.6	1.2	17	1.076	0.095
	FL98203B	328.6	81.2	186	7	95.3	5.3	11	1.117	0.256
	FL98203C	223.9	65.2	95.5	16	360	18.4	18	1.103	0.545
185	FL98204A	118.4	57.5	236.4	16.7	355.2	27	10	1.202	0.098
	FL98204B	265.6	71.6	110.9	16.8	18.7	7.4	7	1.166	0.812
	FL98204C	112.6	67.2	272.2	21.5	5.1	7.2	11	1.104	0.295

Table B-1 AMS Data

		Minimum		Intermediate		Maximum				
Outcrop	Sample #	Decln.	Incln.	Decln.	Incln.	Decln.	Incln.	Kmean	Pj	Tj
	FL98204D	59.7	78.3	272.6	9.8	181.5	6.2	7	1.093	0.164
186	FL98205A	314.6	35.1	87.2	43.9	204.8	25.7	64	1.588	0.972
	FL98205B	80.7	73.5	271.7	16.2	180.8	3	44	1.034	0.075
	FL98205C	225.1	10.2	125.8	41.8	325.9	46.4	51	1.043	0.531
187	FL98206A	140.9	43.8	286.7	40.8	32.9	17.9	70	1.031	0.434
	FL98206B	161.2	71	276.5	8.4	9.1	16.9	61	1.033	-0.193
188	FL98207A	239.9	24.4	143.8	13.2	27.8	61.8	2	1.271	0.2
	FL98207B	79.1	62.8	313.8	16.5	217.3	21	0	1.842	-0.051
	FL98207C	94.4	82.5	268.6	7.5	358.7	0.7	10	1.352	-0.051
189	FL98208A	292.5	63.7	38.1	7.6	131.7	25	11	1.061	-0.129
	FL98208B	323.5	66.1	112.1	20.8	206.5	11.4	14	1.114	0.225
	FL98208C	248.2	76.4	88.5	12.7	357.5	4.5	15	1.098	0.306
190	FL98209A	24.6	71.5	256.2	11.7	163.2	14.1	12	1.098	-0.313
	FL98209B	28.2	72.2	271.6	8.2	179.3	15.7	15	1.091	0.251
	FL98209C	49.4	19.2	161.8	47.6	304.7	36.1	15	1.185	-0.574
191	FL98210A	306.2	83.5	73.3	3.9	163.6	5.2	49	1.044	0.437
	FL98210B	30.9	77.7	259.4	8.2	168.1	9.1	45	1.051	0.464
192	FL98211A	235.3	77.7	68.7	12	338.1	2.8	13	1.067	0.127
	FL98211B	11.9	57.9	275.8	3.8	183.5	31.8	12	1.11	-0.051
	FL98211C	126.2	52.4	287.8	36.1	24.4	8.9	12	1.104	0.825
193	FL98212A	41	50.4	231.5	39.1	137.3	5.1	8	1.115	0.356
	FL98212B	260.5	19.4	132.5	60.3	358.5	21.7	8	1.197	-0.081
194	FL98213A	42.9	64.8	263.5	19.7	168	15.1	-7	1.197	0.121
	FL98213B	60.2	65.8	299.5	12.9	204.7	20.1	-7	1.178	-0.037
195	FL98214A	158.3	66.6	292.8	16.9	27.7	15.7	-11	1.162	-0.26
	FL98214B	314.6	4.6	51.9	57.5	221.7	32.1	-9	1.182	0.624
	FL98214C	235.4	63.2	92.7	21.9	356.6	14.7	-3	2.006	0.416
196	FL98215A	38.9	73.7	209.3	16.1	300	2.6	15	1.062	0.346
	FL98215B	244.7	35.7	117.4	40.1	358.8	29.6	14	1.062	-0.744
197	FL98216A	139.2	78.6	282.6	9.1	13.7	6.8	-5	1.192	0.154
	FL98216B	286.2	51.6	93.2	37.7	188.1	6.3	-6	1.276	0.06
	FL98216C	90.2	57	251.8	31.6	347	8.4	-7	1.319	0.167
198	FL98217A	142.7	50.9	284.9	32.7	27.6	19	6	1.181	0.624
	FL98217B	63.3	70.4	276.1	16.7	183.1	10	7	1.214	0.114
	FL98217C	90	71.6	258.9	18.1	349.9	3.3	9	1.178	0.164
199	FL98218A	323.7	72.4	105.8	14	198.4	10.4	41	1.057	0.23
	FL98218B	13.3	81.2	261.6	3.3	171.1	8.1	54	1.03	-0.244
	FL98218C	93.9	47.5	283.4	42.1	189.1	4.8	59	1.037	-0.173
200	FL98219A	65.8	74.5	264.5	14.8	173.3	4.8	76	1.037	0.08
	FL98219B	61.5	83.2	270.8	6	180.4	3.3	59	1.022	0.082
201	FL98220A	133.3	84	265.6	4	355.9	4.4	36	1.059	-0.129
	FL98220B	285.2	74.9	57.5	10.3	149.5	10.9	41	1.033	0.391
	FL98220C	58.9	86.1	166.4	1.2	256.5	3.7	40	1.069	0.474
	FL98220D	236.9	79.5	144.6	0.4	54.5	10.5	45	1.034	0.473
202	FL98221A	278.2	19.7	74.4	68.7	185.4	8	25	1.045	-0.263
	FL98221B	108	55.2	298.1	34.4	204.9	4.8	29	1.076	0.018
203	FL98222A	217.5	76.9	122	1.3	31.6	13.1	43	1.033	0.293

Table B-1 AMS Data

		Minimum		Intermediate		Maximum				
Outcrop	Sample #	Decln.	Incln.	Decln.	Incln.	Decln.	Incln.	Kmean	Pj	Tj
	FL98222B	292.3	77.4	199.5	0.6	109.3	12.5	41	1.05	0.69
	FL98222C	249.5	76	49.7	13.2	140.7	4.6	41	1.045	0.768
204	FL98223A	61.1	82.1	271.1	6.9	180.6	3.9	37	1.029	0.098
	FL98223B	53.2	82.9	257.8	6.4	167.5	2.9	29	1.039	0.461
	FL98223C	311.1	84.9	51.1	0.9	141.1	5.1	37	1.032	0.174
205	FL98224A	235.2	87.6	85.9	2.1	355.8	1.2	24	1.068	0.388
	FL98224B	347.7	72.8	105.6	8.2	197.8	15	19	1.089	0.08
	FL98224C	129	77	234.7	3.6	325.5	12.5	21	1.032	0.15
206	FL98225A	274.3	76.1	135	10.7	43.3	8.9	62	1.029	0.339
	FL98225B	145.7	81.7	299.7	7.5	30.2	3.6	55	1.034	0.767
207	FL98226A	70.3	52.1	330	7.9	234	36.7	-11	1.137	0.854
	FL98226B	178.2	64	341.5	25	74.6	6.6	-10	1.261	0.354
	FL98226C	154.1	35.3	264.7	26.5	22.5	43.1	-14	1.091	-0.485
208	FL98227A	265	50.6	18.8	18.4	121.4	33.5	-1	1.845	0.149
	FL98227B	233.7	57.7	35.9	31.1	130.8	8	0	7.94	0.129
	FL98227C	168.7	76.2	322.2	12.4	53.6	6	0	28.855	0.299
209	FL98228A	187.3	61.8	349.3	27	83.1	7.5	-25	1.047	-0.63
	FL98228B	251.1	46.7	126.7	28	18.8	30	-24	1.038	-0.325
	FL98228C	110.4	75.9	7.5	3.2	276.8	13.7	-25	1.044	-0.797
	FL98228D	273.2	4.1	12.5	65.6	181.4	24	-27	1.033	-0.327
210	FL98229A	312.3	46.6	121.4	42.9	216.5	5.5	2	1.571	-0.23
	FL98229B	225	87.4	225	82	45	2.6	-2	1.718	-0.209
211	FL98230A	273.8	9.7	177.1	34.4	17.3	53.9	1	2.045	-0.357
	FL98230B	279.1	41.5	17.6	9.5	117.9	46.9	15	1.045	-0.133
212	FL98231A	342.8	9.9	114	75.1	250.9	10.9	-19	1.021	0.503
	FL98231B	336	5.5	69.8	34.2	238.1	55.2	-21	1.032	-0.136
	FL98231C	11.1	7	178.1	82.8	280.9	1.6	-16	1.094	0.446
213	FL98232A	110	82.2	273.1	7.4	3.4	2.2	-5	1.174	0.367
	FL98232B	96.6	47.6	226.9	30.6	333.9	26.3	-5	1.313	0.438
	FL98232C	311.1	69.2	110.3	19.5	202.7	6.8	-7	1.136	0.23
	FL98232D	207.7	51.7	28.7	38.3	298.3	0.5	-1	1.9	0.29
214	FL98233B	74.4	27.2	184.5	33.7	314.6	44	0	7.162	0.547
	FL98233C	272.6	45.5	75.1	43.1	173.5	8.9	2	1.96	-0.059
	FL98233D	2.5	2.5	95.3	47.7	270.2	42.2	-3	9.694	-0.277
215	FL98234A	96.7	49.4	318.6	32.6	214.1	21.5	10	1.13	0.107
	FL98234B	359.6	32.8	125.5	42.3	247.5	30.2	10	1.077	-0.233
	FL98234C	71.6	57.8	199.6	21.1	299	23	9	1.131	0.3
	FL98234D	44	65.2	253.1	22	158.7	10.9	11	1.092	0.417
216	FL98235A	268.1	36.3	140.5	39.7	22.6	29.4	-3	1.759	0.138
217	FL98236A	250.2	53.7	131.3	19.5	29.9	29.2	-1	2.294	0.259
	FL98236B	124.2	12.4	25.6	34.2	231.2	53	0	10.057	-0.334
	FL98236C	26.8	53.8	267.3	19.8	165.8	28.9	-1	5.042	0.906
218	FL98237A	99.4	73.1	303.7	15.5	211.8	6.6	26	1.045	0.994
	FL98237B	234.1	55	107.9	22.5	6.6	25.3	30	1.057	-0.045
	FL98237C	*153.6*	*41.9*	*360*	*45*	*256.1*	*13.5*	*22*	*1.043*	*0.562*
219	FL98238A	97	78.7	260.6	10.9	351.2	3.1	21	1.059	0.51
	FL98238B	289.6	84.2	114.4	5.8	24.4	0.5	22	1.071	0.721

Table B-1 AMS Data

		Minimum		Intermediate		Maximum				
Outcrop	Sample #	Decln.	Incln.	Decln.	Incln.	Decln.	Incln.	Kmean	Pj	Tj
	FL98238C	291.7	57.6	132.4	30.7	36.8	9.4	25	1.049	0.178
	FL98238D	74.9	82.6	221.8	6.2	312.2	4	25	1.077	0.771
220	FL98239A	324.6	59	197.7	19.9	99	22.8	5	1.421	-0.138
	FL98239B	108.6	40.8	248.6	41.6	358.9	21.3	2	1.456	0.093
221	FL98240A	20.6	19.4	282.2	22.7	147.2	59.4	84	1.01	0.335
	FL98240B	97.2	10.1	305.9	78.5	188.1	5.4	49	1.031	-0.711
222	FL98241A	245.2	79.7	102	8.3	11.1	6.1	9	1.086	0.02
	FL98241B	279	58.4	145.5	22.9	46.4	20.5	8	1.189	0.24
223	FL98242A	284.3	37	104.4	53	14.3	0.1	13	1.12	-0.173
	FL98242B	275	13.2	139.1	71.9	7.9	12.1	13	1.158	-0.165
224	FL98243A	3.6	85.7	257.1	1.2	167	4.1	41	1.08	0.611
	FL98243B	78.7	77.3	273.3	12.3	182.6	3.1	59	1.072	0.332
	FL98243C	148.1	59.7	24.8	17.8	286.7	23.7	54	1.071	0.259
	FL98243D	220.1	74.4	56.6	15	325.4	4.2	40	1.071	0.348
225	FL98244A	139.9	78.6	282.6	9.1	13.7	6.8	24	1.033	0.008
	FL98244B	69.5	75.7	265.9	13.7	174.9	3.9	23	1.086	0.489
	FL98244C	264.5	75.5	106	13.5	14.8	5.1	23	1.071	0.141
226	FL98245A	94	65.1	301.4	22.4	207.1	10.3	9	1.055	-0.187
	FL98245B	276.3	48.5	65.5	37.2	167.9	15.7	9	1.112	-0.584
227	FL98246A	229.1	80.4	75.3	8.6	344.7	4.2	21	1.081	0.741
	FL98246B	37.3	77.1	245.2	11.4	154	5.9	20	1.056	0.285
228	FL98247A	302.4	79	95.7	9.9	186.6	4.9	53	1.047	0.658
	FL98247B	318.4	81.5	195.4	4.7	104.8	7.1	50	1.042	0.793
229	FL98248A	72.5	78.6	221.8	9.8	312.8	5.7	21	1.085	0.428
	FL98248B	172.4	85.8	321.5	3.6	51.6	2.1	19	1.083	-0.853
	FL98248C	87.8	65.7	206.2	12.1	300.8	20.7	18	1.056	0.411
230	FL98249A	39	81.6	179.9	6.5	270.5	5.3	85	1.047	0.628
	FL98249B	22	82.8	176.5	6.5	266.8	3.1	78	1.053	0.496
	FL98249C	6.2	84.1	147.4	4.6	237.7	3.7	113	1.055	0.891
231	FL98250A	295.6	56.2	93.3	31.8	189.8	10.3	14	1.093	0.515
	FL98250B	218.6	66.5	324.7	6.9	57.6	22.3	15	1.098	0.306
	FL98250C	215.5	66.8	108.3	7.2	15.4	21.9	25	1.059	0.58
232	FL98251A	42.1	62.1	254.4	24.2	158.4	13.2	-1	1.708	-0.51
	FL98251B	174.5	41	53.4	30.7	300	33.7	-6	1.127	0.451
	FL98252A	263.1	0.4	353.4	45.7	172.7	44.3	5	1.237	0.217
	FL98252B	189.8	71.2	5.9	18.8	96.3	1.2	-2	1.508	-0.24
233	FL98253A	305.3	10.9	180	71.6	38.1	14.7	1	1.468	-0.048
	FL98253B	233.3	79.3	107.6	6.3	16.7	8.6	4	1.286	-0.6
	FL98253C	78.2	82	197.3	3.9	287.8	7	2	1.556	0.269
234	FL98254A	180	71.6	310.5	12.2	43.5	13.6	-12	1.061	0.44
	FL98254B	57.4	44.4	223.9	44.8	320.7	6.8	-2	1.279	-0.141
	FL98254C	309.6	38.2	171.2	43.6	58.4	22.2	-13	1.069	-0.095
	FL98254D	239.8	43	71.2	46.4	335.1	5.7	-1	2.632	-1
235	FL98255A	3.8	79.7	247.2	4.7	156.5	9.2	9	1.17	0.71
	FL98255B	307	40.1	152.3	48.1	47.5	10.6	15	1.091	-0.367
236	FL98256A	71.2	73.5	267	15.9	175.8	4.3	22	1.084	0.35
	FL98256B	192.7	5.2	92.2	63.4	285.2	26	24	1.213	-0.016

Table B-1 AMS Data

		Minimum		Intermediate		Maximum				
Outcrop	Sample #	Decln.	Incln.	Decln.	Incln.	Decln.	Incln.	Kmean	Pj	Tj
	FL98256C	60.5	1	328.7	60.5	151	29.5	21	1.118	0.28
237	FL98257A	92.5	2.5	360	45	185	44.9	3	1.273	-0.052
	FL98257C	162.6	0.9	71.3	54.6	153.3	35.4	-2	1.952	0.039
238	FL98258A	345.1	52.2	163.5	37.8	154.1	0.8	1	1.735	0.323
	FL98258B	203	66.9	70.1	16.2	335.3	16	1	39.738	0.752
	FL98259A	309.3	79	89.7	8.5	180.7	6.9	7	1.374	0.677
	FL98259C	307.1	81.9	98.5	7.1	189	3.8	4	1.741	0.589
239	FL98260A	40.8	11.4	305.9	22.8	155.3	64.2	-6	2.524	0.402
	FL98260B	114.2	71.9	227.9	7.5	320.1	16.4	-3	1.3	-0.046
	FL98261A	90	71.6	277.9	18.3	187.1	2.4	1	2.003	-0.731
	FL98261B	249.7	72	68.2	18	158.3	0.4	-2	1.536	0.213
240	FL98262A	255.9	17.6	164.5	4.5	60.6	71.8	-10	5.938	0.403
	FL98262B	50.7	15.1	290	62.1	147.2	22.9	-13	2.281	0.262
	FL98262C	244.1	79	129.8	4.6	39	10	-11	1.065	0.441
	FL98262D	254.2	64.3	42.8	22.4	137.9	12.1	-10	4.854	0.663
241	FL98263A	159.6	62.8	335.9	27.2	66.6	1.5	3	1.371	0.399
	FL98263B	303.1	4.8	74.3	82.8	212.6	5.4	0	2.663	0.801
	FL98263C	72.5	7.3	190.2	74.6	340.7	13.5	2	1.364	0.077
	FL98263D	233.9	62.8	86.9	23.3	351.1	13.2	0	2.508	-0.637
242	FL98264A	352.2	80.1	100.3	3.1	190.8	9.4	3	2.323	0.855
	FL98264B	303.7	85	143.5	4.7	53.3	1.7	6	1.747	0.777
243	FL98265A	290.3	23.6	149.2	60.7	27.7	16.4	-13	1.094	0.188
	FL98265B	135.6	40.7	15.7	30.1	262.1	34.7	-14	1.035	-0.192
	FL98265C	300.6	68.1	173.8	13.5	79.6	16.9	-13	1.061	-0.237
244	FL98266A	242.9	72.3	105	13.3	12.2	11.4	-5	1.59	0.321
	FL98266B	118.6	44.2	12.2	16.1	267.5	41.4	-5	1.172	-0.298
245	FL98267A	259.5	7.8	35.7	79.2	168.5	7.4	4	1.537	0.453
246	FL98268A	216.8	44.8	71.1	39.7	325.5	17.9	3	1.467	-0.139
	FL98268B	102.3	39.3	198.1	7.1	296.6	49.8	-1	1.629	-0.081
247	FL98269A	332.6	71.5	96.5	10.6	189.4	15	-7	1.088	0.677
	FL98269B	2.8	43.6	124.4	28.8	235.1	32.6	-4	2.516	0.679
	FL98269C	203.2	53.2	69.6	27.3	327.1	22.7	-7	1.226	-0.331
	FL98269D	105.5	83	266.6	6.6	356.8	2.3	-7	1.169	0.307
248	FL98270A	169.6	69.2	43.7	12.5	310	16.3	1	1.72	0.587
	FL98270B	123.9	67.6	20.4	5.5	288.2	21.7	7	1.153	0.304
249	FL98271A	79.7	79.9	273.3	9.8	182.9	2.3	3	2.677	-0.338
	FL98271B	322.5	70.3	148	19.6	57.3	1.7	3	1.084	-0.316
	FL98271C	311.7	52.9	205.6	11.8	107.4	34.5	2	1.685	0.317
	FL98271D	81.8	20.3	214.2	61.2	344.3	19.5	2	1.432	0.495
250	FL98272A	161.2	67.8	295	15.8	29.4	15.2	16	1.069	0.288
	FL98272B	118.9	20	3.9	49.2	223	33.8	17	1.078	-0.213
251	FL98273A	342.8	42.2	99.5	26.3	210.8	36.4	-13	1.081	0.611
	FL98273B	74.1	39.4	289.4	44.8	180	18.4	-17	1.047	-0.24
	FL98273C	265.5	55.8	110.7	31.6	13.3	11.8	-15	1.069	0.413
	FL98273D	271	51.4	78.1	37.9	173	6.3	-17	1.066	0.106
252	FL98274A	305.6	75.6	120.5	14.4	210.8	1.2	-1	1.568	0.424
	FL98274B	296.5	64.2	105.6	25.4	197.6	4.3	-1	1.649	0.259

Outcrop	Sample #	Minimum Decln.	Minimum Incln.	Intermediate Decln.	Intermediate Incln.	Maximum Decln.	Maximum Incln.	Kmean	Pj	Tj
253	FL98275A	111.6	49.1	263.7	37.4	4.8	14.1	-6	1.157	-0.301
	FL98275B	176.7	30	48	47.2	284.1	27.3	-5	2.014	0.542
	FL98275C	286.5	61.6	74.5	24.6	170.7	13.2	-2	1.24	-0.566
254	FL98276A	63	27.8	327.5	10.3	219.1	60.1	-21	1.048	-1
	FL98276B	158.4	42.2	47.8	21.3	298.5	40.2	-19	1.031	0.34
	FL98276C	54.3	21.1	318.8	13.9	197.6	64.4	-19	1.247	-0.252
	FL98276D	196.4	53.2	288.7	1.7	20	36.8	-21	1.097	0.221
255	FL98277A	163.5	85.8	283.1	2.1	13.2	3.7	-12	1.103	0.19
	FL98277B	99.3	40.2	200.8	13.3	305.3	46.8	-14	1.371	-0.17
	FL98277C	20.6	48.4	273.9	14.3	172.3	38.1	-11	1.962	0.612
	FL98277D	307.4	65.7	180.1	15.3	84.9	18.4	-11	2.124	-0.23
256	FL98278A	127.1	46.8	358.5	30.3	250.8	27.6	-12	1.603	0.537
	FL98278B	301.7	57	161.5	26.5	62.1	18.2	-11	2.049	-0.507
257	FL98279A	130.4	48.9	267.2	32.5	12.4	22.3	3	1.311	-0.557
	FL98279B	348.3	75.8	79.5	0.3	169.5	14.2	2	1.353	0.551
258	FL98280A	341	60.3	92	11.6	187.9	27	48	1.064	0.651
259	FL98281A	63.5	7.7	325	47.7	160.3	41.2	-1	10.469	0.518
	FL98281B	312.5	3	218.4	53.9	44.7	35.9	-5	2.158	0.139
	FL98281C	259.1	61.2	80.7	28.8	350.3	0.7	23	1.054	0.509
260	FL98282A	119.7	43.7	275.9	43.7	17.8	12.2	14	1.167	-0.894
	FL98282B	282.1	50.7	104.9	39.3	13.8	1.3	16	1.209	-0.43
	FL98282C	112.3	65.1	227.5	11.2	322.1	22	14	1.209	0.349
	FL98282D	317.9	1.9	221.8	72.9	48.5	17	16	2.926	-0.078
261	FL98283B	97.7	71.5	268.5	18.3	359.4	2.8	-3	1.592	0.171
	FL98283C	273.2	71.7	87	18.2	177.7	1.9	2	1.633	-0.277
	FL98283D	226	64.6	70.9	23.3	336.8	9.5	-3	1.7	0.006
	FL98284A	167.3	68.5	52.1	9.5	318.8	19.1	-5	1.192	0.043
	FL98284B	141	75	256.4	6.6	347.9	13.4	-4	1.311	0.504
262	FL98285A	209.5	18.2	102.9	41	317.6	43.4	-11	1.126	-0.36
	FL98285B	31.9	32.8	261.8	45	141	27	-7	1.328	0.523
	FL98285C	50.6	82	273.1	5.9	182.6	5.4	-4	1.325	0.548
	FL98286A	321.1	66.8	61.7	4.5	153.6	22.7	-10	1.149	-0.167
	FL98286B	134	78.7	262.1	7	353.2	8.8	-5	1.547	-0.349
	FL98286C	77.5	68.7	277.3	20.1	184.8	6.6	-6	1.152	-0.532
263	FL98287A	228.3	65.3	328.4	4.6	60.5	24.2	-11	1.066	0.441
	FL98287B	108.8	43.4	270	45	9.7	9.5	-9	1.149	0.842
264	FL98288A	184	10.3	279	5.8	15.7	49.1	-5	1.239	-0.46
	FL98288B	266.4	10.8	107.5	78.5	357.2	4	-4	1.181	0.46
	FL98288C	283	54.5	93.7	35.2	186.8	4.4	-5	1.813	0.703
	FL98288D	207	50.8	312.5	12.3	51.7	36.5	-5	1.087	-1
265	FL98289A	234.9	34	107.7	41.8	347.3	29.5	-12	1.052	-0.66
	FL98289B	352.3	85.9	105.2	1.6	195.3	3.8	-20	1.18	-0.235
266	FL98290A	74.5	76.9	269.3	12.6	178.6	3.2	20	1.103	-0.076
	FL98290B	341.6	81.6	161.6	8.4	90.6	19	19	1.057	0.804
	FL98290C	221.2	3.3	131	2.7	2.2	85.8	21	1.146	-0.351
267	FL98291A	85.1	28.1	341.2	24.3	216.9	51.3	23	1.036	-0.494
	FL98291B	302.6	75.2	95.3	13.2	186.9	6.5	32	1.059	0.77

Table B-1 AMS Data

Outcrop	Sample #	Minimum Decln.	Minimum Incln.	Intermediate Decln.	Intermediate Incln.	Maximum Decln.	Maximum Incln.	Kmean	Pj	Tj
	FL98291C	102.7	78.4	261.3	10.8	352.1	4.1	31	1.045	0.153
268	FL98292B	4.5	57.4	138.2	23.8	237.9	20.9	0	2.639	0.512
	FL98292C	360	71.6	257.1	4.3	165.7	17.9	1	2.032	-0.275
269	FL98293A	59.3	45.3	312.3	16.1	208.2	40.2	5	1.284	0.697
	FL98293B	101.8	61.9	301.1	26.7	207.1	8	2	1.265	-0.281
270	FL98294A	120.5	65.6	273.2	22	7.4	10.1	-1	3.564	0.333
	FL98294B	57.5	5.9	323.9	31.4	157	57.9	-1	8.218	0.664
	FL98295A	87	23.7	223.2	58.7	348.2	19.2	-1	1.554	-0.415
271	FL98296A	263.7	71.6	166.6	2.4	75.8	18.3	-3	1.351	-0.266
	FL98296B	238.6	74	129.7	5.3	38.3	15.1	0	3.242	0.542
	FL98296C	185.9	80.7	73.6	3.6	343.1	8.6	3	1.418	0.467
272	FL98297A	118.9	14.5	8.3	53.7	218.3	32.5	-10	1.061	0.014
	FL98297B	171	74.1	70.1	3.1	339.2	15.5	-9	1.121	0.616
	FL98297C	160.5	26	335.8	64	69.6	1.8	-5	1.223	0.629
273	FL98298A	78.6	51.3	217.3	31	320.4	20.7	-10	1.096	0.353
	FL98298B	241.8	62.8	347.2	7.8	81	25.9	2	2.124	0.407
	FL98298C	40.4	62.8	270	18.4	173.3	19.3	-11	1.069	-0.707
274	FL98299A	162.4	73.7	286.5	9.3	18.8	13.3	6	1.188	0.486
	FL98299B	232.1	58.5	83.1	27.7	345.7	13.8	5	1.255	-0.021
	FL98299C	294.7	74.5	122	15.4	31.5	1.9	6	1.141	0.143
275	FL98300A	39.7	74.5	237.1	14.8	145.9	4.4	38	1.044	0.507
	FL98300B	270.5	73.4	74.7	16	166	4.3	38	1.038	0.435
276	FL98301A	144.5	45.7	308.2	43.1	46	8.2	-31	1.032	0.007
	FL98301B	350.4	68	174.4	21.9	83.8	1.4	-30	1.026	-0.244
	FL98301C	134.5	8.3	26.2	65	228.1	23.4	-26	1.032	-0.747
	FL98301D	255.6	53.4	95	35.1	358.4	9.4	-31	1.043	0.836
277	FL98302A	136.6	34.5	270	45	27.9	25.1	-14	1.032	1
	FL98302B	79.4	29.2	220.2	54.2	338.4	18.9	-16	1.099	0.724
	FL98302C	306	78.5	48.1	2.4	138.6	11.2	-13	1.086	0.47
	FL98302D	189.7	66.2	309	12.2	43.6	20.1	-13	1.088	-0.438
278	FL98303A	104.1	37.9	288.6	53.5	195.7	2.5	2	1.423	-0.355
	FL98303B	268	39.5	53.8	45.1	162.7	17.8	0	8.604	0.09
	FL98303C	142.8	61.7	285.2	23.1	22	15.4	2	1.462	-0.427
	FL98304A	281.3	26.2	160.4	46.3	29.3	32.1	-11	1.036	0.506
	FL98304B	325.1	63	218.2	8.4	124.2	25.5	-10	1.048	0.211
279	FL98305A	59.5	36.1	207	49.2	317	16.5	39	1.031	-0.327
	FL98305B	219.3	58.6	2.7	26.1	100.9	16.2	35	1.033	0.64
	FL98305C	350.5	82.1	184.1	7.7	93.9	1.8	39	1.035	0.151
280	FL98306A	266.3	65.1	100.7	24.2	8.3	5.5	-9	1.159	-0.107
	FL98306B	137.3	40.3	29.1	20.2	279.2	42.8	-8	1.151	0.304
	FL98306C	80.4	10.5	190	61.2	345.1	26.5	-9	1.35	-0.65
281	FL98307A	25.9	74.1	117.7	0.5	207.9	15.9	-8	1.074	-0.318
	FL98307B	248.1	33.4	27.5	49	143.5	20.9	-9	1.13	-0.137
	FL98307C	88.1	63.5	255.2	25.9	347.7	5.1	-11	1.103	-0.067
282	FL98308A	237.4	63.3	108.4	17.5	12	19.4	-14	1.09	0.352
	FL98308B	291.8	6.3	198.6	26.7	34	62.5	-9	1.129	0.809
	FL98308C	65.1	26.8	317.5	31	187.6	46.8	-13	1.067	-0.095

		Minimum		Intermediate		Maximum				
Outcrop	Sample #	Decln.	Incln.	Decln.	Incln.	Decln.	Incln.	Kmean	Pj	Tj
	FL98308D	222	12.6	315	13.3	90	71.6	-8	1.126	-0.376
283	FL98309A	278.4	11.8	185.8	11.9	52.4	72.8	-13	1.157	-0.648
	FL98309B	36	64.4	250.6	21.5	155.3	13.2	-12	1.114	-0.206
284	FL98310A	308	73.7	89.7	12.9	181.9	9.7	20	1.126	-0.636
	FL98310B	220.8	67.9	128.2	1.1	37.8	22.1	11	1.127	-0.405
285	FL98311A	243.2	87.6	104.2	1.8	14.1	1.6	5	1.356	0.133
	FL98311B	130.5	56.9	296.9	32.3	30.8	6.2	5	1.341	0.006
286	FL98312A	316.1	81.2	121.1	8.5	211.5	2.2	84	1.027	-0.124
	FL98312B	16.8	82.2	274.1	1.7	183.9	7.6	86	1.034	0.111
287	FL98313A	242.2	44.1	17.8	36.4	126.8	23.9	-2	1.693	0.396
	FL98313B	128.7	46.3	225.8	6.7	322.1	42.9	-12	1.064	0.015
	FL98314A	223.3	5.6	326.1	66	130.8	23.2	2	3.731	-0.396
	FL98314B	128.8	85.5	293.9	4.3	24	1.1	-1	2.144	-0.23
288	FL98315A	317.8	73.7	125.5	15.9	216.5	3.3	3	1.76	0.304
	FL98315B	295.1	69.4	198.8	2.4	107.9	20.5	5	1.525	0.689
289	FL98316A	252.9	55.8	97.1	21.7	360	11.3	4	1.39	0.865
	FL98316B	219.2	39.6	319	11.6	62.3	48	3	1.585	0.609
290	FL98317A	244.4	68.1	66.5	21.9	336.2	0.7	14	1.111	0.355
	FL98317B	159.9	77.3	222.9	9.3	291.5	8.5	11	1.11	0.355
	FL98317C	81.7	62.9	319.5	15.2	223.3	21.9	11	1.243	0.912
	FL98317D	307.6	77	117	12.8	207.5	2.3	10	1.083	0.268
291	FL98318A	315.7	66.5	124.4	23.1	216.2	4.1	3	1.616	0.329
	FL98318B	174	3.9	83.4	8.3	288.9	80.8	-4	1.703	-0.154
292	FL98319A	223.2	66.5	12.9	20.6	107	10.9	11	1.091	0.22
	FL98319B	102.2	73.5	249.1	13.9	341.3	8.6	6	1.25	0.335
293	FL98320A	338.3	69.8	128.4	17.7	221.4	9.4	20	1.077	0.217
	FL98320B	36.5	85.8	169.1	2.9	259.3	3.1	15	1.054	0.509
294	FL98321A	268.2	80	106.6	9.5	16.1	3.1	-13	1.074	0.567
	FL98321B	335.9	79	113.9	8.2	205	7.2	-13	1.138	0.207
	FL98321C	263.1	25.8	111.4	61.2	358.9	11.9	-9	1.086	0.269
295	FL98322A	212.2	0.6	122	12.1	305.2	77.8	-10	1.208	0.794
	FL98322B	103.8	58.7	266.7	30.1	1.2	7.6	-18	1.056	0.213
	FL98322C	244.3	75.3	74.6	14.5	343.9	2.5	-18	1.068	0.347
	FL98322D	232.9	2.9	336.5	78	142.3	11.7	-11	1.035	0.506
296	FL98323A	246.1	45.6	106.9	36.6	359.9	21.5	-28	1.049	-0.131
	FL98323B	72.8	36.6	228	50.7	333.5	12.3	-29	1.038	0.803
297	FL98324A	267	47.1	97.9	42.4	2.9	5.4	12	1.165	-0.875
	FL98324B	3.5	37.6	249.1	28.2	132.9	39.5	13	1.173	-0.575
	FL98324C	226.1	11.4	14	76.6	134.7	6.9	12	1.097	-0.437
298	FL98325A	237.4	68	107.7	14.5	13.4	16.2	15	1.082	0.35
	FL98325B	97.6	66.7	294.3	21.7	201.8	5.9	16	1.078	0.349
299	FL98326A	82.9	74	302.4	12.5	210.2	9.9	-1	1.807	-0.682
	FL98326B	115.1	38.3	293.1	51.7	24.3	1	-3	1.57	-0.066
300	FL98327C	103.4	51.9	281.9	38	12.5	0.8	-3	1.348	0.642
301	FL98328A	214.7	80	109.3	2.7	18.9	9.6	16	1.063	0.015
	FL98328B	268.7	81	62.6	8.1	153.2	3.9	17	1.071	0.017
	FL98328C	245	66.5	92.6	21	358.8	9.9	13	1.126	0.617

Table B-1 AMS Data

		Minimum		Intermediate		Maximum				
Outcrop	Sample #	Decln.	Incln.	Decln.	Incln.	Decln.	Incln.	Kmean	Pj	Tj
	FL98328D	290.1	59.4	107.3	30.6	198	1.2	17	1.084	0.02
302	FL98329A	7.8	58.1	151.2	26.6	249.7	16.3	21	1.055	0.464
	FL98329B	275.7	2.7	160.3	83.7	5.9	5.7	15	1.073	0.288
	FL98329C	282.9	58.4	116	31	22.5	5.8	19	1.042	0.259
	FL98329D	260.9	82	88.3	7.9	358.2	1	22	1.089	-0.137
303	FL98330A	222.1	64.8	99.7	14.1	4.3	20.3	10	1.132	-0.046
	FL98330B	239.3	52	123	19.1	20.8	31.4	8	1.102	0.517
	FL98330C	153.4	65.9	280.7	15.2	15.8	18.3	11	1.125	-0.36
304	FL98331A	225.2	42.4	110.3	24.7	359.7	37.4	-8	1.194	-0.393
	FL98331B	91.2	80.9	220.8	5.9	311.5	7	-9	1.15	0.413
	FL98331C	97	68.5	205.7	7.2	298.4	20.1	-8	1.074	-0.318
305	FL98332A	132.8	30.5	330.5	58.2	227.5	8	-16	1.05	-0.239
	FL98332B	57.1	42.1	169.2	22.7	279.3	39.4	-17	1.047	0.26
	FL98332C	270.2	57	62.7	29.9	160.1	12.6	-16	1.1	0.023
306	FL98333A	103.5	22.7	221.7	48.6	358	32.5	-33	1.04	-0.222
	FL98333B	263.2	24.4	105.4	63.9	357.2	8.7	-33	1.014	-0.197
307	FL98334A	242.6	47.6	66.7	42.3	334.9	2.1	31	1.036	0.461
	FL98334B	211.8	81.4	104.5	2.6	14.2	8.2	28	1.043	0.342
	FL98334C	258.3	46.1	137.6	26.2	29.4	32.3	32	1.09	-0.05
308	FL98335A	184.2	81.6	82.4	1.7	352.1	8.2	3	1.769	0.483
	FL98335B	233.9	54.3	82.3	32.3	343.5	13.5	3	1.259	-0.457
	FL98335C	225.8	70	110.8	8.8	17.9	17.9	11	1.125	-0.203
	FL98335D	67.6	80.1	273.8	8.9	183.1	4.3	2	1.605	0.721
309	FL98336A	79.8	8.1	175.6	35.2	338.7	53.6	6	1.135	0.279
	FL98336B	163.9	60.4	350.1	29.4	258.6	2.7	3	1.325	0.548
	FL98336C	75.8	67.2	213.6	17.3	308.1	14.4	0	2.729	0.45
310	FL98337A	97.6	67.5	268.1	22.2	359.5	3.3	-19	1.076	0.443
	FL98337B	15.8	11.6	262	63	111.1	24	-19	1.035	-0.135
311	FL98338A	108.3	77.2	259.7	11.3	350.9	6	0	3.358	-0.051
	FL98338B	124.8	57.2	269	27.6	7.8	16.3	-2	1.48	0.006
	FL98338C	33.6	65.9	278.6	10.7	184.3	21.4	-3	1.213	0.189
312	FL98339A	250.8	6.4	351	57.9	156.9	31.4	15	1.093	0.553
	FL98339B	259.4	72.1	134.8	10.4	42.1	14.4	10	1.114	0.297
	FL98339C	239.3	52.8	89.5	33.3	349.5	14.7	15	1.061	0.125
	FL98339D	277.8	48.9	18	8.8	115.4	39.8	10	1.072	0.722
313	FL98340A	94	61.6	282	28.2	190.2	3.3	6	1.193	0.312
	FL98340B	84.8	54.7	180.4	4	273.2	35.1	7	1.186	0.83
	FL98340C	256.2	82.4	43.8	7.2	134.3	5.2	4	1.214	0.294
	FL98340D	180	45	38.9	37.9	292	20.5	5	1.075	-0.487
314	FL98341A	275.1	40.2	89.2	49.6	182.6	2.9	-2	2.211	0.371
	FL98341B	281	76.3	86.6	13.3	177.4	3.3	44	1.093	0.302
	FL98341C	233.7	60.6	360	18.4	97.7	22	-12	1.056	-1
	FL98341D	344.9	61.5	231	12.4	135	25.2	0	9.7	-1
315	FL98342A	350.8	43.4	248.8	12.5	146.5	43.9	-26	1.04	0.406
	FL98342B	226.2	19.9	14.6	67	132.1	11.1	-24	1.042	-0.392
	FL98342C	53.8	25.9	265.8	60.2	150.6	13.7	-25	1.031	-0.243
316	FL98343A	132.4	84.5	238.9	1.6	329.1	5.3	75	1.057	0.699

Table B-1 AMS Data

		Minimum		Intermediate		Maximum				
Outcrop	Sample #	Decln.	Incln.	Decln.	Incln.	Decln.	Incln.	Kmean	Pj	Tj
	FL98343B	189	85.2	295.7	1.4	25.8	4.6	74	1.053	0.379
317	FL98344A	80.2	53.1	213.9	27.5	316.4	22.7	4037	1.016	0.416
	FL98344B	79.4	52.3	199.8	21.4	302.6	29.4	4190	1.016	0.47
	FL98344C	78.9	61.6	192.2	12.1	288	25.3	4145	1.02	0.409
318	FL98345A	5.2	65.1	119.7	10.9	214.2	22.1	23	1.08	-0.43
	FL98345B	132.3	69.2	278.8	17.5	12.2	10.8	21	1.069	0.441
319	FL98346A	62.1	32	267.7	55.3	159.7	12	3	1.201	0.187
	FL98346B	49.1	64.5	309.2	4.7	217	25	4	1.772	-0.697
320	FL98347A	309.8	65.8	182.1	15.4	86.9	18.2	6	1.11	-0.408
	FL98347B	318.5	63.4	101.4	21.8	197.3	14.5	3	1.505	-0.19
321	FL98348A	232.7	82.3	68.2	7.4	338	2	12	1.099	0.353
	FL98348B	141.6	77.2	261.9	6.5	353.2	11	12	1.12	0.705
	FL98348C	65.2	46.3	279.3	38.3	174.7	17.7	9	1.39	0.522
322	FL98349A	21.6	84.8	119.8	0.7	209.8	5.1	35	1.103	0.638
	FL98349B	355	77.7	127.4	8.4	218.7	8.9	32	1.158	0.824
	FL98349C	29.5	85.4	197.8	4.5	287.9	0.9	29	1.12	0.809
323	FL98350A	308.5	39	59.4	23.8	172.5	41.6	-24	1.029	-0.136
	FL98350B	245.3	71.3	68.1	18.7	337.8	0.9	-30	1.03	-0.327
324	FL98351A	257.8	66.6	96.3	22.3	3.6	6.7	-1	1.976	0.523
	FL98351B	221.4	32.5	353.8	46.6	113.9	25.3	-1	5.476	-0.401
325	FL98352A	117.4	44.1	319.1	43.1	218.6	11.3	20	1.059	-0.153
	FL98352B	106.6	51.5	0.4	12.6	261.1	35.7	36	1.042	0.209
	FL98352C	154.9	73	25.9	10.9	293.3	12.9	21	1.077	0.267
	FL98352D	141	58.8	260.4	16.5	358.6	25.6	41	1.032	0.391
326	FL98353A	92.8	81.6	278.7	8.2	188.6	0.8	45	1.036	0.382
	FL98353B	61.9	76.8	220.8	12.4	311.8	4.6	44	1.038	0.506
327	FL98354A	254	16.5	12.3	57.9	155.5	26.6	-17	1.078	0.095
	FL98354B	275.8	57.5	121.3	30	24.5	11.5	-15	1.127	-0.236
328	FL98355A	343.8	25.7	94.5	36.3	227.3	42.8	-28	1.055	0.344
	FL98355B	70.9	16.9	328	36.3	181.2	48.7	-24	1.059	0.014
	FL98355C	162.7	82	11	7	280.5	3.8	-27	1.049	0.242
	FL98355D	112.6	24.6	345.3	52.9	215.4	25.9	-27	1.056	0.58
329	FL98356A	58	76.8	258.9	12.3	167.9	4.6	2	1.735	0.323
	FL98356B	289.2	61.9	43.2	12.2	138.9	24.9	2	1.622	0.477
	FL98356C	262.5	62.3	43.4	22.2	140	15.8	3	1.375	0.342
	FL98356D	317.3	50.5	106	35.2	207.4	15.7	2	1.19	0.043
330	FL98357A	107	81.7	265.1	7.7	355.5	3.1	22	1.071	-0.319
	FL98357B	104.2	68.2	257.2	19.7	350.5	9.2	22	1.094	-0.28
	FL98357C	227.7	77	67.5	12.2	336.5	4.3	17	1.072	0.823
331	FL98358A	90.9	40.7	249.8	47.3	351.5	10.7	30	1.093	-0.015
	FL98358B	295.4	86.3	96.9	3.5	187	1.2	33	1.049	-0.114
	FL98358C	267.2	54.1	75	35.7	169.2	5.1	29	1.055	0.608
332	FL98359A	116.1	52.3	219.4	10.1	316.8	35.9	4	1.77	-0.484
	FL98359B	276.9	47.9	100	42	8.6	1.6	4	1.358	0.3
	FL98359C	139.8	70.4	230.3	0.2	320.4	19.6	1	6.322	0.047
	FL98359D	299.6	78.3	102.9	11.2	193.5	3.3	4	1.375	0.012
333	FL98360A	209.5	72.7	76.4	12	343.7	12.2	10	1.116	-0.14

Table B-1 AMS Data

		Minimum		Intermediate		Maximum				
Outcrop	Sample #	Decln.	Incln.	Decln.	Incln.	Decln.	Incln.	Kmean	Pj	Tj
	FL98360B	248.3	61.9	139.9	9.5	45.2	26.2	4	1.385	0.156
334	FL98361A	153.8	78	294	9.3	25.3	7.6	131	1.015	-0.498
	FL98361B	338.7	88.4	139.1	1.5	229.1	0.5	190	1.028	0.757
	FL98361C	203.8	80.6	305.6	1.9	35.9	9.2	269	1.02	0.55
336	FL98363A	85.9	45.7	281.3	43.2	183.9	7.8	28	1.04	-0.447
	FL98363B	126.2	77.5	286	11.8	16.9	4.2	38	1.037	0.435
	FL98364A	225.3	53.5	91.8	27	349.6	22.6	33	1.04	0.392
	FL98364B	66.2	82.2	283.5	6.2	193	4.7	28	1.062	-0.044
	FL98364C	11.2	76.1	246.5	8	154.9	11.3	39	1.055	0.25
337	FL98365A	81.7	0.7	171.8	1	278.4	85.7	-30	1.033	0.008
	FL98365B	130.9	1.3	22.8	55.3	40	34.6	-29	1.336	0.024
338	FL98366A	278.6	42.6	166.6	22.1	57.3	39.2	5	2.748	0.217
	FL98366B	46.2	46.3	297	17.4	192.6	38.5	10	1.607	0.548
	FL98366C	101.5	72.5	260.6	16.4	352.4	5.9	11	1.037	-0.494
	FL98366D	295.9	75.1	48.5	5.8	139.9	13.6	2	131.605	0.634
339	FL98367A	324.7	65.3	177	21.3	82.2	12	-23	1.079	0.426
	FL98367B	310.7	27.8	56.7	27.6	183.5	48.9	-23	1.103	0.24
340	FL98368A	331.6	26.3	218	39	85.8	39.7	-21	1.081	0.195
	FL98368B	176.9	23.9	287.9	39	63.7	41.5	-21	1.221	-0.943
	FL98368C	152.9	81.2	5.8	7.4	275.1	4.7	-22	5.399	-0.092
341	FL98369A	349.2	6.8	243.6	66.1	82.1	22.8	-13	1.077	-0.771
	FL98369B	3.3	36.4	121.3	32.4	239.7	36.9	-14	1.051	-0.131
	FL98369C	150.7	81	306.1	8.2	36.6	3.7	-15	1.076	-0.256
342	FL98370A	143	42.4	253.3	20.8	2.2	40.4	14	1.11	0.092
	FL98370B	176.9	23.9	22.3	63.8	271.4	10	19	1.126	0.159
343	FL98371A	277.7	85.1	118.6	4.9	28.5	1.3	42	1.029	0.505
	FL98371B	354.8	68	198.3	20.3	105.3	8	47	1.036	-0.168
	FL98371C	2.4	49.4	233.8	28.1	128.2	26.7	49	1.031	0.34
	FL98372A	153.4	29.6	58.3	0	333.4	60.4	12	1.07	-0.488
	FL98372B	38.3	72.3	216.5	17.7	306.7	0.5	14	1.057	-0.49
	FL98372C	292.8	69.3	175.9	9.7	82.7	18.1	14	1.11	-0.447
344	FL98001A	109.6	69.2	299.9	20.1	208.7	3.7	58	1.021	-0.329
	FL98001B	33	75.3	251.1	11.7	159.3	8.8	49	1.054	0.319
	FL98373A	102.9	69.2	321.2	16.6	227.5	12.2	9	1.178	0.496
	FL98373B	289.5	62.7	83.2	24.9	178.2	10.7	8	1.296	0.017
	FL98373C	171.4	76.4	22.9	11.6	291.5	6.9	9	1.262	0.445
	FL98374A	33.2	60.6	288.9	7.9	194.7	28.1	2	1.31	0.999
	FL98374B	347.2	66.7	160.3	23.1	251.3	2.5	6	1.417	-0.5005
345	FL98375A	306.8	46.1	135.2	43.6	41.2	4.2	1	1.747	0.528
	FL98375B	8.1	35.1	128.2	35.5	248.4	35.2	0	3.879	-0.214
	FL98375C	233.6	69.6	113.2	10.7	19.8	17.2	3	1.371	0.399
346	FL98376A	102	53.6	205.9	10	302.9	34.5	-6	1.141	-0.476
	FL98376B	155.1	80.9	62	0.5	331.9	9.1	-5	1.239	-0.038
	FL98376C	131.4	57.5	291.3	30.9	26.8	9.2	-5	1.174	-0.734
347	FL98377A	241.9	76.2	88.5	12.4	357.1	6	-12	1.085	0.2
	FL98377B	252.7	43.2	111.8	39.6	3.6	20.8	-10	1.114	0.474
	FL98377C	119.9	73.5	212.4	0.7	302.6	16.5	-8	1.094	-0.229

Table B-1 AMS Data

		Minimum		Intermediate		Maximum				
Outcrop	Sample #	Decln.	Incln.	Decln.	Incln.	Decln.	Incln.	Kmean	Pj	Tj
348	FL98378A	85.6	86.2	252.4	3.7	342.5	0.9	26	1.271	0.533
	FL98378B	38.4	80.6	254.7	7.6	163.9	5.5	23	1.073	0.512
349	FL98379A	75	48.8	203.9	28.8	310	26.7	14	1.307	0.192
	FL98379B	286.6	78.3	73.6	9.8	164.7	6.2	12	1.185	-0.296
350	FL98380C	16	55.1	232.2	29.9	132.6	16.2	23	1.107	0.65
351	FL98381A	13.7	73.6	125.4	6.2	217.1	15.1	24	1.039	0.561
	FL98381B	83.6	71.3	268.5	18.6	178	1.5	25	1.052	-0.374
	FL98381C	275.5	70.8	143.9	13	50.6	13.9	23	1.065	-0.185
352	FL98382A	333.4	76	86	5.4	177.3	12.8	10	1.126	-0.479
	FL98382B	15.3	77.4	268.8	3.6	178.1	12.1	10	1.184	-0.017
	FL98382C	188.5	85.5	21.2	4.4	291.1	1	11	1.15	0.281
	FL98383A	193.9	83.4	55.2	4.9	324.8	4.3	10	1.077	0.267
	FL98383B	83.7	75	252.8	14.8	343.5	2.7	5	1.314	0.208
353	FL98384A	66.8	73.3	290.4	12.2	198	11.2	7	1.132	0.575
	FL98384B	199.1	81.9	73.7	4.7	343.2	6.6	16	1.1	0.484
354	FL98385A	147.8	44.9	239.7	2	331.7	45	1	6.217	0.594
	FL98385B	100.4	29.3	279.8	60.7	10.2	0.2	-1	2.59	0.372
	FL98386A	135.7	41.4	261.7	33.7	14.7	30.3	-4	1.602	0.488
	FL98386B	102	33.4	301.9	54.9	198.2	9.4	-2	1.479	0.204
355	FL98387A	113	81.8	266.9	7.4	357.4	3.6	27	1.052	0.698
	FL98387B	225.2	75.3	354.1	9.4	86	11.3	27	1.052	-0.131
356	FL98388A	147.6	33.2	302.7	54.2	49.7	11.9	5	4.809	0.164
	FL98388B	276.9	43.8	100.8	45.3	8.8	2.1	-5	1.269	0.432
357	FL98389A	199.9	73.9	300.2	3	31.1	15.8	16	1.08	-0.213
	FL98389B	322.9	36.1	70.6	22.6	185.4	45.3	15	1.418	0.852
358	FL98390A	223	84.8	318.1	0.5	48.1	5.2	41	1.061	0.263
	FL98390B	130.5	76.5	236.3	3.7	327.2	12.9	41	1.068	0.473
	FL98390C	302.7	71.1	50.1	5.8	142	17.9	31	1.124	0.002
359	FL98391A	281.9	65.5	84.8	23.5	177.6	6.4	43	1.073	0.414
1*	CY9701A	82.4	47	316	29	208.4	28.8	6	1.168	-0.163
	CY9701B	282.5	71.6	16.6	1.5	107.2	18.5	7	1.173	0.308
	CY9701C	312.4	80.6	128.4	9.4	218.6	0.6	7	1.158	0.127
	CY9701D	342.5	16.6	237.9	40.3	90.1	45	11	1.048	0.607
	CY9701E	344.6	72.8	129.4	14.1	221.8	9.6	9	1.073	0.16
2*	CY9702A	29.5	33.2	151.1	38.8	273.6	33.7	9	1.074	-0.126
	CY9702B	91.3	57	252.4	31.5	347.8	8.6	5	1.2	0.626
	CY9702C	313.5	52	84.4	27.1	187.9	24.5	6	1.116	-0.116
3*	CY9703A	18.5	82.1	107.4	3	198.4	7.9	9	1.102	0.134
	CY9703B	73.3	14.4	295.6	70.8	166.4	12.4	7	1.095	0.165
	CY9703C	241.4	12.8	355.5	61	145.3	25.6	8	1.11	-0.538
	CY9703D	12.9	69.8	244.8	12.9	151.1	15.4	7	1.096	-0.121
4*	CY9704A	306.4	15.3	213.9	8.8	95.2	72.3	-2	2.974	-0.402
	CY9704B	271.4	12.4	118.2	76.2	2.8	6.1	-2	8.492	-0.465
	CY9704C	234.6	55.8	110.8	20.6	10.3	25.9	-2	1.363	0.216
5*	CY9705A	69.2	74.2	267.4	15.1	176.1	4.8	15	1.114	0.085
	CY9705B	292.5	58.8	127.8	30.3	33.8	6.8	16	1.05	0.012
	CY9705C	177.6	17.5	342.3	71.8	86.2	4.6	16	1.04	-0.662

Table B-1 AMS Data

		Minimum		Intermediate		Maximum				
Outcrop	Sample #	Decln.	Incln.	Decln.	Incln.	Decln.	Incln.	Kmean	Pj	Tj
	CY9705D	272.9	23.3	171.8	24.3	41.2	55.3	15	1.078	0.468
6*	CY9706A	270	45	59	40.7	163.4	16	-6	1.168	0.43
	CY9706B	151.6	16.4	299	70.8	58.7	9.8	-6	2.502	0.169
	CY9706C	298.1	81.8	87.8	7.2	178.4	4.2	-6	3.265	-0.294
	CY9706D	241.1	25.9	360	45	132.1	33.8	-7	1.138	-0.169
	CY9706E	8.6	67.7	118.3	7.8	211.3	20.8	-7	1.13	-0.535
7*	CY9707A	74.4	69.9	266.5	19.6	175.1	3.8	-1	1.129	-0.536
	CY9707B	328	72.1	82.8	7.8	175.1	16.1	0	3.047	0.658
	CY9707C	309.6	83.8	51	1.3	141.1	6.1	0	3.367	0.277
	CY9707D	289.5	56.7	178.9	13.1	81.3	30	-1	3.367	0.277
	CY9707E	274.1	62.2	74.3	26.5	168.4	8.1	-1	2.908	0.248
8*	CY9708A	63.2	33.8	225.1	54.8	327.4	8.6	-8	1.086	-0.123
	CY9708B	226.3	82.2	15.4	6.8	105.8	4	-8	1.245	-0.057
	CY9708C	275.3	51.8	32.8	20	135.4	31	-8	1.174	0.267
9*	CY9709A	340.5	63.2	100.1	14.1	195.9	22.4	-11	1.075	-0.743
	CY9709B	263.9	13.6	30.5	68.1	169.6	17	-11	1.107	0.025
	CY9709C	237.6	81.2	80.9	8.1	350.5	3.5	-12	1.04	-0.191
	CY9709D	319.6	62.5	213.3	8.4	119.2	26	-12	1.07	-0.0488
	CY9709E	22.3	38.3	218.9	50.5	118.8	8.3	-11	1.053	-0.322
	CY9709F	239.6	49	134.3	13.1	33.8	38	-11	1.071	0.265
	CY9710A	69.4	60.3	266.6	24.5	189.3	15.9	-8	1.106	-0.087
	CY9710B	352.8	78.2	228.4	6.8	137.1	9.8	-11	1.064	-0.128
	CY9710C	275.3	14.1	72.7	74.8	183.9	5.6	-9	1.12	0.298
	CY9710D	82.7	14.4	296.9	72.8	175.1	9.3	-10	1.072	0.159
10*	CY9711A	125.8	30	0.1	45	235.1	29.8	-2	1.323	-0.681
	CY9711B	282.1	48	61.8	34.3	166.9	21	-1	1.538	0.298
	CY9711C	79.9	49	287.8	37.5	186.6	14.1	-1	1.991	0.718
	CY9711D	80.7	56.5	267.8	33.3	175.6	3.3	0	4.522	0.405
11*	CY9712A	90.1	45	297.8	41.5	194.8	14.3	-18	1.059	0.608
	CY9712B	83.1	30.4	275.1	59	176.1	5.3	-18	1.083	0.086
	CY9712C	99.8	37.5	267.6	51.8	5.3	5.8	-18	1.068	0.347
	CY9712D	36.7	84.6	146.6	1.9	236.8	5.2	-19	1.031	0.007
	CY9713A	93.8	9.6	357.3	34.5	197.1	53.8	-7	1.127	-0.307
	CY9713B	349.5	40.3	134.3	44	242.9	18.5	-8	1.075	0.348
	CY9713C	84.8	9.9	180.1	26.5	335.8	61.3	-8	1.115	-1
	CY9713D	228.3	42.3	83.9	41.7	336.4	18.9	-9	1.129	0.12
	CY9713E	280	40	69.3	45.8	176.3	15.9	-8	1.25	0.211
12*	CY9714A	292.3	73.6	102.7	16.3	193.4	2.7	18	1.083	0.086
	CY9714B	327.4	73.4	69.3	3.5	160.3	16.1	16	1.037	0.009
	CY9714C	45	85.4	225.1	4.6	225.1	54.8	17	1.045	0.719
	CY9714D	89.2	30	257.3	59.3	356.1	5.3	21	1.053	0.103
13*	CY9715A	23.4	74.6	273.4	5.4	181.9	14.4	24	1.051	0.012
	CY9715B	112.6	54	284.3	35.8	17.1	4	22	1.041	0.121
	CY9715C	270	45	40	32.8	149.1	27.1	25	1.049	-0.492
	CY9715D	287.8	41.5	100.3	48.3	194.4	3.8	24	1.028	-0.136
	CY9715E	104.1	28.1	224.6	43.5	353.3	33.5	23	1.07	-0.59
14*	CY9721A	76.3	31.9	277	56.5	172.4	9.6	-2	1.622	0.337

Table B-1 AMS Data

		Minimum		Intermediate		Maximum				
Outcrop	Sample #	Decln.	Incln.	Decln.	Incln.	Decln.	Incln.	Kmean	Pj	Tj
	CY9721B	263.5	22.5	18.6	45.8	156.4	35.7	-5	1.243	-0.114
	CY9721C	267.3	16.6	35.8	64.3	171.4	19	-3	1.275	0.474
	CY9721D	306.9	45	87.9	37.8	194.9	20.5	-6	1.138	0.522
15*	CY9722A	307.8	61.7	103.4	26.1	198.4	10.1	3	1.305	-0.045
	CY9722B	235.9	79.1	66.6	10.8	336.1	2	5	1.096	0.221
	CY9722C	95.8	25.4	341.6	40.8	207.9	38.7	5	1.291	0.579
	CY9722D	149.6	77.4	250.1	2.3	340.5	12.4	5	1.167	0.285
16*	CY9723A	88.6	18.4	246.1	70.3	356.1	6.9	8	1.138	0.425
	CY9723B	92.2	10.1	308.3	77.6	183.4	7.2	12	1.22	0.246
	CY9723C	81.3	16.8	294.5	70.2	174.4	10.3	15	1.088	-0.056
	CY9723D	323	61.8	94.7	19.5	191.9	19.4	11	1.105	-0.811
	CY9723E	103.3	61.8	284.5	28.3	194.3	0.6	13	1.094	-0.145
	CY9723F	246.9	74.9	66.8	15.1	344.3	18.1	9	1.221	0.375
	CY9723G	103.1	54.8	322.9	57.3	202.3	18.4	12	1.061	0.44
	CY9723H	253.8	4.6	224.1	57	338.1	17.5	13	1.111	0.309
	CY9723I	12.3	78.2	113.3	23	203.8	11.6	8	1.075	0.018
17*	CY9724A	42.2	80.3	287.4	4.1	196.6	8.8	17	1.0107	0.246
	CY9724B	335.1	81.8	106.9	5.4	197.6	6.1	20	1.081	0.267
	CY9724C	121.7	87.6	266.4	2	356.4	1.5	20	1.08	0.267
	CY9724D	299.5	80.1	115.3	9.9	205.4	0.8	16	1.116	0.547
	CY9724E	188.1	85.2	291.3	1	21.3	4.8	21	1.119	0.583
	CY9724F	292	75.1	97.3	14.4	188.3	3.7	20	1.096	0.075
	CY9724G	43	82.4	291.1	2.8	200.8	7.1	22	1.097	0.165
18*	CY9725A	96.9	31.1	305.1	55.7	195.1	13.1	-19	1.046	0.122
	CY9725B	95.7	38	247.6	48.5	354.1	14.3	-20	1.066	-0.216
	CY9725C	93.4	17.8	310.5	68.1	187.4	12.4	-21	1.041	-0.101
	CY9725D	133.4	5.2	233.4	62.8	40.8	26.5	-21	1.053	0.284
	CY9725E	82.8	62.3	272.4	27.4	180.3	4	-22	1.059	0.674
	CY9726A	90.1	23.1	197.9	35.8	334.5	45.3	-11	1.91	0.22
	CY9726B	94.4	29.5	250.9	58.3	358.5	10.6	-10	1.107	0.295
	CY9726C	284.1	44.2	90.1	45	187.1	7.2	-13	1.047	0.343
	CY9726D	90.1	45	278.6	44.7	184.4	4.3	-12	1.126	0.358
	CY9726E	254.9	32.8	126.6	44	5.2	28.3	-6	1.368	0.398
	CY9726F	92.8	19.1	234.6	66.2	358	13.8	-13	1.084	0.11
	CY9727A1	260.4	41.7	67.3	47.7	164.6	6.6	11	1.087	-0.18
	CY9727A2	296.6	41.8	90.1	45	194.1	13.6	12	1.092	-0.438
	CY9727A3	108.3	59	249.9	25.3	348.1	16.8	10	1.05	-0.189
	CY9727A4	96.1	9.9	188.4	13.3	330.3	73.3	14	1.12	0.519
	CY9727A5	278	21.6	149.9	57.2	17.9	23.4	12	1.074	-0.094
19*	CY9727B1	238.1	74.3	78.2	14.8	346.9	5.2	7	1.122	0.139
	CY9727B2	210.6	74.3	54.8	14.4	323.1	6.3	13	1.083	-0.255
	CY9727B3	165.8	58.3	331.8	30.9	65.4	6.3	15	1.045	0.153
	CY9727B4	194.9	69.2	89.4	5.8	357.4	20	19	1.053	0.013
	CY9727B5	197.1	64.8	57	19.9	321.4	14.9	19	1.057	0.104
20*	CY9728A	301	77.1	100.1	12.1	191.1	4.4	26	1.046	0.177
	CY9728B	39.7	71.8	130.4	0.3	220.4	18	36	1.062	-0.351
	CY9728C	279.8	66.1	74.8	22	168.4	9.1	47	1.03	-0.423

Table B-1 AMS Data

		Minimum		Intermediate		Maximum				
Outcrop	**Sample #**	**Decln.**	**Incln.**	**Decln.**	**Incln.**	**Decln.**	**Incln.**	**Kmean**	**Pj**	**Tj**
	CY9728D	292.5	65.3	53.8	13.4	148.9	20.4	34	1.035	0.641
	CY9728E	64.6	77.2	245.9	12.9	155.9	0.3	28	1.051	0.154
21*	CY9729A	57.7	81.2	261	8.1	170.4	3.5	13	1.083	0.29
	CY9729B	40.5	75.8	261.3	10.9	169.4	9.1	13	1.069	0.347
	CY9729C	326.9	56.5	123.3	31.3	220.1	10.9	13	1.03	0.007
	CY9729D	315	70.8	135.1	0.1	135.1	19.3	11	1.101	0.807
22*	CY9730A	83.8	64.9	266.3	25	175.9	0.9	-14	1.142	0.683
	CY9730B	287.5	38.8	127.3	49.2	25.6	10.1	-14	1.034	0.208
	CY9730C	305.6	53.8	53.8	12.9	152.4	33.2	-13	1.036	-0.192
	CY9731A	140.9	34.7	276.5	45.8	33.3	23.6	-15	1.103	-0.448
	CY9731B	95.6	20.1	331.5	56.8	195.6	25.3	-13	1.123	-0.097
	CY9731C	282.5	73.6	114.2	16.1	23.1	3.2	-14	1.059	-0.745
	CY9731D	322.1	18	147.8	71.8	52.7	1.6	-14	1.028	0.007
23*	CY9732A	276.8	63.3	76.9	25.3	170.8	7.8	-10	1.064	0.674
	CY9732B	300.5	46.2	80.8	36.5	187.1	20.9	-10	1.048	0.211
	CY9732C	245.9	74.4	83.6	14.9	352.4	4.6	-9	1.087	0.269
	CY9732D	97.8	7.8	195.4	44	360	45	-10	1.029	-0.328
	CY9732E	55	65.3	301.8	10.3	207.6	22.3	-7	1.053	0.013
34*	CY9748A	31.4	43.8	125.1	3.8	219.1	46	3	1.228	-0.387
	CY9748B	90.1	45	281.5	44.5	185.8	5.8	0	5.456	-0.56
	CY9748C	43.5	36	180.1	45	295.4	23.1	0	4.455	-0.561
	CY9748D	33.2	56.5	236.6	31.3	139.9	10.9	1	1.313	0.546
	CY9748E	27.3	35.3	267.3	35.3	147.3	35.3	4	1.134	-0.306
35*	CY9749A	19.6	76.4	137.9	6.6	229.3	11.9	100	1.092	0.65
	CY9749B	39	71.2	295	4.7	203.4	18.1	92	1.065	0.573
	CY9749C	15.8	74.7	141.4	9.1	233.4	12.3	67	1.088	0.708
	CY9749D	13.1	68.4	169.9	20	262.8	7.8	88	1.082	0.35
	CY9750A	117.4	58.2	8.3	11.6	271.6	29.3	65	1.079	0.662
	CY9750B	128.1	48.5	339	37.3	236.6	15.6	69	1.179	0.693
	CY9750C	118.6	60.3	318.9	28.3	224.1	8.8	57	1.082	0.723
	CY9750D	106.6	65.1	303.3	24	210.4	6.3	80	1.077	0.89
	CY9750E	108.7	65.3	260.4	22	354.6	10.6	75	1.082	0.962
36*	CY9751A	262	52.7	84.1	37.3	353.3	1	157	1.052	0.377
	CY9751B	264.5	54.8	97.1	34.7	3	5.9	136	1.057	0.489
	CY9751C	255.4	46	74.4	44	164.9	0.4	146	1.044	0.483
37*	CY9752A	54.5	76.3	286	8.6	194.4	10.6	24	1.064	0.478
	CY9752B	92.6	66.3	276.6	22.9	185.9	1.5	25	1.066	0.264
	CY9752C	86.9	14.1	338.5	51.7	186.9	34.8	27	1.066	0.54
	CY9752D	216.8	61.5	77.2	22.5	340	16.5	23	1.078	-0.637
43*	CY9766A	102.2	23	335.8	54.5	203.8	25.5	7	1.122	-0.083
	CY9766B	92.6	20.1	297.3	68.1	185.6	8.4	5	1.33	0.012
	CY9766C	101.2	46.5	261	41.7	0.3	10.3	3	1.361	-0.442

Distribution of AMS Foliatic

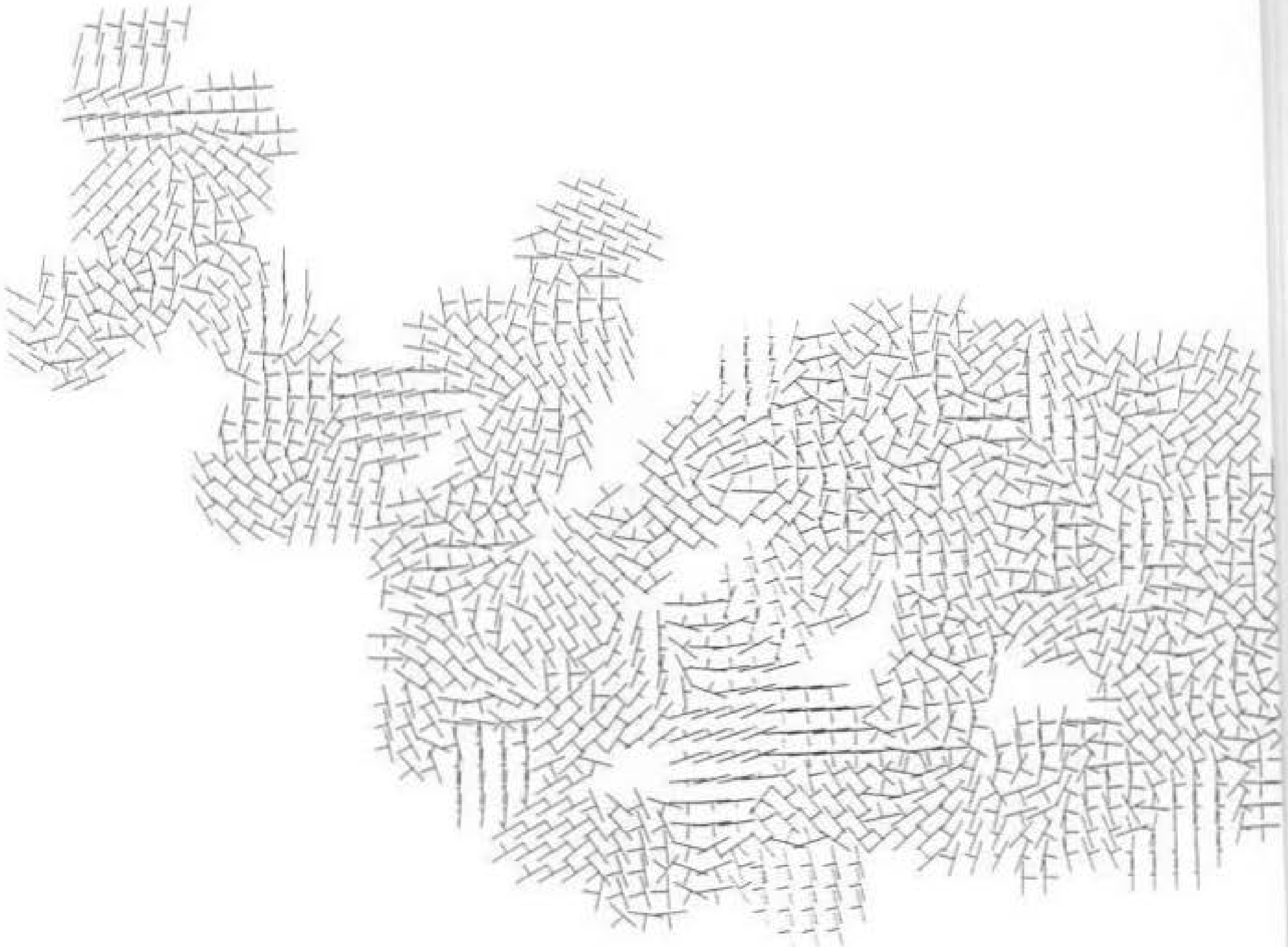

Figure B-1 Spatial distribution of AMS foliation data. Averaging stations are locatec
is include within that station's average where the data is weighted with r

›n Orientation Spatial Averaging

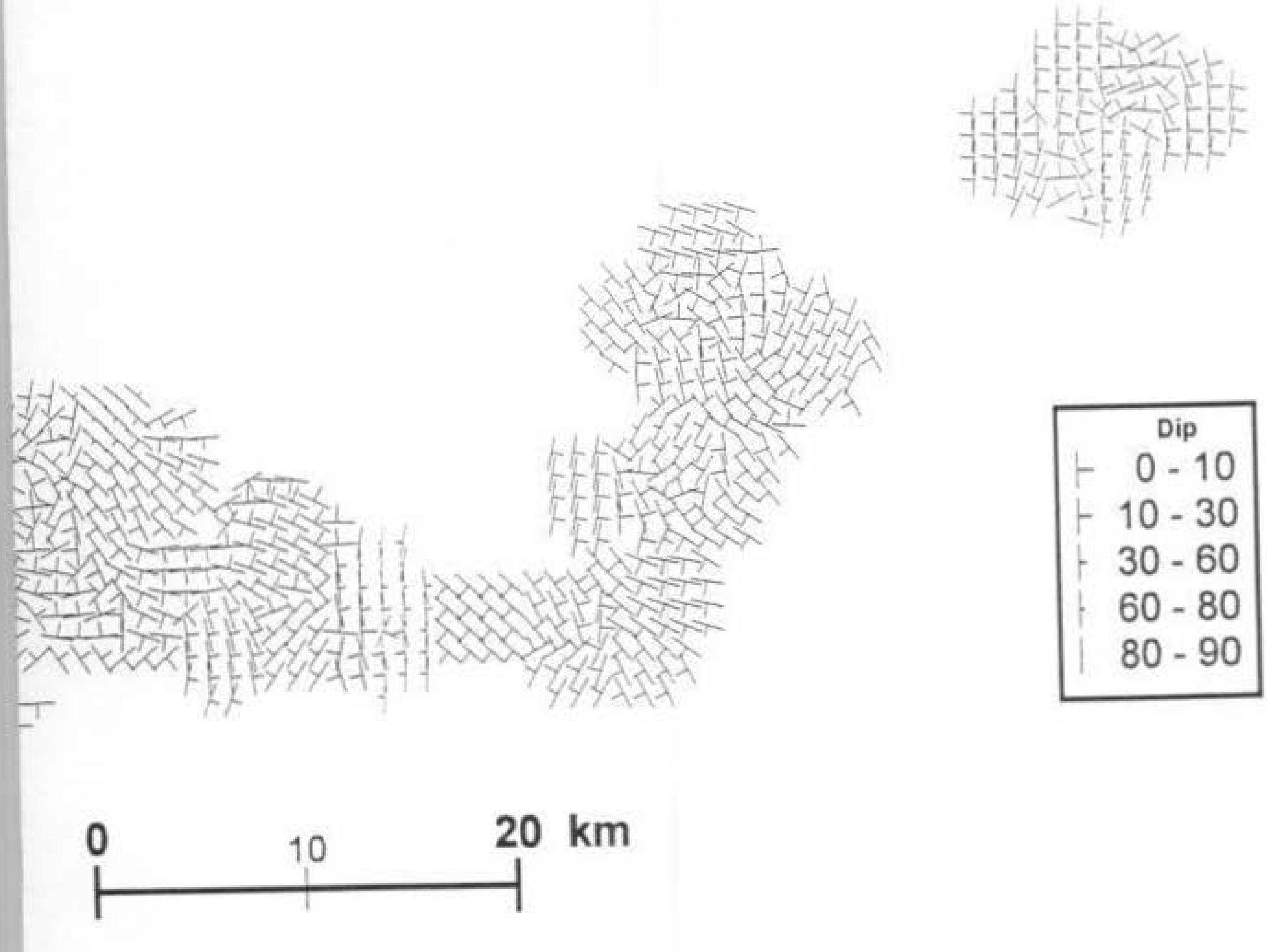

l one kilometer apart both in the N-S and E-W directions. Data within a 2.5 km radius of a station
espect to their distance from the station.

Distribution of AMS Linea

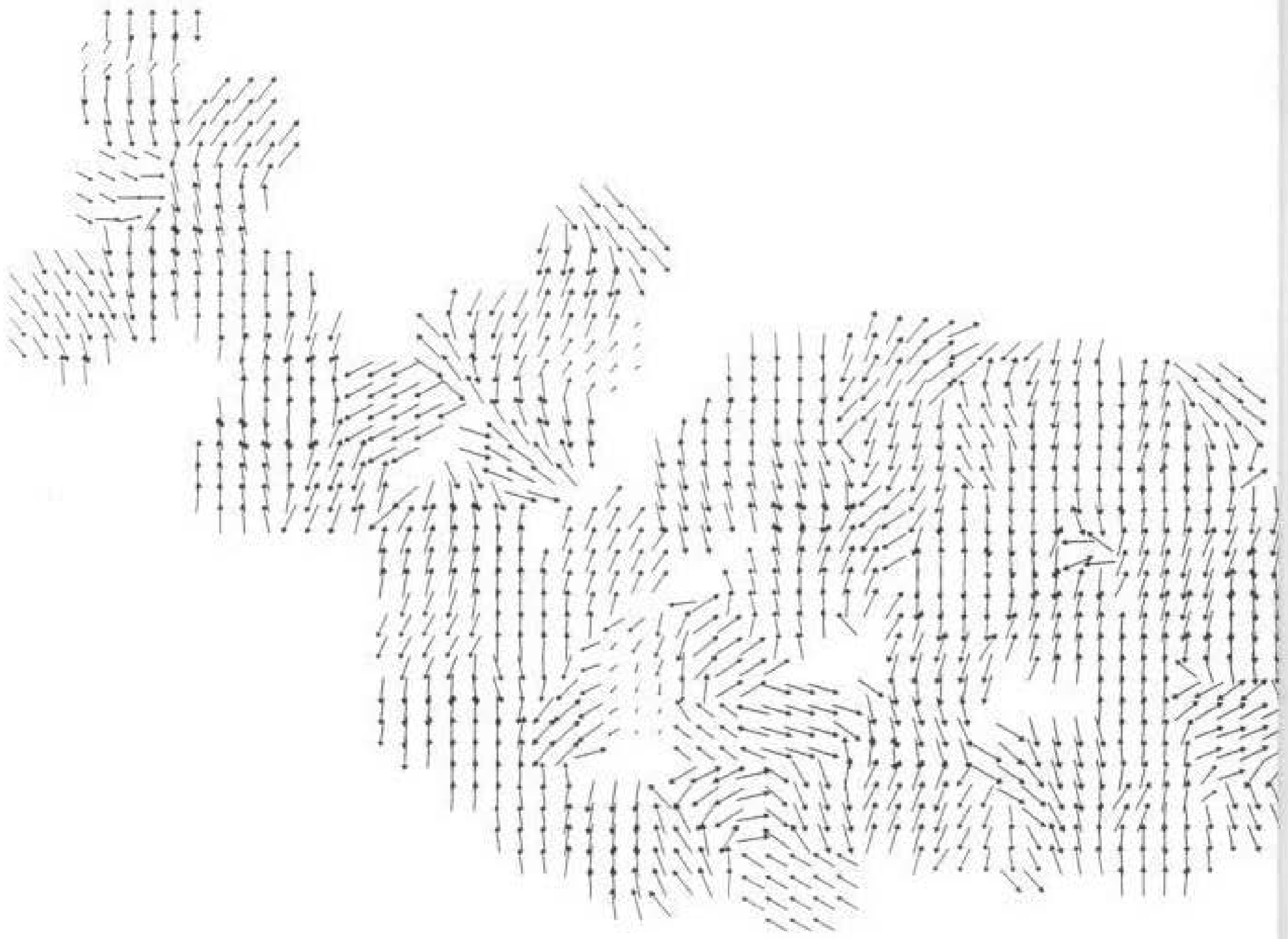

Figure B-2 Spatial distribution of AMS lineation data. Averaging stations are locate
is include within that station's average where the data is weighted with r

ation Orientation Spatial Averaging

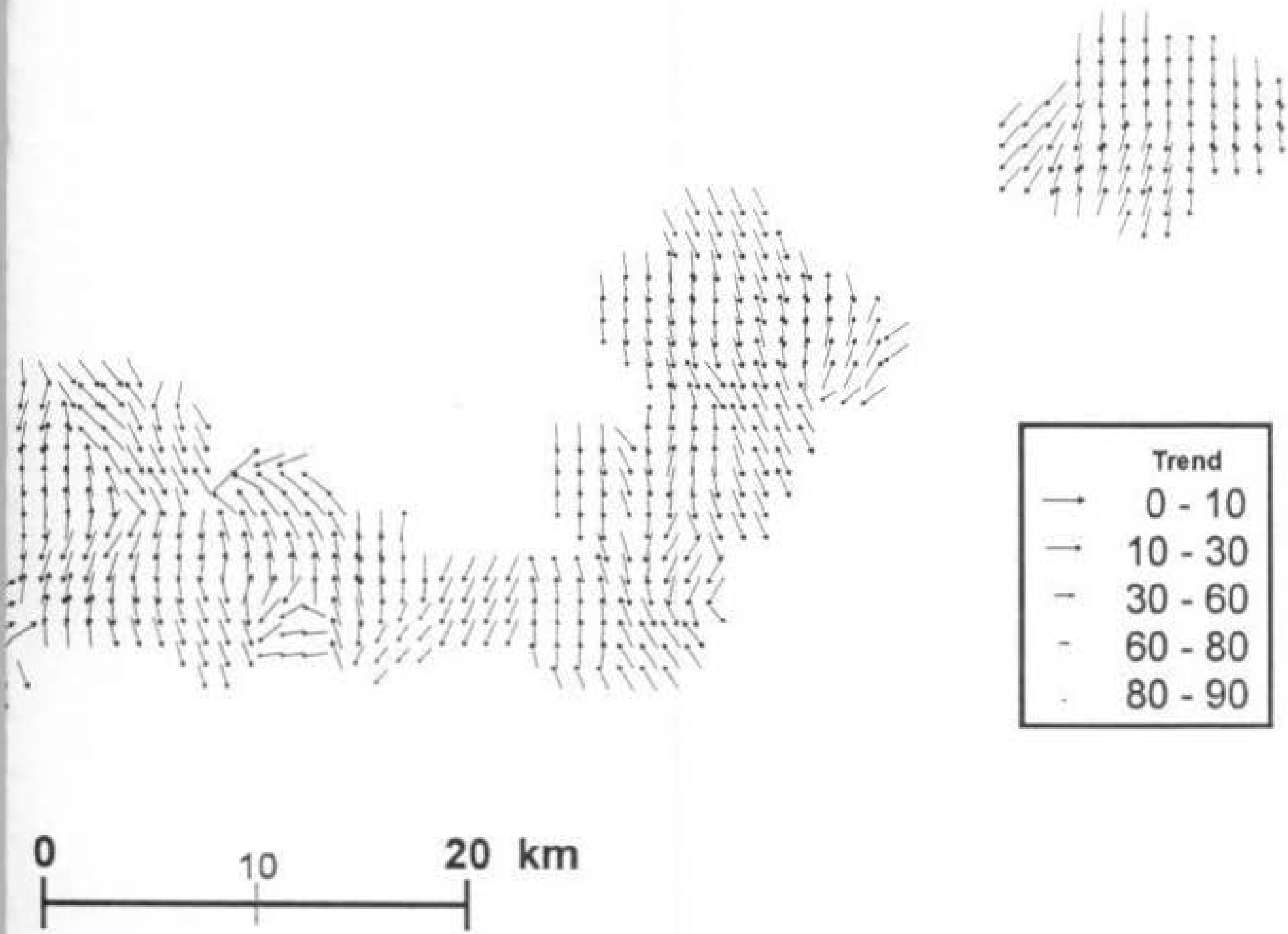

d one kilometer apart both in the N-S and E-W directions. Data within a 2.5 km radius of a station
espect to their distance from the station.

Appendix C

Anisotropy of Anhysteretic Remanence Magnetization Data (AARM)

Table C-1 AARM Data

		minimum		intermediate		maximum				
Outcrop	Sample	decln.	inclin.	decln.	inclin.	decln.	inclin.	Kmean	Pj	Tj
5	FL98004A	143.8	77	317.6	12.8	47.9	1.3	3	1.06	0.014
	FL98005D	1.3	17.4	268.3	9.5	150.9	69.9	4	1.044	0.01
6	FL98006A	39.2	15	245.6	73.3	131.1	7	1	1.072	0.996
7	FL98007C	53.9	51.7	200.6	33.3	301.9	16.4	1	1.089	-0.998
8	FL98008A	334.2	73.5	225.6	5.3	134.1	15.4	1	1.089	0.997
10B	FL98013A	241.6	69.6	116.6	11.9	23.1	16.1	1	1	1
11	FL98014A	190.6	59.7	91.3	5.3	358.3	29.7	2	1.052	-0.996
12	FL98015A	270.1	56.1	160.8	12.4	63.2	30.8	4	1.042	0.01
13	FL98016A	249.6	16.1	150.6	28.4	5.5	56.5	3	1.036	0.993
	FL98017B	250.2	31.8	140.1	28.9	17.5	44.2	3	1.062	0.015
14	FL98018A	223.1	69.6	62.4	19.3	330.2	6.2	3	1.099	0.997
	FL98019B	243.2	55.6	135.6	11.6	38.2	31.7	3	1.087	0.351
15	FL98020B	320.2	77.8	215.4	3.1	124.7	11.6	167	1.061	0.154
	FL98024A	214.9	38.4	114.2	13.2	8.7	48.5	1	1	1
	FL98024C	11.4	36.1	223.5	49.1	113.8	16.2	1	1.077	-0.997
19	FL98025A	242	42.3	46.8	46.6	145	7.6	1	1.116	0.997
	FL98026A	358.2	73	245.1	6.8	153.2	15.4	1	1.105	0.997
23	FL98030B	179.3	83.4	358.4	6.5	88.5	0	1	1	1
25	FL98032B	4.5	41.2	233.3	36.9	120.9	26.8	1	1.343	0.395
28	FL98035B	300.1	79.7	184.1	4.5	93.3	9.2	3	1.064	0.015
30	FL98038A	245.4	58.8	350.9	9.1	86.1	29.4	1	1.111	0.026
31	FL98039A	244	61.3	357.3	12.1	93.2	25.4	2	1.152	-0.302
32	FL98040A	230.3	58.8	348.7	16	86.7	25.9	1	1.105	0.997
35	FL98043B	270.2	76.1	132.4	10.3	40.7	9.1	21	1.076	0.61
36	FL98044B	232	71.2	128.5	4.5	37	18.1	26	1.044	0.462
37	FL98045B	263.5	73.1	118.3	14	26	9.2	1	1.089	0.997
38	FL98046B	196.9	59.1	87.2	11.3	351	28.2	1	1.082	0.997
39	FL98047D	121.6	51.5	272.5	34.7	12.7	14.3	1	1.105	0.997
40	FL98048A	244.3	67.8	151.2	1.2	60.7	22.1	4	1.028	0.991
43	FL98052A	2.4	16.4	262.4	30.3	117	54.5	8	1.049	0.508
44	FL98054A	226.5	29.7	332.9	26.3	96.7	48.2	7	1.165	0.203
46	FL98056A	124.8	74	320.3	15.4	229.2	4.1	2	1.052	-0.996
	FL98057C	129.7	35.7	265.8	45.1	21.6	23.4	1	1.125	0.029
47	FL98058A	101	69.8	258.2	18.6	350.6	7.2	0	1	1
48	FL98059A	100.4	54.5	321.2	28.3	220.2	19.4	3	1.14	0.23
49	FL98060A	176.3	63.3	319.7	22	55.7	14.3	3	1.066	0.016
54	FL98065A	189.9	56.7	292.6	8.1	27.7	31.9	4	1.428	0.529
57	GBFL002C	123.6	83.5	262.7	4.8	353	4.2	1	1.089	0.997
58	GBFL003D	274.6	5.8	10.6	45.4	178.9	43.9	3	1.2	0.045
59	GBFL004A	170.4	77.6	300.6	8.1	31.9	9.4	2	1.297	0.698
60	GBFL005C	127.2	74.2	318.9	15.5	228	3	2	1.402	0.607
61	GBFL006A	263.8	69.3	134.3	13.5	40.5	15.4	1	1.237	0.378
62	GBFL007A	119	56.9	297.3	33.1	27.8	0.8	4	1.132	0.229
67	FL98069A	113.8	67.8	323.8	19.5	230.1	10.3	2	1.116	-0.998
68	FL98070A	102	72.3	311.1	15.5	218.9	8.2	1	1.205	0.372
69	FL98071B	117.3	55.1	333.1	29.5	233.2	16.9	1	1.195	0.998
73	FL98075B	122.2	56.4	308.8	33.4	216.8	3	2	1.146	0.362
74	FL98076A	143.2	39.1	276.5	40.1	30.3	25.5	3	1.09	0.351
76	FL98079A	147.4	72.1	313.7	17.4	44.9	4	1	1.089	0.997
78	FL98081A	205.6	84.3	309.2	1.3	39.3	5.4	3	1.324	0.801

Table C-1 AARM Data

		minimum		intermediate		maximum				
Outcrop	Sample	decln.	inclin.	decln.	inclin.	decln.	inclin.	Kmean	Pj	Tj
79	FL98082A	144.3	73	308.7	16.3	40	4.2	5	1.304	0.699
80	FL98083A	157.9	81.8	300	6.5	30.5	5	3	1.26	0.472
81	FL98084B	327.2	86.8	153.2	3.1	63.1	0.3	9	1.229	0.483
82	FL98085B	310.4	63.8	149.1	24.9	55.6	7.3	2	1.138	-0.305
83	FL98086A	58.3	84.1	216.1	5.4	306.3	2.1	6	1.336	0.895
84	GBFL010B	189.5	71.6	80	6.3	348	17.1	0	1.129	0.998
88	FL98090A	90.5	25	252.9	63.8	357.3	6.9	1	1	1
	FL98090B	234.3	59.8	344.9	11.5	81	27.4	1	1.077	-0.997
91	FL98093D	343.9	36	243.5	13.9	136	50.5	0	1	1
92	FL98094B	257.5	66.2	357.7	4.4	89.6	23.2	1	1.181	0.041
96	FL98098B	142.2	60	305.9	28.9	39.9	7	7	1.026	0.006
97	FL98099B	296.4	69.4	186.3	7.3	93.8	19.1	1	1.181	0.041
98	FL98100A	269.9	8.4	167.6	55	5.5	33.6	7	1.048	-0.996
106	FL98108A	262.1	82.4	138.4	4.2	48	6.2	5	1.311	0.345
112	FL98116A	276.4	74.6	46.8	10	138.9	11.4	1	1.082	0.997
114	FL98118B	348.2	72	244.3	4.4	152.9	17.3	0	1.129	0.998
122	FL98126B	122.8	1.6	213.4	17.6	27.8	72.2	1	1.105	-0.998
128	FL98135B	329.9	67.8	224.3	6.2	131.8	21.1	2	1.041	0.994
132	FL98140B	265.3	65.4	355.7	0.2	85.8	24.5	3	1.105	0.354
134	FL98142B	164.1	47	266.2	11	5.9	40.8	2	1.095	0.022
136	FL98144A	97.2	11.7	206.5	57.7	0.5	29.5	1	1	1
138	FL98147B	183.8	73.9	307.3	8.9	39.4	13.1	1	1	1
140	FL98149A	350.4	73.7	90	2.7	180.8	15.9	1	1.064	0.996
142	FL98151A	0.4	74.8	201.8	14.1	110.4	5.2	1	1.181	0.041
143	FL98152A	149.3	53.3	280.4	26	22.9	23.8	9	1.09	0.021
145	FL98154D	148.9	64.6	284.2	18.6	19.9	16.6	1	1.2	0.045
147	FL98158B	136.8	47	274.5	34.5	20.8	22.1	2	1.174	0.04
	FL98159B	145.6	45.6	274.6	31.6	23.3	27.5	2	1.083	0.02
148	FL98160B	180.5	63.2	287.1	8.2	21	25.2	1	1.181	0.041
	FL98161A	155.8	66.3	297.6	19	32.4	13.5	1	1.2	0.045
151	FL98166A	155.3	66.3	289.5	17	24.5	15.9	2	1.133	0.36
152	FL98167B	178.2	69.7	298.5	10.5	31.7	17	6	1.138	0.032
	FL98168B	145.3	71.7	301.5	16.7	33.6	6.9	10	1.123	0.194
153	FL98169B	159.5	54.4	275.8	17.5	16.2	29.7	3	1.212	-0.096
154	FL98170B	135	54.6	310.2	35.3	41.8	2.2	1	1.181	0.041
158	FL98174B	93.9	58.1	235.2	25.8	333.9	17.2	0	1.234	0.998
163	FL98181B	168.6	66.2	302	16.8	37	16.3	5	1.243	0.816
	FL98182A	172.3	65.4	320.9	21.3	55.5	11.6	4	1.21	0.157
164	FL98183C	135	46.4	321.6	43.3	228.5	3.3	45	1.105	-0.042
165	FL98184C	171.6	43.7	283	20.8	31	38.9	13	1.146	-0.533
166	FL98185B	151.8	51.4	281.9	27.1	25.8	25	10	1.096	0.353
167	FL98186C	167.2	48.3	309.9	35.2	54.1	19.2	9	1.118	0.118
168	FL98187A	119.4	43.5	307.2	46.2	213.1	3.9	4	1.09	0.515
169	FL98188B	158.7	41.7	302.5	42.1	50.7	19.1	5	1.122	0.028
170	FL98189A	121.1	29.1	27	7.3	284.3	59.8	1	1.061	0.996
171	FL98190A	125.8	50.9	316.3	38.6	222.2	5.2	5	1.137	0.682
172	FL98191A	125.4	46.2	359.8	29.1	251.5	29.3	1	1.18	0.368
176	FL98195B	141.2	47.6	264.6	26.7	11.6	30.2	1	1.117	0.027
180	FL98199B	156.9	54.4	312.8	33.1	50.4	11.4	5	1.074	0.017
183	FL98202A	358.6	54.9	264.5	2.9	172.4	34.8	1	1.089	0.997

Table C-1 AARM Data

		minimum		intermediate		maximum				
Outcrop	Sample	decln.	inclin.	decln.	inclin.	decln.	inclin.	Kmean	Pj	Tj
	FL98202C	93.6	87.9	276.1	1.6	186.1	0.1	1	1.082	-0.998
184	FL98203C	149	46.7	287.3	35.2	33.7	21.9	1	1.117	0.027
186	FL98205C	152.8	39.1	260	19.9	10.6	44.1	6	1.081	0.218
187	FL98206A	166.5	48.3	278.9	18.7	23	35.6	4	1.095	0.022
190	FL98209A	105.9	37.4	359.4	20.4	247	45.6	1	1.089	0.997
191	FL98210B	163.9	61.4	295.2	19.7	32.7	19.7	6	1.127	0.029
193	FL98212A	125.5	34.2	254	42.6	13.9	28.4	1	1.153	0.035
200	FL98219A	159.2	39.2	281.1	32.8	36.4	33.5	10	1.086	-0.091
201	FL98220C	152.3	47	275.6	27	23.2	30.4	6	1.096	0.023
202	FL98221B	136.5	43.3	296	44.8	36.5	10.4	2	1.105	0.025
203	FL98222C	149.8	57.2	282.9	23.7	22.7	21.2	1	1.217	-0.29
204	FL98223A	142.9	42.3	264.1	29.5	16	33.3	1	1.2	0.045
206	FL98225A	135.9	8	44.3	11.4	260.4	75.9	2	1.09	0.021
211	FL98230B	219	7.5	104.4	72.3	311.2	15.8	1	1.089	-0.998
218	FL98237C	225.2	64.5	123.6	5.4	31	24.7	1	1	1
219	FL98238A	254.6	59.7	116.7	23.4	18.5	18	7	1.03	0.992
220	FL98239A	239.9	62.4	355.1	12.5	90.8	24.1	1	1.155	0.998
221	FL98240A	218	69.1	109.8	6.8	17.3	19.6	17	1.054	0.564
222	FL98241A	113.8	41.6	344.1	35.7	231.8	27.8	5	1.1	0.614
223	FL98242A	148.1	46.4	266.3	24.2	13.7	33.7	6	1.077	-0.183
224	FL98243A	114.7	47.3	292.2	42.6	23.4	1.2	12	1.095	0.471
225	FL98244C	150.5	41.8	266.8	26.3	18.5	36.7	7	1.082	-0.316
226	FL98245A	139.4	31.9	267.2	44.6	29.6	28.5	1	1.068	-0.997
227	FL98246B	153.7	73.2	318.5	16.2	49.7	4.1	4	1.11	0.518
228	FL98247A	161.5	58.3	281.4	17.1	20	25.7	8	1.107	-0.086
229	FL98248B	153	49.7	277.9	25.9	23.2	28.5	6	1.103	0.024
230	FL98249C	107.5	67	333.4	16.3	238.7	15.5	22	1.117	0.304
231	FL98250C	61.8	70.6	323.5	2.9	232.5	19.1	3	1.085	0.35
	FL98252A	136.4	38.1	253.3	30	9.5	37.4	2	1.127	-0.307
236	FL98258B	283.1	87.1	71.8	2.4	161.9	1.4	4	1.191	0.733
	FL98259C	244.1	71.1	121.2	10.5	28.3	15.5	5	1.224	0.247
	FL98261A	202.5	58.8	302.6	6.1	36.2	30.4	3	1.162	-0.164
241	FL98263A	153.7	34.6	46.8	22.9	290.4	46.5	1	1.137	0.998
242	FL98264B	139.5	87.3	281.8	2.1	11.9	1.6	3	1.234	0.998
248	FL98270B	117.7	32.3	349.5	44.4	227.6	28.4	3	1.098	0.353
249	FL98271A	134.5	45.1	268.7	34.8	17.2	24.5	5	1.12	0.028
257	FL98279B	101.7	64.4	320.6	20.4	225	14.7	3	1.105	-0.312
258	FL98280A	140.4	61.3	309.4	28.2	41.9	4.6	1	1.077	0.996
261	FL98283C	166.9	59.2	290	18	28.3	24.1	3	1.168	0.236
264	FL98288C	245	24.7	119.6	51.4	348.8	27.4	0	1	1
266	FL98290C	146.6	45.6	291.9	38.8	37.1	18.1	1	1.064	-0.997
269	FL98293A	147.7	34.6	270.8	38.5	31.4	32.7	2	1.09	0.021
271	FL98296C	184.4	56.3	280	3.7	12.4	33.4	3	1.138	0.032
275	FL98300A	142.6	21	237.1	11.3	353.7	65.7	2	1.08	0.019
278	FL98303A	134	36.2	295.3	52.3	37.2	9.1	3	1.111	0.026
279	FL98305C	150.9	50.2	312.6	38.3	49.9	9	1	1.072	0.996
285	FL98311A	158.4	57	296.5	25.8	36.2	19.1	2	1.112	-0.31
286	FL98312B	136.3	55.9	290.2	31.2	27.8	12.1	23	1.11	-0.175
	FL98314A	154.7	50.2	282.7	27.2	27.6	26.7	1	1.125	0.029
289	FL98316A	134.8	66.7	43.7	0.4	313.5	23.2	3	1.13	0.521

Table C-1 AARM Data

		minimum		intermediate		maximum				
Outcrop	Sample	decln.	inclin.	decln.	inclin.	decln.	inclin.	Kmean	Pj	Tj
292	FL98319A	177.2	49.1	271.7	3.9	5.1	40.7	1	1.096	0.997
293	FL98320A	139.3	46.2	310	43.4	44.5	4.6	1	1.082	0.997
303	FL98330C	134.2	44.3	253.3	26.5	2.9	34.1	5	1.055	0.345
307	FL98334A	204.1	47.8	307	11.4	46.8	39.8	1	1.166	-0.999
308	FL98335C	137.6	38.5	272	41.3	26.1	24.9	2	1.127	-0.307
315	FL98342C	135.8	70	294.6	18.6	26.9	6.7	0	1	1
316	FL98343A	119.1	60.9	300.1	29	209.9	0.4	14	1.132	0.762
317	FL98344A	117.8	49	220.5	10.7	319.4	38.9	352	1.103	0.415
318	FL98345A	267.7	70.7	159.7	6.1	67.7	18.1	7	1.041	0.342
319	FL98346A	244.2	67.1	343.8	4	75.5	22.4	3	1.074	0.996
320	FL98347A	277.1	71.6	184	1	93.7	18.3	1	1.237	0.378
321	FL98348A	279.9	83	178.4	1.3	88.2	6.7	1	1.064	0.996
322	FL98349B	73.2	85.6	163.8	0	253.8	4.3	8	1.201	0.734
325	FL98352B	121.5	78.6	30.4	0.2	300.4	11.3	9	1.033	-0.327
326	FL98353B	280.1	83.2	174	1.8	83.8	6.4	2	1.1	0.023
329	FL98356A	111.1	40.1	357.7	25.3	244.9	39.4	1	1.111	0.026
330	FL98357A	94.3	48	194.8	9.2	292.8	40.4	2	1.046	-0.995
331	FL98358B	251.4	7.2	150.7	55.4	346.3	33.5	1	1.077	-0.997
333	FL98360A	170.1	62.1	287.9	13.9	24.2	23.7	2	1.181	0.041
334	FL98361A	158.3	55.9	282.6	20.8	23.1	25.5	15	1.092	0.022
336	FL98363A	133.7	39.8	322	49.8	227.1	4	2	1.105	0.025
	FL98364B	134.9	42.2	286.7	44.1	31.3	14.5	1	1.111	0.026
338	FL98366D	145.2	44.4	271.8	31.4	21.8	29.3	4	1.101	-0.483
343	FL98371B	65.7	42	335.3	0.3	244.9	47.9	1	1.077	-0.997
	FL98372A	210	74.6	1.8	13.5	93.5	7	0	1.194	-0.999
344	FL98001B	72.5	53.4	306.1	23.7	203.7	25.9	4	1.086	0.02
345	FL98375B	147.5	40.3	277.1	37	30.7	28	3	1.082	0.35
348	FL98378A	58.5	68.9	216.2	19.5	308.9	7.3	6	1.225	0.846
349	FL98379A	121.2	55.4	301.2	34.6	211.3	0.1	6	1.111	0.68
350	FL98380C	313.6	57.2	152.5	31.3	57.2	8.6	12	1.068	0.016
351	FL98381A	32.7	68.3	198.7	21	290.6	4.7	6	1.047	0.343
	FL98383B	187.6	58.3	284	3.9	16.4	31.4	1	1.133	0.031
353	FL98384A	161.3	69	289	13.2	22.9	16	3	1.335	0.801
	FL98384B	137.6	74.5	306.3	15.2	37	2.9	4	1.331	0.673
355	FL98387B	131.2	16.1	313.5	73.8	221.4	0.6	1	1.137	0.996
356	FL98388A	240.1	78	114.8	7	23.6	9.7	1	1.142	0.033
357	FL98389A	60.8	79.8	312.4	3.3	221.9	9.7	2	1.127	-0.307
358	FL98390A	264.1	83.5	124.2	6	34	2.2	6	1.279	0.87
359	FL98391A	188.7	67.5	302.6	9.5	36.1	20.1	6	1.098	0.023
1*	CY9701D	142.5	60	300.4	28	35.5	9.5	1	1	1
4*	CY9704B	146.5	73.1	276.1	10.9	8.6	12.6	0	1.166	-0.999
5*	CY9705D	264.8	51.7	112.5	34.8	12.8	13.6	8	1.022	0.005
12*	CY9714D	93.4	10.8	188.7	25.5	342.3	61.9	1	1.105	-0.998
13*	CY9715B	148.9	53.3	279.7	25.9	22.2	23.9	1	1.181	0.041
17*	CY9724B	221.7	79	38	10.8	128.1	0.6	11	1.106	0.808
19*	CY9727A4	108.7	33.8	318.3	52.4	208.7	14.5	1	1	1
34*	CY9748C	71.9	43.3	339.3	2.7	246.5	46.6	1	1.077	-0.997
35*	CY9749B	17	79.7	157.1	7.8	248	6.4	29	1.166	0.998
	CY9750C	118.6	62.8	222.7	7.1	316.2	26	10	1.159	0.865
36*	CY9751C	246.8	48.4	129.8	21.09	24.5	33.2	164	1.126	0.24

Table C-1 AARM Data

		minimum		intermediate		maximum				
Outcrop	**Sample**	**decln.**	**inclin.**	**decln.**	**inclin.**	**decln.**	**inclin.**	**Kmean**	**Pj**	**Tj**
37*	CY9752A	163.3	68.3	301.5	16.5	35.6	13.6	5	1.125	0.358

Distribution of AARM Foliati

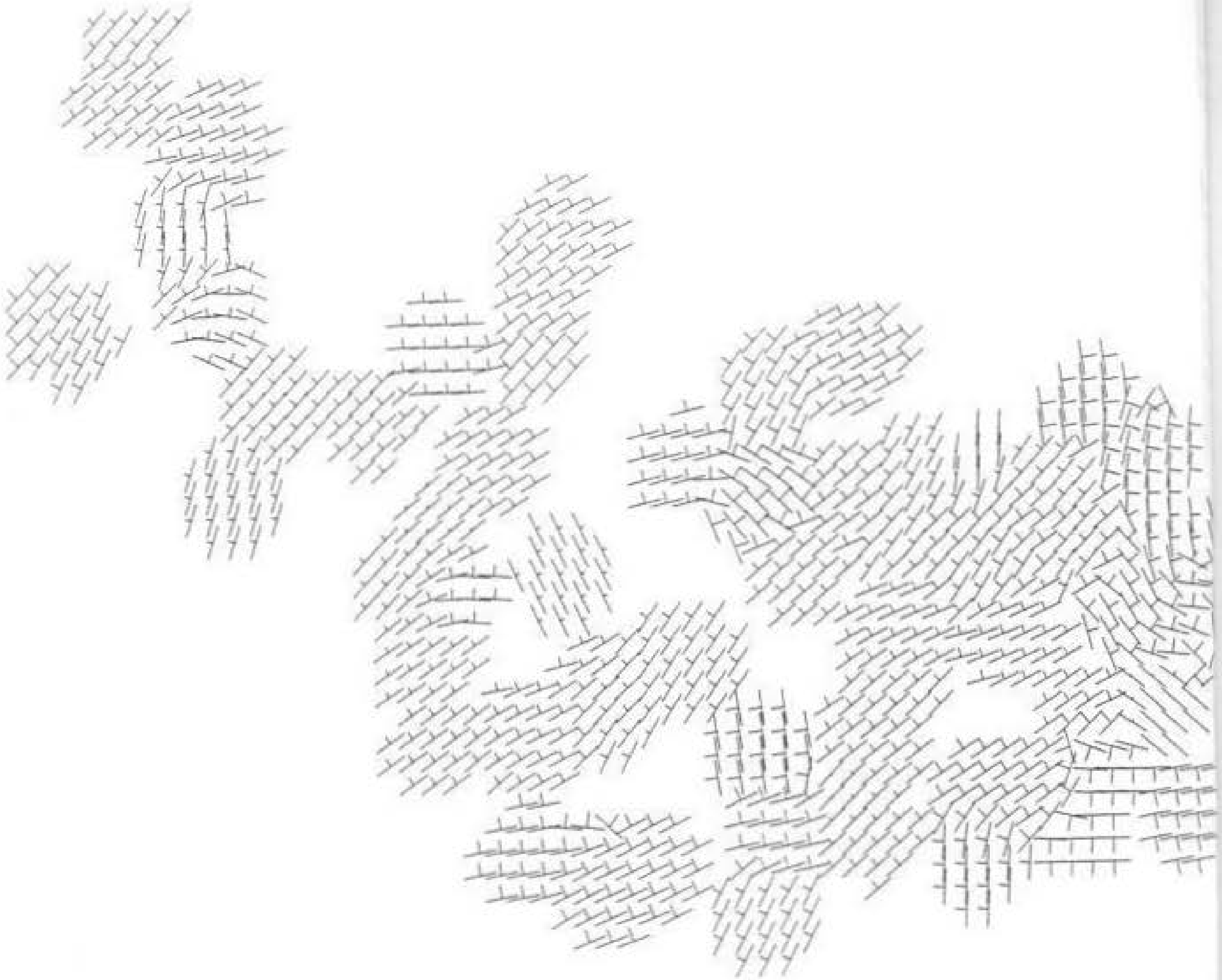

Figure C-1 Spatial distribution of AARM foliation data. Averaging stations are locat
is include within that station's average where the data is weighted with r

on Orientation Spatial Averaging

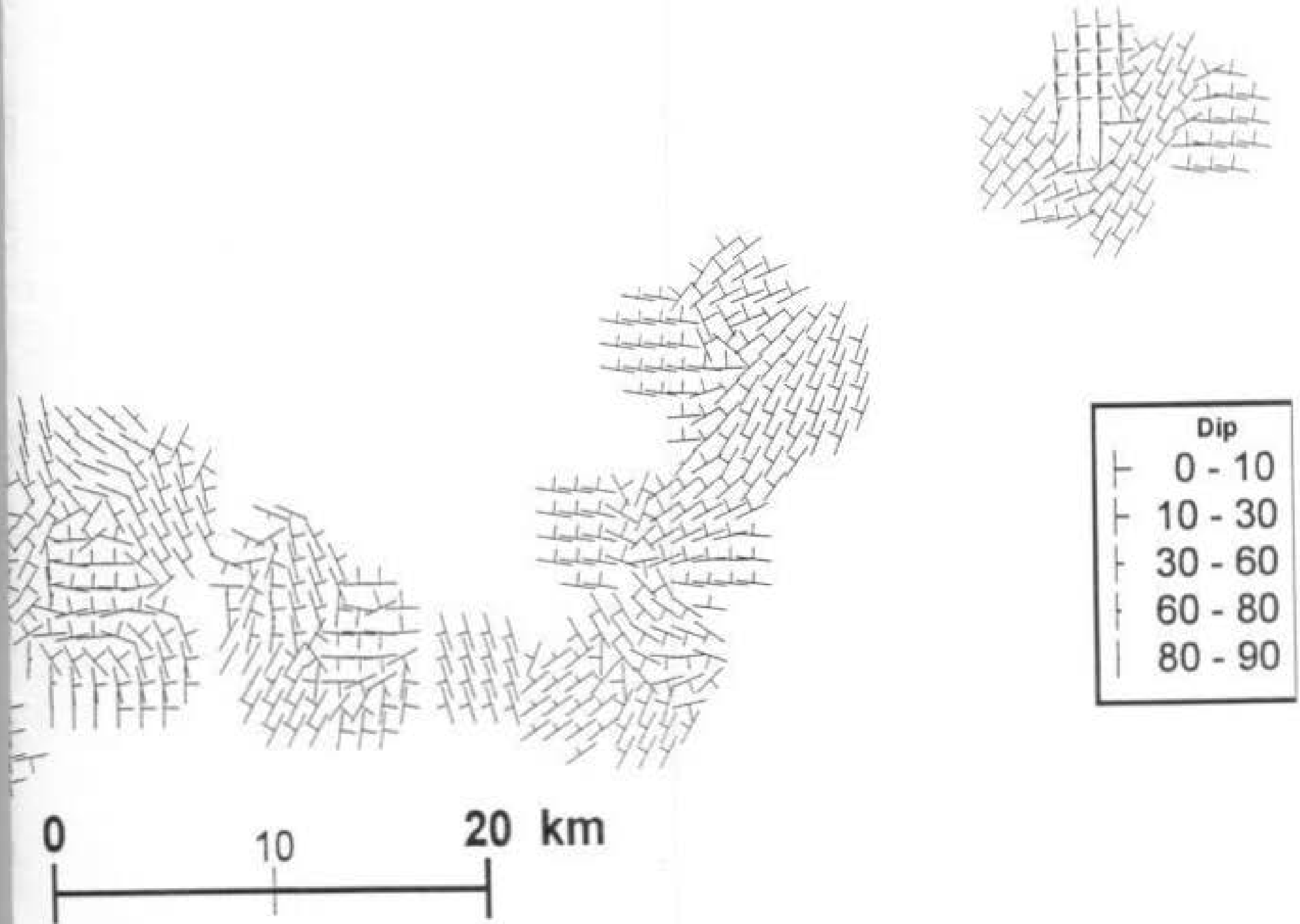

d one kilometer apart both in the N-S and E-W directions. Data within a 2.5 km radius of a station
spect to their distance from the station.

Distribution of AARM Line

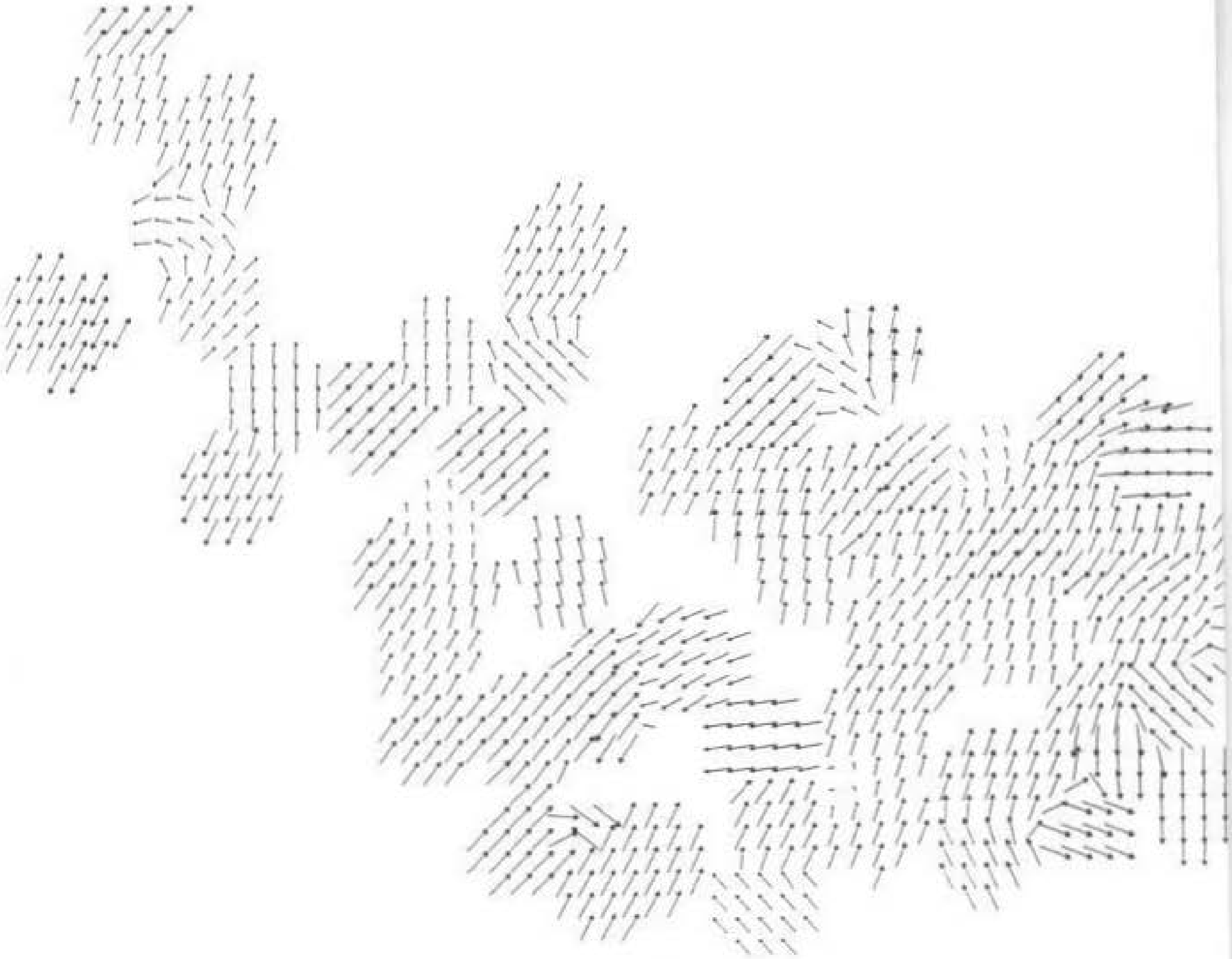

Figure C-2 Spatial distribution of AARM lineation data. Averaging stations are locat is include within that station's average where the data is weighted with re

ation Orientation Spatial Averaging

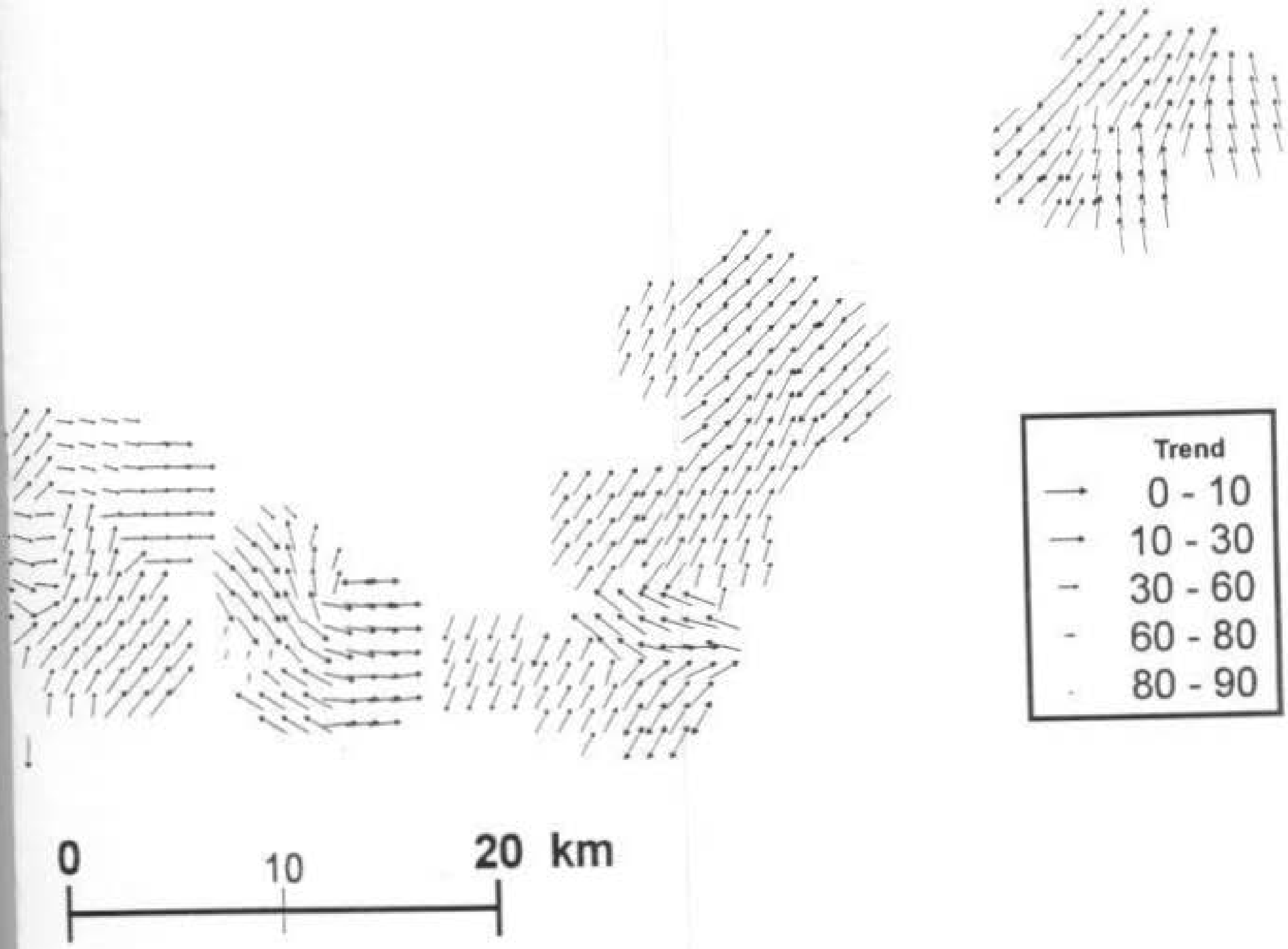

d one kilometer apart both in the N-S and E-W directions. Data within a 2.5 km radius of a station
spect to their distance from the station.

Appendix D

Hysteresis Loop and Coercivity of Remanence Data

Table D-1 High Field Susceptibility Data

Sample #	Mass (kg)	Kmatrix (m^3/kg)	Kferro (m^3/kg)	Ktotal (m^3/kg)	Kf/Ktotal	
FL98003A	5E-06	7.075E-09	1.323E-11	7.088E-09	0.0019	paramagnetic matrix
FL98007A	4E-07	-3.845E-08	5.386E-08	1.541E-08	3.4959	diamagnetic matrix
FL98011A	7E-07	-1.433E-08	7.616E-08	6.184E-08	1.2317	diamagnetic matrix
FL98019A	3.3E-06	7.414E-09	1.299E-08	2.041E-08	0.6367	paramagnetic matrix
FL98021A	8E-07	4.473E-09	3.016E-10	4.775E-09	0.0632	paramagnetic matrix
FL98023A	4E-07	-6.874E-08	8.108E-08	1.234E-08	6.5703	diamagnetic matrix
FL98025A	3.5E-06	6.434E-09	2.011E-08	2.654E-08	0.7576	paramagnetic matrix
FL98031A	2.1E-06	1.069E-08	1.495E-09	1.219E-08	0.1227	paramagnetic matrix
FL98037A	3.3E-06	3.669E-10	9.139E-09	9.506E-09	0.9614	paramagnetic matrix
FL98041A	2.3E-06	1.234E-09	1.714E-08	1.837E-08	0.9328	paramagnetic matrix
FL98043A	4.4E-06	1.102E-08	5.026E-08	6.128E-08	0.8202	paramagnetic matrix
FL98045A	2.9E-06	8.821E-09	1.933E-08	2.815E-08	0.6866	paramagnetic matrix
FL98047A	7.7E-06	1.722E-08	1.117E-08	2.839E-08	0.3935	paramagnetic matrix
FL98049A	1.8E-06	1.239E-08	3.590E-08	4.829E-08	0.7434	paramagnetic matrix
FL98051A	1.9E-06	-3.317E-09	4.569E-08	4.237E-08	1.0783	diamagnetic matrix
FL98053A	5.1E-06	4.675E-09	1.605E-08	2.072E-08	0.7744	paramagnetic matrix
FL98055A	3.9E-06	1.257E-08	2.717E-08	3.973E-08	0.6837	paramagnetic matrix
FL98057A	4E-06	1.608E-08	2.693E-08	4.301E-08	0.6261	paramagnetic matrix
FL98059A	6.2E-06	1.722E-08	1.933E-08	3.654E-08	0.5289	paramagnetic matrix
FL98061A	3.1E-06	8.507E-09	2.011E-08	2.861E-08	0.7027	paramagnetic matrix
FL98063A	5.6E-06	1.546E-08	8.976E-09	2.443E-08	0.3674	paramagnetic matrix
FL98065A	2.3E-06	2.689E-08	4.487E-08	7.176E-08	0.6253	paramagnetic matrix
FL98067A	3.3E-06	1.062E-08	3.397E-08	4.458E-08	0.7618	paramagnetic matrix
FL98069A	6.6E-06	1.533E-08	1.647E-08	3.180E-08	0.5180	paramagnetic matrix
FL98071A	3.6E-06	1.835E-08	3.141E-08	4.976E-08	0.6313	paramagnetic matrix
FL98073A	2.9E-06	4.247E-09	6.613E-09	1.086E-08	0.6089	paramagnetic matrix
FL98075A	1.9E-06	5.881E-09	5.984E-09	1.186E-08	0.5043	paramagnetic matrix
FL98077A	2.1E-06	1.156E-08	1.796E-08	2.952E-08	0.6083	paramagnetic matrix
FL98079A	6.4E-06	1.659E-08	1.450E-08	3.109E-08	0.4665	paramagnetic matrix
FL98081A	4.2E-06	1.520E-08	1.933E-08	3.453E-08	0.5597	paramagnetic matrix
FL98083A	3.8E-06	9.010E-09	2.792E-08	3.693E-08	0.7560	paramagnetic matrix
FL98085A	2.2E-06	2.450E-08	1.323E-07	1.568E-07	0.8438	paramagnetic matrix
FL98087A	3E-06	-5.190E-10	1.796E-08	1.744E-08	1.0298	diamagnetic matrix
FL98089A	2.1E-06	7.929E-09	1.396E-08	2.189E-08	0.6378	paramagnetic matrix
FL98091A	4.2E-06	1.223E-08	2.452E-08	3.674E-08	0.6672	paramagnetic matrix
FL98093A	2.2E-06	2.111E-08	3.307E-08	5.418E-08	0.6104	paramagnetic matrix
FL98097A	2.1E-06	1.571E-08	2.513E-08	4.084E-08	0.6154	paramagnetic matrix
FL98099A	2.3E-06	1.787E-08	1.985E-08	3.772E-08	0.5263	paramagnetic matrix
FL98101A	1.7E-06	1.596E-09	1.206E-08	1.366E-08	0.8832	paramagnetic matrix
FL98104B	1.5E-06	5.479E-09	6.283E-09	1.176E-08	0.5342	paramagnetic matrix
FL98105A	1.4E-06	6.120E-09	6.283E-09	1.240E-08	0.5066	paramagnetic matrix
FL98107A	2E-06	6.999E-10	8.419E-09	9.119E-09	0.9232	paramagnetic matrix
FL98109A	1.2E-06	-9.638E-10	1.759E-08	1.663E-08	1.0580	diamagnetic matrix
FL98111A	4.5E-06	4.159E-09	1.654E-08	2.070E-08	0.7990	paramagnetic matrix
FL98113A	3.8E-06	3.745E-09	5.236E-09	8.981E-09	0.5830	paramagnetic matrix
FL98115A	5.4E-06	1.131E-08	2.856E-08	3.987E-08	0.7164	paramagnetic matrix
FL98117A	6E-06	2.589E-09	2.792E-08	3.051E-08	0.9152	paramagnetic matrix
FL98119A	3.1E-06	5.315E-09	2.856E-08	3.388E-08	0.8431	paramagnetic matrix
FL98121A	2.5E-06	-2.388E-09	2.139E-08	1.900E-08	1.1257	diamagnetic matrix

Table D-1 High Field Susceptibility Data

Sample #	Mass (kg)	Kmatrix (m^3/kg)	Kferro (m^3/kg)	Ktotal (m^3/kg)	Kf/Ktotal	
FL98123A	3.6E-06	-4.335E-09	3.427E-08	2.993E-08	1.1448	diamagnetic matrix
FL98125A	4E-06	-8.922E-10	1.538E-08	1.449E-08	1.0616	diamagnetic matrix
FL98127A	5.9E-06	1.546E-08	1.169E-07	1.323E-07	0.8832	paramagnetic matrix
FL98131A	2.2E-06	7.163E-09	8.976E-09	1.614E-08	0.5562	paramagnetic matrix
FL98133A	2.5E-06	1.294E-08	5.744E-08	7.038E-08	0.8161	paramagnetic matrix
FL98135A	2.1E-06	8.256E-09	8.976E-09	1.723E-08	0.5209	paramagnetic matrix
FL98137A	5.8E-06	1.835E-08	2.792E-08	4.627E-08	0.6035	paramagnetic matrix
FL98139A	4.1E-06	1.172E-08	1.396E-08	2.568E-08	0.5435	paramagnetic matrix
FL98141A	3.6E-06	6.157E-09	2.416E-08	3.032E-08	0.7969	paramagnetic matrix
FL98143A	2.2E-06	1.608E-08	1.933E-08	3.541E-08	0.5458	paramagnetic matrix
FL98145A	4.3E-06	1.195E-08	1.704E-08	2.899E-08	0.5878	paramagnetic matrix
FL98147A	5.3E-06	1.533E-08	1.571E-08	3.104E-08	0.5061	paramagnetic matrix
FL98149A	5.5E-06	1.935E-08	1.647E-08	3.583E-08	0.4598	paramagnetic matrix
FL98151A	4.2E-06	2.852E-09	2.513E-08	2.798E-08	0.8981	paramagnetic matrix
FL98153A	6.4E-06	1.307E-08	1.450E-08	2.757E-08	0.5260	paramagnetic matrix
FL98155A	3.7E-06	3.229E-09	3.968E-08	4.291E-08	0.9247	paramagnetic matrix
FL98157A	9.3E-06	2.689E-08	1.156E-08	3.845E-08	0.3007	paramagnetic matrix
FL98159A	4.1E-06	3.267E-08	2.284E-08	5.552E-08	0.4115	paramagnetic matrix
FL98161A	3.6E-06	1.985E-08	3.141E-08	5.127E-08	0.6127	paramagnetic matrix
FL98165A	5E-06	8.696E-09	1.047E-07	1.134E-07	0.9233	paramagnetic matrix
FL98167A	3.9E-06	8.168E-09	3.016E-08	3.833E-08	0.7869	paramagnetic matrix
FL98169A	1.7E-06	1.935E-08	1.698E-08	3.633E-08	0.4673	paramagnetic matrix
FL98173A	5E-06	9.852E-09	9.299E-09	1.915E-08	0.4856	paramagnetic matrix
FL98175A	1.1E-06	-1.596E-09	1.733E-08	1.573E-08	1.1014	diamagnetic matrix
FL98177A	3.8E-06	2.186E-09	1.033E-08	1.251E-08	0.8253	paramagnetic matrix
FL98181A	4E-06	-2.199E-09	1.142E-07	1.120E-07	1.0196	diamagnetic matrix
FL98183A	5.7E-06	6.673E-09	9.666E-08	1.033E-07	0.9354	paramagnetic matrix
FL98185A	7.1E-06	2.300E-08	2.732E-08	5.031E-08	0.5430	paramagnetic matrix
FL98187A	3.2E-06	5.516E-09	2.513E-08	3.065E-08	0.8200	paramagnetic matrix
FL98191A	4.4E-06	1.923E-08	2.248E-08	4.171E-08	0.5390	paramagnetic matrix
FL98193A	3.8E-06	1.382E-08	3.307E-08	4.690E-08	0.7053	paramagnetic matrix
FL98195A	2.2E-06	1.307E-08	2.416E-08	3.723E-08	0.6490	paramagnetic matrix
FL98197A	3E-06	1.998E-08	4.833E-08	6.831E-08	0.7075	paramagnetic matrix
FL98199A	3.4E-06	9.311E-09	2.284E-08	3.216E-08	0.7104	paramagnetic matrix
FL98201A	2.9E-06	4.725E-09	5.675E-08	6.147E-08	0.9231	paramagnetic matrix
FL98203A	3.1E-06	1.282E-08	3.491E-08	4.773E-08	0.7314	paramagnetic matrix
FL98205A	2.7E-06	1.621E-08	3.491E-08	5.112E-08	0.6829	paramagnetic matrix
FL98209A	3E-06	1.111E-08	2.185E-08	3.296E-08	0.6630	paramagnetic matrix
FL98211A	3.3E-06	1.064E-08	2.513E-08	3.578E-08	0.7025	paramagnetic matrix
FL98213A	2.7E-06	-1.910E-09	3.723E-08	3.532E-08	1.0541	diamagnetic matrix
FL98215A	6.1E-06	1.171E-08	1.033E-08	2.204E-08	0.4686	paramagnetic matrix
FL98217A	4.7E-06	8.005E-09	2.095E-08	2.895E-08	0.7235	paramagnetic matrix
FL98219A	8.2E-06	2.086E-08	1.323E-08	3.409E-08	0.3881	paramagnetic matrix
FL98221A	4.1E-06	1.809E-08	1.972E-08	3.781E-08	0.5214	paramagnetic matrix
FL98223A	8.1E-06	2.073E-08	1.047E-08	3.121E-08	0.3356	paramagnetic matrix
FL98225A	2.9E-06	3.996E-08	5.464E-08	9.460E-08	0.5776	paramagnetic matrix
FL98227A	5.8E-06	6.911E-09	9.666E-09	1.658E-08	0.5831	paramagnetic matrix
FL98229A	7.9E-06	2.300E-09	1.396E-08	1.626E-08	0.8586	paramagnetic matrix
FL98231A	6.4E-06	-5.353E-09	1.753E-08	1.218E-08	1.4396	diamagnetic matrix

Table D-1 High Field Susceptibility Data

Sample #	Mass (kg)	Kmatrix (m^3/kg)	Kferro (m^3/kg)	Ktotal (m^3/kg)	Kf/Ktotal	
FL98233A	5.9E-06	7.251E-09	1.346E-08	2.071E-08	0.6499	paramagnetic matrix
FL98235A	5.5E-06	6.710E-09	1.069E-08	1.741E-08	0.6145	paramagnetic matrix
FL98237A	3.9E-06	1.860E-08	1.714E-08	3.574E-08	0.4796	paramagnetic matrix
FL98239A	4E-06	8.306E-09	1.714E-08	2.545E-08	0.6736	paramagnetic matrix
FL98241A	4.6E-06	1.174E-08	1.984E-08	3.158E-08	0.6283	paramagnetic matrix
FL98243A	5.2E-06	1.017E-08	4.054E-08	5.070E-08	0.7995	paramagnetic matrix
FL98245A	5.1E-06	1.066E-08	1.299E-08	2.365E-08	0.5494	paramagnetic matrix
FL98247A	5.8E-06	2.149E-08	3.141E-08	5.290E-08	0.5938	paramagnetic matrix
FL98249A	3E-06	2.739E-08	6.613E-08	9.353E-08	0.7071	paramagnetic matrix
FL98251A	6.8E-06	8.118E-09	1.704E-08	2.516E-08	0.6773	paramagnetic matrix
FL98253A	3E-06	6.446E-09	1.984E-08	2.629E-08	0.7548	paramagnetic matrix
FL98257A	4.4E-06	7.351E-09	2.284E-08	3.020E-08	0.7566	paramagnetic matrix
FL98259A	4.6E-06	7.251E-09	4.188E-08	4.913E-08	0.8524	paramagnetic matrix
FL98261A	8.5E-06	1.043E-08	1.142E-08	2.185E-08	0.5227	paramagnetic matrix
FL98263A	5.7E-06	8.444E-09	1.216E-08	2.060E-08	0.5902	paramagnetic matrix
FL98265A	2.5E-06	-1.747E-09	1.571E-08	1.396E-08	1.1251	diamagnetic matrix
FL98267A	3.6E-06	8.671E-09	2.337E-08	3.204E-08	0.7294	paramagnetic matrix
FL98269A	7.7E-06	5.466E-09	5.026E-09	1.049E-08	0.4790	paramagnetic matrix
FL98271A	4.2E-06	6.572E-09	1.508E-08	2.165E-08	0.6965	paramagnetic matrix
FL98277A	1.3E-06	4.021E-09	4.825E-09	8.846E-09	0.5455	paramagnetic matrix
FL98279A	3.9E-06	6.760E-09	2.130E-08	2.806E-08	0.7591	paramagnetic matrix
FL98281A	2.3E-06	1.634E-08	3.056E-08	4.690E-08	0.6517	paramagnetic matrix
FL98283A	3E-06	3.594E-09	1.571E-08	1.930E-08	0.8138	paramagnetic matrix
FL98285A	2E-07	2.739E-09	3.222E-09	5.961E-09	0.5405	paramagnetic matrix
FL98289A	3.6E-06	-2.626E-10	2.432E-08	2.405E-08	1.0109	diamagnetic matrix
FL98291A	3.6E-06	1.684E-08	1.571E-08	3.255E-08	0.4826	paramagnetic matrix
FL98301A	4.7E-06	-1.234E-09	6.613E-09	5.379E-09	1.2294	diamagnetic matrix
FL98303A	3.8E-06	8.507E-09	1.216E-08	2.067E-08	0.5884	paramagnetic matrix
FL98305A	3.7E-06	2.111E-08	2.284E-08	4.396E-08	0.5197	paramagnetic matrix
FL98307A	5.4E-06	4.386E-09	1.591E-08	2.029E-08	0.7839	paramagnetic matrix
FL98309A	2.7E-06	-7.929E-09	6.701E-08	5.909E-08	1.1342	diamagnetic matrix
FL98311A	3.3E-06	8.947E-09	2.327E-08	3.222E-08	0.7223	paramagnetic matrix
FL98313A	5.5E-06	4.838E-09	4.928E-09	9.766E-09	0.5046	paramagnetic matrix
FL98315A	5.4E-06	9.135E-09	1.216E-08	2.130E-08	0.5710	paramagnetic matrix
FL98317A	6.5E-06	1.709E-08	1.289E-08	2.998E-08	0.4300	paramagnetic matrix
FL98319A	8.3E-06	1.206E-08	8.976E-09	2.104E-08	0.4266	paramagnetic matrix
FL98321A	2.7E-06	3.393E-09	6.982E-09	1.037E-08	0.6730	paramagnetic matrix
FL98323A	2.7E-06	-7.225E-09	6.613E-09	-6.120E-10	-10.8070	diamagnetic matrix
FL98325A	1.05E-05	1.935E-08	1.019E-08	2.954E-08	0.3449	paramagnetic matrix
FL98327A	6E-06	7.917E-09	9.484E-09	1.740E-08	0.5450	paramagnetic matrix
FL98329A	3.9E-06	1.684E-08	1.416E-08	3.100E-08	0.4568	paramagnetic matrix
FL98331A	3.6E-06	5.843E-09	1.547E-08	2.131E-08	0.7258	paramagnetic matrix
FL98333A	6.5E-06	-7.112E-09	1.047E-08	3.359E-09	3.1175	diamagnetic matrix
FL98335A	3.2E-06	8.268E-09	1.478E-08	2.305E-08	0.6412	paramagnetic matrix
FL98337A	4.8E-06	2.136E-09	4.833E-09	6.969E-09	0.6935	paramagnetic matrix
FL98339A	3.1E-06	1.407E-08	1.933E-08	3.340E-08	0.5786	paramagnetic matrix
FL98341A	4.6E-06	1.051E-08	1.478E-08	2.528E-08	0.5845	paramagnetic matrix
FL98343A	3.9E-06	9.990E-09	4.487E-08	5.486E-08	0.8179	paramagnetic matrix
FL98345A	6.1E-06	2.212E-08	1.621E-08	3.833E-08	0.4230	paramagnetic matrix

Table D-1 High Field Susceptibility Data

Sample #	Mass (kg)	Kmatrix (m^3/kg)	Kferro (m^3/kg)	Ktotal (m^3/kg)	Kf/Ktotal	
FL98347A	4E-06	9.965E-09	2.717E-08	3.713E-08	0.7316	paramagnetic matrix
FL98349A	6.1E-06	1.546E-08	4.487E-08	6.033E-08	0.7438	paramagnetic matrix
FL98351A	2.2E-06	2.765E-09	2.095E-08	2.371E-08	0.8834	paramagnetic matrix
FL98353A	4.3E-06	3.066E-08	1.206E-08	4.272E-08	0.2824	paramagnetic matrix
FL98357A	7.3E-06	2.161E-08	7.917E-09	2.953E-08	0.2681	paramagnetic matrix
FL98359A	3E-06	8.356E-09	4.629E-08	5.465E-08	0.8471	paramagnetic matrix
FL98361A	3E-06	3.380E-08	6.792E-08	1.017E-07	0.6677	paramagnetic matrix
FL98363A	3.9E-06	1.822E-08	9.550E-09	2.777E-08	0.3439	paramagnetic matrix
FL98365A	2.1E-06	-7.590E-09	1.206E-08	4.473E-09	2.6966	diamagnetic matrix
FL98367A	5.6E-06	-4.247E-09	8.767E-09	4.520E-09	1.9397	diamagnetic matrix
FL98369A	3.1E-06	3.418E-09	5.347E-09	8.765E-09	0.6100	paramagnetic matrix
FL98371A	1.6E-06	3.858E-08	1.860E-08	5.718E-08	0.3253	paramagnetic matrix
FL98373A	1.9E-06	1.571E-09	1.571E-08	1.728E-08	0.9091	paramagnetic matrix
FL98375A	2.1E-06	1.102E-09	1.323E-08	1.433E-08	0.9231	paramagnetic matrix
FL98379A	9E-07	1.057E-08	9.047E-09	1.962E-08	0.4612	paramagnetic matrix
FL98385A	1.2E-06	3.895E-09	1.109E-08	1.498E-08	0.7400	paramagnetic matrix
FL98387A	2.6E-06	8.482E-09	6.982E-08	7.830E-08	0.8917	paramagnetic matrix
FL98389A	5E-06	1.508E-08	9.424E-09	2.450E-08	0.3846	paramagnetic matrix
FL98391A	1.2E-06	1.948E-08	1.596E-07	1.791E-07	0.8912	paramagnetic matrix
GBFL001A	5.1E-06	4.649E-09	6.283E-09	1.093E-08	0.5747	paramagnetic matrix
GBFL003A	3E-06	1.608E-08	4.188E-08	5.797E-08	0.7225	paramagnetic matrix
GBFL007A	3.4E-06	1.063E-08	3.723E-08	4.786E-08	0.7779	paramagnetic matrix
GBFL009A	2.2E-06	6.333E-09	2.856E-08	3.490E-08	0.8185	paramagnetic matrix

Table D-2 Magnetization and Coercivity Parameters Data

Sample #	Hc (mT)	Hcr (mT)	Hcr/Hc	Mr/Ms
FL98003A	13.6	22.8	1.676	0.199
FL98007A	8.43	33.8	4.009	0.1
FL98011A	9.43	23.7	2.513	0.124
FL98019A	14.8	29.2	1.973	0.211
FL98021A	174	25.1	0.144	0.335
FL98023A	7.14	24	3.361	0.105
FL98025A	11.4	25.3	2.219	0.147
FL98031A	21.6	25.3	1.171	0.184
FL98037A	9.26	22.2	2.39	0.135
FL98041A	9.16	22.7	2.478	0.143
FL98043A	22	57.5	2.614	0.217
FL98045A	11.3	23.4	2.071	0.165
FL98047A	19.5	27.7	1.421	0.235
FL98049A	10.5	25.7	2.448	0.135
FL98051A	9.06	21.8	2.406	0.15
FL98053A	10.5	23.1	2.2	0.167
FL98055A	9.99	22.3	2.232	0.152
FL98057A	11.5	28.1	2.443	0.167
FL98059A	15.4	39.3	2.552	0.207
FL98061A	12.2	23.7	1.943	0.168
FL98063A	17.4	22.6	1.299	0.212
FL98065A	13.5	26.3	1.948	0.175
FL98067A	9.72	25.7	2.644	0.154
FL98069A	15.5	40.4	2.606	0.212
FL98071A	9.48	31.6	3.333	0.141
FL98073A	11.2	22.5	2.009	0.155
FL98075A	11.7	22.4	1.915	0.139
FL98077A	11	24.3	2.209	0.153
FL98079A	16.5	34.9	2.116	0.216
FL98081A	12.9	24.6	1.907	0.184
FL98083A	12.5	25.9	2.072	0.165
FL98085A	10.2	29.1	2.853	0.152
FL98087A	8.83	24.5	2.775	0.149
FL98089A	8.78	19.9	2.267	0.121
FL98091A	12.6	24.3	1.929	0.169
FL98093A	14.6	33.8	2.315	0.157
FL98097A	13.3	29.7	2.233	0.152
FL98099A	19.7	32.9	1.67	0.232
FL98101A	16.2	44.7	2.759	0.208
FL98104B	31.1	28	0.9	0.424
FL98105A	15	34	2.267	0.164
FL98107A	12	32.9	2.742	0.149
FL98109A	12.8	29.4	2.297	0.139
FL98111A	11.8	27.2	2.305	0.173
FL98113A	11.8	23.8	2.017	0.174
FL98115A	12.7	24.4	1.921	0.188
FL98117A	8.97	22.4	2.497	0.16
FL98119A	9.99	21.1	2.112	0.149
FL98121A	8.33	21.8	2.617	0.143
FL98123A	8.06	19.5	2.419	0.13

Table D-2 Magnetization and Coercivity Parameters Data

Sample #	Hc (mT)	Hcr (mT)	Hcr/Hc	Mr/Ms
FL98125A	9.18	22.4	2.44	0.148
FL98127A	46	58.6	1.274	0.596
FL98131A	10.8	23.5	2.176	0.166
FL98133A	10.2	23.6	2.314	0.159
FL98135A	12.1	34.5	2.851	0.171
FL98137A	13	23.4	1.8	0.18
FL98139A	12.7	22.8	1.795	0.174
FL98141A	9.98	22.2	2.224	0.12
FL98143A	9.86	22.1	2.241	0.141
FL98145A	12.7	22.3	1.756	0.177
FL98147A	13.6	29.6	2.176	0.179
FL98149A	16	28.6	1.788	0.192
FL98151A	7.7	20.4	2.649	0.174
FL98153A	14.9	32.8	2.201	0.197
FL98155A	9.88	20.8	2.105	0.157
FL98157A	22.6	32	1.416	0.239
FL98159A	13.1	24.2	1.847	0.163
FL98161A	12.1	25.8	2.132	0.162
FL98165A	17.4	34.8	2	0.24
FL98167A	13.4	31.7	2.366	0.179
FL98169A	18.8	25.2	1.34	0.258
FL98173A	21.1	31.3	1.483	0.286
FL98175A	10.1	26	2.574	0.116
FL98177A	10.7	25.8	2.411	0.132
FL98181A	13.6	28.9	2.125	0.191
FL98183A	11.3	21.9	1.929	0.199
FL98185A	18.9	39.9	2.111	0.215
FL98187A	12	24.5	2.042	0.174
FL98191A	14.6	30.1	2.062	0.19
FL98193A	11.8	27.7	2.347	0.155
FL98195A	10.3	35.7	3.466	0.148
FL98197A	11.7	24.3	2.077	0.179
FL98199A	10.1	22.3	2.208	0.155
FL98201A	9.25	22.9	2.476	0.096
FL98203A	10.6	20.2	1.906	0.156
FL98205A	14	35.2	2.514	0.194
FL98209A	11.8	26.8	2.271	0.143
FL98211A	11.9	24.6	2.067	0.158
FL98213A	8.65	23.8	2.751	0.134
FL98215A	16.2	32.6	2.012	0.211
FL98217A	11	22.9	2.082	0.148
FL98219A	21.2	229.8	1.406	0.239
FL98221A	13.3	27	2.03	0.169
FL98223A	20	30.5	1.525	0.216
FL98225A	13.8	34	2.464	0.144
FL98227A	11.5	22.8	1.983	0.153
FL98229A	10.1	21.8	2.158	0.124
FL98231A	8.55	22.8	2.667	0.138
FL98233A	12.3	20.1	1.634	0.184
FL98235A	12.7	21.2	1.669	0.18

Table D-2 Magnetization and Coercivity Parameters Data

Sample #	Hc (mT)	Hcr (mT)	Hcr/Hc	Mr/Ms
FL98237A	12.6	18.1	1.437	0.166
FL98239A	11.1	22.2	2	0.163
FL98241A	14.5	33.6	2.317	0.199
FL98243A	17.8	41.6	2.337	0.227
FL98245A	13.4	21.2	1.582	0.191
FL98247A	16.7	36.2	2.168	0.216
FL98249A	16.3	38.9	2.387	0.195
FL98251A	12.3	19.6	1.593	0.177
FL98253A	9.89	20.8	2.103	0.139
FL98257A	10.7	21.6	2.019	0.157
FL98259A	15.1	29.8	1.974	0.211
FL98261A	18.8	42	2.234	0.247
FL98263A	14.9	30.4	2.04	0.197
FL98265A	9.06	22	2.428	0.143
FL98267A	10.6	21.1	1.991	0.156
FL98269A	14.9	21.5	1.443	0.192
FL98271A	13	24.7	1.9	0.193
FL98277A	11.8	25.8	2.186	0.127
FL98279A	12.1	24.5	2.025	0.163
FL98281A	26.4	74.4	2.818	0.298
FL98283A	9.24	24.3	2.63	0.152
FL98285A	10.7	22.2	2.075	0.008
FL98289A	10.3	24.5	2.379	0.141
FL98291A	13	33.8	2.6	0.185
FL98301A	9.05	21.7	2.398	0.147
FL98303A	24.2	95.5	3.946	0.3
FL98305A	12.9	27.3	2.116	0.175
FL98307A	12.4	24.6	1.984	0.184
FL98309A	8.7	19.3	2.218	0.15
FL98311A	11.6	23.1	1.991	0.17
FL98313A	15	23.1	1.54	0.206
FL98315A	11.6	22.4	1.931	0.166
FL98317A	15.9	27.7	1.742	0.204
FL98319A	17.9	31.3	1.749	0.223
FL98321A	11.6	21.8	1.879	0.166
FL98323A	7.49	20.5	2.737	0.125
FL98325A	22.1	35.5	1.606	0.227
FL98327A	13	27	2.077	0.177
FL98329A	12.8	27.1	2.117	0.17
FL98331A	10.8	21.8	2.019	0.16
FL98333A	7.64	21	2.749	0.128
FL98335A	12	23.7	1.975	0.18
FL98337A	11.1	21.3	1.919	0.171
FL98339A	11.1	22.7	2.045	0.16
FL98341A	12.2	21.1	1.73	0.165
FL98343A	15.7	33.4	2.127	0.227
FL98345A	17	37.5	2.206	0.223
FL98347A	11.5	23.5	2.043	0.165
FL98349A	19.6	40	2.041	0.246
FL98351A	24.2	56.2	2.322	0.261

Table D-2 Magnetization and Coercivity Parameters Data

Sample #	Hc (mT)	Hcr (mT)	Hcr/Hc	Mr/Ms
FL98353A	21.5	39.5	1.837	0.215
FL98357A	27.5	47.8	1.738	0.263
FL98359A	10.8	23.5	2.176	0.144
FL98361A	19.8	45.8	2.313	0.222
FL98363A	18.7	39.8	2.128	0.218
FL98365A	9.13	36	3.943	0.144
FL98367A	11.9	25	2.101	0.176
FL98369A	12.9	23.6	1.829	0.166
FL98371A	16.4	30.5	1.86	0.169
FL98373A	12.9	31.3	2.426	0.154
FL98375A	11.7	38.2	3.265	0.14
FL98379A	23	42.2	1.835	0.262
FL98385A	13.7	25.8	1.883	0.183
FL98387A	10.3	24.3	2.359	0.181
FL98389A	19.6	37.1	1.893	0.212
FL98391A	14.3	31.1	2.175	0.16
GBFL001A	14.1	24.7	1.752	0.195
GBFL003A	10.7	29	2.71	0.112
GBFL007A	13.4	35	2.612	0.167
GBFL009A	10.4	23.7	2.279	0.144

Appendix E

Maps

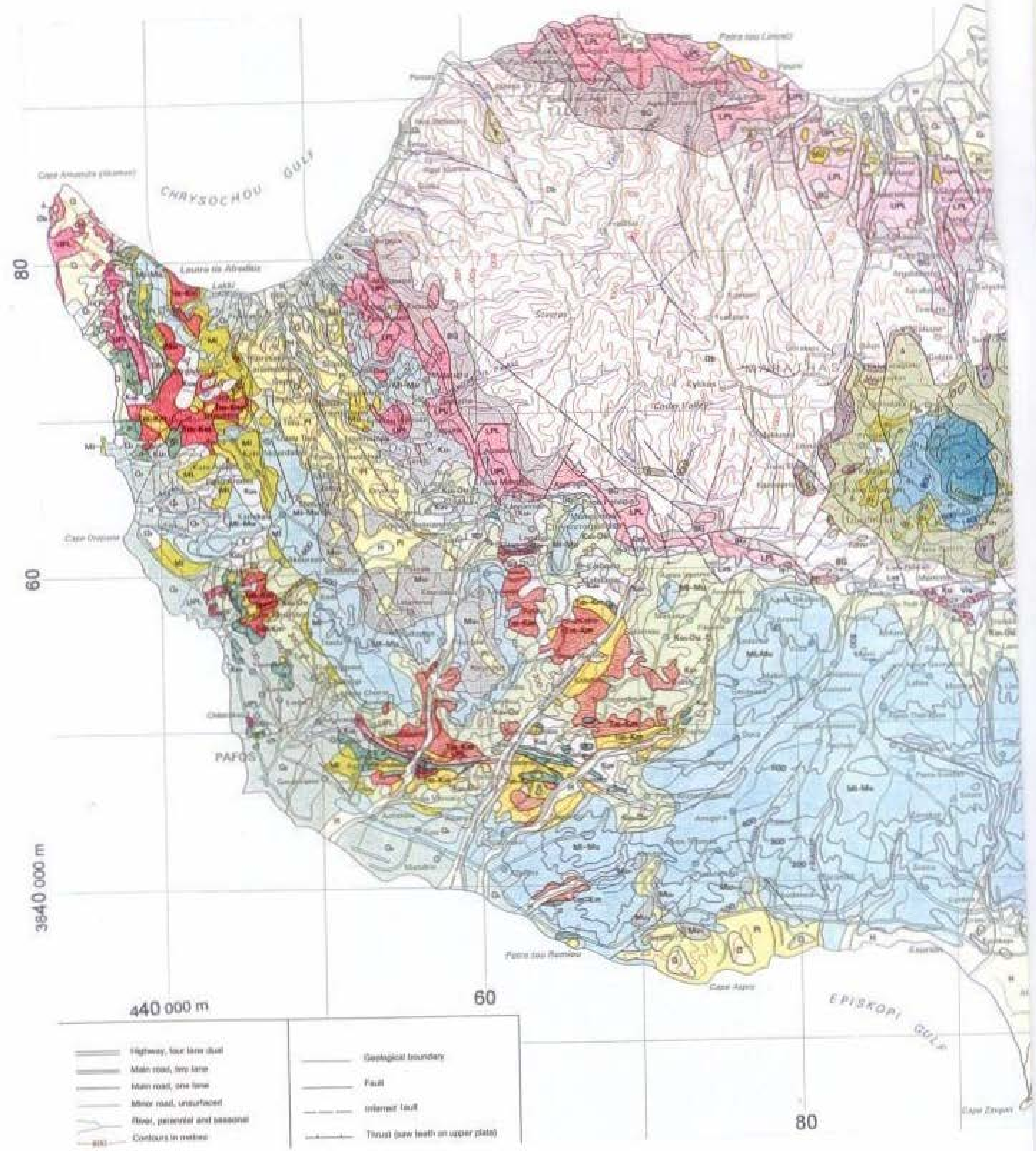

CHRYSOCHOU GULF
PAFOS
EPISKOPI GULF
80
60
3840 000 m
440 000 m
60
80
Highway, four lane dual
Main road, two lane
Main road, one lane
Minor road, unsurfaced
River, perennial and seasonal
Contours in metres
Geological boundary
Fault
Inferred fault
Thrust (saw teeth on upper plate)

MAP SHEET B - Solid Geology of the study Area

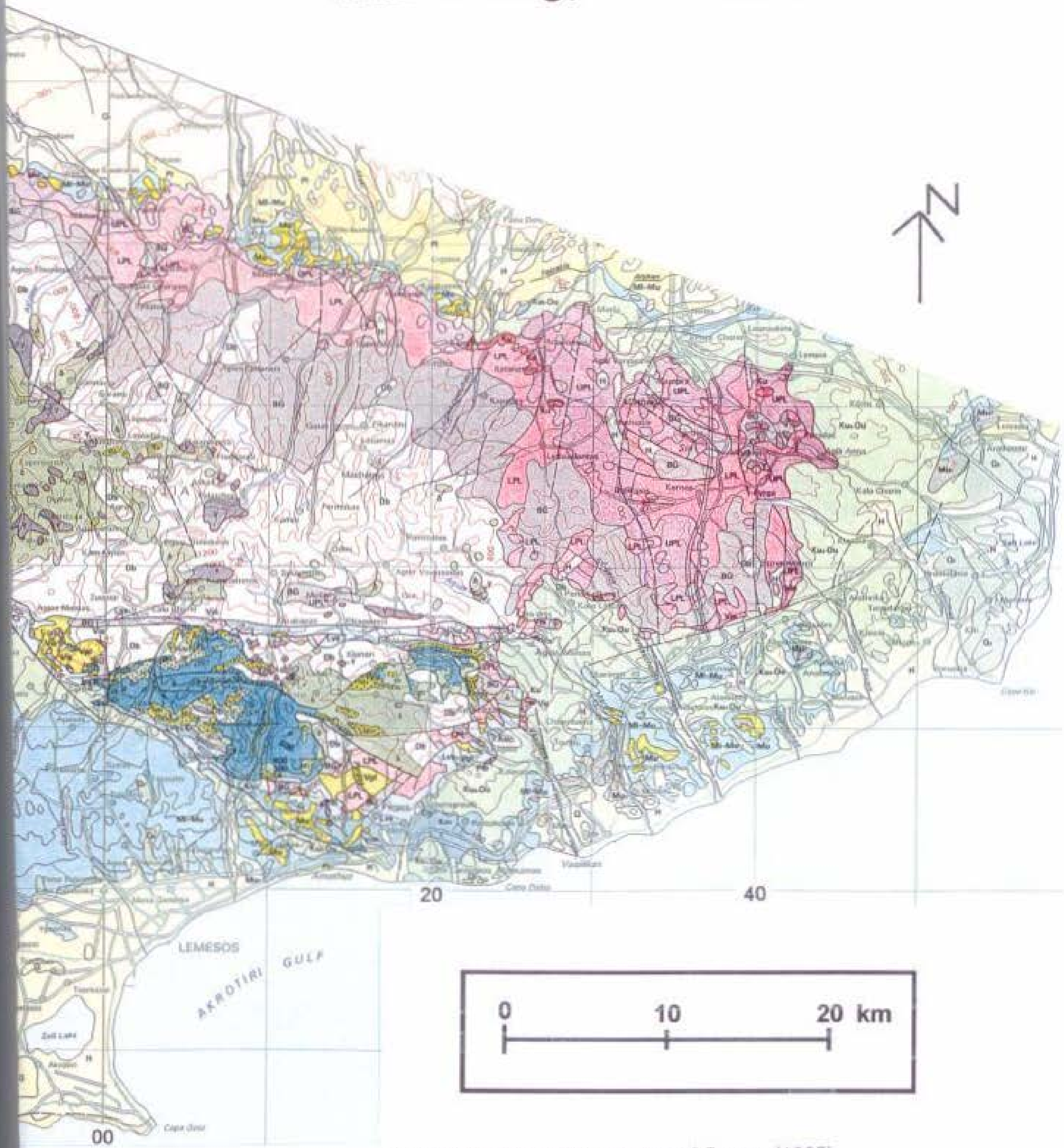

Geological Survey Department of Cyprus (1995)

Key to geological terrains in MAP SHEET B

CIRCUM TROODOS SEDIMENTARY SUCCESSION

	LITHOLOGY	FORMATION	EPOCH		PERIOD
H	Sands, silts, clays and gravels	Alluvium-Colluvium	HOLOCENE		QUATERNARY
Qc	Calcarenites, sands and gravels	Terrace deposits	PLEISTOCENE		QUATERNARY
Q1	Gravels, sands and silts	Fanglomerate	PLEISTOCENE		QUATERNARY
Q	Biocalcarenites, sandstones, sandy marls and conglomerates	Apalos-Athalassa Kakkaristra	PLEISTOCENE		QUATERNARY
Pl	Biocalcarenites, sandstones, silts, gravels, sandy marls, marls, limestones and conglomerates	Nicosia	PLIOCENE		NEOGENE
Mu	Gypsum alternating with chalky marls and marly chalks	Kalavasos	UPPER	MIOCENE	NEOGENE
Mu	Biostrome and bioherm reef limestones (Koronia Member)	Pakhna	MIDDLE	MIOCENE	NEOGENE
Ml-Mu	Chalks, marls, marly chalks, chalky marls and calcarenites	Pakhna	MIDDLE	MIOCENE	NEOGENE
Ml	Biostrome and bioherm reef limestones (Terra Member)	Pakhna	LOWER	MIOCENE	NEOGENE
Ku-Ou	Chalks, marls, marly chalks, chalky marls with cherts in places as bands or nodules	Lefkara	OLIGOCENE EOCENE PALAEOGENE		PALAEOGENE
Ku	Variably coloured, poorly sorted debrites with angular clasts upto boulder size in a sand and clay matrix. Most clasts are derived from the Mamonia Complex but some are of Troodos ophiolite lithologies	Kathikas	(Maastrichtian)	UPPER	CRETACEOUS
Ku	Melange of older (Triassic-Cretaceous) blocks of yellow quartz sandstone, grey siltstone, serpentinite and other lithologies, entrained in a matrix of silt and bentonitic clay	Moni	(Maastrichtian)	UPPER	CRETACEOUS
Ku	Bentonitic clays interbedded with off-white volcaniclastic sandstones	Kannaviou	(Campanian)	UPPER	CRETACEOUS

TROODOS TERRANE (TROODOS OPHIOLITE)

OLYMPOS (AXIS) SEQUENCE

	LITHOLOGY	FORMATION	UPPER CRETACEOUS (Campanian)	
Ku	Hydrothermal and deep-water sediments: umbers, manganoan shales, pink radiolarian shales and mudstones	Perapedhi		
UPL	Olivine - and pyroxene- phyric, pillow lavas with occasional sheet flows, dykes and hyaloclastites, commonly altered to zeolite facies	Upper Pillow Lavas	VOLCANIC SEQUENCE	UPPER CRETACEOUS (r Cenomanian - Lower Campanian)
LPL	Pillowed and sheet lava flows with abundant dykes and sills, altered to zeolite facies and in places stained with green celadonite	Lower Pillow Lavas	VOLCANIC SEQUENCE	UPPER CRETACEOUS (r Cenomanian - Lower Campanian)
BG	Diabase dykes (>50%) with pillow lava screens, altered to greenschist facies	Basal Group	VOLCANIC SEQUENCE	UPPER CRETACEOUS (r Cenomanian - Lower Campanian)
Db	Diabase dykes upto 3m wide, aphyric and clinopyroxene- and plagioclase-phyric altered to greenschist facies	Sheeted Dykes (Diabase)	INTRUSIVE SEQUENCE	UPPER CRETACEOUS (r Cenomanian - Lower Campanian)
γ	Trondhjemites, granophyres, diorites, quartz-diorites and micro-granodiorites	Plagiogranite	PLUTONIC SEQUENCE	UPPER CRETACEOUS (r Cenomanian - Lower Campanian)
δ	Isotropic gabbros, uralite gabbros, olivine gabbros and layered melagabbros	Gabbro	PLUTONIC SEQUENCE	UPPER CRETACEOUS (r Cenomanian - Lower Campanian)
π	Websterites, clinopyroxenites, orthopyroxenites, and plagioclase-bearing pyroxenites	Pyroxenite	PLUTONIC SEQUENCE	UPPER CRETACEOUS (r Cenomanian - Lower Campanian)
φ	Wehrlites and plagioclase-bearing wehrlites, massive or layered	Wehrlite	PLUTONIC SEQUENCE	UPPER CRETACEOUS (r Cenomanian - Lower Campanian)

	Dunites with subordinate clinopyroxene-dunites	Dunite	
	Tectonized harzburgites with minor dunites and lherzolites	Harzburgite	MANTLE SEQUENCE
	Pervasively serpentinized, tectonized harzburgites with minor dunites and lherzolites	Serpentinite	

ARAKAPAS (TRANSFORM) SEQUENCE

Pb	Angular pillow fragments supported by a matrix of brown-red iron rich mudstone	Pillow Breccia
Vla	Fine-grained interlava volcanogenic sediments: (a) sandstones, grits and silts interbedded with laminated iron and manganese-rich mudstones	Lavas and Volcaniclastic Sediments
Vlb	(b) Coarse polymict breccias with lava, dyke and isotropic gabbro clasts	
Lvs	Olivine - and /or pyroxene - phyric, aphyric pillow lavas with some hyaloclastites, sheet lava flows and dykes, altered to zeolite facies	
Vpl	Vitrophyric pillow lavas, generally olivine-phyric and /or orthopyroxene-phyric	
	Isotropic gabbros, microgabbros and norites	Intrusive Plutonic Rocks
	Poikilitic wehrlites and plagioclase-wehrlites	
	Serpentinite in subvertical shear zones, 50-500m wide	Sheared Serpentinite

MAMONIA TERRANE

	LITHOLOGY	GROUP / FORMATION	EPOCH / PERIOD
Ku	Amphibolite-grade metavolcanics (amphibolites, epidote-hornblende schists), metacherts (quartz-mica schists) and marbles, derived from Dhiarizos Group	Ayia Varvara	U. CRETACEOUS
Tm-Km	Siltstones, calcilutites, radiolarian mudstones, calcarenites and quartzitic sandstones (Episkopi Fm). Stylolitic calcilutites with *Halobia* and ammonites (Marona Fm) Quartzose sandstones with fossil plant remains, mudstones and calcarenites (Vlampouros Fm)	Ayios Photios Group	M. CRETACEOUS - M. TRIASSIC
Tm-Km	Vesicular and amygdaloidal lava breccias, volcaniclastic breccias with volcaniclastic siltstones and radiolarian mudstones (Loutra tis Afroditis Fm). Amygdaloidal or vesicular porphyritic pillow lavas intercalated with pink and grey often recrystallized calcilutites (Fasoula Fm) Partially recrystallized reefoidal limestone breccia occurring as large detached blocks (Petra tou Romiou Fm)	Dhiarizos Group	